SOLUTION ANNEAL HEAT TREATMENT TO ENHANCE MECHANICAL PERFORMANCE OF ADDITIVELY MANUFACTURED IN718

DISSERTATION

David J. Newell, Major, USAF

AFIT-ENY-DS-20-M-274

DEPARTMENT OF THE AIR FORCE
AIR UNIVERSITY

AIR FORCE INSTITUTE OF TECHNOLOGY

Wright-Patterson Air Force Base, Ohio

DISTRIBUTION STATEMENT A. APPROVED FOR PUBLIC RELEASE;
DISTRIBUTION UNLIMITED

The views expressed in this dissertation are those of the author and do not reflect the official policy or position of the United States Air Force, the Department of Defense, or the United States Government.

This material is declared a work of the U.S. Government and is not subject to copyright protection in the United States.

AFIT-ENY-DS-20-M-274

SOLUTION ANNEAL HEAT TREATMENT TO ENHANCE MECHANICAL PERFORMANCE OF ADDITIVELY MANUFACTURED IN718

DISSERTATION

Presented to the Faculty

Graduate School of Engineering and Management

Air Force Institute of Technology

Air University

Air Education and Training Command

in Partial Fulfillment of the Requirements for the

Degree of Doctor of Philosophy in Aerospace Engineering

David J. Newell, B.S.A.E., M.S.M.E.

Major, USAF

March 2020

DISTRIBUTION STATEMENT A. APPROVED FOR PUBLIC RELEASE;
DISTRIBUTION UNLIMITED

AFIT-ENY-DS-20-M-274

SOLUTION ANNEAL HEAT TREATMENT TO ENHANCE MECHANICAL PERFORMANCE OF ADDITIVELY MANUFACTURED IN718

David J. Newell, B.S.A.E., M.S.M.E.
Major, USAF

Approved:

/signed/	15 Jan 2020
Ryan O'Hara, PhD (Committee Chair)	Date
/signed/	16 Jan 2020
Anthony Palazotto, PhD (Committee Co-Chair)	Date
/signed/	16 Jan 2020
Larry Burggraf, PhD (Member)	Date
/signed/	16 Jan 2020
Maj Joshuah Hess, PhD (Member)	Date

Accepted:

/signed/	23 Jan 2020
Adedeji B. Badiru Dean, Graduate School of Engineering and Management	Date

AFIT-ENY-DS-20-M-274

Abstract

The nickel-based superalloy Inconel 718 (IN718) is an excellent candidate among aerospace alloys for laser powder-bed fusion (LPBF) manufacturing. As-built LPBF IN718 has a vertically aligned columnar (001) microstructure which translates into orthotropic mechanical behavior. The post-process heat treatments for IN718 were developed 60 years ago for wrought and cast processes and do not mitigate the columnar microstructure of the LPBF process. Recrystallization is required to remove the columnar microstructure, which would allow for parts to be fabricated on different machines or in different orientations but still achieve the same properties. This research investigated the microstructure of LPBF IN718 as it evolved under a solution treatment of 1160 °C. It was shown that this higher solution temperature mitigated the scan strategy effects and anisotropy resulting from the fabrication process. The grain size, shape, and recrystallization were measured and compared throughout the evolution. Additionally, the X–Y and X–Z planes were compared to find the point in time at which the annealing process resulted in equiaxed, isotropic grains. An equiaxed microstructure was successfully achieved through recrystallization and grain growth. Isotropic tensile properties were achieved following a modified solution treatment at 1160 °C for 4 hours and validated via nanoindentation and tensile testing. Rupture life was not improved by the equiaxed microstructure. Microstructural evolution was simulated in a kinetic Monte Carlo simulation using a novel approach of combining the stored energy of the as-built LPBF IN718 with the boundary energy and pinning particles within SPPARKS. The resulting models accurately approximated the experimental results of recrystallized area and JMAK model constants.

Acknowledgments

This document would not exist without the assistance from a small army of supporters. I am deeply grateful for the help I received along my path to completing this dissertation.

I would like to first thank my advisor, Dr. Ryan O'Hara, for your guidance during this experience, as well as letting me run free to explore the realm of metals additive manufacturing. Your curiosity for knowledge has made this an adventure in discovery for both of us. I would like to thank my co-chair, Dr. Anthony Palazotto, for providing me with the benefit of your incredible depth of knowledge. I would also like to thank my committee members, Dr. Larry Burggraf and Maj Joshuah Hess, for their time and guidance. I would like to thank Greg Cobb for his extensive assistance throughout my research - proof reader, co-author, and SEM guru. Thank you to Jamie Smith, Mike Ranft, and Dr. Volodymyr Sabelkin in AFIT/ENY; without your support my laboratory experiments would not have been possible. And thank you to Ben Doane and Travis Shelton for fabricating my many specimens.

I also received a great deal of help from researchers external to AFIT. I would like to start with those people by thanking Dr. Mike Kirka at Oak Ridge National Lab. Your early advice was invaluable when I began my research into IN718 and additive manufacturing. I would like to thank Tommy Cissel, formerly of AFRL/RX, for taking the time to teach me how to prepare my many metallographic specimens. I would like to extend a hearty thanks to Austin Gerlt with AFRL/RXCM for your assistance with Stochastic Parallel PARticle Kinetic Simulator (SPPARKS) and recrystallization theory. Additionally, thank you to Dr. Eric Payton for your assistance with the modeling (and allowing me nearly unfettered access to Austin).

David J. Newell

Table of Contents

Page

Abstract iv

Acknowledgments v

Table of Contents vi

List of Figures x

List of Tables xv

List of Acronyms xvii

Nomenclature 1

I. Introduction 5

1.1 Overview 5
1.2 Motivation of Research 6
1.3 Problem Statements 11
1.4 Summary of Methodology 15
1.4.1 Metallography 15
1.4.2 Mechanical Testing 16
1.4.3 Kinetic Monte Carlo Simulation 16
1.5 Organization of Dissertation 16

II. Background 19

2.1 Traditional Material Processing 19
2.1.1 Wrought and Cast 20
2.1.2 Mechanical Finishing 21
2.1.3 Heat Treatments 21
2.1.3.1 Stages of Annealing 27
2.1.3.2 Curvature-driven Grain Growth 28
2.2 Background on Superalloys 29
2.2.1 High Temperature Materials 29
2.2.2 Nickel-base Superalloys 30
2.2.3 Development of Alloy 718 32
2.3 Alloy 718 35

Page

2.3.1 Chemical Composition . . . 35
2.3.2 Phases and Precipitates . . . 37
2.3.3 IN718 Heat Treatments . . . 41
2.3.3.1 Annealing . . . 42
2.3.3.2 Stress Relief . . . 43
2.3.3.3 Solution Treatment . . . 44
2.3.3.4 Homogenization and Hot Isostatic Press (HIP) . . . 44
2.3.3.5 Aging . . . 45
2.3.3.6 Quenching . . . 45
2.3.4 Heat Treatment Standards . . . 46
2.3.5 Mechanical Properties . . . 49
2.3.5.1 IN718 Standards . . . 49
2.3.5.2 Anisotropy of Powder-bed Fusion (PBF) Metals . . . 49
2.3.5.3 Hardness . . . 51
2.3.5.4 Tensile Strength . . . 55
2.3.5.5 Creep Resistance . . . 56
2.4 Additive Manufacturing of Metals . . . 58
2.4.1 Powder-bed Fusion Processes . . . 60
2.4.1.1 Laser Powder-bed Fusion . . . 60
2.4.1.2 Electron Beam Melting . . . 61
2.4.2 AM Process Factors . . . 63
2.4.2.1 Process Parameters . . . 64
2.4.2.2 Scan Strategy . . . 66
2.5 Kinetic Monte Carlo (KMC) Modeling . . . 70
2.5.1 Quantification of Energy . . . 74
2.5.2 Johnson-Mehl-Avrami-Kolmogorov (JMAK) model . . . 79

III. Microstructural Characterization . . . 81

3.1 Introduction . . . 82
3.2 Methodology . . . 92
3.2.1 Material . . . 92
3.2.2 Scan Strategies . . . 93
3.2.3 Post-process Heat Treatments . . . 94
3.2.4 Microstructural Characterization . . . 95
3.2.5 Mechanical Testing . . . 95
3.3 Results and Discussion . . . 98
3.3.1 Microstructural Characterization . . . 98
3.3.2 Recrystallization . . . 103
3.3.3 Texture Reduction . . . 108
3.3.4 Grain Growth . . . 110
3.3.5 Mechanical Testing . . . 112

Page

3.4 Conclusions . . . 118

IV. Mechanical Testing . . . 121

4.1 Recap of Background . . . 122
4.1.1 Hardness Recap . . . 122
4.1.2 Tension Recap . . . 122
4.1.3 Creep Recap . . . 123
4.2 Methodology, Mechanical Testing . . . 124
4.2.1 Specimen Fabrication . . . 124
4.2.1.1 Hardness Specimen Fabrication . . . 124
4.2.1.2 Tension Specimen Fabrication . . . 126
4.2.1.3 Creep Specimen Fabrication . . . 130
4.2.2 Post-process Heat Treatments . . . 131
4.2.2.1 Hardness Specimen Heat Treatments . . . 131
4.2.2.2 Tension Specimen Heat Treatments . . . 132
4.2.2.3 Creep Specimen Heat Treatments . . . 133
4.2.3 Methodology, Hardness Testing . . . 134
4.2.4 Methodology, Tension Testing . . . 135
4.2.5 Methodology, Creep Testing . . . 135
4.3 Results and Discussion, Mechanical Testing . . . 137
4.3.1 Results, Tensile Testing . . . 137
4.3.2 Discussion, Tension Testing . . . 143
4.3.2.1 Anisotropy of Tensile Properties . . . 143
4.3.2.2 Yield and UTS . . . 145
4.3.2.3 Elongation at Fracture . . . 148
4.4 Results, Creep-rupture Testing . . . 150
4.5 Discussion, Creep Testing . . . 151
4.5.1 Microstructural Differences of the Creep Specimens . . . 152
4.6 Mechanical Summary . . . 160

V. Microstructure Modeling . . . 161

5.1 Background on Modeling Recrystallization Dynamics . . . 161
5.1.1 Rejection Kinetic Monte Carlo (rKMC) Model and Parallel Processing . . . 162
5.1.2 Curvature-driven Growth as Currently Implemented in SPPARKS . 164
5.1.3 Simulating Pinning Particles . . . 166
5.1.4 Defining SPPARKS Parameters and Executing via Scripts . . . 168
5.1.4.1 Existing SPPARKS Parameters . . . 169
5.1.4.2 Layout of a SPPARKS Script . . . 171
5.1.5 Limitations of SPPARKS . . . 171

Page

5.2 Implementing Stored Energy to Drive Recrystallization 173
5.2.1 Introducing Experimental Data into SPPARKS 174
5.2.2 Combining Stored Energy with Boundary Energy 177
5.2.3 Manipulating Stored Energy within SPPARKS 178
5.2.4 Selecting Suitable Parameter Ranges 180
5.2.5 Optimization Problem and Quality Metrics 184
5.3 SPPARKS Model Results 186
5.4 SPPARKS Model Discussion 192
5.5 Conclusion 198

VI. Conclusions and Recommendations 201

6.1 Microstructural Summary and Contributions 201
6.2 Mechanical Summary and Contributions 203
6.3 Modeling Summary and Contributions 205
6.4 Recommendations 206

Bibliography 207

Appendix: Tabulated Tensile Data 219

List of Figures

Figure Page

1.1 Basic scan strategies used for LPBF: a) strip, b) continuous or snaking, and c) island 14

2.1 Wrought IN718 grains are visible in an EBSD IPF map of a wrought IN718 specimen 22

2.2 Representative heat-treatment process for IN718 24

2.3 Effect of test temperature of tensile properties of cold rolled and aged sheet, IN718 from NASA Materials Data Handbook 31

2.4 First production uses of IN718 34

2.5 Alloy 718 relative input weights for a typical CF6 engine (C-5 Galaxy) 35

2.6 Solidification phase diagram for IN718 39

2.7 Time-temperature-transformation (TTT) diagram for IN718, showing specified heat treatments 43

2.8 Solution treatments used by other researchers with precipitate solvus temperatures 47

2.9 Schematic illustration of indentation load-displacement data showing important measured parameters 53

2.10 Load-displacement plot for LPBF IN718 annealed at 1160 °C/8 h 54

2.11 LPBF schematic 61

2.12 AFIT's Concept Laser *M2 cusing* DMLM metal 3D printer 62

2.13 Arcam A2 EBM schematic 63

2.14 Relationship between effective power and speed in determining the weldability of IN718 66

Figure Page

2.15 Processing regimes for SLM of Ti-6Al-4V depending on laser power and scanning velocity: (I) “processing window, (II) “overheating, (III) “incomplete melting, and (OH) “severe overheating 67

2.16 2D single-track simulation results 67

2.17 Examples of scan strategies 68

2.18 Hexagonal and square kernels with 3rd nearest neighbor 76

2.19 GOS and KAM maps of an as-built specimen 78

2.20 GOS and KAM maps of an 1160 °C/4 h specimen 78

2.21 Typical JMAK recrystallization kinetics during annealing 79

3.1 Three scan strategies commonly used throughout metal additive manufacturing. 83

3.2 Comparison of wrought and as-built LPBF IN718 in the X–Y orientation . . . 84

3.3 Comparison of wrought and as-built LPBF IN718 in the X–Z orientation 85

3.4 FCC IPF and texture intensity legends for all figures 86

3.5 Photos of microstructural examination specimens 93

3.6 Measurements and orientations of the cylindrical tensile specimens 97

3.7 IPF maps of the as-built specimens printed using various scan strategies 99

3.8 IPF maps at 4 hours 100

3.9 IPF maps of the island strategy at various anneal times, X–Y orientation 101

3.10 IPF maps of the island strategy at various anneal times, X–Z orientation 102

3.11 Grain orientation spread (GOS) distribution plots of two representative X–Z island specimens 105

3.12 Recrystallized area as a function of anneal time and view orientation 106

3.13 Average grain size as a function of annealing time and view orientation 107

3.14 Average IPF peak intensities of the as-built, 4-, and 8-hour annealed X–Z specimens 109

Figure Page

3.15 Nanoindentation hardness (H_{IT}) as a function of annealing time and specimen orientation . . . 114

3.16 $YS_{0.2}$ and UTS results for specimens treated with CHT and MHT . . . 116

4.1 Mounted pucks are loaded in the specimen tray of the iMicro nanoindentor for hardness tests . . . 125

4.2 The transverse cross-sections of the cylindrical and rectangular dog-bones are shown with notional slices shown as red stripes . . . 127

4.3 Rectangular dog-bone specimens were built with a 10 mm × 2.5 mm cross-section and a 40 mm gauge length in the 50 mm reduced section . . . 128

4.4 The creep specimen was designed per ASTM E8/E8M . . . 130

4.5 The iMicro nanoindentor was used to conduct hardness tests on the solution-treated LPBF IN718 specimens. Each test consisted of 9 indentations arranged in a 3 × 3 grid with 40 μm spacing. . . . 134

4.6 A creep-rupture experiment is underway on the MTS 810 servo hydraulic machine . . . 136

4.7 Two comparable, representative stress-strain curves from tension testing are shown for specimens P09 and P24 . . . 138

4.8 $YS_{0.2}$ and UTS results for CHT and MHT tension tests . . . 139

4.9 Anisotropy of the tension tests showing the differences between the conventional and modified heat treatments . . . 144

4.10 Comparison of as-built, CHT, and MHT tension test results . . . 146

4.11 The creep-rupture life is presented for CHT and MHT specimens in the horizontal and vertical build orientations . . . 150

4.12 The etched microstructure is shown in the as-built (a) and 8-hr annealed (b) conditions via SEM. . . . 154

Figure Page

4.13 Optical image of the fracture surface of a vertical CHT specimen 155

4.14 SEM microscopy was used to investigate the fracture surfaces of a vertical CHT creep specimen 156

4.15 Mixed-mode fracture of a vertical MHT creep-rupture specimen 157

4.16 Notional fracture paths in MHT creep-rupture specimens are shown by the green lines 158

5.1 SPPARKS performs parallel processing by subdividing the domain across multiple processors 165

5.2 Curvature is calculated by the total number of neighboring pixels in a different grain 167

5.3 A sample SPPARKS input file is shown with the four sections demarcated by the three sets of #==== 172

5.4 The EBSD data for the as-built X–Z specimen, D18, was used as the input for the SPPARKS simulations 176

5.5 The unique grain map of the as-built specimen used as the SPPARKS input provides a little more detail into the grains 176

5.6 Flow chart for pre-processing EBSD data to create a SPPARKS input. 177

5.7 SPPARKS quality metrics (1 of 2) as a function of T_B, dispersion rate, propagated energy, and mulitplied energy 189

5.8 SPPARKS quality metrics (2 of 2) as a function of added energy, pin fraction, runs per recovery loop, and recovery fraction per loop 190

5.9 SPPARKS KAM and grain maps of the simulation input and output for the optimized parameter set 191

5.10 Side-by-side comparison of an 1160 °C/8 h annealed specimen with the simulated SPPARKS KAM map from Run 301 192

Figure Page

5.11 Appearance of annealing twins in annealed IN718 microstructure 193

5.12 Comparison of an 1160 °C/8 h annealed specimen and the SPPARKS unique grain maps 194

5.13 Comparison of carbides in the annealed and simulated microstructures 196

List of Tables

Table		Page
2.1	IN718 Chemical Composition Limits (wt%)	36
2.2	Possible phases in IN718	37
2.3	Standard solution treatments for IN718	46
2.4	AMS 5662 two-step aging for IN718	46
2.5	Anneal heat treatments of other researchers	48
2.6	Tensile and hardness minimum requirements of IN718 forgings	50
2.7	Stress-rupture minimum requirements of IN718 forgings	50
2.8	Synonymous PBF terminology	60
2.9	Build parameters for LPBF and EBM	62
2.10	Typical layer thickness, powder particle size, and minimum feature sizes of PBF and DED processes	64
3.1	Summary of Build Parameters	92
3.2	Chemical Composition of Powderized Alloy	93
3.3	Heat treatment parameters used for the LPBF IN718 tensile specimens	97
3.4	Recrystallized Area Fraction (%) corresponding to Figure 3.12	106
3.5	Average Grain Diameter (μm) corresponding to Figure 3.13	111
3.6	Summary of Hardness Testing	113
3.7	Summary of Tensile Testing	117
4.1	Summmary of fabricated tension test specimens	129
4.2	Heat treatment parameters used for the LPBF tension specimens	132
4.3	Summary of $YS_{0.2}$ and UTS with anisotropy for cylindrical dog-bones	141
4.4	Summary of E and ε_f with anisotropy for cylindrical dog-bones	141
4.5	Summary of $YS_{0.2}$ and UTS with anisotropy for rectangular dog-bones	142

Table Page

4.6 Summary of E and ε_f with anisotropy for rectangular dog-bones 142

4.7 Hall-Petch constants 148

4.8 Hall-Petch comparisons 149

4.9 Creep-rupture results 150

5.1 List of existing SPPARKS functions and parameters 169

5.2 List of stored-energy parameters for SPPARKS 178

5.3 List of SPPARKS functions and parameters 181

5.4 SPPARKS parameter ranges for initial screening test 183

5.5 Experimental values used as targets for the SPPARKS simulations 184

5.6 Equation (5.9) presents the non-linear, constrained optimization problem: . . . 186

5.7 SPPARKS parameters from selected screening tests 187

5.8 SPPARKS parameters from selected screening tests 188

A.1 Tensile test results for the vertical (90°) rectangular dog-bones 219

A.2 Tensile test results for the horizontal (0°) rectangular dog-bones 220

A.3 Tensile test results for the vertical (90°) cylindrical specimens 221

A.4 Tensile test results for the diagonal (45°) cylindrical specimens 222

List of Acronyms

Acronym Definition

AC air cooling

AM additive manufacturing

AMS aerospace materials specifications

ASTM American Society for Testing and Materials

BCT body-centered tetragonal backscattered electrons

CAD computer-aided design

CHT conventional heat treatment

CSA conventional solution anneal

CM247LC nickel alloy CM247, low carbon

CNC computer numerical control

δ delta

DED direct energy deposition

DMD direct material deposition

DMLM direct metal laser melting

DMLS direct metal laser sintering

E Young's modulus

Acronym Definition

ε_f elongation at failure

EBM electron-beam melting

EBSD electron backscatter diffraction

EDM electrical discharge machining

EDS energy dispersive X-ray spectroscopy

FCC face-centered cubic

FWHM full width at half maximum

γ gamma

γ' gamma prime

γ'' gamma double-prime

GOS grain orientation spread

HIP hot isostatic pressing

H_{IT} indentation hardness

H_V Vickers hardness

HRc Rockwell hardness C

IN625 Inconel 625

IN718 Inconel 718

IN738LC Alloy 738, low carbon

Acronym Definition

IPF inverse pole figure

ISO International Organization for Standarization

JMAK Johnson-Mehl-Avrami-Kolmogorov

KAM kernel average misorientation

KMC Kinetic Monte Carlo

LENS laser engineered net shaping

LPBF laser powder-bed fusion

LPF laser powder forming

LSF laser solid forming

MHT modified heat treatment

MSEA Materials Science and Engineering: A

MSA modified solution anneal

OM optical microscopy

PBF powder-bed fusion

PWHT post weld heat treatment

RAC rapid air cooling

rKMC rejection Kinetic Monte Carlo

SEM scanning electron microscopy

Acronym Definition

SLM selective laser melting

SPPARKS Stochastic Parallel PARticle Kinetic Simulator

STA solution-treatment and aged

TEM transmission electron microscopy

Ti6-4 Titanium 6Al-4V

TTT time-temperature-transformation

UTS ultimate tensile strength

XRD X-ray diffraction

$YS_{0.2}$ 0.2% yield strength

Ni nickel

Cr chromium

Fe iron

Co cobalt

Al aluminum

Ti titanium

Nb niobium

NbC niobium carbide

Mo molybdenum

Nomenclature

Elemental Symbols

Al	Aluminum
Co	Cobalt
Cr	Chromium
Fe	Iron
Mo	Molybdenum
Nb	Niobium
NbC	Niobium Carbide
Ni	Nickel
Ti	Titanium

Dimensional Symbols

$\ln K$	Avrami intercept	$unitless$
σ_0	Friction or flow stress [46]	$force/area$
σ_y	Yield stress	$force/area$
σ_x	Tensile strength, traverse direction	$force$
σ_z	Tensile strength, build direction	$force$
τ	Absolute homologous temperature	*normalized temp* ($unitless$)

ε_f	Elongation at fracture	*percent strain*
D	Beam diameter	*length*
d	Average grain diameter	*length*
E	Young's modulus	$force/area$
H_V	Vickers hardness	*unitless*
H_{IT}	Indentation hardness	$force/area$
h_{max}	Maximum displacement, instrumented indentation test	*distance*
HRc	Rockwell hardness C	*unitless*
k_y	Constant in Hall-Petch equation	*unitless*
L	Powder layer thickness	*length*
n	Avrami exponent	*unitless*
P	Beam power	*power*
P_{max}	Applied force, instrumented indentation test	$force$
S	Contact stiffness, instrumented indentation test	$force/length$
T_B	Boltzmann temperature	*unitless*
T_m	Melting temperature	*temperature*
T_{oper}	Operating temperature	*temperature*
UTS	Ultimate tensile stress	$force/area$
V	Scan velocity	$distance/time$

X_V	Recrystallized fraction	$unitless$
$YS_{0.2}$	0.2%-offset yield strength	$force/area$

Microstructural Phases (Section 2.3.2)

δ	delta, a detrimental secondary phase	Ni_3Nb
γ	FCC gamma matrix	Ni
γ'	gamma prime, a strengthening secondary phase	$Ni_3(Al,\ Ti)$
γ''	gamma double-prime, a strengthening secondary phase	Ni_3Nb
MC	metal carbide, typically NbC in AM IN718	(Nb, Ti)C

This page intentionally left blank.

SOLUTION ANNEAL HEAT TREATMENT TO ENHANCE MECHANICAL PERFORMANCE OF ADDITIVELY MANUFACTURED IN718

I. Introduction

The major objectives of this research into laser powder-bed fusion (LPBF) Inconel 718 (IN718) were to: identify a solution treatment that would drive recrystallization, examine the microstructural changes, compare the microstructure to conventional heat treatments, test the mechanical properties, and develop a model to simulate the microstructural evolution. These objectives are introduced here in Chapter 1 and expanded in Section 1.3. Chapter 2 presents background information on additive metals and heat treatments. Chapter 3 and Chapter 4 discuss the microstructure and mechanical properties, respectively. Chapter 5 presents the Kinetic Monte Carlo model as implemented using Stochastic Parallel PARticle Kinetic Simulator (SPPARKS). Chapter 6 presents the conclusions of this research.

1.1 Overview

Advances in the additive manufacturing (AM) of metals are revolutionizing the design and production of critical aerospace components. IN718 is the most widely used superalloy in aerospace applications [118] and highly suited for fabrication by powder-bed fusion (PBF) AM techniques [14, 84, 137]. This research looks for a post-process recrystallization heat treatment to refine the grain morphology of PBF IN718 to resemble wrought IN718.

Grain morphology is highly dependent on both the thermal history and solidification process of a part during fabrication. The resulting grain properties influence static and dynamic mechanical properties such as tensile strength and creep resistance. Producing

AM grains with similar morphology to wrought IN718 is an important step in fabricating AM parts with mechanical properties comparable to wrought parts, as well as generating isotropic behavior. Post-process heat treatments provide the best opportunity to modify the as-built grain morphology. Variations to the existing solution treatment have been explored to produce changes in the microstructure of LPBF IN718. This research included microstructural analysis and mechanical testing of LPBF-fabricated IN718 specimens. Additionally, Kinetic Monte Carlo (KMC) modeling was used to substantiate the linkage between post-process heat treatments and the microstructure. A modified solution anneal (MSA) was identified for LPBF IN718 that generates a more wrought-like microstructure with improved isotropic behavior.

1.2 Motivation of Research

In 1959, Huntington Alloys (Special Metals Corporation, Huntington, WV) introduced a new nickel-based superalloy, Inconel® 718 (IN718) [14]. IN718 possessed a maximum operating temperature (650° C) suitable for high-temperature applications and, compared to existing aerospace alloys, was much less susceptible to post weld heat treatment (PWHT) cracking. This resistance to cracking during the stress relief of welds allowed for the welding of much larger components and, when combined with the high allowable operating temperature, led both General Electric Aircraft Engines (now GE Aviation, Evendale, OH) and Pratt & Whitney (PW, East Hartford, CT) to readily adopt the new alloy for the design and construction of large and complex welded turbine assemblies [95, 118].

The initial research into IN718 was published by its creator, Dr. H. L. Eiselstein of Huntington Alloys [35]. Up until that time, most age-hardened superalloys relied on the stable Ni_3Ti gamma prime (γ') secondary phase for strengthening. However, Dr. Eiselstein identified a new, metastable Ni_3Nb gamma double-prime (γ'') phase as responsible for the age-strengthening effect in IN718. The γ'' was characterized using X-ray diffraction (XRD)

to identify the crystal structure, and the composition was found by chemical analysis, which can now be achieved via energy dispersive X-ray spectroscopy (EDS). During his research, Dr. Eiselstein identified the importance of solution treatments to the formation of strengthening phases. Dr. Eiselstein conducted hardness tests on specimens aged at various temperatures to identify the maximum strengthening effect of the precipitates. His research laid the foundation for the two-step aging heat treatment which remains the standard heat treatment prescribed in aerospace materials specifications (AMS) 5662 [114, 115].

Research into IN718 in the following decades analyzed the microstructural evolution of the grains and precipitates in response to different fabrication techniques and solution treatments [17, 88, 119]. A major concern was the segregation of niobium (Nb) occurring during the slow solidification of cast and wrought techniques, which resulted in the formation of Laves and delta (δ) phases in as-built material [104, 125]. Both Laves and δ phases are detrimental to the age-hardening of IN718, as they sequester Nb needed for γ'' to form. Researchers were able to identify the precipitate phases and the segregation of Nb using EDS in conjunction with scanning electron microscopy (SEM) and transmission electron microscopy (TEM). Long-duration (up to 120 hours) homogenization treatments were used on wrought and cast parts to return the precipitates to solution and mitigate the Nb segregation, but full homogenization could not be reached in a cost-effective amount of time [19].

Dr. Eiselstein's research included the mechanical properties of the new alloy in the solution-treatment and aged (STA) condition. At room temperature, heat treated IN718 ultimate tensile strength (UTS) and 0.2% yield strength ($YS_{0.2}$) are roughly comparable to Titanium 6Al-4V (Ti6-4). However, Ti6-4 has a maximum operating temperature of 420 °C. IN718 has a much higher service limit and retains sufficient mechanical properties up to 650 °C. The creep resistance of IN718 was of particular interest to the aerospace industry. The development of turbines necessitated a material that would maintain its

strength at elevated temperatures. Creep and stress-rupture tests were conducted to evaluate the long-term effect of exposure to the high temperatures and loads. Additionally, high-temperature fatigue tests (crack growth) were performed and reported. One challenge to the developers of IN718 was balancing the creep and fatigue performance. On one hand, larger grains of the wrought material improved creep resistance, but on the other hand, small grains resulted in better fatigue performance. As a result, the current heat treatments were chosen which provide a trade-off between tensile strength, fatigue, and creep resistance [22, 133, 134].

Laser cladding of IN718 appeared in the late 1980's for repairing or coating existing parts. By the mid-1990's, the same technology had evolved into direct energy deposition (DED), one of the first AM techniques for which IN718 was adopted. By 1995, EOS (Electro Optical Systems GmbH, Munich, Germany) had patented a process called "selective laser melting (SLM)," in which a laser melts powdered alloys, layer by layer, to form solid parts [122][1]. In 2002, Arcam (Arcam AB, Mölndal, Sweden) installed the first commercial electron-beam melting (EBM) systems, which used an electron beam in place of a laser to melt the powder [6]. Additive techniques allowed for the production of the increasing complexity of turbine components. In addition, these new AM processes were thermodynamically similar to the welding techniques for which IN718 had been optimized. Combining the required manufacturing complexity and IN718's ability to be fused by laser and electron beams, IN718 became a top candidate for the additive manufacturing of aerospace metals.

Starting around 2000, researchers began exploring the material properties of AM IN718 guided by the previous studies of wrought microstructure and mechanical properties. The research began with attempts to create near fully dense (>99%) parts by both ensuring high-quality powder and minimizing manufacturing defects [150]. These studies looked

[1]This dissertation will use the term LPBF when referring to SLM and other similar laser powder-bed processes.

at process parameters such as laser power and beam velocity to create process maps to establish suitable process windows for printing solid parts. As with the wrought material, researchers used SEM and TEM techniques to characterize the microstructure while testing for mechanical properties. They quickly discovered that the fast solidification rates of powder-bed processes resulted in a much different microstructure; PBF grains were much smaller than wrought grains, the grains tended to grow elongated parallel to the build direction, and precipitates did not evolve as previously experienced in wrought and cast components. This posed a problem for researchers attempting to directly compare the mechanical properties of wrought and AM specimens. This was due to the fact that many of the models predicting material strength were based on grain morphology and precipitates of wrought specimens. The mechanical properties of the AM material with columnar grains were also shown to vary based on the build orientation. This anisotropy presents a significant challenge for material scientists and engineers to predict material strength properties of complex geometries.

The scan strategy used by PBF processes is another factor to be considered in evaluating the microstructure of AM IN718. In 2011, Liu et al. [71] showed that different scan strategies resulted in variations in the localized as-built microstructure, and differences remained in the microstructure after the parts were solution treated and aged. Limited research has been presented on the effects of heat treatments on the microstructural differences of various scan strategies and whether the effect of scan strategy can be mitigated.

Recent work with AM IN718 has attempted to generate a more homogeneous microstructure structure by recrystallizing the as-built microstructure. LPBF IN718 parts achieved partial recrystallization (50%) using a 4-hour solution treatment at 1160 °C by Amato et al. [3]. Other researchers have expressed concern with using higher temperatures that can result in grain growth after recrystallization, which is beneficial for

creep-rupture properties, but detrimental to tensile and fatigue behavior. More testing is required of recrystallized IN718 to determine how detrimental, if at all, higher levels of recrystallization are to these mechanical properties.

A new standard for heat treatment was published in 2018 specifically for metal parts made via PBF [11]. The new standard, ASTM F3301, maintains the previous IN718 solution treatment (954 °C, >10 min, air cool) and age-hardening treatments (718 °C for 8 hours, furnace cool to 621 °C, hold at 621 °C until total aging time has reached 18 hours, air cool) from AMS2774 [114]. ASTM F3301 adds a new stress relief treatment (1065 °C for 1.5 hours), and a new hot isostatic pressing (HIP) treatment (not less than 100 MPa, 1120–1185° C for 4 hours). The time and temperatures of this HIP treatment are similar to the solution treatment used by Amato et al. [3] to produce recrystallization of the AM grains. HIP treatment results in the closing of internal voids in the as-built AM parts, providing an improvement in mechanical properties at higher temperatures.

As researchers continue testing the mechanical properties of AM IN718, work has begun to develop thermal finite-element models of the complex interactions between the energy source and powder bed. The goal of these models is to calculate the thermal history and predict the microstructure for a full 3D-printed part. The computational power required and model resolution has limited most current efforts to one- and two-dimensional models of only single tracks of melted powder. In these studies, researchers compare the model output to the results of their AM system and calibrate model parameters as needed. Much work still needs to be done with existing models not only to capture an entire build, but also to calculate the effects of post-process heat treatments. Once a high-fidelity thermal model could be validated, different heat treatments can be virtually tested and the need for costly experimental work greatly reduced. Additionally, new developments in kinetic Monto Carlo models appear to open a path for modeling the annealing process on the microstructure.

1.3 Problem Statements

The goal of this research was to understand how the solution treatment impacts the microstructure and mechanical properties of LPBF IN718. The generation of a homogeneous microstructure with equiaxed grains, i.e., with an aspect ratio of 1:1, was pursued by recrystallization of the as-built microstructure. Full dissolution of the detrimental δ and Laves phases was attempted to improve the tensile and hardness performance in the STA condition. It was also hypothesized that creep performance would be improved owing to the increase in average grain size after the modified heat treatment (MHT).

The aging treatment for IN718 is well-established and understood. It has been developed to produce the strengthening γ'' and γ' secondary phases. The effectiveness of the aging treatment is directly related to the homogenization of the solution-treated material. Therefore this research looked solely into a variation of the solution treatment. A more detailed introduction of heat treatments is provided in Section 2.1.3. The specific IN718 treatments are discussed in Section 2.3.3.

Problem Statement 1: The fine columnar grains and strong texture of AM IN718 result in anisotropic mechanical properties. Recrystallization and grain growth need to be achieved to mitigate these AM process effects.

The solution treatment for wrought IN718 has a temperature range of 930–1010 °C. However, the solvus temperature of δ is 1020 °C, and the solvus temperature of Laves is 1160 °C. As a result, only a fraction of δ phases and no Laves phases are dissolved. This has been an acceptable trade-off for wrought IN718 as the δ phases prevent grains from growing during the heat treatment process. A higher solution temperature is necessary to fully dissolve the δ and Laves phases to allow for grain growth during the annealing treatment.

The grains in PBF IN718 exhibit a pronounced columnar shape and crystal orientation parallel to the build (Z) direction. This is caused by the high thermal gradients during the manufacturing process. The mechanical properties of AM IN718 display a strong anisotropy as a result of this directional dependence. Wrought grains exhibit an equiaxed shape with a random crystallographic orientation. As a result, wrought IN718 exhibits an isotropic material behavior. Recrystallization of the columnar grains can reduce the strong texture. Amato et al. [3] reported up to 50% recrystallization using a solution treatment of 1160 °C for 4 hours; however the authors did not explicitly report on the grain morphology or texture (crystal orientation) of the recrystallized regions.

After a material has fully recrystallized, it may start to experience grain growth. Larger grains are detrimental to the tensile strength and fatigue resistance, but they are beneficial to creep-rupture resistance. Wrought materials have very large grains (ASTM grain size 5, average grain diameter 63.5 μm) [115]. Current solution treatments are designed to limit grain growth by the presence of grain boundary δ phases. Since AM IN718 specimens start out with a much finer grain size (ASTM grain size 11, average grain diameter 7.9 μm), it is hypothesized in this research that the grain boundary δ can be removed by the solution treatment and the grains allowed to grow without harming the mechanical properties.

Hypothesis 1.A: Full dissolution of δ and Laves will allow the grains to recrystallize, removing the AM process-induced columnar grains.

Objective 1.A: Characterize the grain morphology and material texture in the as-built and modified solution-treated LPBF IN718 specimens using electron backscatter diffraction (EBSD). Compare to LPBF IN718 specimens treated with the original solution treatment. This objective is addressed in Chapter 3.

Hypothesis 1.B: Achieving recrystallization will reduce the anisotropy of the LPBF IN718 specimens.

Objective 1.B: Conduct tensile tests on LPBF IN718 specimens printed at 0°, 45°, and 90° (w.r.t. build direction). Test specimens in the as-built, conventional solution anneal (CSA) + aged, and MSA + aged conditions. Compare results to identify the existing anisotropy and resulting improvement in isotropic behavior. This objective is addressed in Chapter 3.

Problem Statement 2: Different manufacturers use different scan strategies to print LPBF parts, creating small differences in the microstructure of the as-built parts.

There are various scan strategies used to fabricate LPBF parts. Some basic strategies are shown in Figure 1.1. Each strategy produces unique variations on individual parts, even within the same build. Solution treatments can provide a homogenizing effect on the microstructure. This homogenization may help to reduce these microstructural variations, eliminating any difference between the parts. Limited research has been reported comparing the difference of various scan strategies after solution treatments.

Hypothesis 2: If recrystallization and grain growth are achieved by the modified solution treatment, then scan-strategy differences in the microstructure can be eliminated.

Objective 2: Conduct EBSD analysis on the as-built and modified solution-treated parts. Compare the microstructure of specimens built using different scan strategies after being treated with the MSA. This objective is addressed in Chapter 3.

Problem Statement 3: The grain size of IN718 influences its tensile strength and creep resistance. Modifying the grain size through annealing will change the mechanical properties.

Hypothesis 3: The MSA will result in smaller grains at shorter annealing times and larger grains at longer times. The smaller grains will result in increased tensile strength as predicted by the Hall-Petch relationship [45]. The larger equiaxed grains will result in better creep performance.

Objective 3: Compare tensile and creep tests results with grain sizes and annealing time. Characterize the relationship between grain size and mechanical property. This objective is addressed in Chapter 3 and Chapter 4.

Problem Statement 4: Mesoscale simulations of LPBF IN718 have simulated the creation of columnar grain structures, but they have not accounted for the residual stresses within the as-built LPBF IN718 material.

Simulations of the solidification behavior of LPBF IN718 have simulated the creation of columnar structures [110]. Additional research has used SPPARKS to model annealing behavior with equiaxed grains and to a lesser extent, abnormal and columnar grain structures [111]. However, these KMC simulations relied on curvature-driven growth and ignored the stored energy of residual stresses within the material.

Hypothesis 4: An implementation of KMC models within SPPARKS can incorporate residual stresses from EBSD data and be successfully calibrated using a precise set of experimental data. This model can simulate the grain growth and recrystallization such that the final grain sizes, recrystallized fraction, and rates of growth are matched to the experimental data.

Objective 4: Incorporate experimental EBSD data as the seed for SPPARKS simulations. Conduct a parameter optimization using SPPARKS to perform kinetic Monte

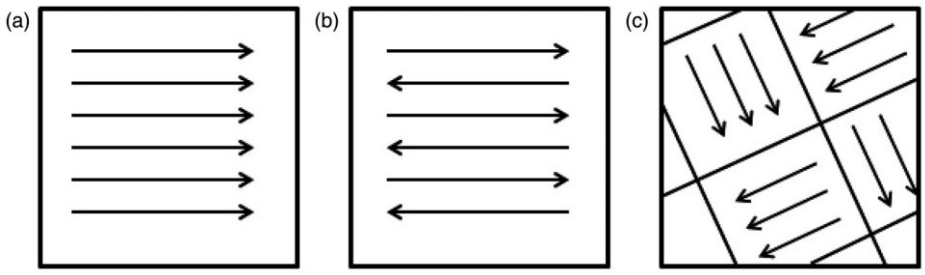

Figure 1.1: Basic scan strategies used for LPBF: a) strip, b) continuous or snaking, and c) island. Figure modified from [117, Fig. 16]

Carlo simulations with the as-built microstructure to simulate the microstructural evolution. Find a parameter set that matches the average grain size, recrystallized fraction, and Johnson-Mehl-Avrami-Kolmogorov (JMAK) variables of the experimental microstructural data. The experimental data for this objective is obtained in Chapter 3, and the objective is addressed in Chapter 5.

1.4 Summary of Methodology

To evaluate the proposed hypotheses, the microstructure of varying solution-treated LPBF IN718 specimens were characterized and the mechanical properties tested. IN718 specimens were printed using LPBF and subjected to varying solution treatments with a range of exposure times and temperatures. The microstructural evolution of the annealed specimens was characterized by optical microscopy (OM) and SEM. Mechanical properties were evaluated by hardness testing. A selection of the annealed specimens were subjected to the standard aging heat treatment and tested in the solution-treatment and aged (STA) condition (aging treatment per AMS 5662 [115]). Hardness, tension, and creep testing were conducted on these specimens. The microstructural development and mechanical properties were characterized and compared to both wrought and IN718 STA specimens treated with the original solution treatment (per AMS 5662 [115]). Kinetic Monte Carlo simulations were run using SPPARKS and calibrated using the previously-obtained EBSD data.

1.4.1 Metallography.

Metallography is the study of the structure and composition of metal alloys through microscopic examination. The primary tools used to characterize the microstructure were OM and SEM. The SEM analysis included EBSD and EDS. EBSD analysis provided details of the grain structures and was used to evaluate the amount of recrystallization that occured, as well as quantifying the change in microstructural texture. EDS quantified the elemental composition and was used to identify segregation of specific elements (e.g.,

Nb) as well as identify secondary and precipitate phases such as niobium carbide (NbC). Specimens were characterized by grain size, grain shape, and grain texture.

1.4.2 Mechanical Testing.

Mechanical testing was conducted on the conventionally heat-treated CHT and MHT LPBF IN718 specimens. Nano-indentation testing measured the Young's modulus (E), indentation hardness (H_{IT}), and Vickers hardness (H_V). Tension testing measured E, $YS_{0.2}$, UTS, and elongation at failure (ε_f) per ASTM E8 standards [7]. Rupture testing was conducted at 650 °C to evaluate the high temperature material deformation (time to rupture) per ASTM E139 standards [8]. Hardness, tensile, and rupture properties of the LPBF specimens with the MHT were compared against LPBF and wrought specimens with the conventional heat treatment (CHT) to evaluate the differences between solution treatments.

1.4.3 Kinetic Monte Carlo Simulation.

Using a novel implementation, the grain growth of LPBF IN718 was modeled using Stochastic Parallel PARticle Kinetic Simulator (SPPARKS) [43]. SPPARKS is a kinetic Monte Carlo simulation written by Sandia National Labs. The main purpose of SPPARKS is modeling materials at a mesoscale level, meaning between the atomic scale and continuum mechanics. While SPPARKS is more commonly used to model grain formation, for this research the code was modified to account for recrystallization behavior of IN718. Models were generated of simulated annealed IN718 and compared to the EBSD data collected during the metallographical examination.

1.5 Organization of Dissertation

The following chapters of this dissertation expand on the contents presented in this first chapter.

Chapter 1 (p. 5) provides the context for the research conducted in this dissertation.

Chapter 2 (p. 19) introduces heat treatments since their inclusion is necessary for discussing superalloys in general and IN718 in particular. A brief history is provided on

superalloys and the development of IN718, leading into the properties of IN718. This chapter also presents the additive manufacturing of metals, and how IN718 has been involved with AM processes. The final section covers the state of modeling efforts for additive metals processing.

The methodology, results, and discussions are broken down into the three key areas of microstructural characterization, mechanical testing, and SPPARKS modeling. Each of these areas is given its own chapter, Chapter 3, Chapter 4, and Chapter 5 respectively.

Chapter 3 (p. 81) covers the tools used to characterize the microstructure, the influence of heat treatments on microstructural characteristics (e.g., average grain size, texture, etc.), and the results of some initial tensile testing. The chapter consists solely of the journal paper accepted to Materials Science and Engineering: A (MSEA), which has a 2018 Journal Impact Factor of 4.081 per Clarivate Analytics [25, 38]. MSEA's principal focus is the relationship between microstructure, processing, and mechanical strength of structural materials.

Chapter 4 (p. 121) includes additional hardness and tension testing (beyond that included in Chapter 3) and rupture testing to quantify the mechanical properties, and the related anisotropy, of LPBF IN718.

Chapter 5 (p. 161) focuses primarily on SPPARKS as the modeling tool of choice to simulate the evolution of the microstructure resulting from the modified annealing process.

This page intentionally left blank.

II. Background

The scope of the research contained in this dissertation requires the introduction and discussion of several fields of engineering that all intersect with the laser fusion of powdered metal alloys and are directed to the research objectives outlined by the Problem Statements in Chapter 1. The background begins with a discussion of materials processing concepts in Section 2.1 (p. 19), including post-process heat treatments. An understanding of this topic will be helpful to the reader before proceeding to subsequent sections. Section 2.2 (p. 29) defines high-temperature materials, and more specifically superalloys, and then provides a brief history of superalloys culminating with the development of Inconel 718 (IN718). Section 2.3 (p. 35) provides a detailed description of IN718. The precipitate phases of IN718 are discussed in detail in Section 2.3.2 (p. 37), as well as the specific heat treatment processes used to generate the strong material properties of IN718. Section 2.4 (p. 58) introduces additive manufacturing (AM) processes in general and then focus on powder-bed fusion (PBF). PBF is further broken down into laser powder-bed fusion (LPBF) and electron-beam melting (EBM). The discussion introduces several metal alloys that have been shown to be well-suited to PBF processes.

2.1 Traditional Material Processing

This section introduces terminology and background on traditional material processing, and then expands on how this processing is applied to IN718. Traditional manufacturing methods of wrought and cast are introduced in Section 2.1.1. Understanding the output from the traditional manufacturing processes will aid in the discussion on heat treatments. General terms and concepts for heat treatments are introduced in Section 2.1.3. This terminology assists in the discussion of IN718-specific heat treatments in Section 2.3.3. The

mechanical properties of wrought and cast solution-treatment and aged (STA) IN718 are compared to STA LPBF IN718 in Section 2.3.5.

All of the processes presented in this section impart some amount of heterogeneity during the fabrication. Solidification and working processes introduce internal strains as a result of applied thermal and mechanical stresses. These residual strains may be imparted through the result of mechanical processes (hot- or cold-working, rolling, forging) or through thermal processes such as thermal expansion and contraction. The strain is carried through a deformation of the material's crystal lattice. During fabrication, these residual strains may accumulate unevenly, especially for larger parts with non-uniform cooling. The strain distorts the primary gamma (γ) matrix of IN718, which can impact the grain morphology and mechanical properties. Heat treatments are used to mitigate the heterogeneity and residual stresses of metals.

2.1.1 Wrought and Cast.

There are two traditional methods of manufacturing IN718. *Wrought* processes are a family of techniques that involve physically working a material to create a final part shape. Common wrought processes include forging, die casting, hot-working, cold-working, and extruding. *Casting* is the other traditional method and involves melting a material, then pouring the molten material into a mold to create a part. Wrought IN718 typically provides higher mechanical properties (e.g., tensile strength and creep resistance) than casting; however, casting allows for the creation of more complex geometries.

Investment casting is a common casting technique for IN718. Investment casting creates a ceramic mold around a wax prototype. This technique can produce complex components with internal piping and cooling passages to reduce weight and the number of parts. The wax is removed by heating the mold, melting out the wax and leaving a void space. The mold is then filled with a molten liquid to create the metal part with the same design as the wax prototype. After solidifying, the mold is broken apart to free the new

part. This method produces the complex geometries that AM processes are well-suited to replace.

Cast and wrought processes produce regular-shaped grains with similar horizontal and vertical dimensions. Grains of this shape are termed *equiaxed*. Cast and wrought grains exhibit similar characteristics regardless of the direction the material is viewed. Figure 2.1 shows the electron backscatter diffraction (EBSD) pattern of a wrought IN718 specimen. Several grains appear to have a stripe running through them–this is known as crystal twinning, and it occurs when two crystal lattices share lattice points. For the IN718 FCC crystal structure, these twins have specific angle relationships defined by the crystal geometry regardless of chemical composition. The twins can be considered together as one effective grain and are often counted as such during metallographic analysis. For IN718, twinning does not occur in the as-built AM specimens. The appearance of crystal twinning helps indicate the presence of recrystallization.

2.1.2 Mechanical Finishing.

Mechanical processing may be required to clean up a part after the fabrication process. Metals are typically machined in the annealed and stress-relieved condition when the metal is softer and more easily machined. The final aging heat treatments are applied after machining to harden and strengthen the part. A small subset of the specimens in this research will receive mechanical finishing. However, most of the mechanical specimens were tested with the as-fabricated surface finish to reflect as-built surface conditions that would be found in operational uses.

2.1.3 Heat Treatments.

Heat treatments are metallurgical processes used to alter the chemical and mechanical properties of a metal alloy by intentionally heating and cooling the material. Heat treatments do not refer to incidental heating of the manufacturing process, which will also be an important factor when considering the high-energy PBF processes. Heat treatments

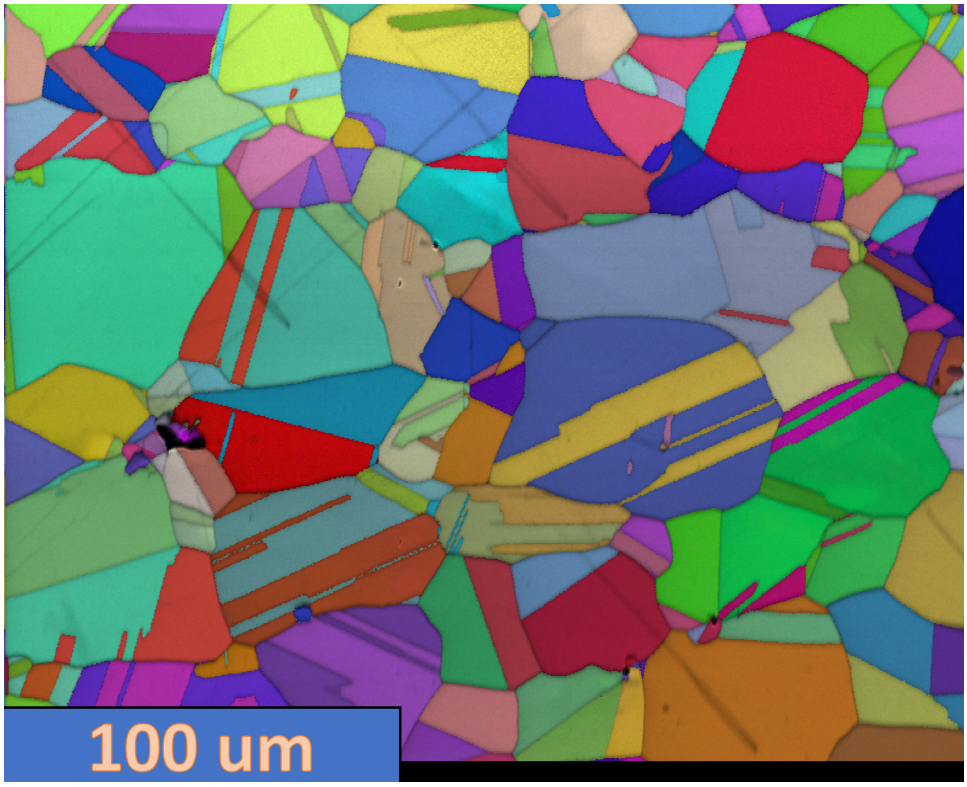

Figure 2.1: Wrought IN718 grains are visible in an EBSD IPF map of a wrought IN718 specimen. Image by G. Cobb, AFIT/ENY.

are intentional post processes, applied once the part has reached its final physical form. All of these processes are conducted at temperatures below the melting point of the material, but high enough so that thermal diffusion can occur within the material.

For the heat treating of IN718, there are four processes to be concerned with: *annealing*, *hot isostatic pressing* (HIP), *aging*, and *cooling*. Annealing is used to undo stresses introduced during fabrication. HIP is used to reduce porosity in fabricated parts. Aging increases strength through the creation of precipitates to enhance the material matrix. Cooling is applied after each annealing, HIP, and aging step to cool the material and control or halt the phase transformations within the microstructure. Water or oil *quenching* is cooling by immersion in a liquid bath.

The heat treatment for IN718 typically involves annealing, quenching, aging, and quenching again. A representation of the heat treatment for wrought IN718 is shown in Figure 2.2. Processing of AM IN718 will often include a stress-relief cycle as the first step and prior to removing the parts from the build plate. This difference between wrought and AM post-processing is discussed further in Section 2.3.3 (p. 41), along with more details on the treatments specific to wrought or AM IN718.

Annealing is "a high-temperature treatment designed to produce a recrystallized grain structure and softening in a work-hardened alloy" [114]. The temperatures for annealing must be high enough to activate thermal diffusion; some materials have a defined recrystallization temperature, which is the lower bound for annealing. Thermal diffusion is the process by which atoms in a crystal structure reorient themselves to minimize the stored energy of the system; this is discussed more with the modeling in Section 2.5. There are multiple purposes for annealing a metal alloy: removal of built-up stresses (stress relieving), dissolving of precipitates (solution annealing), and ensuring the alloying elements are evenly distributed (homogenization). There are three stages associated with

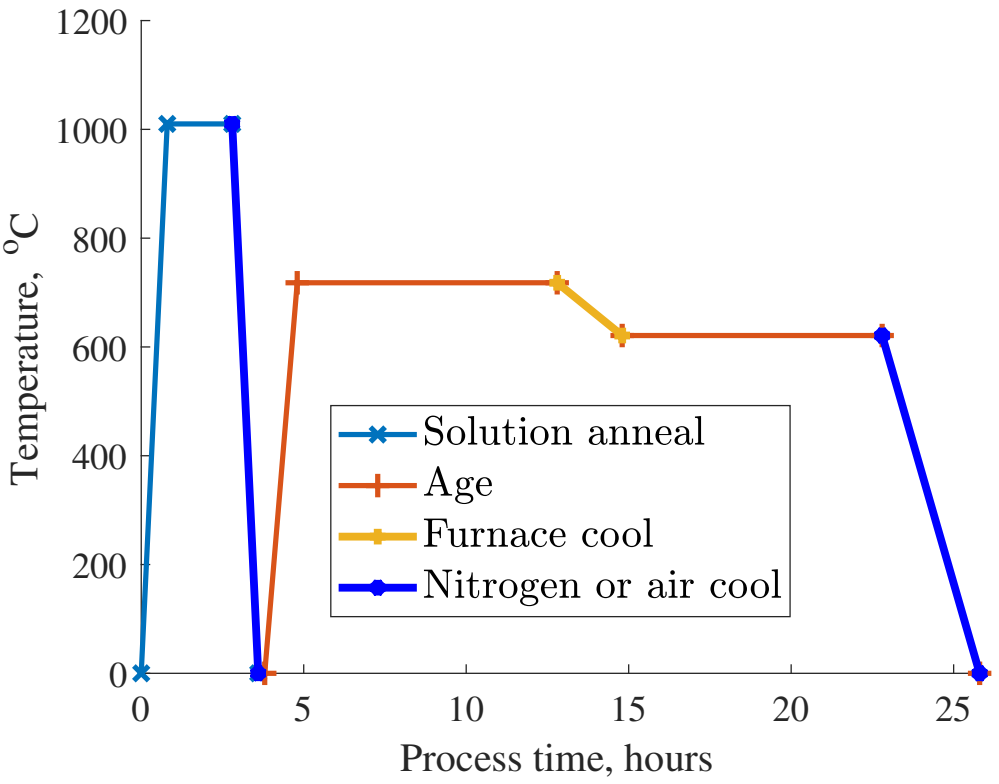

Figure 2.2: Representative heat-treatment process for IN718

the annealing process: recovery, recrystallization, and regrowth. These stages will be discussed in Section 2.1.3.1.

Stress relieving is a specific annealing treatment that removes stresses introduced during fabrication, also via thermal diffusion. These residual stresses can result from mechanical processes like hot- or cold-working, or thermal processes such as thermal expansion and contraction. During fabrication, these residual stresses may accumulate unevenly within the part and build plate, especially for larger parts. For LPBF, if a part is separated from the build plate while the stresses are not uniformly distributed, one or both of the part and build plate will warp. For this reason, stress relieving is performed prior

to removal of the build plate, especially for larger parts. Most stress-relief treatments are relatively quick (30 min) compared to solution annealing or homogenizing.

Solution annealing, also referred to as solution treatment or solutioning, is a specific annealing process that dissolves existing precipitates back into the solution. The temperatures for solution annealing are typically the same or slightly higher than stress relieving but held for a longer duration (1–4 hours). Solution annealing is a critical pre-treatment for age hardening, as the dissolution of all precipitates allows for proper forming of the strengthening phases. *The solution treatment of IN718 is the focus of the research outlined in this dissertation.*

Homogenizing is the last annealing treatment explicitly applicable to IN718. Homogenization relies on atomic diffusion within the matrix to evenly distribute the various alloying elements. This prevents the formation of some secondary phases, such as Laves, that require a sufficiently high concentration of specific elements to form. Diffusion activity increases with temperature, so a high temperature needs to be applied for a longer duration of time (typically >4 hours) to allow for sufficient movement of atoms. After homogenization is complete, the material is left in an ideal solutioned state.

Hot isostatic pressing (HIP) is a heat treatment with the addition of an applied pressure. It is commonly used to reduce porosity within fabricated cast or AM parts. Similar to homogenization, the HIP process relies on diffusional movement to seal pores (closed by the applied pressure). To ensure sufficient diffusion, the temperatures required for HIP are similar to those used for homogenization. Researchers are currently looking to accomplish HIP and solution treatment simultaneously [58].

Aging, or age hardening, is an "intermediate temperature heat treatment causing hardening and strengthening of the alloy by the precipitation of intermetallic compounds and, in some instances, of carbides from supersaturated solid solutions" [114, p. 12].

Precipitation hardening is synonymous with age hardening[2]. Age hardening works by raising the material temperature enough so that secondary phases can form within the microstructure.

Cooling reduces the temperature of the material to a point where the microstructural changes are stopped or at least greatly slowed down. Cooling can be provided by "air, oil, water, water-polymer solutions, salt, brine, argon, helium, hydrogen, nitrogen, and vacuum" [114]. *Air cooling* (AC) is the "rate at which the parts, separated from one another sufficiently to allow free movement of air between them, would cool to room temperature after being removed from the furnace and placed in ambient air without forced motion of the air" [114]. *Rapid air cooling* (RAC) is the "rate at which the parts, separated from one another sufficiently to allow free movement of air between them, would cool to room temperature after being removed from the furnace and placed in shop air with rapid motion of the air forced over the parts by a fan or blower" [114]. *Quenching* is performed by immersing the part in a bath to cool much more quickly than air cooling; quenching is often performed to halt transformations in cases where undesirable precipitates or secondary phases are able to form rapidly after heat treatment. If a part is undergoing a two-stage heat treatment, *furnace cooling* is often allowed. This is much slower than air cooling or quenching and is enacted by reducing the furnace temperature over a defined time period, e.g.- 100 °C per hour. Furnace cooling can be used when the metallurgical transformations are relatively stable, and to reduce the number of handling steps. Typical rates for air cooling are 100–300 °C per minute. RAC is loosely defined as being faster than air cooling and can reach rates of 30 °C per second (1800 °C per minute). Water quenching can reach cooling rates up to 150 °C per second [136].

Each of these heat treatments is applied during the fabrication of IN718, whether it is wrought, cast, or additively manufactured. The application of solution annealing and aging

[2]This dissertation will use the term aging or age hardening to avoid confusion in the extensive discussion of the precipitate phases formed during aging.

is critical to the strength of the finished material. The specific times and temperatures of the overall process will be discussed in Section 2.3.3.

2.1.3.1 Stages of Annealing.

As a material undergoes annealing, it will attempt to minimize its internal energy by reorganizing its crystal structure. This reorganization takes effect in three distinct stages. The three stages of annealing are:

1. Recovery
2. Recrystallization
3. Grain Growth

As an annealing treatment is applied, these stages will occur sequentially as listed. Some heat treatments are specifically trying to complete one stage as fully as possible without initiating the next stage. For example, stress relieving is designed to achieve recovery without reaching recrystallization. Understanding these three stages is helpful when evaluating annealed microstructure. Each stage has visible and measurable differences that can be evaluated to determine the relative completeness of each stage. Using these metrics, it is possible to compare different annealed microstructures to determine the effectiveness of an applied temperature and treatment time.

Recovery is a process by which deformed grains can reduce their stored energy by removing or rearranging defects in their crystal structure. These defects increase the tensile strength of a material. The recovery process reduces the dislocation density of the material, and results in a decrease in the material's ultimate tensile strength (UTS) and 0.2% yield strength ($YS_{0.2}$), with a corresponding increase in ductility.

Recrystallization is a process by which deformed grains are replaced by new defect-free grains that nucleate and grow until the original grains have been entirely consumed. Recrystallization is usually accompanied by a reduction in the strength and hardness of a material and a simultaneous increase in the ductility. Recrystallization is differentiated

from recovery and grain growth. In recovery, high angle grain boundaries (those with greater than a 10° misorientation) do not migrate. In grain growth, the driving force is due to the overall reduction in grain boundary length throughout the material [50]. Recrystallization can also be accompanied by grain growth as recrystallized grains appear to consume the prior deformed grains.

Grain growth is the increase in size of the grains. In annealing, grain growth occurs after recovery and recrystallization are complete. At that point the only way to further reduce the internal energy of the material is to reduce the grain boundary area, or the length when looking at a 2D image. The Hall-Petch effect relates the grain size of a material to its tensile strength. As grain size increases, tensile strength will decrease. However, at high temperatures the creep behavior (both Coble and Herring-Nabarro) shows the opposite relationship as the increase in grain size and boundary increases the amount of energy required to cause grain boundary sliding [56]. Balancing the trade-off between tensile and creep behavior requires choosing a heat treatment that either promotes or prohibits grain growth.

2.1.3.2 Curvature-driven Grain Growth.

During the recrystallization and grain growth stages of annealing, movement of the boundaries is driven by desire to reduce the energy of the system. In idealized grain growth, the boundary movement is driven by the local curvature in an effort to decrease the overall grain boundary area (or length in 2D). Curvature-driven grain growth occurs because of the geometry-influence energy of the grain boundaries. Grain boundaries represent regions of higher energy due to the partially bonded atoms on the surface of the crystal lattice. These surface atoms have a higher energy state when compared to the atoms inside the crystal. The density of partially bonded surface atoms increases as the radius of curvature decreases. This increase in density thereby increases the energy of the boundary, making the grain surface more susceptible to erosion [126]. In order to reduce this energy, the

grain boundaries must move toward the center of curvature, resulting in the curvature-driven grain growth. Existing research has focused on modeling curvature-driven grain growth [103, 111, 143]. However, this idealized version of grain growth ignores other contributions to the energy of the system. Specifically, this research looks at including the residual stresses of the as-built LPBF IN718 in the modeling of the annealing behavior of the microstructure.

2.2 Background on Superalloys

The history and development of high temperature materials, superalloys, and IN718 are covered here to illustrate the operational requirements and limits of the alloy. This section is presented to provide sufficient background to the reader to appreciate the evolution of high-temperature metals, culminating in the research on IN718. As metals additive manufacturing continues to grow, it is predicted the development of future superalloys will be tuned to the AM processes will follow a similar developmental path as IN718 as documented by Eiselstein [35].

2.2.1 High Temperature Materials.

High temperature materials are defined as those that can maintain their properties at elevated working temperatures. Most metals have an operational temperature limit up to about 50% of the melting point (on an absolute scale, i.e., Kelvin), above which the material properties are reduced and linear elastic assumptions are no longer valid. Reed [109] provides three characteristics desirable in high-temperature materials.

First, the material must be able to withstand loading at an operating temperature close to its melting point. To compare a material's operating temperature, T_{oper}, to its melting point, T_m, researchers have defined an *absolute homologous temperature*, τ, as given in Equation (2.1). High temperature materials are considered materials with $\tau \geq 0.6$. [109]

$$\tau = \frac{T_{oper}}{T_m} \tag{2.1}$$

Second, the material must maintain its strength for long time periods. Tensile strength is typically considered for standard operating temperatures, but at high temperatures creep resistance must be considered. When a material is exposed to loading at high temperatures, the material may experience plastic deformation even though the load is much less than the room temperature $YS_{0.2}$. The loss of tensile strength as a function of temperature is presented in Figure 2.3 [84]. If this plastic deformation is allowed to continue, the material will eventually rupture. Depending on how this failure is characterized, this phenomenon is referred to as *creep resistance*, *creep-rupture strength*, or *stress-rupture strength*. Creep is the time-dependent plastic deformation under a fixed stress at an elevated temperature and will be discussed further in Section 2.3.5.5 [57]. Due to the environment in a turbine engine, creep resistance is as important for high temperature materials as $YS_{0.2}$ and UTS. Fatigue, or cycle, capability is also a concern for high temperature materials. Turbine components experience high temperatures, loading, and cycling [109]. Figure 2.3 shows the loss of tensile strength of IN718 as a function of temperature demonstrating the material's strength at higher temperatures. The curves for UTS and $YS_{0.2}$, labelled F_{tu} and F_{ty} respectively, drop slowly with an increase in temperature from room temperature up to 600–650 °C. After 650 °C, both values show a precipitous drop demonstrating the practical limit of IN718 application. The percent elongation (Elong, %), shown at the bottom of Figure 2.3, increases with the test temperature and corresponding to the loss of tensile strength.

Third, the material must tolerate severe operating environments. For metals, this means resisting corrosion and oxidation in applications ranging from coal power generation to aircraft turbines to deep-sea drilling. [109]

2.2.2 Nickel-base Superalloys.

Superalloys are a nickel-based family of high-temperature alloys developed extensively for the aerospace industry. "The technological development of the superalloys is

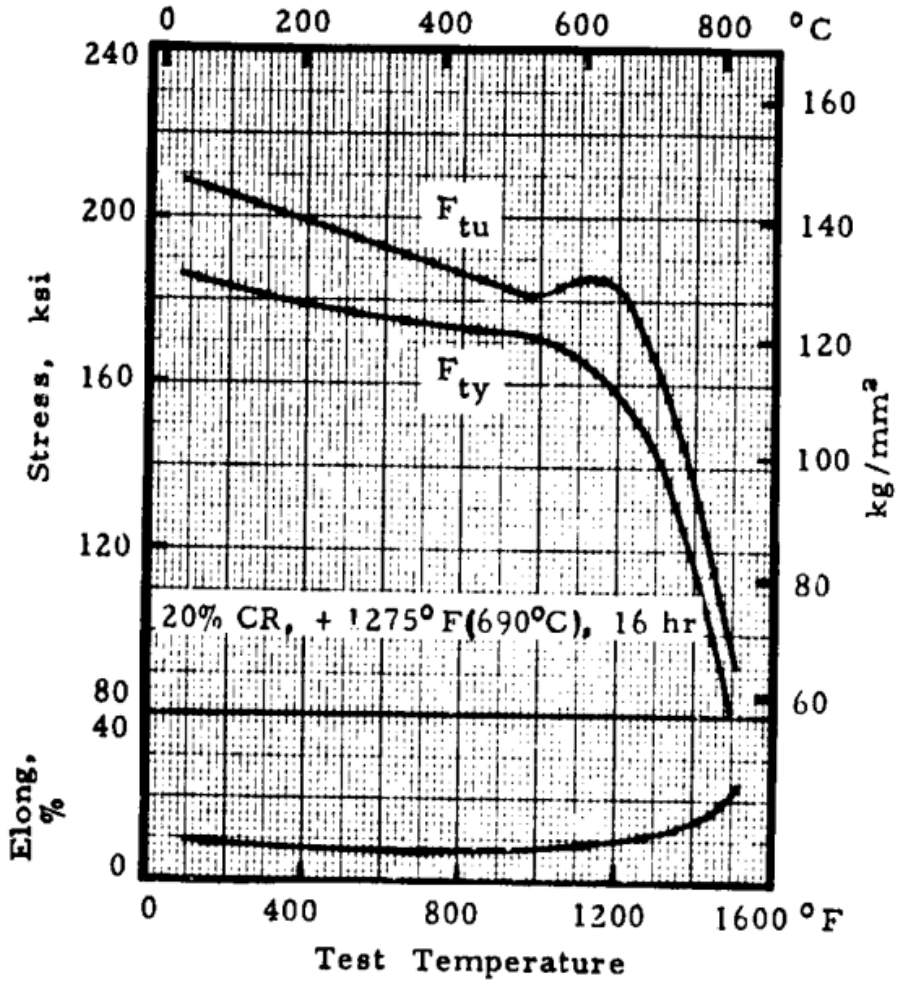

Figure 2.3: Effect of test temperature of tensile properties of cold rolled and aged sheet, IN718 from NASA Materials Data Handbook ([84, Fig.7.4143, p. 46]). The curves for UTS and $YS_{0.2}$, labeled F_{tu} and F_{ty} respectively, drop slowly with an increase in temperature from room temperature up to 600–650 °C. After 650 °C, both values show a precipitous drop demonstrating the practical limit of IN718 application. The percent elongation is also shown in the chart, with an increase in elongation related to the increase in test temperature and also corresponding to the loss of tensile strength. NASA figure used in accordance with NASA's Media Usage Guidelines [29].

linked inextricably to the gas turbine engine" [109, p. 2]. The chemical composition of superalloys consists of up to 14 alloying elements, with the principal alloying elements nickel (Ni), chromium (Cr), iron (Fe) and cobalt (Co). The resulting properties of superalloys are high tensile strength, high resistance to creep, and resistance to oxidation and corrosion. These traits are required of turbine components. Superalloys are used in locations where typical high-strength titanium (Ti) and aluminum (Al) aerospace alloys are not feasible due to the loss of strength and/or corrosion associated with combustion.

Ni is the preferred basis for high-temperature alloys. Justification for the use of Ni as the solvent is provided by Reed [109, pp. 25-29]: Ni's face-centered cubic (FCC) crystal structure; its moderate cost; and low rates of thermally activated processes. Ni has an FCC crystal structure which is both tough and ductile. Ni is stable in the FCC form without any phase transformations from room temperature to its melting point. Other transition metals that display these properties are the platinum group metals which are dense and very expensive. Ni possesses a low rate of thermally activated diffusion which provides microstructural stability, and therefore creep resistance, at elevated temperatures. The resulting high strength and corrosion resistance of superalloys has also seen their use expand to non-aerospace applications such as the biomedical and petrochemical industries [34].

2.2.3 Development of Alloy 718.

The Inconel® family of Ni-based alloys was developed by the International Ni Company in the 1930s, hence the prefix on the alloy of "inco" [147]. The trademark for the brand name of Inconel is currently held by the Special Metals Corporation group of companies [129]. Other names for this family of alloys refers to them by their 3-digit identifier as Ni Alloy XYZ or Alloy XYZ. There is also a unified numbering standard specified jointly by ASTM and SAE. For example, Inconel 718 (IN718) is also referred to

throughout literature as any of: Ni Alloy 718; Alloy 718; UNS N07718. For this paper, the nomenclature Inconel 718 and IN718 will be used.

IN718 was incidentally discovered during the search for a solid-solution-strengthened non-age-hardenable alloy by H. L. Eiselstein of Huntington Alloys (Special Metals Corporation, Huntington, WV) [36, 118]. During screening tests, Eiselstein found that adding niobium (Nb) resulted in an unexpectedly large aging response. The resulting alloy had strength comparable to the best superalloys available. In addition, this new alloy lacked the sensitivity to strain-age cracking of previous alloys, which had posed a problem during post-weld heat treatments [69]. The original search for a solid-solution-strengthened alloy would eventually result in Inconel 625 (IN625) in 1962 [36].

> *Every GEAE engine family applies 718 as the material of choice to applications below approximately 650 °C (1200 °F).* [118]

Engineers at General Electric Aircraft Engines (GE Aviation, Evendale, OH) recognized that this new alloy presented an ease of manufacturing over Rene 41 with similar performance. With its excellent balance of tensile and creep properties at a reasonable cost, GE adapted IN718 for use in the X211 nuclear engine and GE4 supersonic transport turbine [118]. Even though neither of these programs were released for production, the programs provided a basic understanding of the alloy's behavior.

IN718 made its first GE production appearances in the 1960's with the J93 engine for the prototype XB-70 (Figure 2.4a), as well as the TF39 turbofan engine for the C-5 Galaxy (Figure 2.4b), both programs for the US Air Force [118]. The TF39 turbofan would be further developed into the CF6 family of engines (Figure 2.4c). Figure 2.5 illustrates the breakdown of the CF6-6 engine by material weight, showing that IN718 comprises 34% of a finished engine. The alloy was used in forgings, airfoils, and critical hardware [118].

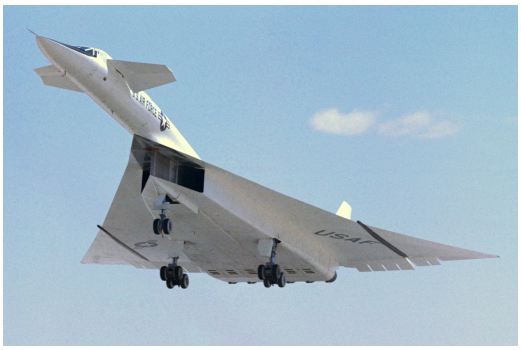

(a) XB-70 (NASA photo [85] used in accordance with NASA's Media Usage Guidelines [29].)

(b) C-5M (photo by TSgt Brad Fallin [140])

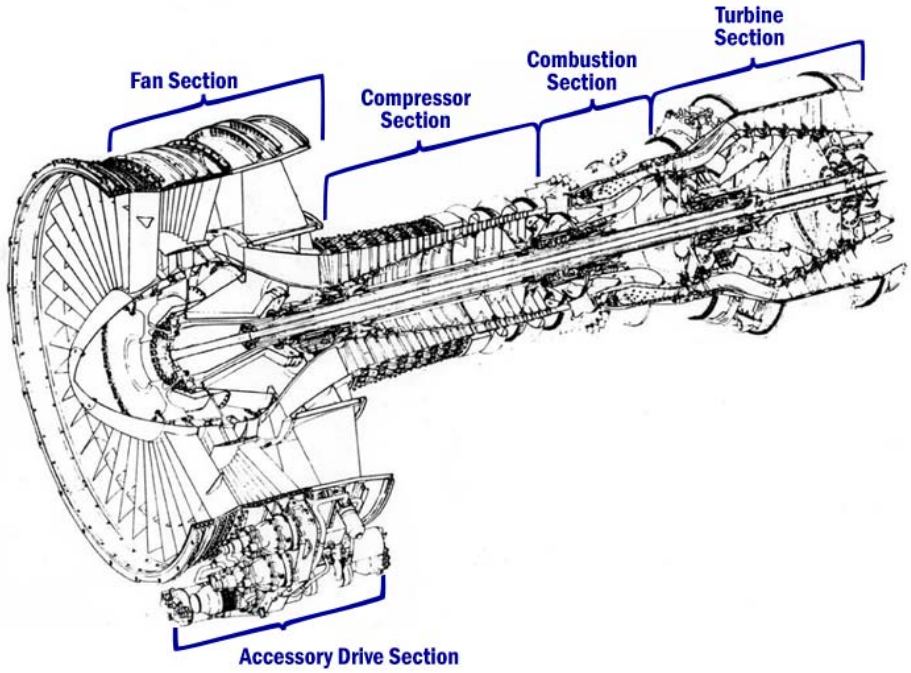

(c) CF6-6 cutaway (FAA image [40])

Figure 2.4: First production uses of IN718

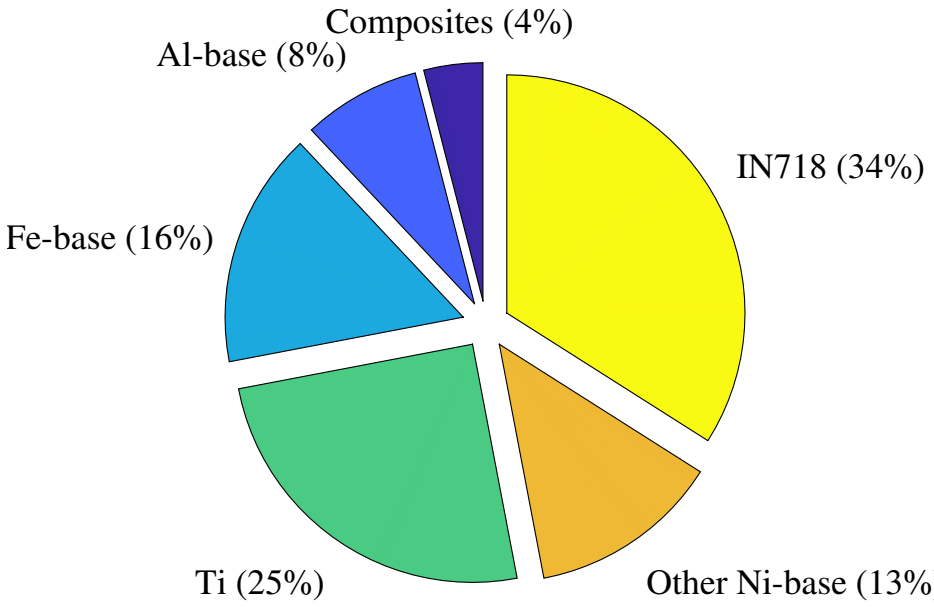

Figure 2.5: Alloy 718 relative input weights for a typical CF6 engine (C-5 Galaxy). Adapted from [118].

2.3 Alloy 718

Inconel 718 (IN718) is the most prevalent superalloy in use by the aerospace industry [118]. The high temperature properties of IN718 are the result of its unique microstructure. The mechanical strength and corrosion resistance of the alloy have proven useful in other industries as well. In addition to aircraft turbines, IN718 is used in large electrical turbines, nuclear reactors, oil drilling equipment, and rocket engines. IN718 is the alloy of choice for high-strength applications in temperatures up to 650 °C.

2.3.1 Chemical Composition.

IN718 is a Ni-Cr based superalloy. The chemical composition is provided in Table 2.1 and is primarily composed of Ni (55%) and Cr (20%). Cr is added to the Ni base to enhance corrosion resistance and provide protection from oxidation. As discussed in more detail in Section 2.2.2, Ni provides the FCC structure as well as phase stability. Iron is also added to serve as a secondary FCC base element. Molybdenum (Mo) provides solid solution

strengthening as it displaces Ni in the FCC matrix. This displacement by the slightly larger Mo atom (145 pm radius for Mo, 135 pm for Ni) results in a residual strain in the FCC matrix. Coherency straining is also relevant to the strengthening precipitate phases and will be discussed further in Section 2.3.2. Nb, Ti, and Al are important for the formation of precipitate phases.

Table 2.1: IN718 Limiting Chemical Composition (wt%), based on [115]

Element	**min**	**max**	
Chromium	17.00	21.00	
Nickel	50.00	55.00	
Molybdenum	2.80	3.30	
Niobium (Columbium)[N]	4.75	5.50	
Titanium	0.65	1.15	
Aluminum	0.20	0.80	
Iron[*]	(11.14)	(24.40)	
Carbon, Manganese, Silicon, Phosphorus, Sulfur, Cobalt, Boron, Copper, Lead, Bismuth, and Selenium	–	≤ 1.00	each

Note for the reader: While Niobium was adopted internationally in 1949 as the name for element 41, some of the foundational IN718 papers, e.g. Eiselstein [35], refer to Columbium (Cb)

* Iron min and max wt% are only specified as "remainder" in [115]; (values) are presented here for the reader's convenience.

2.3.2 Phases and Precipitates.

As discussed in Section 2.2.3, IN718 possesses several unique traits compared to previous superalloys that led to its widespread use. IN718's resistance to post weld heat treatment (PWHT) cracking and creep resistance are directly tied to the precipitates found within the microstructure. Table 2.2 presents an overview of all the precipitates that can form in IN718.

Table 2.2: Possible phases in IN718 (adapted from [34] and [116])

Phase	**Crystal structure**	**Formula**	**Solvus temp., °C**
gamma (γ)	FCC	Ni	1227-1320 (solidus)
			1260-1364 (liquidus)
gamma prime (γ')	FCC (ordered $L1_2$)	$Ni_3(Al,\ Ti)$	850-910
gamma	BCT (ordered $D0_{22}$)	Ni_3Nb	910-940
double-prime (γ'')			
delta (δ)	Orthorhombic	Ni_3Nb	1020
	(ordered $D0_a$)		
MC (metal carbide)	Cubic (B_1)	(Nb, Ti)C	1260-1305
Laves	Hexagonal (C_{14})	Fe_2Nb	1160
		Fe_2Ti	
		Fe_2Mo	

A material *phase* is defined as a domain in which the chemical composition and crystal structure are uniform. A phase in a metal alloy is a region of the material that can be independently distinguished or defined by its chemical composition and crystal structure. Chapter 3 discusses the methods used to identify the composition and crystal structure of IN718 specimens. As an example of independent phases, the principal γ matrix and γ'

precipitates are both arranged in an FCC crystal structure. The γ matrix is composed of Ni, but γ' is $Ni_3(Al, Ti)$. Therefore the γ matrix and γ' precipitates are categorized as separate phases. As another example, the chemical composition of the γ'' and δ phases of IN718 are both Ni_3Nb. However, γ'' has a body-centered tetragonal (BCT) crystal structure whereas δ is orthorhombic, so γ'' and δ are independently distinguishable phases.

Primary phases and secondary phases are important to the discussion of IN718 phases and phase transformations. A *primary phase* is one that forms during the solidification of the material. For IN718, the primary phases are γ, Laves, and carbides and can be seen in Figure 2.6. A *secondary phase* is one that forms after solidification as a result of phase transformations. For IN718, the secondary phases are γ', γ'', and δ. These secondary phases precipitate out of the solution as submicroscopic particles when the material is left at an elevated temperature. For this reason, the submicroscopic secondary phases are also referred to as *precipitates*.

The bulk phase for IN718 is the Ni-based γ phase, an FCC structure. The alloying elements are present in the solid solution within this γ matrix. Precipitate phases are critical to the properties of IN718 as will be laid out in this section. γ'' and γ' precipitates are secondary phases and the main contributors to IN718's strength. The δ phase is another secondary phase, but it does not contribute to the strengthening. Laves phase is a primary phase that forms in the presence of elemental segregation of Nb during solidification. The presence of these phases is dependent on the material processing, both during fabrication and in post-process heat treatments.

γ'' is the primary strengthening precipitate for IN718. γ'' is a coherent Ni_3Nb phase with a BCT ($D0_{22}$) structure. *Coherency* of a secondary phase indicates that the phase establishes itself using the lattice points of the primary phase. This results in a minimal disruption of the crystal structure, preserving the mechanical properties that depend on slip planes and dislocation movements within the crystal structure. These precipitates are not

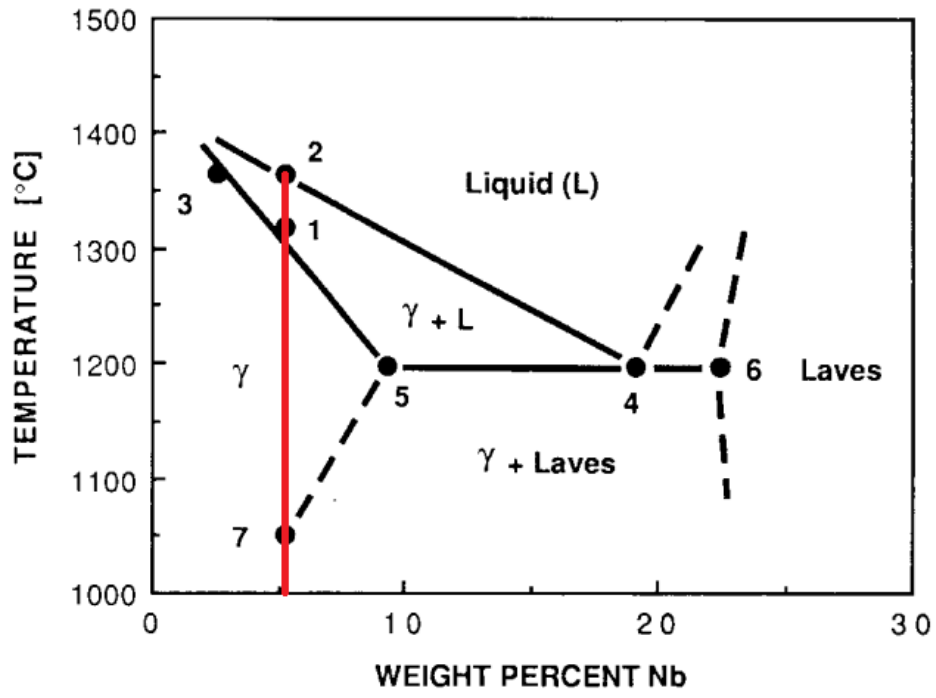

Figure 2.6: Solidification phase diagram for IN718. The red line indicates the AMS 5662 standard chemical composition of IN718 (4.75–5.50% Nb). Adapted from [61].

the same size as the Ni or Fe atoms they are displacing from the γ matrix, resulting in localized coherency straining [88]. This precipitate coherency straining is a strengthening mechanism of the aged IN718 similar to the coherency straining of Mo atoms mentioned in Section 2.3.1. The γ'' precipitates are disc-shaped with a diameter of 20–40 nm after standard aging treatments.

γ' is a coherent $Ni_3(Al, Ti)$ phase with an FCC ($L1_2$) structure. γ' also contributes to the strengthening of IN718 by coherency straining, although it precipitates in lower volumes than γ''. The precipitation of γ' depends on the content of Ti and Al, which cumulatively account for less than 2% of IN718 by weight, compared to γ'' which relies on Nb at up to 5.5%. The result is a γ''/γ' ratio of approximately 3:1 in the age-hardened condition.

γ' had previously enjoyed prominence as the primary strengthening precipitate for many of the superalloys replaced by IN718 such as René 41 (UNS N07041), Udimet 700, Inconel alloy X-750 (UNS N07750), and Waspalloy (UNS N07001) [69]. γ'' has a solvus temperature of 910–940 °C, slightly higher than γ', but it is enough to provide IN718 with additional resistance to PWHT cracking [35].

γ'' begins to precipitate at temperatures above 550 °C. The range between the precipitation and solvus is important for the age hardening treatments (discussed further in Section 2.3.3). After the standard age hardening treatment, γ'' will make up approximately 13% by volume; γ' will be approximately 4% [94].

γ'' is a metastable precipitate. It is able to form due to the rapid, non-equilibrium cooling process during solidification in both traditional forming and AM fabricated IN718. The δ precipitate is the stable phase of γ'' and will form when exposed at length to temperatures exceeding 650 °C. The size of the γ'' precipitates grows rapidly above 750 °C; subsequently, these start to be replaced by the stable δ phase. The increase in δ phase leads to brittleness and results in an "overaging" of the alloy [125]. δ primarily forms on the grain boundaries, where it acts to pin the grain boundaries. This can help prevent grain growth during heat treatments, which is desirable for tensile properties (Hall-Petch relationship). However, large quantities of δ consume the niobium content of the matrix, leading to lower precipitation of the desired γ'' phase, resulting in a lower strength of the material. This has been shown to decrease creep resistance as a result of this grain boundary softening [16].

Laves phase requires a concentration of Nb higher than the composition of IN718. However, the Laves phase can form due to segregation of Nb during solidification. Formation of Laves phases is, similar to δ, detrimental to the strength as it prevents γ'' from forming [119]. Regions surrounding Laves and δ phases are typically void of γ'' due to this "Ni denudation". Laves also provides a site for crack initiation and propagation.

The homogenization process is intended to prevent these Laves phases from forming by reducing the concentration of Nb necessary to allow precipitation of the Laves phase.

Metal carbides (MC), most commonly niobium carbides (NbC), have been reported in the microstructure of IN718, but appear to have no direct influence on the mechanical properties. However, similar to δ, the carbides pin the grain boundaries which limits grain growth during heat treatments [24, 72]. The carbides are a primary phase. The high solvus of the carbides (1260–1300 °C, [17]) makes it impractical to return the elements to solution without remelting the material. The carbides are present in small enough quantities so as to not sequester Nb to the detriment of γ'' and γ' precipitation. The carbides have two morphologies that appear in IN718. Small, spheroidal carbides appear on the grain boundaries as well as within the grains. Thin MC carbide films can also appear on the grain boundaries, which has been shown to reduce notch ductility [15, 135]. The distribution of carbides has also been shown to affect creep behavior as a result of a change to the material's fracture toughness [70].

2.3.3 IN718 Heat Treatments.

Heat treatments are applied to metal alloys to control the microstructure of the material. Heat treatments were introduced in Section 2.1.3. This section discusses the specific applications of heat treatments to the processing of IN718. All of the following processes are used for both wrought and AM IN718. The standard heat treatment for IN718 is a solution treatment followed by a two-step aging. The solution treatment dissolves any Laves phases or precipitates that may have formed during the fabrication process. This ensures the alloying elements are available to form the strengthening precipitates during the aging process. As discussed in the Problem Statements, a proper solution treatment is critical to achieving the maximum strength of IN718. In addition to the solution treatment, this section will also discuss stress relieving, homogenizing, aging, and quenching.

IN718 is hardened by the precipitation of secondary phases (e.g., gamma prime and gamma double-prime) into the metal matrix. The precipitation of these nickel-(aluminum, titanium, niobium) phases is induced by heat treating in the temperature range of 1100–1500 °F (590–820 °C). For this metallurgical reaction to properly take place, the aging constituents (aluminum, titanium, niobium) must be in solution (dissolved in the matrix); if they are precipitated as some other phase or are combined in some other form, they will not precipitate correctly and the full strength of the alloy with not be realized. To perform this function, the material must first be solution heat treated (solution annealed is a synonymous term). -IN718 data Sheet, Special Metals [129]

Figure 2.7 presents the time-temperature-transformation (TTT) diagram for wrought IN718 developed by Thompson et al. [137] (shown as adapated by Mostafa et al. [82]). The diagram maps out the various phases that can be found in IN718 and the time and temperatures at which they develop or transform. For example, the γ' and γ'' can be seen starting in the earliest transformation as indicated by the lower left 'lobe' of the diagram. The aging process of IN718 is superimposed on the TTT diagram to illustrate the strengthening-phase formation. The first leg of the aging process, 'Aging 1', extends just until it reaches the lobe indicating the start of δ. The creep testing temperature of 649 °C is also superimposed to illustrate the operational limit of IN718 with respect to the δ-phase transformation. The orange circles are added as reference points for the stress relief treatment of AM LPBF, as well as the solution treatment used by Amato et al. [3] to generate a recrystallized microstructure in LPBF IN718.

2.3.3.1 Annealing.

For IN718, in general, annealing can be considered as any heat treatment above 940 °C. Stress relief, solution treatment, and homogenization are all various types of annealing used for processing IN718. The general purpose of these treatments is to

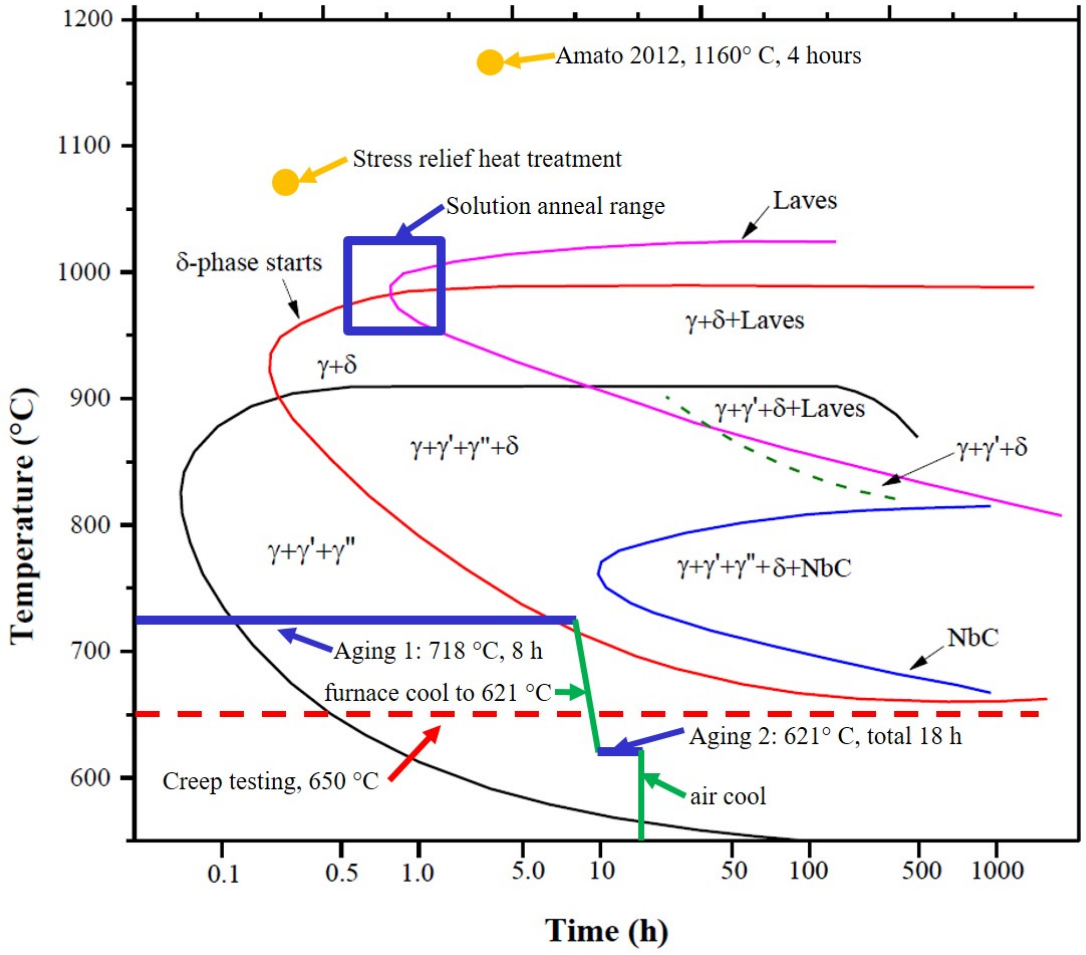

Figure 2.7: Time-temperature-transformation (TTT) diagram for IN718, showing specified heat treatments. Adapted from [82, Fig. 3].

remove stresses introduced during the fabrication process and to homogenize the chemical elements.

2.3.3.2 Stress Relief.

ASTM F3055 prescribes the stress relief process for IN718 at 1065 °C ±15 °C for 90 min −5/ + 15 min [9]. The temperature is above the δ, γ'', and γ' solvus temperatures, but is for a relatively short duration. This will dissolve some of the precipitates during

stress relieving but longer durations are required to fully dissolve them all. A stress relief was applied to several of the components used in this research. Additional discussion on the application of stress relief to this research is included in Section 4.2.4 (p. 135) and Section 4.2.2 (p. 131).

2.3.3.3 Solution Treatment.

The Problem Statements presented in Section 1.3 are directly tied to the solution treatment of IN718. The most common solution treatment prescribed for IN718 is in the range of 941–1010 °C for one hour per 25 mm of part thickness [115]. Referring to Table 2.2, this prescribed solution temperature is above the solvus temperature for both the γ'' and γ' precipitates but below the δ solvus. In the microstructure of IN718, the δ phase does not provide any mechanical strength, but its presence on the grain boundaries (in small quantities) prohibits grain growth. Smaller grains are preferred for increased tensile strength, as will be discussed with the Hall-Petch relationship in Section 2.3.5. For traditional IN718, the grain sizes of as-fabricated material were already much larger than PBF grains. Problem Statement #1 questions whether it is necessary to preserve the grain boundary δ to restrict the grain growth, or if it is more beneficial to dissolve these Ni_3Nb precipitates, returning the Nb to solution. A solution temperature of 1160 °C would dissolve the Laves phase in addition to δ, γ'', and γ'. This research looks to combine the solution treatment and homogenization treatment.

2.3.3.4 Homogenization and Hot Isostatic Press (HIP).

Applying a solution treatment for an extended period of time can result in homogenization of the material. The undesirable Laves and δ are only able to form where Nb has concentrated due to segregation during solidification. Homogenization can remove these concentrations and prevent the δ and Laves phases from readily reforming. ASTM F3055 prescribes a HIP in the range of 1120–1185 °C for 4 hours with an applied pressure of 100 MPa (almost 1000× standard atmospheric pressure) [9]. As discussed

for the solution treatment, 1160 °C is a good choice of temperature as it is the solvus temperature of the undesirable Laves phases. Holding the as-fabricated material at 1160 °C for 4 hours ensures: a) dissolving of all the precipitate phases (γ'', γ', δ, and Laves), and b) the elemental composition has time to homogenize. The purpose of the pressure applied by HIP is tied to the porosity of the PBF material. Applying high pressure during the homogenization process squeezes closed any pores. Diffusion bonding is enabled by the elevated temperature and works to permanently close the pore. In a general sense, homogenization is the best attempt to bring the material to an ideal solution condition. HIP treatments are being looked at as the best method to solution treat or homogenize the material while also removing defects that formed during manufacturing [58].

2.3.3.5 Aging.

The purpose of the aging process is to generate sufficient quantities of the strengthening γ'' (Ni_3Nb) and γ' ($Ni_3(Ti, Al)$) phases. A sufficient solution treatment is an important precursor to the aging process as it frees the constituent elements from the Laves and δ phases. The AMS 5662 age-hardening process for IN718 is: 1) hold at 718 °C for 8 hours; 2) furnace cool to 621 °C; 3) hold at 621 °C until a total precipitation time of 18 hours; and 4) air cool [115]. A material that has undergone solution treatment followed by aging is described as being in the solution-treated and aged (STA) condition. Mechanical properties are often prescribed based on the STA condition, such as those given in Section 2.3.5.

2.3.3.6 Quenching.

Quenching plays an important role during the post-process heat treatment of IN718. As shown in Figure 2.7, slow cooling after a solution annealing can allow δ and Laves phases to re-form. A fast cooling is required to prevent this formation, so water cooling or quenching is usually recommended after annealing. Slower cooling rates are acceptable

after the aging process since the aging temperature is below that precipitation temperature of δ or Laves.

2.3.4 Heat Treatment Standards.

AMS 5662 and ASTM B637 both prescribe the same solution treatment and aging for IN718. This is the default heat treatment for IN718 and provides excellent resistance to creep and stress-rupture up to 704 °C and oxidation resistance up to 982 °C. IN718 in the AMS 5662 condition is only solution annealed. The standard solution treatment is shown in Table 2.3. After the aging (i.e, precipitation) treatment, the IN718 is in the AMS 5663 condition. Both AMS 5662 and AMS 5663 prescribe the same solution treatment and aging and are shown in Table 2.4. [113, 115]

Table 2.3: Standard solution treatments for IN718

Spec	**Temp (°C)**	**Time**	**Cooling**
ASTM B637[10]	924–1010	≥1/2 hour	AC or faster
AMS 2774[114]	954	1 hour per 25 mm (≥10 minutes)	AC
AMS 5662[115]	941–1010	"time commensurate with thickness"	AC or faster

AC - air cooling

Table 2.4: AMS 5662 two-step aging for IN718 [10, 115]

Step	**Temp (°C)**	**Time**	**Cooling**
1st	718	8 hrs	FC (55 °C per hour) to 621 °C
2nd	621	hold for total time of 18 hrs	AC

AC - air cooling; FC - furnace cooling

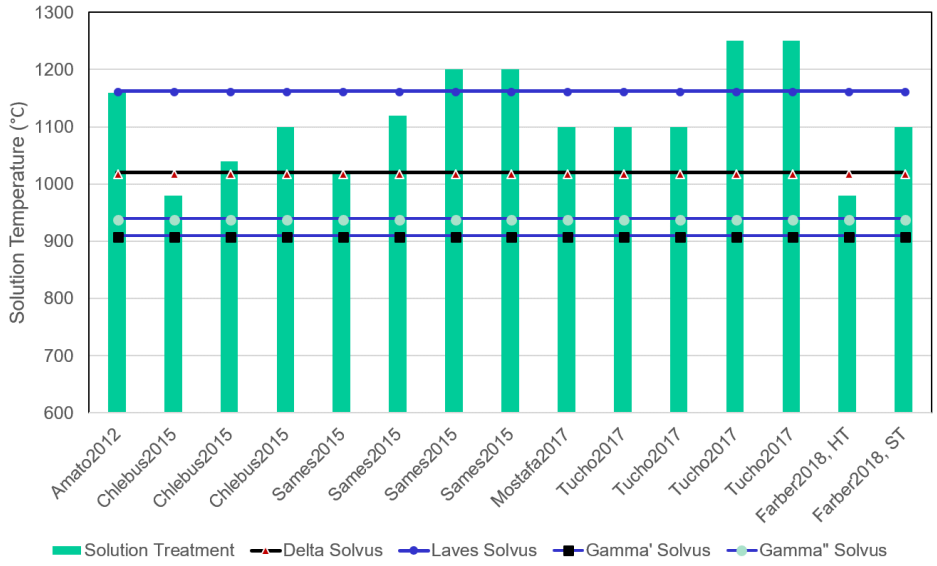

Figure 2.8: Solution treatments used by other researchers with precipitate solvus temperatures

Many researchers have looked at the effects of varying the solution temperatures and times. A selection of solution temperatures is visually depicted in Figure 2.8 with the values for the temperatures and times given in Table 2.5. The primary takeaway from these two graphics is that many of these researchers were not solution annealing the IN718 specimens above the Laves solvus temperature of ≈1160 °C.

Table 2.5: Anneal heat treatments of other researchers

Paper	**Temp (°C)**	**Time (hours)**
Amato et al. [3]	1160	4
Chlebus et al. [23]	980–1100	1
Sames [116]	1020–1200	1–4
Mostafa et al. [82]	1100	1
Tucho et al. [139]	1100 or 1250	1 or 7
Farber et al. [41]	980–1100	1–1.5

2.3.5 Mechanical Properties.

Materials researchers in AM IN718 seek to match the performance of cast or forged IN718, depending on the application. Cast properties are compared to higher porosity AM parts, where cost may be a higher consideration than mechanical performance. Forged properties are compared with higher-density AM parts (i.e., 99.5% dense). The heat treatments described in the previous section are critical to achieving the highest tensile and creep strengths for both traditionally formed and AM IN718. This section describes the various standards for IN718, and the different mechanical properties that are of interest for research and applications.

2.3.5.1 IN718 Standards.

AMS 5662 and ASTM B637 are effectively the same heat treatment standard for IN718 as shown in Section 2.3.4. This treatment creates IN718 parts with excellent resistance to creep and stress-rupture up to 704 °C and oxidation resistance up to 982 °C. These standards also define the minimum mechanical requirements of the STA material. The minimum requirements for tensile behavior and hardness are prescribed for room temperature testing. For elevated testing at 649 °C, the minimum requirements for tensile and stress-rupture behavior are prescribed. The minimum tensile and hardness requirements are shown in Table 2.6 using the longitudinal properties from AMS 5662. AMS 5662 also provides long-transverse and transverse tensile properties as the forgings have a slight anisotropic behavior. The stress-rupture requirements are provided in Table 2.7. For the creep-rupture testing to be described in Section 4.2.5, tests will be conducted using the stress requirement of 690 MPa, given here in Table 2.7.

2.3.5.2 Anisotropy of Powder-bed Fusion (PBF) Metals.

High thermal gradients and rapid solidification during the PBF fabrication process result in elongated grains with a vertical crystal orientation. This directionality of the

Table 2.6: Tensile and hardness minimum requirements of IN718 forgings [115]

Test Temperature:	**Room Temp**		**649 °C**	
Property	**Value**	**Units**	**Value**	**Units**
Ultimate Tensile Strength (UTS)	1276	MPa	1000	MPa
0.2% Yield Strength ($YS_{0.2}$)	1034	MPa	862	MPa
Elongation at failure (ε_f)	4	%	12	%
Reduction of Area	15	%	15	%
Brinell Hardness [10]	331		–	

Table 2.7: Stress-rupture minimum requirements of IN718 forgings [10]

Test Temperature:	**649 °C**	
Property	**Value**	**Units**
Stress	690	MPa
Minimum Hours	23	hours
Elongation at failure (ε_f)	5	%

material results in a strong anisotropy of mechanical behavior. Anisotropy is undesirable for the design of complex geometries as any loads on the part will result in a strain response along the path of least resistance. Generating an isotropic material is preferable from a design perspective.

Anisotropy in mechanical properties is typically defined by Equation (2.2), where σ_x and σ_z are the tensile strength ($YS_{0.2}$ or UTS) in the transverse or build direction, respectively [2, Eq 1]. Tensile testing by Strößner et al. [130] showed anisotropic behavior up to 10% in the as-built and various heat-treated conditions for LPBF IN718. Cloots et al. [26] performed tensile testing on LPBF Alloy 738, low carbon (IN738LC) and found similar results, with anisotropy up to 20%.

$$\frac{\sigma_x - \sigma_z}{\sigma_x} \times 100\% \tag{2.2}$$

2.3.5.3 Hardness.

Instrumented indentation tests, aka microhardness tests, can determine mechanical properties directly from load and displacement measurements [89, 90]. For metals, the hardness can be tied directly to the tensile strength [96]. Micro-hardness tests range in scale from micro-indentation down to nano-indentation, and at the lowest limit to atomic force microscopy. For the nomenclature, the nano- and micro- refer to the expected displacement response, h, in meters of the indentation technique [93]. Atomic force microscopy operates on the atomic scale, i.e., the expected displacement is 10^{-10} m or 1 Å (Angstrom), and is not typically used in characterizing structural macro-materials. Rockwell hardness C (*HRc*) tests are also found in older literature. *HRc* tests presents a macro measurement which is useful in determining material homogeneity and bulk behavior, but it lacks the resolution necessary to draw conclusions of individual grain behavior. The techniques typically used to characterize metals are micro- and nano-indentation, which will be the bounds of hardness testing in this research. The technique used to perform micro- and nano-

indentation tests is nearly identical and follows the basic principles outlined by Oliver-Pharr [89, 90]. The primary difference between micro- and nano- tests is the relative size of the indenter (or probe) and the accuracy of the instrumentation.

The indenter tip is a suitably hard material in a specific geometric shape. The Berkovich tip is one of the most common tips and consists of a three-sided diamond pyramid. When the tip is pressed into the test material, both the applied force, P_{max}, and displacement, h, are measured. The resulting data is similar to stress-strain data from tension tests. Contrary to tension tests, the elastic modulus is measured during unloading of the tip. As the test force is unloaded, it is assumed that only elastic deformations are recovered. The unloading stiffness, $S = dP/dh$, is defined as the slope of the curve immediately after the point of unloading [90]. Oliver and Pharr [90] provides a mathematical relationship to deconvolute the stiffness measurement into the Young's modulus.

Figure 2.9 presents a representative load-displacement curve from the seminal paper on instrumented hardness testing by Oliver and Pharr [89]. Figure 2.10 shows a load-displacement curve from nano-indentation data taken in this research and presented in more detail in Section 3.3.5 (p. 112) and Section 4.2.3 (p. 134). The data in both plots start at (0,0) for both load and displacement, then follows the loading path until it reaches the maximum load, P_{max}, and maximum displacement, h_{max}. The value of P_{max} is chosen by the researcher and must take into account the hardness of the indenter, the expected hardness of the material, and the stiffness of the load frame. P_{max} can be found experimentally by running a calibration test before starting the full hardness evaluation. The contact stiffness, S, is illustrated as the slope of the unloading line immediately upon unloading. The control software then takes these measurements and calculates Young's modulus (E) and an approximated $YS_{0.2}$. Wrought IN718 typically has a *HRc* of 20 or less in the annealed condition. After aging, the *HRc* increases drastically to 40–45. This difference in hardness

provides a benefit to manufacturing where machining can be done on the annealed material relatively easily, instead of attempting to work with the incredibly hard, aged material [118].

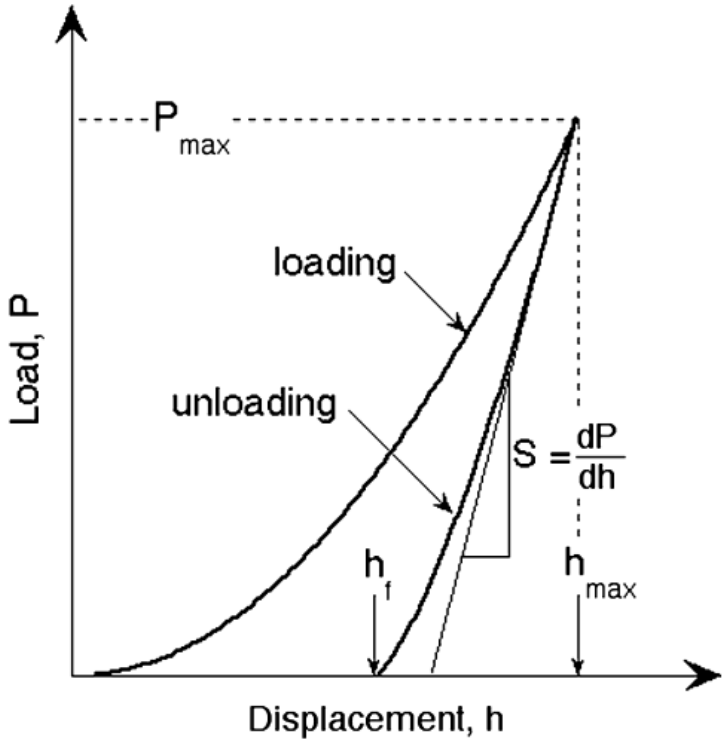

Figure 2.9: Schematic illustration of indentation load-displacement data showing important measured parameters. [90, Fig. 1]

Nano-indentation testing has been used extensively in quantifying the mechanical properties of IN718, both wrought and AM. The hardness of as-built AM IN718 is typically higher than annealed wrought material, but not as strong as aged-wrought material [3]. Using a macro *HRc* measurement, Strößner et al. [130] reported no measurable anisotropy in LPBF IN718 and an STA hardness of 45 *HRc* for two different solution treatments (980 °C/1h and 1065 °C/1h) and the conventional aging treatment. This result shows a

comparable hardness between the LPBF and wrought IN718, and it also indicates that macro-hardness techniques may not reveal the anisotropy caused by texture and grain shape and size.

More recently, Jiang et al. [54] reported Vickers hardness (H_V) microhardness, nanohardness, and E of LPBF IN718 using a modified solution treatment of 1120 °C with various durations. Hardness tests performed on the X–Y (281.0 H_V) and X–Z planes (254.0 H_V) in the as-built condition showed an anisotropy of 9.6% as a result of the different texture and grain shape between the two orientations. Additionally, the hardness values converged with an increased annealing time as a result of recrystallization. Finally, the hardness showed a marked increase with the application of aging to 391-405 H_V [54]. These results indicate that some measure of anisotropy can be gleaned from microhardness and nanohardness tests.

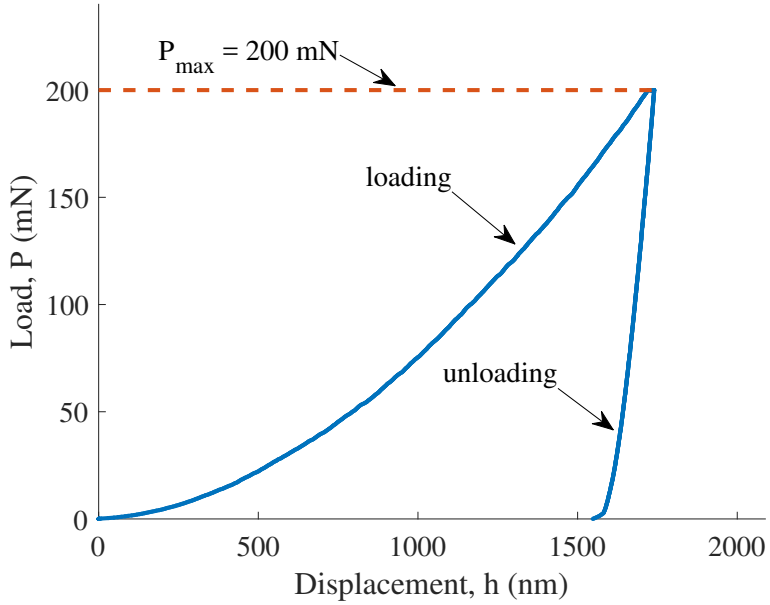

Figure 2.10: Load-displacement plot for LPBF IN718 annealed at 1160 °C/8 h. This is a representative reproduction of Figure 2.9 using experimental data from this research.

2.3.5.4 Tensile Strength.

The tensile strength of a crystalline material can be described by the Hall-Petch relationship [45]:

$$\sigma_y = \sigma_0 + \frac{k_y}{\sqrt{d}} \tag{2.3}$$

where σ_y is the $YS_{0.2}$, σ_0 and k_y are material constants, and d is the grain diameter. For IN718, σ_0 and k_y are material values based on the age-hardening γ' phase of superalloys and typically have values of approximately 300 MPa and 1.7, respectively [126, p. 243]. The Hall-Petch relationship has been shown to apply to most conventional alloys with grains larger than 5 μm in average diameter [50]. The $YS_{0.2}$, σ_y, can be substituted by UTS and the relationship is shown to still hold true. An increase in grain size, represented by the average diameter d, results in a decrease in the tensile strength. This relationship between grain size and tensile strength will be used in conjunction with the microstructural analysis in Chapter 3 and tensile testing in Chapter 4.

Kunze et al. [65] studied LPBF IN738LC and reported on a strong anisotropy in the Young's modulus before and after standard heat treatments. Muñoz-Moreno et al. [83] reported on a dominant ⟨001⟩ texture and anisotropy in as-built LPBF nickel alloy CM247, low carbon (CM247LC). The authors were able to greatly reduce the anisotropy from 40% down to almost zero. The heat treatments applied were greater than the standard heat treatment for CM247LC, and also resulted in recovery and partial recrystallization of the specimens. Muñoz-Moreno et al. [83] concludes that achieving recrystallization is necessary to reduce the anisotropy caused by the texture. The anistropy remaining after the heat treatment was attributed to the elongated grains.

Sames [116] showed the tensile properties of EBM IN718 met $YS_{0.2}$ and UTS standards per ASTM F3055 in the as-built condition, and the elongation at failure (ε_f) values could also be met following a modified solution anneal and aging treatment (1120 °C/2h followed by AMS 5663). Kirka et al. [59] found that the transverse tensile properties

varied with the height within the build volume due to in-site heat treatment caused by the EBM process. Similar to Sames, Kirka et al. [60] found the as-built (in-site heat-treated) parts met UTS and $YS_{0.2}$ properties per ASTM F3055, but not ε_f. Kirka et al. [60] also pointed out that none of the other PBF IN718 results in existing literature met the ε_f requirement.

Kuo et al. [67] looked at how dendrites and δ precipitates affected the tensile properties. They found the solution treated and aged specimens had overall UTS and $YS_{0.2}$ strengths comparable to wrought in either transverse or longitudinal build orientations, but the ductility of the LPBF IN718 was greatly reduced. The horizontal/transverse specimens exhibited worse ductility than the vertical/longtidudinal specimens due to the δ phase arrayed perpendicular to the loading axis.

Strößner et al. [130] showed tensile properties of LPBF IN718 comparable to wrought material in other literature, and also found a strong anisotropic behavior with respect to the build direction. The anisotropy was reduced with a higher temperature solution anneal (1065 °C/1h). Microstructural investigations revealed an increased segregation of niobium at the joints between build layers, resulting in increased δ formation during heat treatments and a reduced tensile strength for the vertical specimens as they included a higher quantity of these joints.

2.3.5.5 Creep Resistance.

Creep is the time-dependent plastic deformation under a fixed stress at an elevated temperature [57]. Creep resistance is one of the most important qualities of IN718 in its use in high-temperature turbine blades. The standard test methods for creep tests are covered by ASTM E139 [8]. Tests are performed to measure the deformation over time and its inverse, creep resistance as well as the total time to rupture. ASTM E139 defines several test methods for evaluating the deformation and fracture in metallic materials [8]. A *creep test* measures the time-dependent strain that occurs in a specimen after the application

of a constant load. A *creep-rupture test* measures progressive specimen deformation (i.e., strain) and time to failure (i.e., rupture). A creep-rupture test generally results in larger deformations than a basic creep test due to the increased time under load. A *stress rupture test* measures the time to failure, but generally does not record the deformation measurements during the test.

Limited published research is available on creep or rupture tests with PBF IN718 as compared to hardness or tension tests. Part of this lack of literature is the significant time investment needed to perform a series of creep tests. For example, a tension test can be conducted in less than 15 minutes, whereas a creep test could last 23 hours (using the standard ASTM B637 [10]) or much longer. Kuo et al. [68] reported test durations in the range of 134–677 hours for various heat treatments on LPBF IN718. Another consideration is the proprietary nature of the aerospace industry, where many companies are conducting materials research related to improving turbine performance and may want to keep proprietary heat treatments and associated performance data out of published articles.

In recent works, Kuo et al. [66, 67] showed that horizontally fabricated LPBF IN718 specimens performed much worse than vertical specimens, both in tensile ductility (a factor of 4:1, [67]) and rupture life (570 hrs vs. $\leq$ 100 hrs [66]). However, these tests were performed at a lower stress than ASTM B637 calls for, 550 MPa vs 650 MPa. Interestingly, the direct-aged LPBF IN718 (i.e., aged without a solution treatment) performed better than all the other heat-treated LPBF IN718. Another important conclusion by Kuo et al. [68] is "the originally recommended heat treatment process, STA-908 °C, for cast and wrought materials is not effective in selective laser melting (SLM)-processed specimens [68, p.12]."

More research is available on the creep behavior of wrought IN718, which should still be applicable to portions of this research. Liu et al. [70] showed that the grain size affects the crack growth behavior during creep, such that larger grain sizes result in an increase in rupture life. Additionally, Liu et al. [70] concluded that the carbide distribution

influences the creep crack growth behavior with the best performance coming from fine carbides homogeneously distributed.

The Laves phase is detrimental to the rupture life [105]. Therefore, a solution treatment that can dissolve the Laves phases could improve rupture performance. Additionally, Radhakrishnan and Thompson [105] concluded that the columnar grains formed via electron beam welding (a technological precursor to metals AM) were beneficial to the creep resistance. In the context of LPBF, the columnar grains would increase the rupture life of vertical specimens when compared to horizontal specimens, which was clearly demonstrated by Kuo et al. [66].

2.4 Additive Manufacturing of Metals

There are multiple additive processes from which metal parts can be fabricated. The principal focus of this paper will be on LPBF IN718. Prior research with EBM and direct energy deposition (DED) processes are also referenced by this work as the post-processing of the AM IN718 is very similar for all three additive processes. The following provides a brief overview of these three processes, then the section continues with a detailed review of metal AM.

Additive manufacturing (AM) is the "process of joining materials to make parts from 3D model data, usually layer upon layer, as opposed to traditional subtractive manufacturing and formative manufacturing methodologies" [52]. Also known as three-dimensional (3D) printing, AM has made tremendous strides since the first metal AM process was developed at the University of Texas at Austin in 1986 [30, 75, 117].

3D printing is capable of creating complex geometries due to how the part is built up during the AM process. This added complexity would add significant costs for subtractive manufacturing processes like computer numerical control (CNC) machining. Modern computer-aided design (CAD) software provides a vast design space for the geometry of AM parts. Additive manufacturing of complex turbine and rockets components is appealing

to the aerospace industry because of this design space, in addition to the lower relative cost for fabrication by AM.

The geometries of turbine parts are dictated by the flow of hot combustion gases, and many components require integrated cooling channels to remove excess heat. These requirements result in complex geometries, which can be expensive to manufacture using traditional techniques. Recent advances [123] in additive manufacturing show how close AM techniques are to becoming commercially producible.

The ASTM F42 Committee on Additive Manufacturing, in cooperation with the International Organization for Standarization (ISO), released ISO/ASTM 52900 to standardize and define AM process terminology [52]. Four of the seven processes defined in ISO/ASTM 52900 are directly applicable to AM of metals.

Powder-bed fusion (PBF) is the "AM process in which thermal energy selectively fuses regions of a powder bed" [52]. The thermal energy source can be a laser, electron beam, or plasma arc. Laser powder-bed fusion (LPBF) and electron beam melting (EBM) are the two most common PBF methods. Both of these PBF processes build parts in a similar fashion. PBF methods will be covered in more detail in Section 2.4.1.

Directed energy deposition (DED) is the "AM process in which focused thermal energy is used to fuse materials by melting as they are being deposited" [52]. DED is similar to PBF processes with respect to the energy source (e.g., laser, electron beam, or plasma arc) used to melt the material. The feed material for DED can be either pre-alloyed powder (similar to PBF) or wire. The primary difference between DED and PBF processes is that the powder or wire material is fed directly into a melt pool, rather than the energy source melting pre-positioned feed stock. DED is unique among the metal AM processes in that it can be used to repair existing parts. Since multiple manufacturers have introduced powder DED systems, numerous synonyms exist for the process: laser powder

forming (LPF), laser solid forming (LSF), direct material deposition (DMD), and laser engineered net shaping (LENS).

2.4.1 Powder-bed Fusion Processes.

The family of powder-bed fusion (PBF) processes consists of LPBF and EBM. The two processes are differentiated by their energy source: laser or electron beam. Laser PBF (LPBF) systems have been developed by several companies and have several synonymous terms for the LPBF process. Electron beam PBF (EBM) systems have a sole manufacturer, Arcam, so the terminology is less diverse. Table 2.8 is provided to assist the reader with the various terms used in the reference literature.

Table 2.8: Synonymous PBF terminology used throughout literature (adapted from [39])

Term used in this dissertation	Commercial name	Machine manufacturer
Laser powder-bed fusion (LPBF)	LaserCUSING	Concept Laser
	Direct metal laser sintering (DMLS)	EOS
	LaserCUSING	Concept Laser
	Direct metal laser melting (DMLM)	GE
	Selective laser melting (SLM)	multiple

2.4.1.1 Laser Powder-bed Fusion.

LPBF uses a high-power laser controlled by a system of lenses and scanning mirror to position the beam onto the powder bed. The scanning mirror is adjusted to trace out the desired scan pattern. A schematic of a typical LPBF system is shown in Figure 2.11. The power and scanning speed of the laser are dependent on the manufacturer. Laser powers range from 80 W to 2 kW. Scanning speeds for the laser beam typically range from 100–2000 mm/s; due to practical limitations (to be discussed in Section 2.4.2.1) typical scan

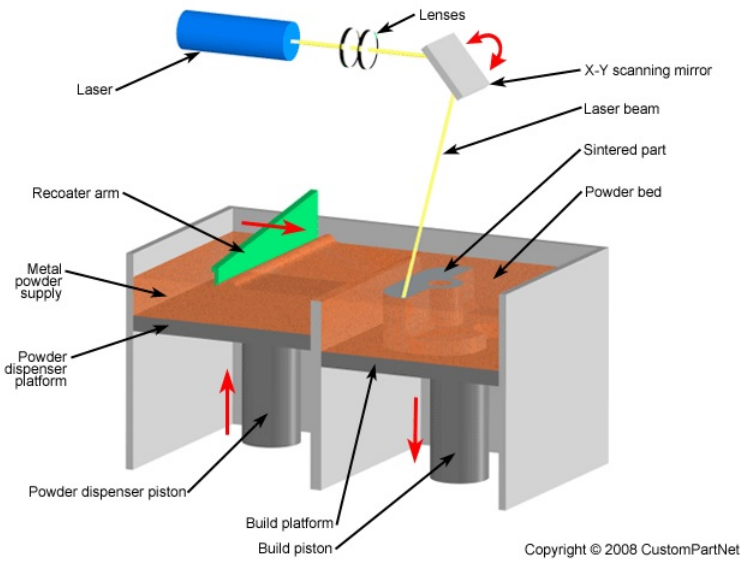

Figure 2.11: LPBF schematic. Image courtesy of CustomPartNet Inc. [28]

speeds for fabrication are in the lower part of that range. The total energy imparted to the powder bed is calculated through several energy metrics discussed later in Section 2.4.2. In preparation for fabrication, the build chamber is filled with an inert gas, typically argon or nitrogen, to prevent oxidation of the metal powder during the melting process. The build chamber or build plate may be heated; typical build chamber temperatures are in the range of 50–200 °C.

The Additive Manufacturing Lab (AniMaL) at AFIT is equipped with a Concept Laser (Lichtenfels, Germany) *M2 cusing* direct metal laser melting (DMLM) metal 3D printer as seen in Figure 2.12. The *M2 cusing* is equipped with a 400 W continuous-wave Ytterbium fiber laser. The beam can be adjusted to have a spot size from 50–180 µm, and typically uses a scan speed of 280–800 mm/s [27].

2.4.1.2 Electron Beam Melting.

EBM uses a collimated beam of electrons, similar to a scanning electron microscope (SEM). The electron beam is manipulated across the powder bed using magnetic coils to

Figure 2.12: AFIT's Concept Laser *M2 cusing* DMLM metal 3D printer

create the desired scan path. A schematic of a typical EBM system is shown in Figure 2.13. The maximum electron beam power for the Arcam A2 system is 3000 W [5]. EBM can achieve faster scanning speeds than LPBF since the electron beam is controlled by magnetic fields instead of a mechanical scanning mirror. The Arcam A2 has a maximum scan speed of 8000 mm/s. See Table 2.9 for a comparison of typical build parameters [127].

Table 2.9: Build parameters for LPBF and EBM (adapted from [127, Table I])

Method	EBM	LPBF
Average beam speed	5000 mm/s	1200 mm/s
Average melt power	500 W	185 W
Layer thickness	50 μm	20 μm
Hatch spacing	0.18 mm	0.1 mm
Powder preheat temp.	950 °C	none

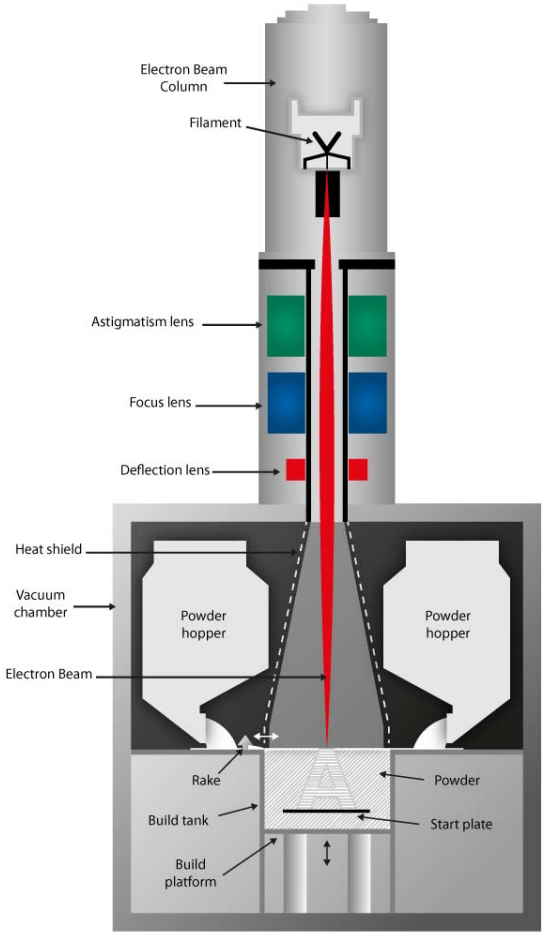

Figure 2.13: Arcam A2 EBM schematic [5]

2.4.2 AM Process Factors.

The PBF build process, and AM manufacturing in general, involves many factors that must be understood to predict the outcome of the process. Much of the research in AM has been devoted to understanding these factors as they comprise the primary differences between AM-fabricated parts and the more traditional cast and wrought alloys. This section provides a basic coverage of three sets of factors: process parameters, scan strategies, and thermal cycling.

2.4.2.1 Process Parameters.

The selection of process parameters will influence the effects of the scan strategy for each build. Process parameters are the "set of operating parameters and system settings used during a single build cycle" [52]. The amount of energy transferred by the beam to the powder bed is determined by the process parameters: beam power, velocity, spot size, layer thickness, and hatch spacing.

Table 2.10: Typical layer thicknesses and minimum feature sizes of PBF processes (adapted from [117, Table 2, p. 7]

	PBF - LPBF [3]	PBF - EBM	powder-DED
Typical layer thickness [117]	10–50 μm	50 μm	100–300 μm
Typical powder distributions	10–45 μm [117]	45–106 μm [117]	50–150 μm [102]
Beam diameter [117]	75–100 μm	100–200 μm	380 μm

Spot size is a measure of the effective diameter of the energy beam. For both laser and electron systems, the energy beam has a Gaussian intensity profile (Equation (2.4)) [141]. The spot size, also commonly reported as *beam diameter*, is expressed as the full width at half maximum (FWHM) (Equation (2.5)) power of the energy beam (e.g., [4]). In other words, the effective beam radius is calculated as the distance from the center to the point at which the intensity is half of the maximum; the effective diameter, or spot size, is twice the effective radius. For comparison of beam diameters for PBF and DED processes, refer back to Table 2.10 on p. 64. [53, 87, 107]

$$I(x) = \frac{P}{\sigma\sqrt{2\pi}} exp\left(-\frac{(x-x_0)^2}{2\sigma^2}\right) \tag{2.4}$$

$$FWHM = 2\sigma\sqrt{2\ln 2} \approx 2.355\sigma \tag{2.5}$$

where $I(x)$ is the intensity, P is the laser power, σ is the standard deviation of the Gaussian distribution, and $x - x_0$ is the distance from the spot center.

Hatch spacing is the distance between centerlines of adjacent scan paths. The hatch spacing controls how much the beam overlaps previously melted areas. Typically, hatch spacing is on the same order of size as the beam diameter. If the hatch spacing is much smaller than the beam diameter, excessive remelting can occur. It will also result in longer build times. A hatch spacing that is larger than the beam size can result in powder remaining unmelted between the scan paths.

In determining the effect of parameters on the melting of the powder, *linear energy density* is often used to define processing windows. The linear energy density is calculated as the beam power, P, divided by the product of scan velocity, V, and beam diameter, D, as shown in Equation (2.6) [92]. It is termed "linear" since it does not take into account the overlap of the hatch spacing. *Global energy density* is defined similarly, with hatch spacing, H, replacing beam diameter, as shown in Equation (2.7) [81]. Alternatively, [124] defines a *volumetric energy density* Equation (2.8) that also takes into account the depth of the powder layer, L.

$$E_l = \frac{P}{V \times D} \tag{2.6}$$

$$E_g = \frac{P}{V \times H} \tag{2.7}$$

$$E_v = \frac{P}{V \times H \times L} \tag{2.8}$$

Regardless of which of these energy density formulas is used, the resulting process maps are similar. Figure 2.14 shows a process map of power vs speed for welding IN718 showing a "weldable" process window. Figure 2.15 shows a similar process map for LPBF Titanium 6Al-4V (Ti6-4), with Zone I given as the processing window [44, 78]. Figure 2.16

provides an example of the processing window in action, showing the cross section of single track melt pool [64]. The images in Figure 2.16a were melted using a constant beam power at variable scan speeds. The melt pools in Figure 2.16b were generated by keeping energy density constant but varying the scan speeds.

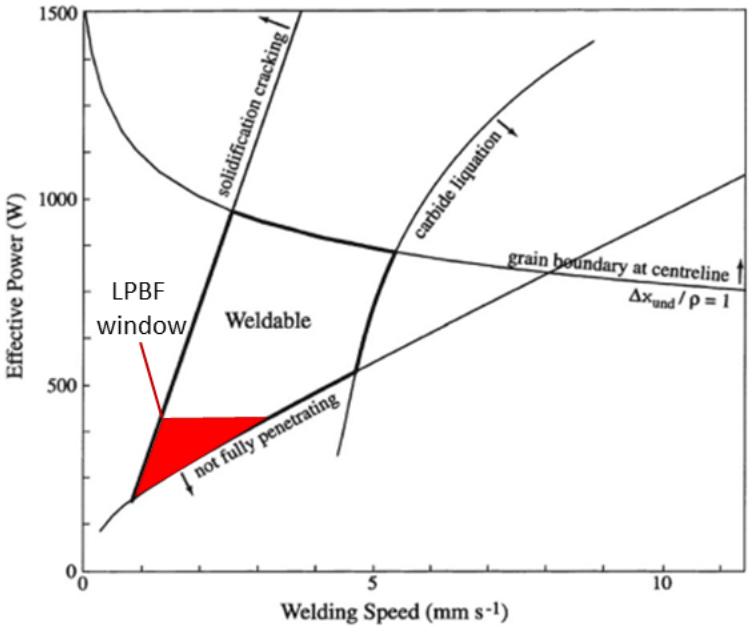

Figure 2.14: Relationship between effective power and speed in determining the weldability of IN718. Adapted from [117, Fig. 24, p. 18].

2.4.2.2 Scan Strategy.

The *scan strategy* is the path the energy source follows while melting the powder bed. While any path could be used as a scan strategy (theoretically), the simple scan paths shown in Figure 2.17 are fully capable of providing fully dense parts [117]. The simplest scan strategies are linear patterns, such as unidirectional (Figure 2.17a) or bi-directional (Figure 2.17(b). Island scanning (Figure 2.17(c)) is a strategy used to reduce the residual stress [20] by dividing the area into a checkerboard pattern, then filling each

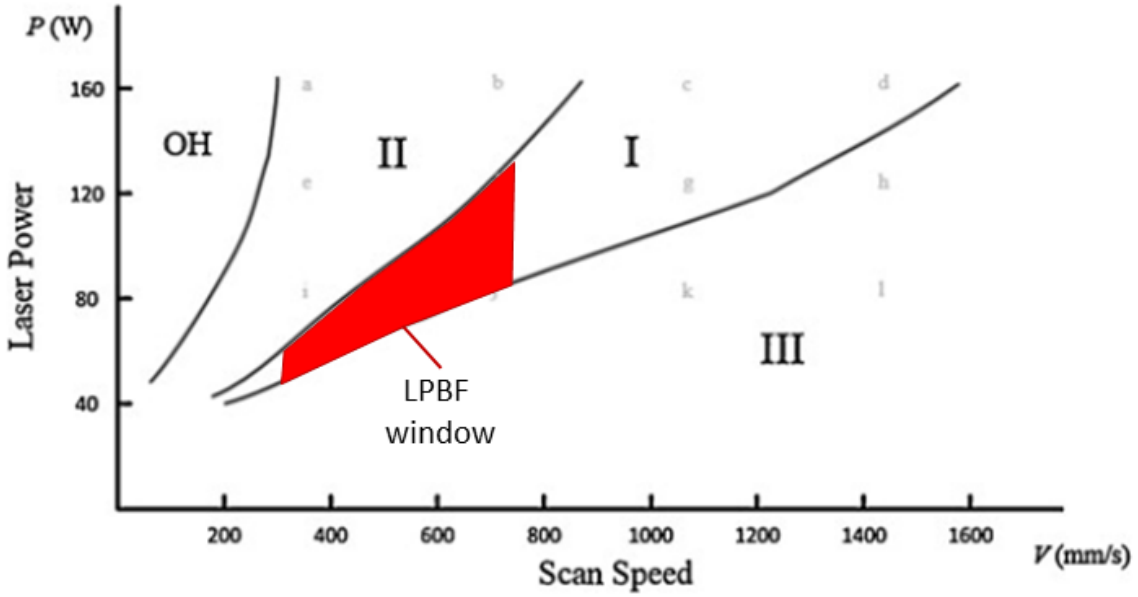

Figure 2.15: Processing regimes for SLM of Ti-6Al-4V depending on laser power and scanning velocity: (I) “processing window, (II) “overheating, (III) “incomplete melting, and (OH) “severe overheating. Adapted from [44] via [78, Fig. 37, p. 46].

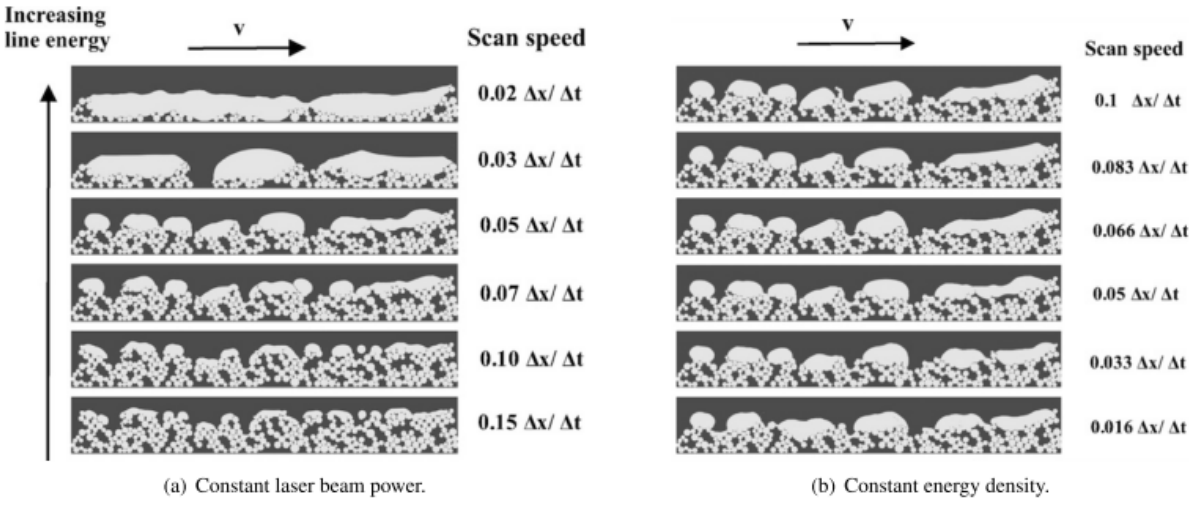

(a) Constant laser beam power.

(b) Constant energy density.

Figure 2.16: 2D single-track simulation results [64]

square with a rotation between each adjacent square by a unidirectional path. Spot melting (Figure 2.17(d)) is a technique used by EBM systems. Many PBF scan strategies contain two different sets of paths: a *contour path* outlines the edge of the part, and a *fill path* melts the bulk of the part. EBM systems typically use spot melting to melt contours and continuous linear melting for the fill (Figure 2.17(e)). LPBF systems typically use a continuous path for the contour, with linear fill paths (Figure 2.17(f)). For each subsequent layer, the scan strategy is typically rotated by a predefined angle to mitigate stress build-up due to scan path direction [117].

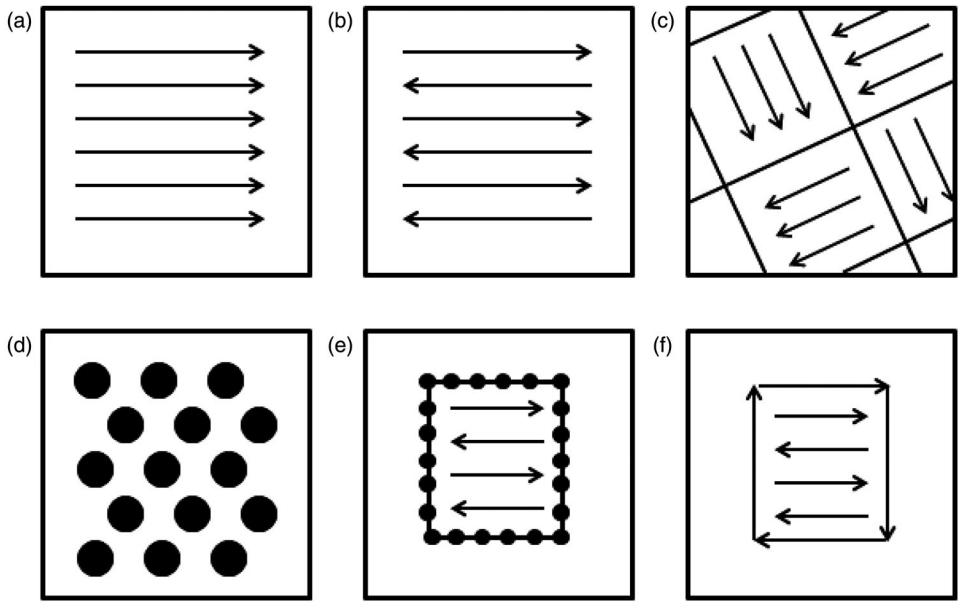

Figure 2.17: Examples of scan strategies. Scan strategies are used to control the energy-source path in metal AM as viewed in the X–Y plane (perpendicular to the build direction): a) raster scan, strip, unidirectional, or concurrent fill, b) continuous, bi-directional, snaking, or countercurrent fill, c) island scanning, d) spot melting, e) spot melting contours with snaking fill and f) line melting contours with snaking fill [117, Fig. 16]

Previous researchers have looked at the effect of scan strategy on the microstructure [21, 71, 76]. The resulting microstructures all consisted of columnar grains aligned with the build direction [21, 74]. Lu et al. [76] found that density and mechanical properties ($YS_{0.2}$ and UTS) were similar regardless of strategy, and the residual stresses were lower for a 5 mm $\times$ 5 mm and larger island strategies. Additionally, multiple researchers have attempted to tie numerical modeling [107] and Kinetic Monte Carlo (KMC) [110] with the scan strategy to predict solidification microstructure. While these researchers thoroughly covered the as-built microstructure, little research has been published on the recrystallization behavior as a result of various scan strategies.

2.5 Kinetic Monte Carlo (KMC) Modeling

The recrystallization of the LPBF IN718 microstructure is highly dependent on the thermodynamics of the system. Models are very useful in simulating and visualizing this behavior at various levels. Macro-level models encompass the bulk behavior of the system, enabling the visualization of grain growth. Micro-level models contain the developments closer in size to the atomic scale. For IN718, the micro level contains the various secondary phases involved in strengthening the material. Mesoscale models lay in between the micro and macro, providing a bridge between the atomistic properties of the micro scale and the bulk properties of the macro scale. Mesoscale modeling also allows for cost-effective simulations across the time domain. The Kinetic Monte Carlo (KMC) model is a powerful computational tool capable of simulating the small-length scales of the micro domain and the larger time scales of the macro domain. KMC has been extensively used in the modeling of solidification and recrystallization behavior of non-additive materials [103, 111, 143], and more recently in additive-specific applications [1, 43, 78, 106, 110, 144]. These efforts are limited to curvature-driven (aka boundary-energy-driven) recrystallization using the Monte Carlo Potts model [103], which evaluates the system energy based on the number of different 'spins' or orientations in the model lattice. The current research extends the previous efforts to incorporate stored-energy-driven recrystallization based on the residual strains in the LPBF microstructure in Chapter 5.

The KMC modeling for this research is carried out through the use of Stochastic Parallel PARticle Kinetic Simulator (SPPARKS). SPPARKS is an open-source KMC simulator developed by Sandia National Laboratories (Albuquerque, NM, USA) for modeling materials at the mesoscale [43]. The basic underpinnings and theory behind the SPPARKS code are provided in detail in [43] and presented in a condensed version in this section, with additional detail presented in Section 5.1 (p. 161). At the most basic level, SPPARKS implements a Metropolis variant of the Monte Carlo method for

solving stochastic scientific problems [79]. This implementation is termed a 'Kinetic Monte Carlo (KMC)' simulation for the fact that the model is used to represent kinetic behavior of fundamental material processes (in contrast to the thermal models discussed briefly in the previous section). A more detailed treatment of the general KMC method is also provided by [142]. More information on the KMC method is provided in Section 5.1 (p. 161).

The annealing and recrystallization behavior of most materials, and LPBF IN718 specifically of interest in this research, is determined by thermally activated atomic diffusion of atoms crossing grain boundaries [50]. The diffusion is treated as a probabilistic transition, where a diffusion rate determines the likelihood that a given boundary particle will reorient from its current crystal lattice to a neighboring lattice with a different orientation, thereby moving to a new grain. However, the KMC model is not calculating the diffusion of each individual atom in a crystal lattice. Instead, it is operating on the mesoscale, and the diffusion is being approximated for point on the lattice defined by the model input. With the 1 μm spacing used in this research, each 1 μm × 1 μm lattice point or pixel approximates around 7.7 million atoms (in a 2D cubic arrangement, using the IN718 lattice constant of 0.36 nm [73, 134]). When a pixel moves from its parent to a neighboring grain, this is termed a 'flip' in the KMC model. All events occurring in the KMC simulations in this research are flips from one grain to another. The rate of diffusion, or probability of reorientation, is given by an Arrhenius equation,

$$r_D = D_0 \exp\left(-\frac{Q}{kT_B}\right) \tag{2.9}$$

where r_D is the average rate of reorientation or probability of a flip, D_0 is a prefactor, Q is the activation energy for diffusion, k is the Boltzmann's constant, and T_B is the Boltzmann (or simulation) temperature [43, 111]. Some versions of Equation (2.9) replace Q with a more general ΔE to represent the energy change associated with the reorientation as in Rollett et al. [111]. While a direct measurement of energy is impractical, Section 2.5.1

presents several qualitative, but quantifiable, measurements that serve as a stand-in for the stored energy of the grains using the EBSD data collected as part of the research detailed in Chapter 3.

The particles of the material in a KMC model are represented as a lattice of points, similar in fashion to the crystal structure of a regular atomic structure. In practice, the scale of this lattice is determined by the resolution of the data feeding the model. The EBSD data shown and analyzed in Chapter 3 (p. 81) and Chapter 5 of this research was collected with a 1 μm spacing. This sets the lattice spacing at 1 μm and also conveniently treats each pixel in the EBSD maps as a lattice point. The overall size of the majority of the scans in this research were approximately 900 μm × 700 μm, with 1 μm spacing.

A KMC model consists of a sequence of Monte Carlo steps, which are designed to correlate the microstructure changes to real physical time in a linear fashion. For the Potts model implemented within SPPARKS this is accomplished by selecting each lattice point in the simulation and attempting flips until as many attempts are made as there are total sites in the lattice. This can be done sequentially by lattice points, but researchers have typically found better results using random selections with repeats allowed [43]. The Potts model, implemented in conjunction with KMC, keeps track of all the possible flips a lattice point can make as shown in Equation (2.10) [37]:

$$P_j = \frac{r_j}{\sum_{i=1}^{N} r_i} \tag{2.10}$$

where P_j is the probability of event j occurring, r_j is the diffusion rate for j as determined by Equation (2.11), r_i is the rate of any particular event in the system, N is the total number of possible states, and $i, j \in [1, N]$. Once all the probabilities are assembled, the KMC uses a random number generator to pick a value between 0 and $\sum P_j$ which determines the final outcome, or flip in this case.

Based on the SPPARKS model from [43, Eq (2)], the flips with a higher rate of occurrence are more likely to be chosen. The rate of each flip, and by extension the

overall grain growth, is driven by the relative energy levels of two neighboring pixels, ΔE (Equation (2.12)), with the lower energy grains appearing to consume neighboring higher energy grains. The energy is defined using EBSD data and discussed further in Section 2.5.1. The specific implementation of the diffusion rate or flipping of a lattice for grain growth is given by Equation (2.11) [43]:

$$r_j = \begin{cases} 1, & \text{if } \Delta E \leq 0 \\ \exp\left(-\frac{Q+\Delta E}{kT_B}\right), & \text{if } \Delta E > 0 \end{cases} \tag{2.11}$$

$$\Delta E = E_{final} - E_{initial} \tag{2.12}$$

where D_0 from Equation (2.9) has been taken as $D_0 = 1$, and ΔE is the difference in energy between the final and initial states. Additionally, as the simulation temperature is increased, the rate of flipping increases which closely approximates the increase in recrystallization from increased annealing temperatures [50]. However, there has been no demonstration of a direct correlation between the value of the Boltzmann temperature, T_B, and the solution treatment of the material.

When secondary phases form in the microstructure, they increase the amount of energy required to move a boundary and are termed 'pinning particles.' In conventionally treated IN718, the δ phase functions as the primary pinning particle and slows the growth of grains during heat treatments. When δ phase is fully dissolved due to sufficient solution temperatures, the carbides have been shown to serve as the new pinning particles. Pinning particles exert a force resisting grain boundary movement via the Smith-Zener pinning pressure, as given by Equation (2.13) [50]:

$$P_{SZ} = \frac{3 f_V \gamma}{r} \tag{2.13}$$

where P_{SZ} is the pinning pressure, f_V is the volume fraction of spherical pinning particles of radius r, and γ is the specific energy of the boundary. From this equation, the pinning pressure decreases as the particle size decreases. So the pinning pressure will decrease

as a particle coarsens during heat treatments. SPPARKS models the pinning particles by replacing a lattice point with a fixed particle, independent of any grain. The quantity of pins is controlled within SPPARKS in the 'pin' command by defining an area fraction of pixels to be converted. The pin command is discussed in more detail in Section 5.1.3 (p. 166).

Previous researchers have used SPPARKS to model abnormal grain growth during annealing [111]. These efforts have looked at the grain growth resulting from an equaixed microstrucuture exposed to annealing temperatures. The evolution of the grains is dependent on the energy of the model and the starting geometry. Grain growth is primarily driven by the boundary energy. Other research has looked at the processing of AM IN718 using SPPARKS to model the particle interactions during solidification [110]; the report is generalized to apply to various AM metals, however it is closely associated with LPBF IN718. Rodgers et al. [110] was also able to model the formation of a columnar microstructure typically seen in as-fabricated LPBF metals. However, no studies have been done to incorporate the residual stresses on the as-built LPBF materials and the effect of this stored energy on the recrystallization dynamics.

2.5.1 Quantification of Energy.

Measuring the precise stored energy is difficult, but it is not essential in order to conduct qualitative modeling. The recrystallization process is driven by relative, not absolute, energy levels. The probability of a change is given by Equation (2.11), and only the relative energy difference, ΔE, appears in the equation. For the purpose of annealing a material, the amount of energy stored in the crystal lattice can be viewed as the difference between the perfect, undeformed lattice and the as-built material with residual strains. The energy of the crystal lattice is stored plastically via defects or elastically via local distortions [148]. The total energy is the sum of the elastic and plastic strains in the specimen. In additive manufacturing processes, the primary source of stored energy in the annealing process is the residual thermal stresses created during the melting and solidification during

fabrication. The residual stresses, whether plastic or elastic, result in localized strain which are visible via EBSD as misorientations, i.e., changes in the normal vector of the crystal planes. There exist numerous methods to quantify the magnitude and distribution of these deformations, and several of these have been shown to be suitable stand-ins for the energy of the recrystallization process [148]. Of the methods presented by Wright et al. [148], this research will present and use grain orientation spread (GOS) and kernel average misorientation (KAM) to evaluate recrystallization and stored energy, respectively.

The GOS is the average difference in orientation between the average grain orientation and all measurements within a grain [42]. The complete formula for calculating GOS is given by:

$$GOS = \frac{1}{N} \times \sum_{A=1}^{N} \left\{ \min \left[\cos^{-1} \left(\frac{\text{trace}\left[g_{ave} \left(h_i g^A \right)^{-1} \right] - 1}{2} \right) \right] \right\} \tag{2.14}$$

where A is the A^{th} measurement point in a grain with N pixels, g_{ave} is the average grain misorientation, g^A is the orientation for pixel A and h_i is the appropriate symmetry element (based on the crystal structure), and the trace of a square matrix $\mathbf{A}$ is the sum of the elements on the main diagonal of $\mathbf{A}$ [146], i.e.:

$$\text{trace}(\mathbf{A}_{n\times n}) = \sum_{i=1}^{n} = a_{ii}$$

In practice, the EDAX software automatically calculates the GOS values based on the crystallographic information collected during the EBSD scan. The GOS approach is used in Chapter 3 on the principle that the GOS value for a recrystallized grain is measurably lower than the GOS of a deformed grain.

The KAM is the average misorientation between the pixel at the center of a specified grid area, or kernel, and its neighbors. EBSD data is often collected in hexagonal grids since neighboring points have identical center-to-center distances. However, many of the data processing functions used in this research require the EBSD data be converted to a square grid for processing. Examples of a hexagonal and square kernel are shown in

Figure 2.18 and defined as the 3rd-nearest neighbors. The KAM can be defined either with respect to all the neighbor pixels in the kernel, or only the pixels on the perimeter. Calculating the KAM for large EBSD scans can be very computationally intensive with large kernels such as the 3rd-nearest neighbor. For this research, KAM is calculated using the perimeter pixels of the kernel. Based on work during this research, this difference in KAM measurements provides an increase in processing speed with no noticeable effects to the misorientation maps.

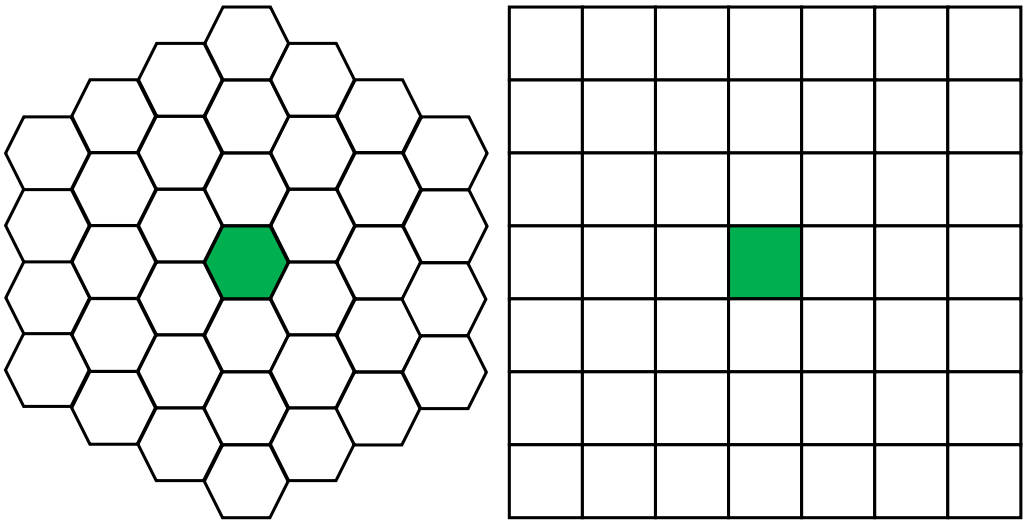

Figure 2.18: Hexagonal and square kernels with 3rd nearest neighbor. The benefit of the hexagonal grid for analysis is that the center-to-center distance is the same for all adjacent pixels in the kernel. Adapted from [148].

There are two main differences between the GOS and KAM measurements as presented here. The reference size for GOS is the entire grain, while it is only the kernel for KAM. Considering that the average grain in as-built LPBF IN718 contains over 250 pixels, the KAM measurement provides a more refined and localized description of the

stored energy. The GOS provides a simple and useful metric to determine if a grain has recrystallized, and KAM allows for a detailed distribution of energy within the grain structure. The GOS metric is used extensively in Chapter 3, and KAM is relied on in Chapter 5 to inform the KMC simulations of the local energy distributions that will drive the recrystallization dynamics. Figures 2.19 and 2.20 present a comparison of GOS and KAM maps for two LPBF IN718 specimens used in the analysis from Chapter 3 and Chapter 5 to illustrate how the metrics differ in their ability to present global and local energy distribution.

Figure 2.19a displays a collection of grains with high GOS values, up to 5°. The GOS is calculated as a single value for the entire grain, with every point in that grain assigned that same value. A 5° misorientation spread is the maximum value for the GOS measurement as a 5° spread is also used in defining each unique grains; a grain with GOS>5° would instead be classified as two (or more) separate grains. In general, GOS values below 3° have been used as an upper bound for identifying recrystallized material. GOS values between 1–3° have been shown to provide similar results for comparing recrystallized fractions [42]. In similar comparisons of AM IN718, a GOS threshold of 1.2° was used to define a recrystallized grain [18]. The GOS map is useful in visually processing the amount of recrystallization, as recrystallized grains have a much lower GOS value. A threshold of 1.2° is used in Chapter 3 to define a recrystallized grain. Contrast Figure 2.19a with Figure 2.20a, where in the latter image the majority of the grains have a low GOS (less than 1.2°) consistent with recrystallization due to the application of the 1160 °C/8 h solution treatment.

The KAM maps shown in Figures 2.19b and 2.20b use the same EBSD data, but present the misorientation calculated in a localized fashion, specifically the 3rd nearest neighbor as illustrated in Figure 2.18. This captures the distribution of the energy more precisely than GOS, which is important when considering the modeling effort to calculate

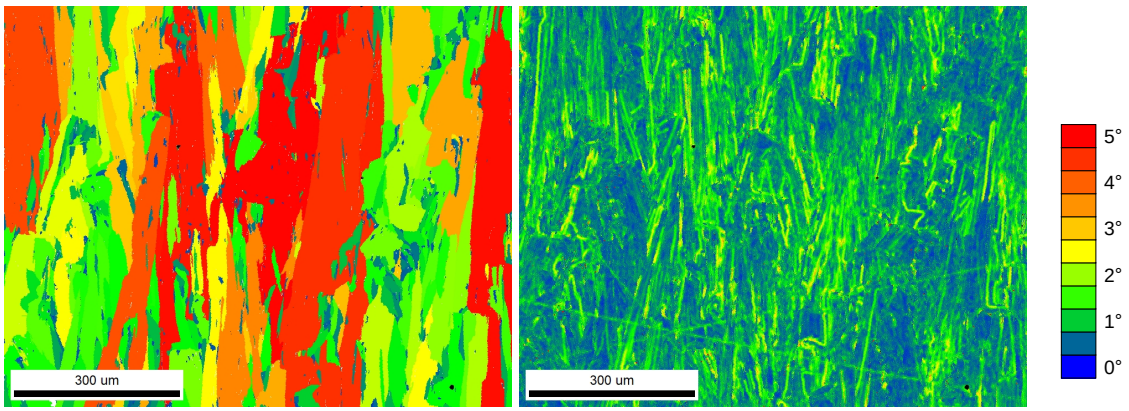

(a) As-built GOS map (b) As-built KAM map

Figure 2.19: GOS and KAM maps of an as-built specimen

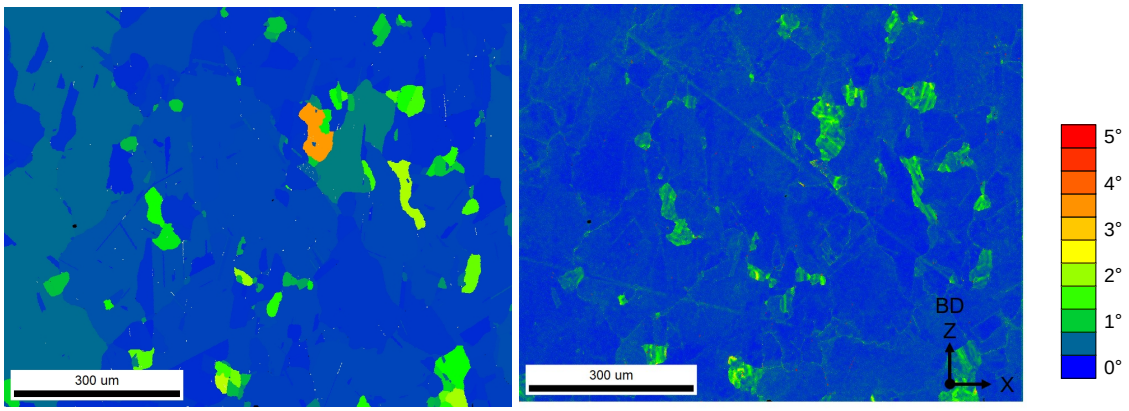

(a) 1160 °C/4 h GOS map (b) 1160 °C/4 h KAM map

Figure 2.20: GOS and KAM maps of an 1160 °C/4 h specimen

energy gradients. A smaller kernel size improves the resolution of the spatial distribution, and a larger kernel size requires more computational time as more pixels are being counted. In order to save some computation, the kernel can be computed using the outermost neighbors with a negligible impact on the quality of the map, as long as the kernel is smaller than the average grain size. A 3rd-nearest neighbor kernel at 1 μm resolution has a

diameter of 7 μm, while the specimens shown in Figure 2.20 have an average diameter of almost 14 μm.

2.5.2 Johnson-Mehl-Avrami-Kolmogorov (JMAK) model.

Work in the area of recrystallization nucleation and growth processes done by Johnson and Mehl [55], Avrami [12], and Kolmogorov [63] lends their names to the Johnson-Mehl-Avrami-Kolmogorov (JMAK) model [50]. The curve illustrated in Figure 2.21 represents the typical recrystallization kinetics as a result of annealing [50]. This curve is described in terms of nucleation and growth processes.

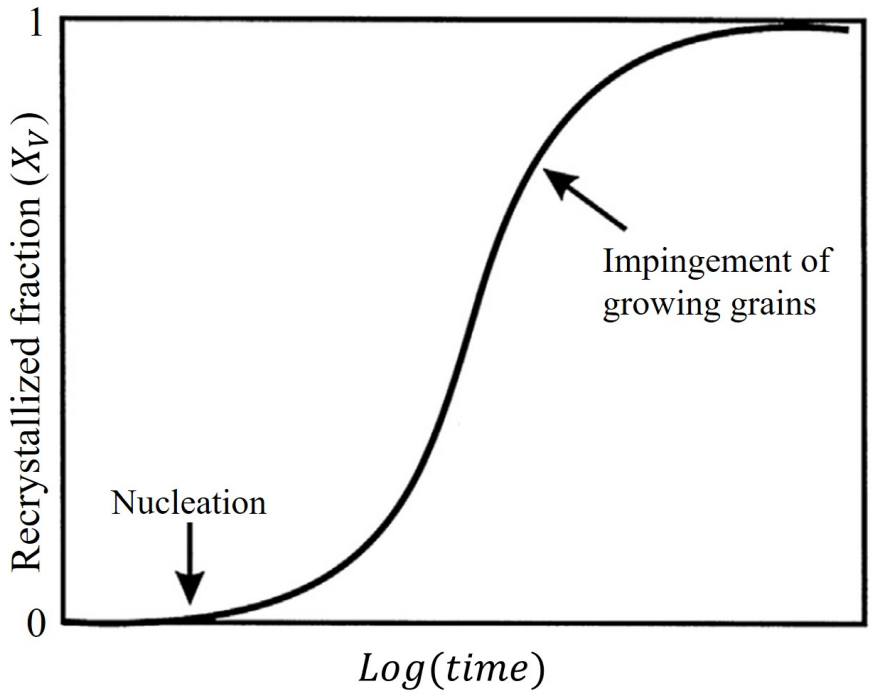

Figure 2.21: Typical JMAK recrystallization kinetics during annealing (adapted from [50]).

The curve in Figure 2.21 can be represented by the JMAK equation, as given in Equation (2.15) from [50]:

$$X_V = 1 - \exp(-Kt^n) \tag{2.15}$$

where X_V is the recrystallized volume fraction, K represents a function that contains the grain nucleation rate and grain growth rate, t is time, and n is the Avrami exponent (typically between 1-4). The relationship between the recrystallization fraction and time is linearized through two logarithmic manipulations of Equation (2.15), resulting in the Avrami equation in Equation (2.16) [143]:

$$X_V = 1 - \exp(-Kt^n)$$

$$1 - X_V = \exp(-Kt^n)$$

$$\frac{1}{1 - X_V} = \exp(Kt^n)$$

$$\ln\{1/(1 - X_V)\} = Kt^n$$

$$\ln[\ln\{1/(1 - X_V)\}] = \ln Kt^n$$

$$\ln[\ln\{1/(1 - X_V)\}] = \ln K + n \ln t \tag{2.16}$$

A plot of $\ln[\ln\{1/(1 - X_V)\}]$ vs $K + \ln t$ yields a straight line of slope equal to the Avrami exponent, n and a vertical intercept of $\ln K$, which is also referred to as the Avrami intercept. The values of $\ln K$ and n can be derived from the intercept and slope of the Avrami plot. This allows for two variables, $\ln K$ and n, to be used to describe each set of experimental data. The JMAK curve appears in Section 3.3.1 and Figure 3.12. $\ln K$ and n are also useful variables for comparing the experimental data from Chapter 3 with the simulations in Chapter 5.

III. Microstructural Characterization

This chapter covers the tools used to characterize the microstructure, the influence of heat treatments on microstructural characteristics (e.g., average grain size, texture, etc), and the results of hardness and tension testing. The contents of this chapter are being published as a stand-along journal paper in Materials Science and Engineering: A (MSEA), which has a 2018 Journal Impact Factor of 4.081 per Clarivate Analytics [25, 38]. MSEA's principal focus is the relationship between microstructure, processing, and mechanical strength of structural materials. The article has been assigned a DOI, and is currently in pre-proof.

DOI: 10.1016/j.msea.2019.138230 [86]

The microstructural analysis in this chapter addresses the research objectives described by Problem Statements 1, 2, & 3. The objectives of Problem Statement 1 are achieved by applying the modified solution temperature of 1160 °C to specimens for time ranging from 1–8 h. The resulting microstructures are characterized using electron backscatter diffraction (EBSD) and compared to the microstructure of specimens in the as-built and conventional heat treatment (CHT) (1010 °C/1 h) conditions. Additionally, the recrystallized fraction is calculated using the grain orientation spread (GOS) metric to evaluate the annealing kinetics. The recrystallization behavior will be an important input to the Kinetic Monte Carlo (KMC) effort in Chapter 5. Hardness and tension testing are performed to evaluate the anisotropy of material properties. The annealed specimens were fabricated using three different scan strategies to accomplish the objective for Problem Statement 2. The microstructural differences in grain size and texture intensity between the scan strategies are examined using EBSD. The hardness and tensile testing revealed the modified heat treatment (MHT) reduced the anisotropy of the 0.2% yield strength ($YS_{0.2}$) by 10% and ultimate tensile strength (UTS) by 4–6%, achieving the objective for Problem Statement 3.

3.1 Introduction

Producing metal structures and components using additive manufacturing (AM) is a rapidly growing research field with the potential to revolutionize traditional manufacturing. Powder-bed fusion (PBF) is a promising branch of metal AM technology. PBF has two main varieties - laser powder-bed fusion (LPBF) and electron-beam melting (EBM) [60]. PBF is very similar with regards to the thermodynamics and chemistry of traditional welding. As a result, metal alloys originally developed for their excellent welding characteristics are seeing a surge of research related to PBF manufacturing.

Inconel 718 (IN718) is one of the most prominent aerospace alloys in use today, even though it was originally developed in the 1950s. IN718 is a highly weldable superalloy and the metal of choice for aircraft turbines and rocket components [35, 118]. The strength and creep resistance of IN718 come from its delayed age-hardening response. To achieve maximum material properties, it typically undergoes a post-process anneal followed by a two-step aging process. The annealing and aging treatments can vary based on the intended application (tensile, creep, fatigue), but the treatments are still very similar to those described by Eiselstein in 1965 [35].

AM will not replace casting or forging for many applications, but the design window for AM allows for complex geometries that would be cost prohibitive or simply infeasible using traditional manufacturing methods. Additive manufacturing converts 3D files into physical parts by slicing the 3D model into thin layers. Each layer is then assigned a scan strategy that controls how the heat source (e.g., laser or electrons) traverses that layer. In LPBF and EBM manufacturing, the printer spreads a thin layer of powder onto a build plate. The beam then fuses the powder based on the location and timing information provided by the scan strategy and sliced part file. The printer then adds another layer of powder and repeats this process to complete the build. Various scan strategies are used to build parts, and multiple strategies can be used within the same layer. Typically, a contour (or skin)

scan is used to define the outline or boundaries of the part, and the outline is filled in using a core strategy. Since the bulk of a material will be built with the core strategy, this strategy will have the largest effect on the overall material properties. The three common core strategies that are covered in this research are presented in Figure 3.1. Each strategy uses a slightly different algorithm to section the bulk area. This difference can result in some localized effects to the microstructure as the algorithm changes the amount of heat at particular points of the build. As a result, parts built using different scan strategies can have different microstructures. Part manufacturing would benefit from a method that could mitigate the differences due to using different scan strategies.

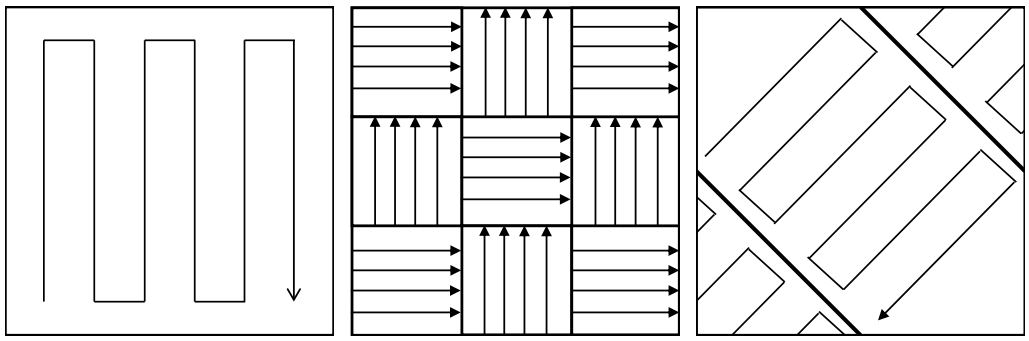

(a) Continuous (b) Island (c) Strip

Figure 3.1: Three scan strategies commonly used throughout metal additive manufacturing. The print strategy affects the thermal stresses due to the build process. Figures are representative only and not shown to scale.

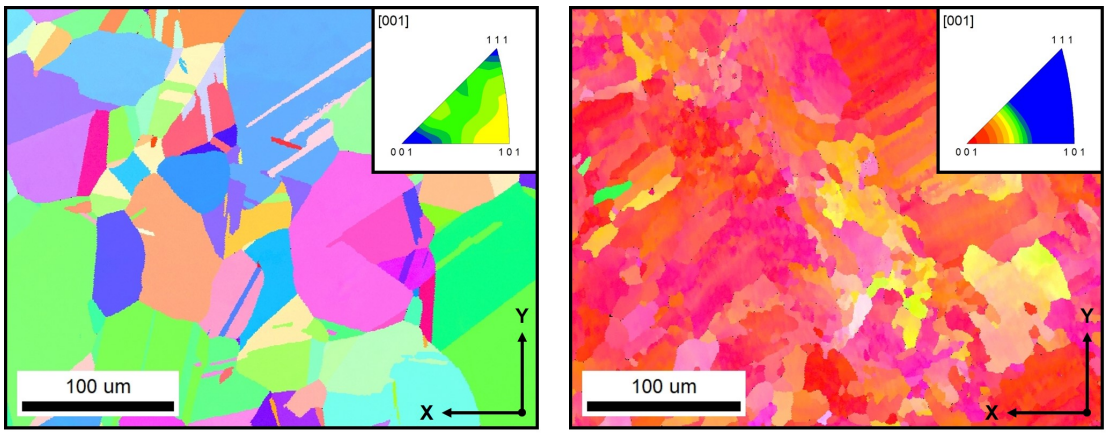

(a) Wrought IN718 (X–Y)

(b) LPBF IN718 (X–Y)

Figure 3.2: In the X–Y orientation, wrought IN718 exhibits equiaxed grains with an average diameter of 40.7 μm and a weak texture (peak intensity = 2.0). The as-built LPBF specimen contains a mix of equiaxed and elongated grains with an average grain diameter of 10.3 μm, and it has a very dominant (001) texture with a peak intensity of 11.1. Annealing twins were combined with parent twins for average grain diameter calculations.

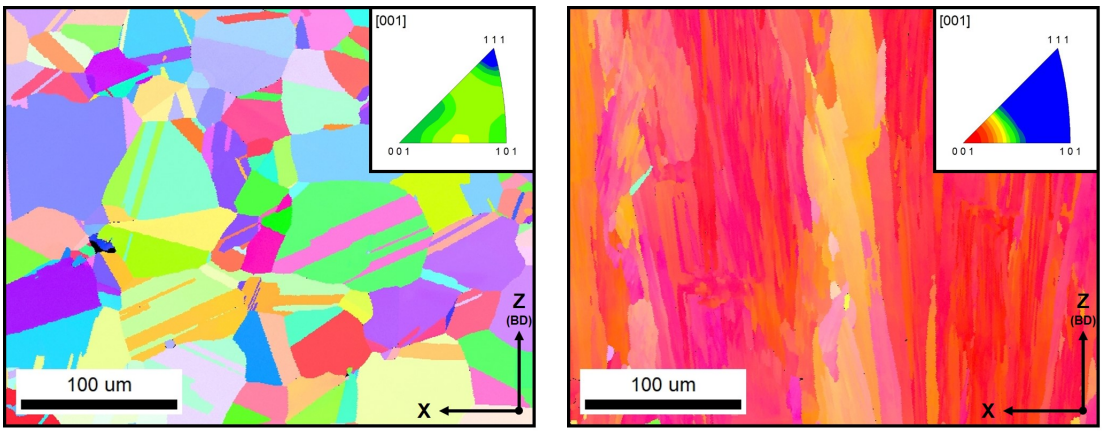

(a) Wrought IN718 (X–Z)

(b) LPBF IN718 (X–Z)

Figure 3.3: In the X–Z orientation, the wrought microstructure is indistinguishable from the X–Y material in Figure 3.2a. The wrought X–Z average grain diameter is 44.0 μm with a weak texture (peak intensity = 1.6). The as-built LPBF X–Z contains dominant columnar grains aligned with both the build direction and (001) grain direction. The average grain diameter for the LPBF specimen is 7.9 μm with a dominant (001) IPF intensity of 15.4. Annealing twins were combined with parent twins for average grain diameter calculations.

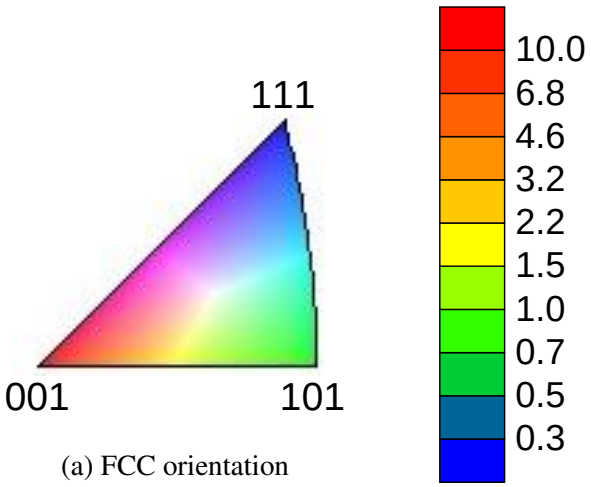

(a) FCC orientation

(b) Texture intensity

Figure 3.4: Figure 3.4a is the standard FCC IPF legend for all the IPF maps presented herein. Figure 3.4b is the graduated legend corresponding to the texture maps; all textures plots are presented at the same intensity scale. For the IPFs provided, red corresponds to the highest IPF intensity of >10.0 (i.e., the given orientation appears 10× more frequently than a specimen with fully random orientation). Green corresponds to a neutral intensity of 1.0, and blue corresponds to the lowest IPF intensity of <0.5 (i.e., the given orientation appears less than half as often as in a fully random specimen).

While the scan strategies may result in a difference in microstructure, the overall manufacturing method plays an even bigger role. All IN718, whether wrought or AM, is subjected to a solution heat treatment to mitigate the fabricated microstructure. A solution treatment is a type of annealing process that dissolves precipitates and secondary phases that formed during the fabrication process. For high-temperature applications, such as jet turbine components, AMS 5662 is the standard for IN718 solution treatments [115]. AMS 5662 prescribes a solution treatment of 941–1010 °C for 1 hour per 25 mm of thickness [114, 115]. Today's LPBF solution treatments are based on the heat treatments developed by Eiselstein and published in 1965 for forged IN718 [35]. Wrought IN718 exhibits equiaxed grains with no preferential crystal orientation (or texture) as shown in Figures 3.2a and 3.3a. The solution anneal dissolves the precipitates, but is designed to limit grain growth. Figure 3.2 shows the X–Y plane. The X–Y, or transverse, plane is perpendicular to the build-direction, Z. Figure 3.3 shows the X–Z, or parallel, plane where the build-direction is aligned vertically to the image.

In contrast to wrought microstructure, LPBF IN718 exhibits a typical microstructure of face-centered cubic (FCC) material as shown in Figures 3.2b and 3.3b. The high energy source of LPBF creates a large temperature gradient within the material during processing. The energy escapes the part by conduction through the build plate, creating the highest temperature gradient in the Z-direction. The preferential crystal growth direction for FCC is the (001) direction. When the (001) crystal orientation aligns with the build Z-direction, the crystals grow rapidly in the vertical direction. The resulting microstructure is dominated by columnar grains aligned with the build direction and a large average grain diameter of 44.0 μm. This preference for (001) growth results in a non-uniform, anisotropic microstructure which translates into orthotropic or anisotropic mechanical behavior. Additionally, the high temperature gradient drives rapid solidification of the microstructure. The rapid solidification limits grain growth, resulting in small,

irregular grains outside of the columnar grains. The end result of the directional growth preference and rapid solidification of the build process is a microstructure dominated by columnar grains in the X–Z plane (build direction) and small (average grain diameter of 10.3 μm), irregular grains in the X–Y plane (transverse direction). Figures 3.2 and 3.3 show a wrought IN718 specimen next to an as-built LPBF specimen for the X–Y and X–Z orientations, respectively. The legends for the IPF maps and IPF figures are provided in Figures 3.4a and 3.4b, respectively.

As shown in Figure 3.2a and Figure 3.3a, wrought grains exhibit an equiaxed shape with a random crystallographic orientation. As a result, the material properties of wrought IN718 are isotropic. Unlike wrought IN718, as-printed AM IN718 has a strong texture (crystal orientation) in the (001) direction associated with the alignment with the build direction. Recrystallization of the columnar grains can reduce this strong texture. Up to 50% recrystallization was reported using a solution anneal of 1160 °C for 4 hours [3]. However, the grain morphology and texture of the recrystallized regions were not explicitly described. The higher temperature for the solution anneal (1160 °C vs 1010 °C in AMS 5662) is necessary to allow recrystallization to occur. Hot isostatic pressing (HIP) is another heat treatment for AM IN718 that can generate recrystallization. ASTM F3055 and ASTM F3301 are newer standards developed for AM metals and prescribe a hot isostatic pressing for additively manufactured, including LPBF, IN718 at 1120–1185 °C for 4 hours [11]. Most HIP treatments in other research for IN718 involve a similar temperature and time as used in this research, 1160 °C for 4 hours [3, 13, 82, 138]. Recent research has also explored “simulated HIP” treatments with an annealing temperature of 1120 °C [54]. The research in this article investigates the effects of the 1160 °C solution anneal without the confounding influence of the high pressures associated with the HIP process.

The lack of an isotropic microstructure or uniform mechanical properties in AM parts is both a challenge and an opportunity when considering engineering design. If

an application requires isotropic material properties, the existing heat treatments based on wrought IN718 are insufficient. Other research is being performed to control the microstructure of AM IN718 parts. For example, Oak Ridge National Laboratory (ORNL) has shown that modifying the EBM process to control the material processing temperature leads to a more isotropic microstructure [31]. However, this work is not readily translated to LPBF due to fundamental differences between EBM and LPBF. Specifically, unlike LPBF, both the focus of the beam and the heating of the build chamber can be rapidly controlled during the EBM process.

As previously stated, IN718 gains its strength from a two-step aging process via precipitation formation. The aging treatment is applied to the material after it has been annealed, driving the precipitation of secondary phases within the material. These precipitates (delta (δ), gamma prime (γ'), and gamma double-prime (γ'')) are responsible for the mechanical strength of the age-hardened IN718, but also cause a corresponding loss in ductility. Ductility in LPBF specimens has been shown to decrease by 50% from the as-built to the annealed and aged condition [145]. For the purposes of this investigation, the age-hardening process is considered as being fully optimized. This research looks to find a solution treatment that will generate an optimal annealed microstructure to then process using the two-step aging as prescribed by AMS 5663: 718 °C for 8 hours, followed by a 2-hour furnace cool to 621 °C and hold for another 8 hours, then air cooled to room temperature [113].

The strengthening precipitates of IN718 can form undesirably during the material fabrication process as a result of slow cooling rates. The solution temperature for these experiments was chosen to dissolve these precipitates and return their constituents to the material matrix. AMS 5662 has a temperature range of 930–1010 °C. However, the solvus temperature of the δ phase is 1020 °C, and the solvus temperature of the Laves phase is 1163 °C [104]. As a result, only a fraction of δ phases and no Laves phases are dissolved

by AMS 5662. Deng et al. reported the presence of rod-like δ phases after annealing per AMS 5662 (980 °C for 1 hour) and δ-free grain boundaries after an elevated solution temperature of 1080 °C for 1 hour [32]. The partial dissolution provided by AMS 5662 has been an acceptable trade-off for wrought IN718 as the δ phases prevent grains from growing during the heat treatment process. Due to the finer grain size of LPBF IN718, a higher solution temperature is necessary to fully dissolve the δ and Laves phases to allow for recrystallization and grain growth during the annealing treatment. For this reason a temperature of 1160 °C is proposed to promote both dissolution and recrystallization.

Larger grains are detrimental to the tensile strength and fatigue resistance based on the Hall-Petch relationship [45], but they are beneficial to creep-rupture resistance [47, 70]. After a material has fully recrystallized, continued heating will result in grain growth. Wrought materials have relatively large grains (ASTM grain size 5, average grain diameter 63.5 μm) [113]. Current solution anneal treatments are designed to limit grain growth by the presence of grain boundary δ phases. Since LPBF IN718 specimens start out with a much finer grain size (ASTM grain size 11, average grain diameter 7.9 μm), the δ phase can be eliminated during annealing to allow for additional grain growth without harming the mechanical properties.

In order to achieve isotropic material properties, the microstructure must be modified by heat treatments that can remove the scan strategy effects and (001) texture from the as-built LPBF IN718 parts. Previous research has investigated the microstructure resulting from traditional heat treatments applied to LPBF IN718 [101, 120, 130] and HIP treatments [82, 138] which have been shown to leave the columnar grains intact. Recent research by Raghavan et al investigated higher temperature annealing (1100 °C and 1200 °C) for 2 hours, and they were able to show that the grain size increased, but the columnar microstructure remained [108]. Based on this research it is clear that annealing at temperatures greater than the δ and Laves phases will alter grain growth and size, but it

remains unknown for how long these conditions should be applied to achieve the desired effects in LPBF IN718.

Anisotropy in mechanical properties is typically defined by Equation (3.1), where σ_x and σ_z are the tensile strength ($YS_{0.2}$ or UTS) in the transverse or build direction, respectively [2, Eq 1]. Tensile testing by Strößner et al. [130] showed anisotropic behavior up to 10% in the as-built and various heat-treated condition. Cloots et al. [26] performed tensile testing on LPBF IN738LC and found similar results, with anisotropy up to 20%.

$$\frac{\sigma_x - \sigma_z}{\sigma_x} \times 100\% \tag{3.1}$$

This research investigates the microstructure resulting from a higher temperature and longer duration anneal to remove the directional dependence of the microstructure and erase scan strategy effects. Recrystallization and the removal of scan strategy effects have big implications for the acceptance of AM parts. If parts can be heat treated to remove any OEM-related microstructural differences, then parts fabricated on different machines can be printed in any orientation and possess the same properties. It is hypothesized that an annealing treatment at 1160 °C will overcome the scan strategy effects and anisotropy of the LPBF process that AMS 5662 is not able to mitigate due to the increased recrystallization and grain growth associated with the higher temperature annealing treatment.

As part of this research, LPBF specimens were printed using a selection of scan strategies. The parts were annealed in air at 1160 °C (2120 °F) for durations of 1–8 hours, followed by a water quench to limit secondary phase formation. The microstructure was examined relative to the AM build direction. Grain properties, texture, and recrystallization were investigated in both the parallel (X–Z plane) and transverse (X–Y plane) directions. A goal of this research is to identify the time and temperature for a post-process treatment that will induce recrystallization and grain growth to generate specimens with equiaxed grains and isotropic properties. No consideration was given to modify the two-step aging process as the aging temperatures are too low to achieve this research's goals.

3.2 Methodology

3.2.1 Material.

IN718 powder was acquired from Powder Alloy Corporation (Loveland, Ohio, USA). The powder's elemental composition is presented in Table 3.2. The alloy was powderized using a gas atomization process producing spherical particles with a distribution of particle diameters between 25–40 μm. A Concept Laser (Lichtenfels, Germany) *M2 cusing* LPBF printer was used to fabricate test specimens from the IN718 powder. The *M2 cusing* is equipped with a 400 W continuous-wave Ytterbium fiber laser.

LPBF specimens were designed specifically for the microstructural characterization to be carried out in this research. Two different specimens were designed for viewing of the X–Y or X–Z plane while eliminating the need to section the specimens. The specimens are shown in Figure 3.5. Both specimen designs contain three 10 mm cubes mounted to a central base. For the build process, each cube was assigned a different core scan strategy (continuous, island, strip) as shown previously in Figure 3.1 surrounded by a 2 mm skin. The 3-in-1 specimen also simplified batch integrity during the heat-treatment processing. The parameter sets for the skin and core strategies are shown in Table 3.1. Volumetric energy density (J/mm^3) shown in the table is calculated as laser power divided by the product of the scan speed, hatch spacing, and layer thickness. The builds were conducted in a protective argon environment to minimize oxidation.

Table 3.1: Summary of Build Parameters

Section	Laser power (W)	Scan Speed (mm/s)	Spot Size (μm)	Hatch spacing (μm)	Layer thickness (μm)	Energy density (J/mm^3)
Core	370	700	180	140	80	47.2
Skin	180	800	130	140	40	40.2

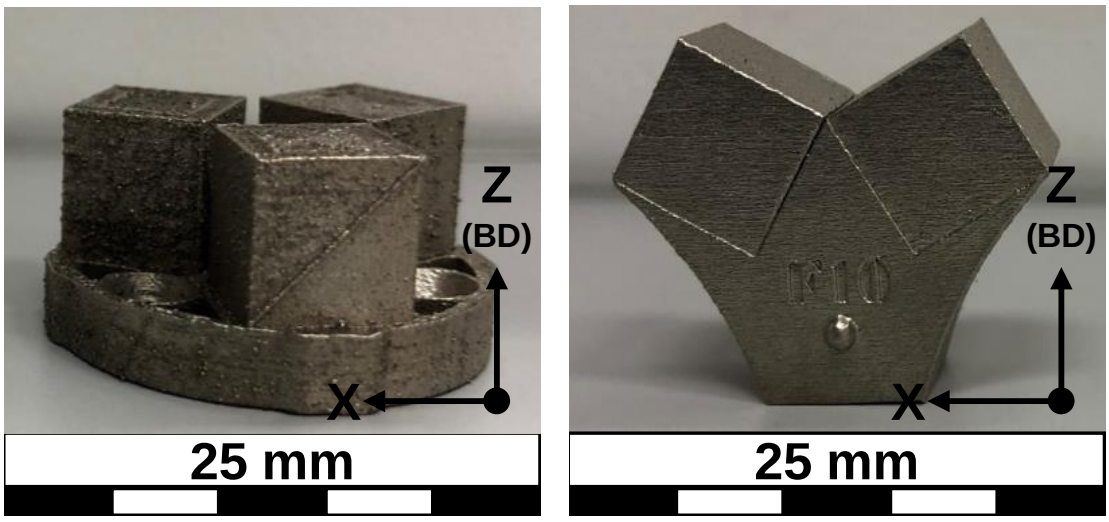

(a) X–Y specimen

(b) X–Z specimen

Figure 3.5: X–Y and X–Z specimens were printed for microstructural examination in the transverse and build directions, respectively. Specimens were designed to incorporate three scan strategies in one specimen for ease of metallographic preparation and batch integrity during heat treatment processing.

Table 3.2: Chemical Composition of Powderized Alloy

Element	Ni	Cr	Fe	Nb+Ta	Mo	Ti	Al	Co	C
wt %	54.05	18.08	17.69	5.32	2.93	0.97	0.45	0.20	0.03

Less than 0.1 wt% of Mn, Si, S, P, B, Cu, Ca, Mg, O, N

3.2.2 Scan Strategies.

The 6 mm × 6 mm core of each specimen was printed using one of three scan strategies provided by Concept Laser: 1) continuous, 2) island, or 3) strip. These strategies are illustrated in Figure 3.1. These three strategies were selected to compare the residual stress

and microstructural evolution during the annealing process and are representative of the common scan strategies associated with the prime OEM vendors of LPBF machines. The continuous strategy applies scan vectors that traverse the entire surface area. This can result in geometry-induced residual stress from concentrations of the thermal energy during dissipation. The island strategy divides the surface area into small squares, then rasters the small squares in a random sequence to spread out the heat. This spreads the thermal energy more evenly across the part, which reduces the overall residual stresses. As such, the island scanning strategy is the standard strategy for production [21]. This research used an island size of 5 mm $\times$ 5 mm, similar to Lu's study [76]. The strip strategy lays between continuous and island. The strip strategy segments the area to be printed into strips of a specified width. It then builds each strip with a raster with the scan vectors perpendicular to the strip length. This research used a 5 mm strip length. The raster for each scan strategy was a meandering bi-directional path with Concept Laser's sky-writing feature disabled.

3.2.3 Post-process Heat Treatments.

The specimens were annealed in air at 1160 °C. Specimens were removed individually at each hour mark and immediately quenched using water. The annealing times for the specimens ranged from 1–8 hours. No aging was performed on the specimens. One specimen was maintained in the as-built condition to serve as a baseline for comparison for the microstructure.

The selected annealing temperature is a noticeable deviation from the heat treatments for wrought IN718 listed in AMS 5662 and AMS 2774 [114, 115]. The higher annealing temperature allows for recrystallization of the microstructure. After recrystallization is achieved, grain growth will begin. Larger equiaxed grains are expected to appear in the specimens that were annealed for longer periods of time since their grains had ample time to grow.

Since the annealing temperature is well above the solvus temperature of the precipitate phases, the IN718 secondary phases (δ, γ', and γ''), as well as any incidental primary Laves phase, should be fully dissolved during the anneal. The water quench applied after the anneal will lock the microstructure and should minimize the formation of secondary phases.

3.2.4 Microstructural Characterization.

The specimens' grain orientation was acquired in a Quanta 450 scanning electron microscope (SEM) (Thermo Fisher Scientific, Waltham, MA, USA) using an EDAX electron backscatter diffraction (EBSD) analyzer (Ametek Materials Analysis Division, Mahwah, NJ, USA). The source beam had an accelerating voltage of 20 kV and a spot size of 8. Specimens were mounted in conductive resin and prepared using standard metallographic polishing techniques with a final polishing step with 0.05 μm colloidal silica. Elemental analysis of the specimens was performed with an EDAX energy dispersive spectroscopy (EDS) analyzer while the EBSD maps were generated.

The EBSD maps were analyzed using EDAX's orientation imaging microscopy (OIM) analysis software. The maps were used to determine the specimens' average grain sizes, degree of recrystallization, and build-direction texture. A grain was defined in the software as a collection of neighboring pixels with misorientations less than 5°. The defined minimum grain size was 5 pixels, and each grain must include more than one row of pixels.

3.2.5 Mechanical Testing.

Nanoindentation tests were performed on the microstructural specimens at room temperature using an iMicro nanoidenter (KLA-Tencor, Militas, CA, USA) with InView software (Nanomechanics, Inc, Oak Ridge, Tenn., USA). Nanoindentation testing provided measurements of the Young's modulus (E), nanoindentation hardness (H_{IT}), and Vickers hardness (H_V). Tests were performed in accordance with ISO 14577, Constant Loading Rate Indentation [51]. The iMicro used a three-sided diamond pyramid Berkovich tip

indenter (TB24324). An initial hardness test was performed on a separate LPBF IN718 specimen to determine the force-response of the system and material. 200 mN was selected as the test force as it was high enough to get the indenter through the surface effects of the mechanical polishing and low enough that the frame stiffness of the testing apparatus would not become significant. The time to load was 10 seconds, the dwell time was 1 second, and the Poisson's ratio was set to 0.3 for IN718 [129]. For each specimen, indentation was performed in the center in a 3×3 grid with 40 μm separation to avoid interference between indentations.

Tensile specimens were designed in accordance with ASTM E8 [7] and tested at room temperature by the Miami Valley Materials Testing Center (Tipp City, OH, USA). 30 specimens were printed in each of the vertical (90°) and diagonal (45°) orientations to enable the measurement of anisotropy. Of those 30, 10 were printed with each scan strategy from Figure 3.1. Horizontal specimens were attempted but were unbuildable due to thermal issues with the build process.

The parts were removed from the build plate via wire electrical discharge machining, then treated with one of two solution anneal treatments: the conventional solution treatment as prescribed by AMS 5662 [115], or the modified solution treatment which was selected from the results of the microstructural characterization. The 10 specimens of each orientation and scan strategy were split evenly between the two solution treatments. Solution treatments and aging were performed in a vacuum furnace at Winston Heat Treating (Dayton, OH, USA). Following the split solution treatment, all specimens were aged using the double-aging treatment per AMS 5663 [113] for IN718 employment in high-temperature applications. The parameters for the solution and aging treatments are shown in Table 3.3.

After the final heat treatment, the parts were machined to their final dimensions as shown in Figure 3.6a. The cylindrical dog-bone specimens have a 10 mm diameter

with a 40 mm gauge length. The gauge section included a 1% taper to improve strain measurements. Tests were performed with an extensometer at a strain rate of 0.0005-0.0006 strain per minute.

Table 3.3: Heat treatment parameters used for the LPBF IN718 tensile specimens

Heat treatment	Cycle parameters - temperature, time, and cooling
Conventional solution treatment (AMS 5662 [115])	1010 °C 1 h, argon cool
Modified solution treatment	1160 °C 4 h, argon cool
Aging (AMS 5663 [113])	718 °C, 8 h, furnace cool to 621 °C, 8 h, argon cool

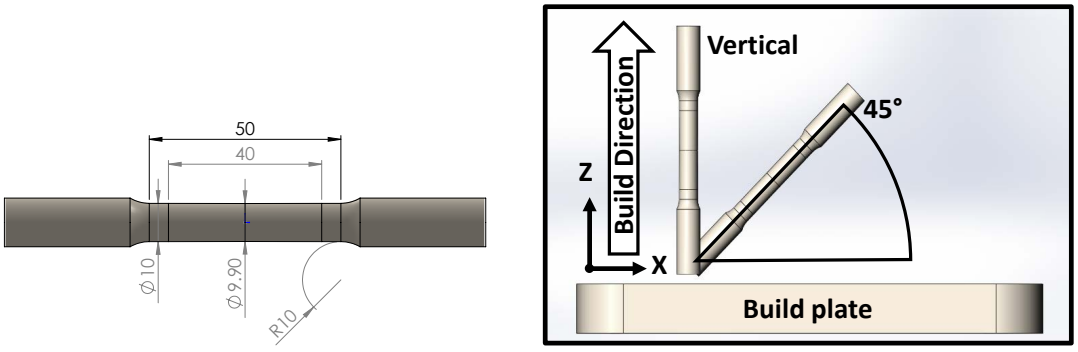

(a) Tensile specimen (b) Build orientations

Figure 3.6: Cylindrical tensile specimens were built with a 10 mm diameter, 40 mm gauge length, and a 1% taper to the middle. Specimens were built in the vertical (90°) and diagonal (45°) orientations.

3.3 Results and Discussion

3.3.1 Microstructural Characterization.

Microstructural characterization was performed by collecting EBSD maps on each specimen. Five maps were collected on the core section for each scan strategy and annealing time in order to generate statistical data. Each map covered an area of approximately 920 μm × 730 μm (0.67 mm^2). The combined scans account for approximately 10% of the specimen core area. Inverse pole figures (IPF) and IPF maps were generated for every combination of scan strategy and annealing time. Grain orientation spread (GOS), grain size, and texture were evaluated using OIM Analysis software (EDAX). Figure 3.7 displays the IPF maps and (001) IPFs of the three scan strategies in the as-built specimens. The maps are oriented along the transverse (X–Y) and parallel (X–Z) planes to the build direction (Z). Texture intensity values were calculated with respect to the specimen's Z-direction. For the X–Y specimens, the (001) crystal direction is orthogonal to the X–Y viewing plane. For the X–Z specimens, the (001) crystal direction is aligned with the vertical direction of the X–Z viewing plane. Texture intensities are normalized with respect to an idealized random specimen; an intensity value of 1.0 at any given orientation indicates that the given orientation appears no more and no less than it would if the specimen exhibited purely random crystal orientations. As seen from the IPFs with each map, the peak intensity value for each scan strategy is located at the (001) vertex. The location of the peak value at the (001) vertex is caused by the previously discussed alignment of the preferred FCC growth orientation and the heat flux of the LPBF process. After 4 hours of annealing, the different specimens achieved a more uniform appearance as the higher annealing temperature achieved recrystallization and grain growth as shown in Figure 3.8. The legends for the IPF maps and IPF figures are provided in Figures 3.4a and 3.4b, respectively.

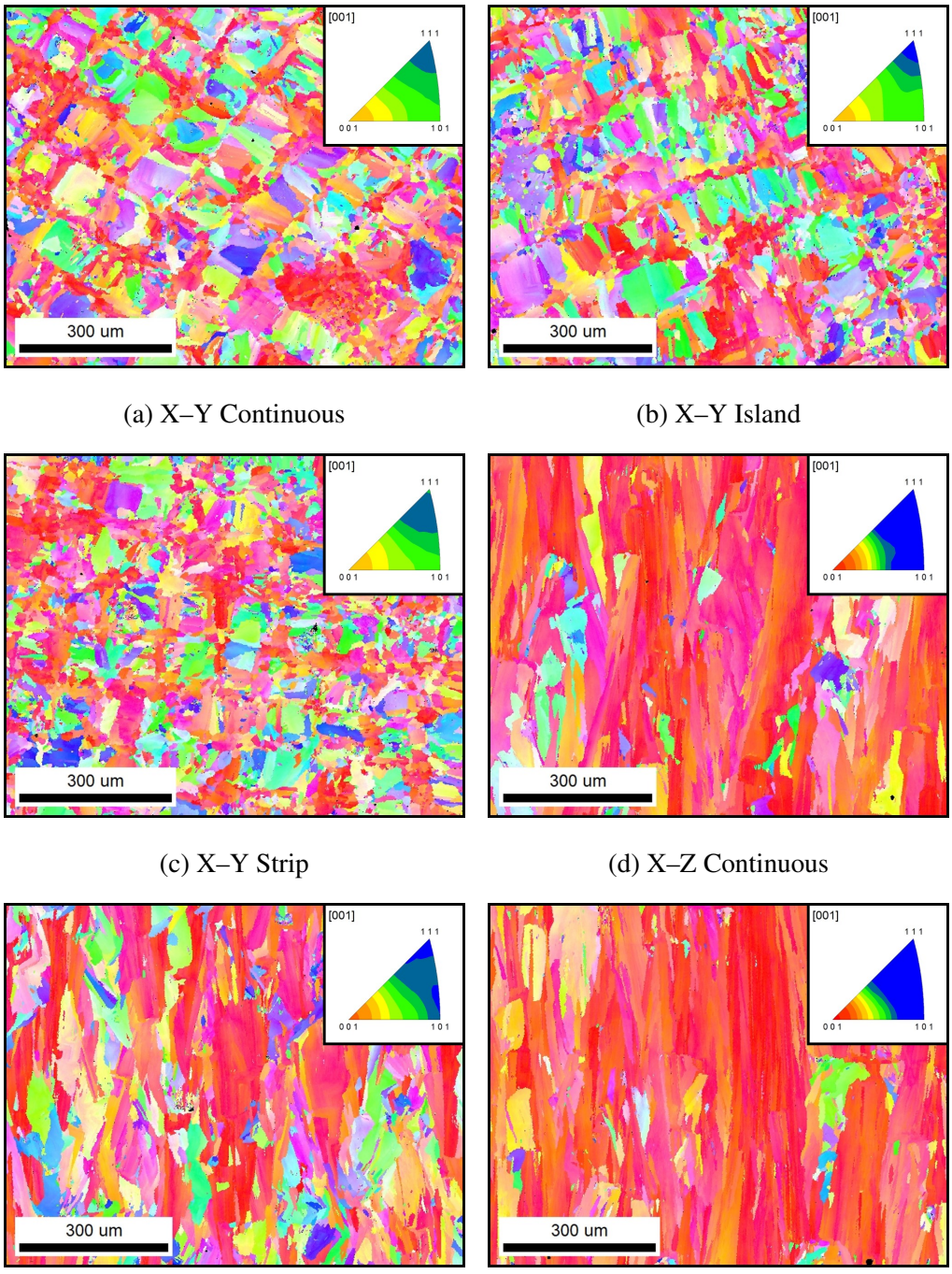

(a) X–Y Continuous

(b) X–Y Island

(c) X–Y Strip

(d) X–Z Continuous

(e) X–Z Island

(f) X–Z Strip

Figure 3.7: IPF maps of the as-built specimens printed using various scan strategies. The X–Y and X–Z maps have very different microstructure. The continuous and strip specimens show a more pronounced IPF intensity around the (001) vertex.

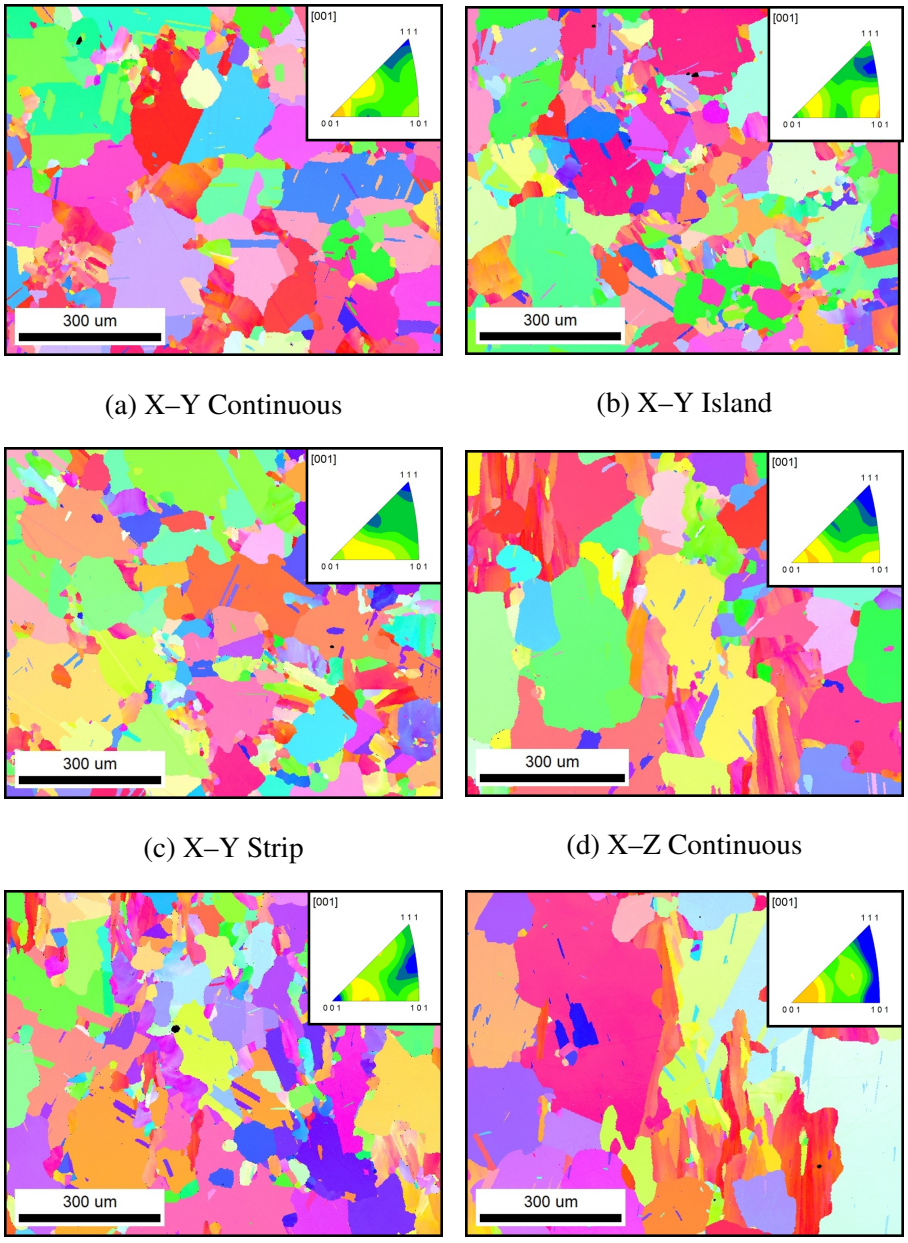

(a) X–Y Continuous

(b) X–Y Island

(c) X–Y Strip

(d) X–Z Continuous

(e) X–Z Island

(f) X–Z Strip

Figure 3.8: At 4 hours, the scan strategies and orientations are nearly indistinguishable based on grain size and texture. These IPF maps visually confirm the hypothesis that annealing at 1160 °C for 4 hours results in an equiaxed microstructure achieved through recrystallization and grain growth, resulting in indistinguishable, hence isotropic, microstructure for each scan strategy.

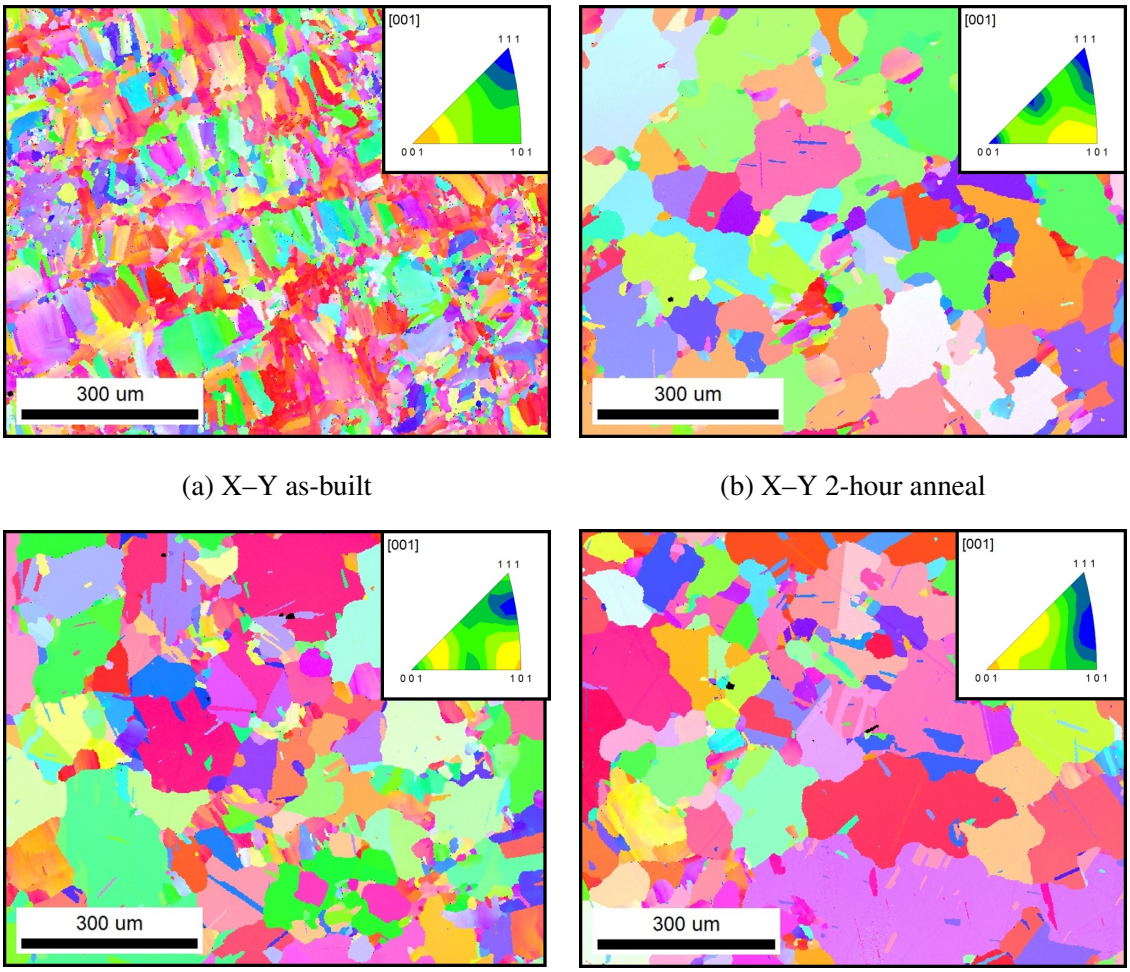

(a) X–Y as-built

(b) X–Y 2-hour anneal

(c) X–Y 4-hour anneal

(d) X–Y 8-hour anneal

Figure 3.9: IPF maps of the island strategy at various anneal times, shown in the X–Y orientation. The initial microstructure is overcome by recrystallization and grain coarsening with increasing anneal times.

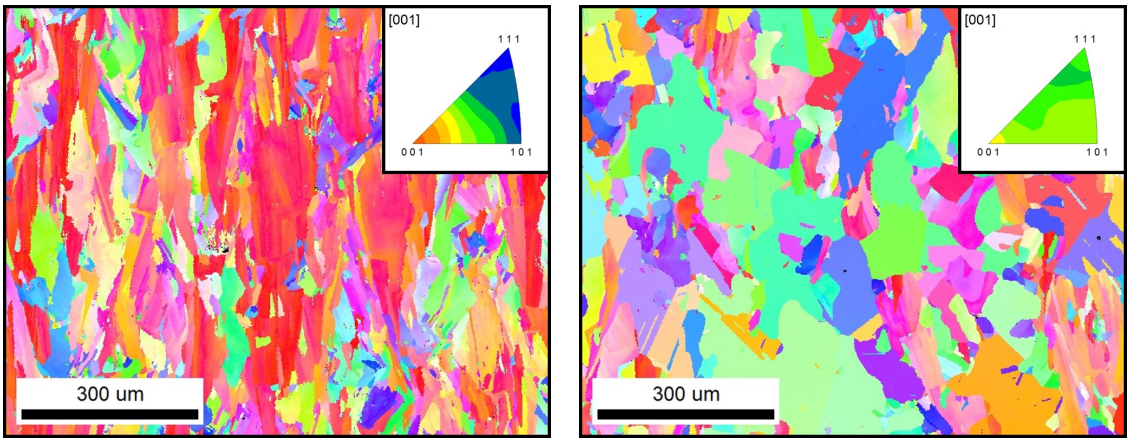

(a) X–Z as-built

(b) X–Z 2-hour anneal

(c) X–Z 4-hour anneal

(d) X–Z 8-hour anneal

Figure 3.10: IPF maps of the island strategy at various anneal times, shown in the X–Z orientation. The initial microstructure is overcome by recrystallization and grain coarsening with increasing anneal times. The X–Y and X–Z microstructures became indistinguishable after 4 hours of annealing at 1160 °C.

The evolution of the microstructure is apparent from viewing the EBSD results. Figures 3.9 and 3.10 displays representative IPF maps and textures for the island scan strategy at annealing times of 0-, 2-, 4-, and 8-hours. Recrystallization and grain growth are visible in both the X–Y and X–Z planes. The as-built X–Y microstructure consists of a patchwork of many grains. The patchwork pattern is the result of the scan paths, with the size of the pattern correlating to the hatch spacing ($\approx$ 140 μm). The as-built X–Z microstructure displays large, columnar grains. Residual strains within a grain appear as a color gradient, while strain-free or recrystallized grains appear monochromatic. At 2-hours, several large, solid-colored grains have appeared as well as some annealing twins. In the 4-hour maps, the X–Y and X–Z images are qualitatively indistinguishable. The average grain diameter ($\approx$ 20 μm) and recrystallized fraction (>80%) have converged as the effects of scan strategy have been mitigated. The 8-hour images continue these trends, with no visible distinction between the X–Y and X–Z images. The final two images are dominated by large, fully-recrystallized grains interspersed with smaller annealing twins. While the maps in Figures 3.9 and 3.10 are provided for the island strategy, the microstructure evolution described here applies to the continuous and strip strategies as well.

3.3.2 Recrystallization.

The amount of recrystallization that has been achieved by annealing can be quantified through the use of the GOS. The GOS is the average deviation in orientation between each point in a grain and the average orientation of the grain [148]. The GOS approach is based on the concept that a deformed grain will exhibit internal strain resulting from deformation of the crystal lattice. A high GOS value indicates a greater deviation of orientations within a grain, thus signifying the presence of residual strains. A lower GOS value indicates a more uniform orientation, such as in a recrystallized grain. In general, GOS values below 3° have been used as an upper bound for identifying recrystallized material. GOS values between 1–3° have been shown to provide similar results for comparing recrystallized fractions

[42]. In the current study, the GOS distribution of the various specimens was examined, with two representative distributions shown in Figure 3.11. The first image shows the as-built spread of grain orientations. The as-built specimen contains many grains with large internal orientation spreads. Recall the OIM Analysis software defines a grain as a set of pixels where neighboring pixels have less than a 5° misorientation. The 4–6° GOS as shown in Figure 3.11a represents a significant amount of residual strain. Figure 3.11b shows the spread after an 8-hour anneal. The higher GOS values (>3.0°) have been mostly eliminated. Over 93% of the specimen area has a GOS value <1.0°, whereas only 11% of the as-built specimen meets this threshold. In similar comparisons of AM IN718, a GOS threshold of 1.2° was used to define a recrystallized grain [18]. The current research continues the use of 1.2° as a suitable threshold for comparing the recrystallized area fractions of LPBF IN718 specimens.

Using this ≤1.2° GOS threshold for recrystallization, the recrystallized area fraction was calculated for each specimen. Figure 3.12 shows the average recrystallized area fraction for each set of specimens. The tabulated values are provided in Table 3.4. As expected from the application of an annealing heat treatment, the recrystallized fraction increases with increased annealing time. All scan strategies maxed out at around 95% recrystallized area, which may form a practical upper-limit to the amount of recrystallization that can be achieved. The X–Y orientations reached >90% after two hours, while the X–Z orientations didn't achieve >90% recrystallization until 4 hours.

When examining the GOS values, it is noticeable that the X–Y orientation has a higher recrystallized fraction at the earlier annealing times. This could indicate a lower residual stress in the X–Y plane than in the build direction. The X–Y specimens maintain this lead over the X–Z specimens until the 4-hour anneal. It is likely the X–Z specimens contain higher residual strains caused by the vertical, columnar grains spanning multiple

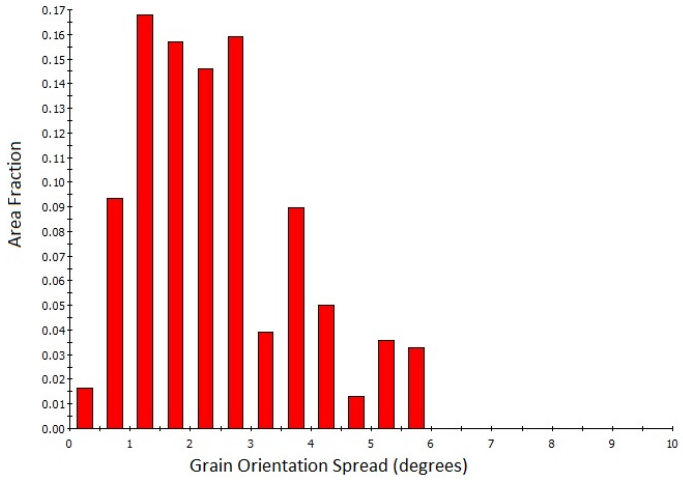

(a) As-built specimen

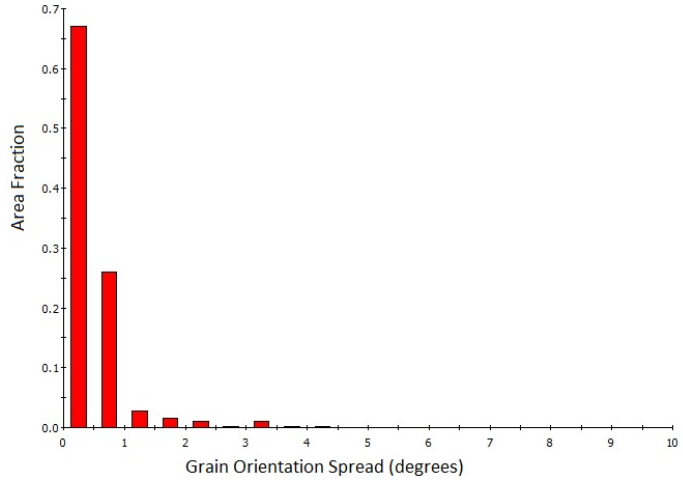

(b) After 8-hr anneal at 1160 °C

Figure 3.11: GOS distribution plots of two representative X–Z island specimens. Figure 3.11a shows the GOS distribution for an as-built X–Z island specimen. The wide range from 0-6° indicates significant residual strains. Figure 3.11b represents another X–Z island specimen after being annealed for 8 hours at 1160 °C. The GOS values have been greatly reduced as the residual strains were relieved during annealing.

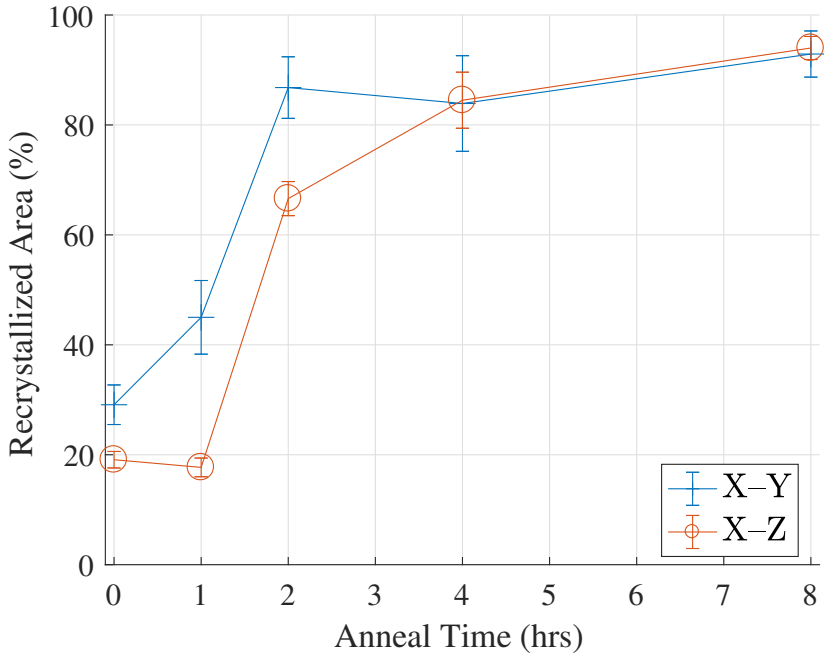

Figure 3.12: Recrystallized area (% area, GOS $\leq$ 1.2°) as a function of anneal time. The recrystallized area increases with annealing time. After 4 hours, the X–Y and X–Z specimens display a uniform value.

Table 3.4: Recrystallized Area Fraction (%) corresponding to Figure 3.12

Anneal Time	0	1	2	4	8
X–Y Avg (Std Dev)	29.1 (3.6)	45.0 (6.7)	86.8 (5.6)	83.9 (8.7)	92.9 (4.2)
X–Z Avg (Std Dev)	19.1 (1.5)	17.7 (1.7)	66.6 (3.1)	84.5 (5.1)	94.0 (2.1)

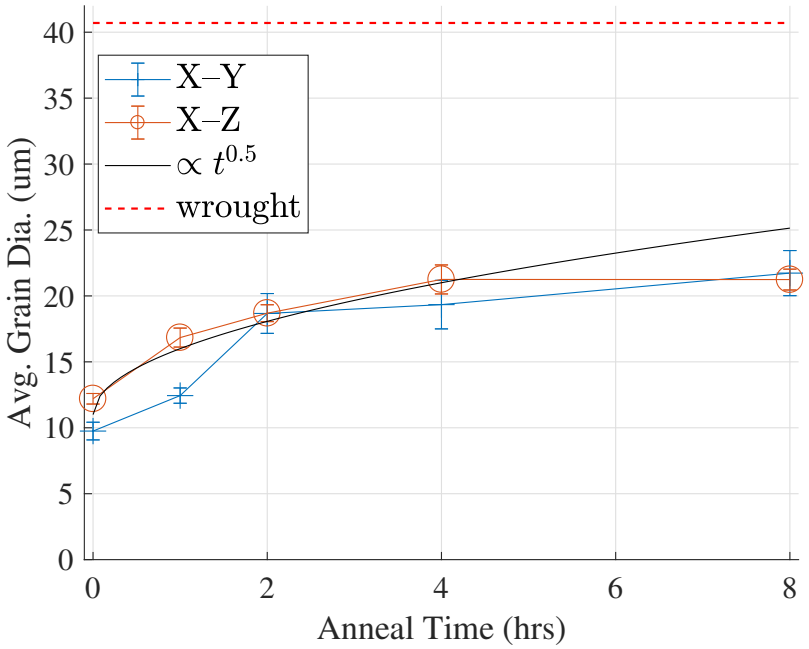

Figure 3.13: Average grain size is presented as a function of annealing time for each scan strategy and view orientation. Edge grains are excluded from the calculations. The $t^{0.5}$ line illustrates the parabolic grain growth given by Equation (3.2). A reference is also shown marking 40.7 μm for the wrought grains from Figure 3.2a. Even after 8 hours of annealing, the LPBF grains are still much smaller than their wrought counterparts.

LPBF layers. Higher initial residual strains require more energy to overcome, resulting in the X–Y specimens recrystallizing at lower anneal times. At 4-hours, this difference is mitigated and there is no longer a difference between the two orientations. This uniform recrystallization at 4 hours and later is significant as it shows that the higher temperature anneal can overcome the LPBF effects on the GOS.

3.3.3 Texture Reduction.

As-built LPBF specimens display a strong (001) texture as a result of the build process and FCC crystal growth. Figure 3.14 shows the evolution of both the (001) and maximum intensity values for the various scan strategies in the X–Z orientation at 0-, 4-, and 8-hours of annealing. The starting values for each intensity are high as a result of the encouraged (001) growth. The starting values are noticeably lower for the island strategy than the continuous or strip. For a larger sample surface, this might be expected as the island strategy spreads out the heat of each print layer, thus minimizing the heat flow in the Z-direction. However, these small specimens do not contain enough individual islands for this to have an influence here. The mechanism for the lower (001) IPF intensity is a possibility for further study.

The (001) and max intensity values decrease with increased annealing time, and the max value is no longer located at the (001) vertex after 4 hours. The max IPF intensities for each strategy are indistinguishable after 4 hours of annealing. The island strategy shows the lowest final (001) peak intensity, achieving an intensity of 1.45 at 8 hours. By comparison, the wrought-annealed specimens in Figures 3.2a and 3.3a have peak intensity values of 2.0 and 1.6 for the X–Y and X–Z orientations, respectively.

The IPF intensities in Figure 3.14 show a marked reduction in the peak (001) intensity. While the grains recrystallize, they have no internal preference for reorientation and no external stimulus encouraging an orientation. The resulting recrystallized grains will then exhibit a reduced texture as presented here. This indicates the recrystallization of the

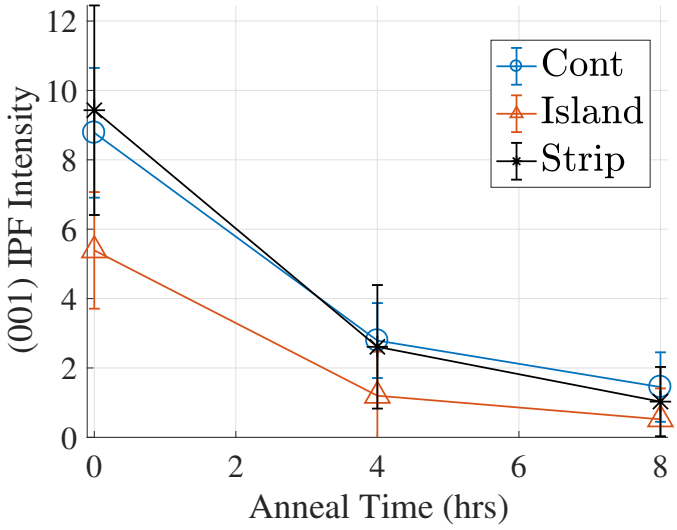

(a) (001) Vertex Intensity

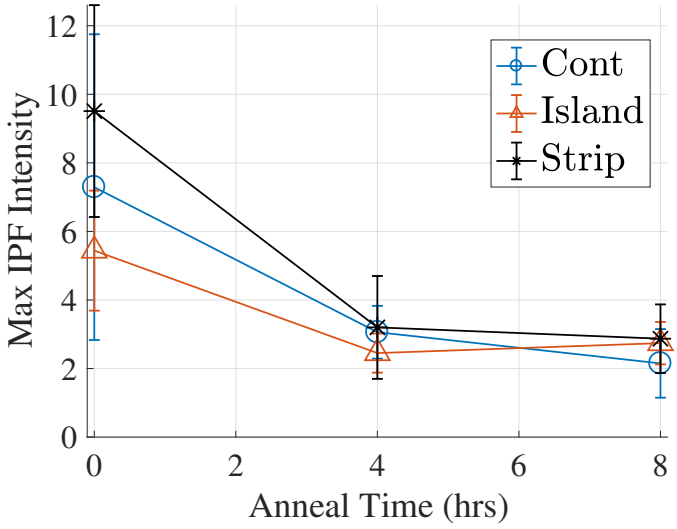

(b) Max Overall Intensity

Figure 3.14: Average IPF peak intensities of the as-built, 4-, and 8-hour annealed X–Z specimens. The highest intensity in the as-built specimens is at the (001) vertex. As the annealing time increases, the max IPF intensity decreases and it is no longer located at the (001) vertex. The effects of the scan strategies are indistinguishable at the 4-hr mark.

grains has increased the randomness of the orientations. The resulting grains are now more isotropic in appearance. The 1160 °C anneal mitigates the texture produced by the LPBF scan strategies.

3.3.4 Grain Growth.

Grain growth is the primary method by which equiaxed grains will be achieved. Figure 3.13 shows the increase in average grain diameter over the increased annealing times. The tabulated values are provided in Table 3.5. As is visibly apparent in Figures 3.9 and 3.10, the grains coarsened with increasing anneal time. This allowed the original columnar grains to transform into equiaxed grains and mitigated the differences between the X–Y and X–Z orientations. The X–Z specimens began with a higher average grain size owing to the presence of the large, columnar grains that dominated the microstructure. As the grains recrystallize and coarsen, the columnar grains are consumed by larger, equiaxed grains. At 2 hours of annealing and longer the average grain sizes between the X–Y and X–Z specimens approach a more uniform size. This is important in achieving an isotropic microstructure. After 4 hours, the X–Y and X–Z average grain diameters (d) have increased by 98% and 74%, respectively. The growth in both orientations appears to approximate a relationship of $d \propto \sqrt{t}$, at least in the first 4 hours, which is close to the traditional parabolic growth model in Equation (3.2) [48]:

$$d^2 = d_0^2 + A\sigma t, \tag{3.2}$$

where d_0 is the as-built average grain diameter, A is a temperature-dependent constant, and t is time.

Small grain sizes are preferred for tensile-limited applications owing to the inverse relationship between tensile strength and grain size in the Hall-Petch equation [45]

$$\sigma_y = \sigma_0 + \frac{k_y}{\sqrt{d}}, \tag{3.3}$$

Table 3.5: Average Grain Diameter (μm) corresponding to Figure 3.13

Anneal Time	As-built	1 h	2 h	4 h	8 h
X–Y Avg (Std Dev)	9.75 (0.67)	12.44 (0.58)	18.67 (1.51)	19.34 (1.84)	21.73 (1.71)
X–Z Avg (Std Dev)	12.20 (0.40)	16.84 (0.72)	18.69 (0.64)	21.25 (1.10)	21.24 (0.79)

where σ_y is the yield stress, σ_0 and k_y are material constants, and d is the grain diameter. For IN718, σ_0 and k_y typically have values of approximately 300 MPa and 1.7, respectively [126, p. 243]. The small grain sizes in as-built LPBF IN718 (7.9 μm, Figure 3.2b) are much smaller than the initial grain sizes in wrought IN718 (40.7 μm, Figure 3.2a). The grain sizes after 4 hours are 74–98% larger than the initial grain sizes, but still below the typical wrought grain sizes of 40+ μm. Corresponding with the Hall-Petch relationship, LPBF IN718 has been shown to produce superior tensile properties as similarly annealed and aged wrought specimens [23]. Amato et al. also showed an increase in tensile properties for LPBF specimens compared to wrought, but only in the annealed condition [3].

For creep-limited applications, the critical material behavior is related to diffusional creep [97]. The Nabarro-Herring model of diffusional creep is given in Equation (3.4), and the Coble model is given in Equation (3.5). Each creep model relates the steady-state strain rate as inversely proportional to the grain diameter.

$$\dot{\varepsilon}_{ss} = \frac{D_{sd}\sigma b^3}{kTd^2} \tag{3.4}$$

$$\dot{\varepsilon}_{ss} = \frac{\alpha_3 D_{gb}\sigma b^4}{kTd^3} \tag{3.5}$$

$\dot{\epsilon}_{ss}$, the steady-state creep rate, is dependent on the applied stress, σ, temperature, T, and material properties of grain diameter, d, diffusivity, D, and Burgers vector, b. α_3 is a constant on the order of unity, k is the Boltzmann constant, D_{sd} is the self-diffusion coefficient, and D_{gb} is the diffusion coefficient along grain boundaries [97]. An increase in

grain size will produce a reduction in the minimum creep rate for each of these models. In theory, this decreased creep rate will result in an increase in creep-rupture life. Therefore the larger grains produced by this research should be favored for creep-limited applications.

3.3.5 Mechanical Testing.

The hardness tests were conducted to measure E, H_{IT}, and H_V for the as-built specimens and the specimens annealed for 1, 2, 4, and 8 hours in both the X–Y and X–Z orientations. Additionally X–Y and X–Z specimens annealed at 1160 °C for 3 hours were also tested for hardness. Table 3.6 provides a summary of the nanoindentation tests. The Young's modulus values range from 173.9 GPa to 210.4 GPa. While the variation in the range is high, there is no correlation with annealing time, orientation, or scan strategy. The range does cover the typical E values of 190–210 GPa reported for wrought and LPBF IN718 [129, 145]. The Vickers hardness values range from a high of 280.5 to a low of 235.7.

The tensile strength (as approximated by H_{IT}) ranges from a high of 2.976 GPa to a low of 2.494 GPa. A loss of tensile strength was expected as a result of the annealing treatment. These results, as seen in Figure 3.15, show a loss of 8-12% in H_{IT}. The loss is not a linear function of annealing time and appears to vary between the X–Y and X–Z orientations in a similar fashion to the change in recrystallized fraction and grain growth (Figures 3.12 and 3.13). The hardness in the X–Y orientation decreases immediately in the 1-hour anneal and reaches a minimum around 3–4 hours. The measurements of the 8-hour X–Y specimen are indistinguishable from the 4-hour X–Y results. The X–Z hardness does not show a marked change until the 2-hour anneal, from which point the hardness decreases until 4 hours. Similar to the X–Y specimens, the measurements of the 8-hour X–Z specimen are not distinguishable from the 4-hour X–Z results. The hardness results did not show a noticeable effect due to the scan strategy.

Table 3.6: Summary of Hardness Testing

Specimen	Young's modulus	Nanoindentation hardness	Vickers hardness
	GPa (Std Dev)	GPa (Std Dev)	(Std Dev)
As-built (X–Y)	175.6 (11.2)	2.825 (0.086)	267.0 (8.1)
As-built (X–Z)	177.9 (6.8)	2.922 (0.093)	276.2 (8.8)
1 h (X–Y)	180.8 (14.6)	2.586 (0.180)	244.5 (17.0)
1 h (X–Z)	180.6 (7.9)	2.967 (0.096)	280.5 (9.1)
2 h (X–Y)	210.4 (12.1)	2.546 (0.073)	240.6 (6.9)
2 h (X–Z)	180.3 (10.0)	2.697 (0.138)	254.9 (13.0)
4 h (X–Y)	179.2 (5.0)	2.494 (0.137)	235.7 (12.9)
4 h (X–Z)	169.2 (10.9)	2.540 (0.159)	240.1 (15.0)
8 h (X–Y)	173.9 (10.5)	2.601 (0.101)	245.9 (9.5)
8 h (X–Z)	197.9 (14.0)	2.577 (0.125)	243.5 (11.8)

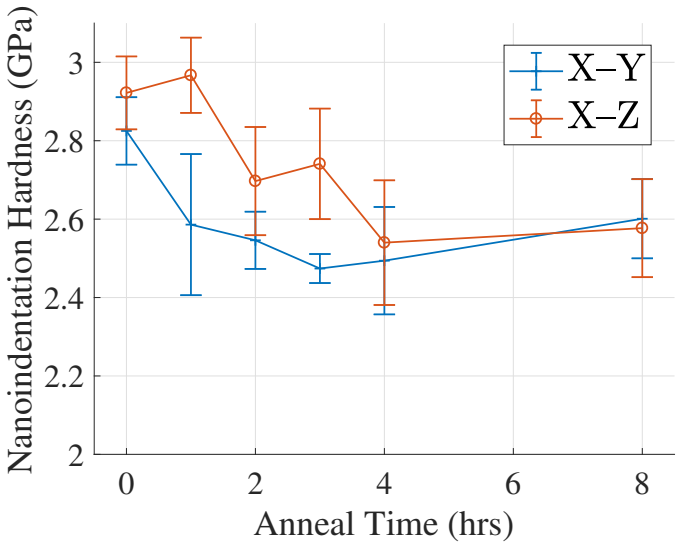

Figure 3.15: Nanoindentation hardness (H_{IT}) as a function of annealing time (as-built, 1-, 2-, 3-, 4-, and 8-hours) and specimen orientation (X–Y, X–Z). The hardness decreases with annealing times up to 4 hours. Additionally, the X–Z hardness results are higher than the X–Y results until the anisotropy vanishes around 4 hours.

A slight anisotropy in hardness, or difference between X–Y and X–Z values, is shown for the as-built specimens in Figure 3.15. As mentioned previously, the X–Y hardness values show a quicker decrease than the X–Z values starting with the 1-hour anneal. At 1 hour, the anisotropy is the largest where the X–Z specimen has not shown any softening. But as the annealing time increases, the rate of change of the X–Y values decreases. By the 4-hour anneal, the hardness values have converged for both specimens indicating the achievement of an isotropic material. This trend holds for the 8-hour specimens as well. A convergence after 4 hours when annealing at 1160 °C is faster than the 16 hours that was previously shown with an annealing temperature of 1120 °C [54].

The results of the tensile testing are shown in Figure 3.16 and tabulated in Table 3.7. In contrast to the hardness tests, these specimens were aged following the solution treatments. The choice of scan strategy was found to have no effect on any of the tensile properties, so the data are presented as only a function of orientation and heat treatment. The largest influence of orientation and heat treatment is apparent in the yield and UTS. As has been shown in previous reports on similar LPBF superalloys, the vertical orientation in this test presents a lower tensile strength [65, 130]. With the conventional heat treatment, the anisotropy (Equation (3.1)) between the stronger 45°and 90°orientations is 15.7% and 8.8% for yield and UTS, respectively. After the modified heat treatment, this anisotropy is greatly reduced to 5.9% and 2.7%. The Young's modulus shows a small difference due to orientation, but not heat treatment, however this anisotropy is relatively small compared to the deviation of the test data. Similarly, the large deviation in the elongation data does not allow for any conclusions to be made on the impact of the orientation or heat treatment.

The Hall-Petch relationship, Equation (2.3), predicts a loss of 15% tensile strength using the X–Z grain diameters from the as-built and 4-hour data in Table 3.5. The 90° specimens show a decrease in $YS_{0.2}$ and UTS of 8.7% and 7.5%, respectively, from the conventional to the modified heat treatments. The 45° specimens show a greater decrease

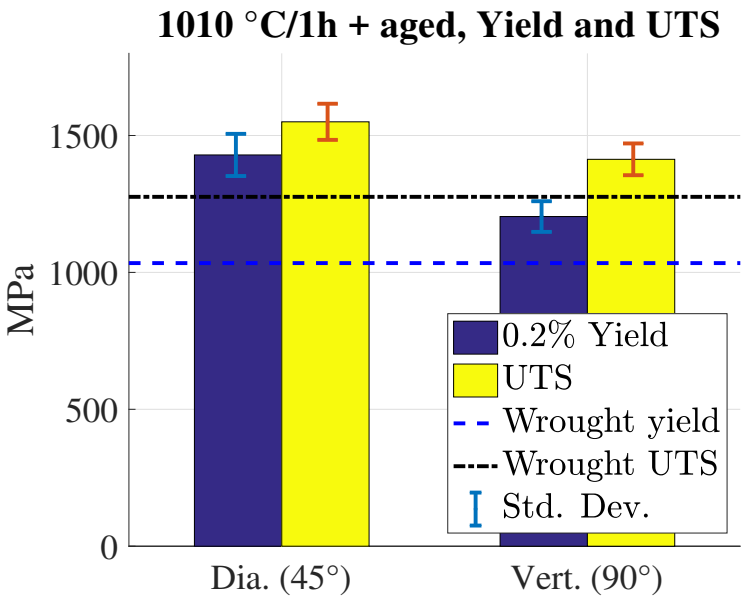

(a) Conventional heat treatment

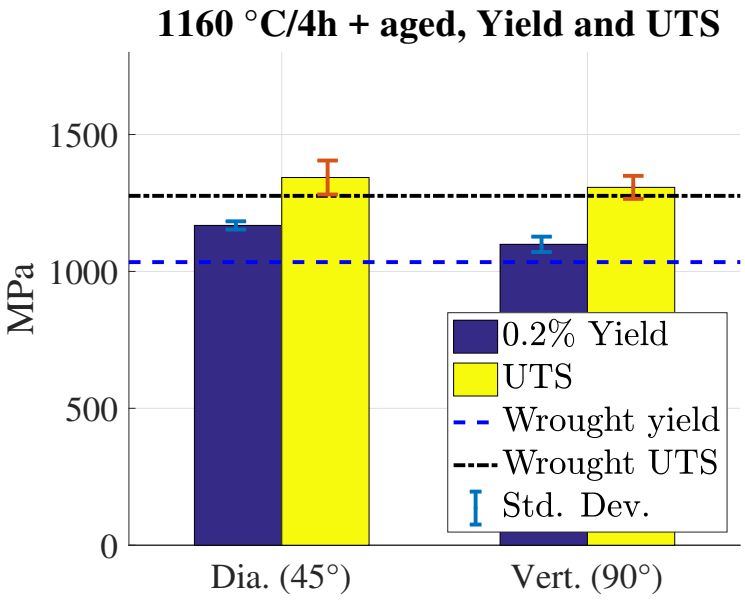

(b) Modified heat treatment

Figure 3.16: Yield and UTS results for specimens heat treated with the conventional (a) and modified (b) heat treatments. The modified treatment results in improved isotropic behavior but a decrease in overall strength.

Table 3.7: Summary of Tensile Testing

Heat treat	Orient.	E	$YS_{0.2}$	UTS	ε_f
		GPa (Std Dev)	MPa (Std Dev)	MPa (Std Dev)	% (Std Dev)
1010 °C/1h + aging	45°	213.4 (2.1)	1429 (77)	1550 (66)	6.3 (3.3)
1010 °C/1h + aging	90°	207.2 (6.9)	1204 (56)	1413 (58)	7.0 (3.8)
1160 °C/4h + aging	45°	210.6 (7.0)	1168 (15)	1343 (62)	9.6 (6.4)
1160 °C/4h + aging	90°	209.8 (3.4)	1099 (28)	1307 (42)	11.0 (5.6)

of 18.3% and 13.4% which is in close agreement with the Hall-Petch prediction. It is possible the residual strains in the build direction (i.e., 90° specimens) are still contributing to the strength of the vertical specimens, or there could be an additional factor such as the age-hardening response. While the isotropic behavior of the material is greatly improved by the modified heat treatment, the overall tensile strength has been reduced considerably to the point that 4 of the 15 90° specimens annealed at 1160 °C failed to meet the wrought standard for UTS of 1276 MPa [113].

Overall, the 4-hour anneal at 1160 °C has greatly improved the isotropic behavior of the LPBF IN718. Achieving isotropic tensile properties requires recrystallizing the microstructure to reduce the residual strains. From Figures 3.12 and 3.13, the average grain diameters converge starting at 2 hours and the recrystallized fractions converge at 4 hours. As shown by the hardness and tensile tests, the 4-hour anneal at 1160 °C is sufficient to achieve isotropic mechanical properties with the trade-off of overall strength in LPBF IN718.

3.4 Conclusions

As hypothesized, annealing LBPF IN718 at 1160 °C resulted in significant changes to the microstructure over the existing AMS annealing treatment. Specifically, an equiaxed microstructure was successfully achieved through recrystallization and grain growth, resulting in an isotropic microstructure for all scan strategies considered. The initial columnar AM grains transitioned to equiaxed at 3–4 hours annealing, and the X–Y and X–Z planes converged at the 4-hour annealing time. Recrystallization plateaued at 5 hours. Grains experienced parabolic growth. The grain sizes after 4 hours are 74–98% larger than the initial grain sizes, but still below the typical wrought grain sizes of 40+ μm. The tensile properties for the LPBF specimens were comparable to wrought material.

The annealing time and orientation were significant factors affecting H_{IT}, H_V, $YS_{0.2}$, and UTS. The greatest effects to the hardness were seen in the differences in the 0–3 hour specimens in the X–Y orientation, and the 0–4 hour specimens in the X–Z direction. This coincides with the large changes in recrystallization and average grain sizes for the same times and orientations. Compared to a "simulated HIP" of 1120 °C [54], the convergence of the X–Y and X–Z planes occurs faster when annealed at 1160 °C.

Tensile specimens annealed at 1160 °C for 4 hours and aged showed a reduction in anisotropy over the conventional heat treatment. However, the overall tensile strength was decreased due to the increase in average grain size. This loss of strength versus isotropy will need to be weighed by designers in their choice of heat treatment for LPBF IN718. The choice of scan strategy did not result in any significant differences in the microstructure.

These findings can have a significant impact on the logistics associated with the procurement of LPBF components. The identification of this heat treatment to generate isotropic properties can allow designers to build AM parts in any orientation, without regard to the scan strategy, and from any manufacturer knowing that the underlying microstructure will be equal given similar powder feed stock and processing conditions.

The microstructural analysis in this chapter addressed the research objectives described by Problem Statements 1, 2, & 3. The objectives of Problem Statement 1 were achieved by applying the modified solution temperature of 1160 °C to specimens for time ranging from 1–8 h. The resulting microstructures were characterized using EBSD and compared to the microstructure of specimens in the as-built and CHT (1010 °C/1 h) conditions. The MHT was successful in eliminating the columnar microstructure by driving recrystallization, resulting in an isotropic microstructure with equiaxed grains at 1160 textdegreeC/4 h and verifying Hypotheses 1.A. By comparison, the CHT specimens retained the columnar grains from the as-built restructure. Additionally, the recrystallized fraction was calculated using the GOS metric to evaluate the annealing kinetics. The recrystallization behavior was an important input to the KMC effort in Chapter 5. Hardness and tension testing confirmed the equaixed microstructure reduced the anisotropy of material properties, further verifying Hypothesis 1.B. The annealed specimens were fabricated using three different scan strategies to accomplish the objective for Problem Statement 2. The microstructural differences in grain size and texture intensity between the scan strategies were found to be negligible as the result of the MHT, verifying Hypothesis 2. This research provided a unique contribution to LPBF IN718 in the sequence of annealing times at an elevated solution temperature and the comparison of solution treatments, grain size, and recrystallized fraction with the hardness and tension testing. The hardness and tensile testing revealed the MHT reduced the anisotropy of the $YS_{0.2}$ by 10% and UTS by 4–6%, achieving the objective for Problem Statement 3. The hypothesis posed with Problem Statement 3 was found to hold true regarding grain size and tensile strength.

This page intentionally left blank.

IV. Mechanical Testing

Mechanical testing of laser powder-bed fusion (LPBF) Inconel 718 (IN718) is necessary to understand how the material responds to mechanical forces and deformations [93]. The mechanical properties are determined by the microstructure, which is influenced by the thermal history. The response of the material depends on the scale of the interactions. Indentation testing uses a small mechanical probe to contact a small volume of material and measures the local behavior. Micro hardness tests can provide more precise directional measurements over macro hardness measurements. Tension and creep testing measure the average mechanical response over a larger test volume.

This chapter addresses the research objective described by Problem Statement 3. Changes in the grain size resulted in a change in mechanical properties as demonstrated through hardness, tensile, and creep-rupture testing. The hardness and tensile testing revealed the modified heat treatment (MHT) reduced the anisotropy of the 0.2% yield strength ($YS_{0.2}$) by 10% and ultimate tensile strength (UTS) by 4–6%. However, the overall $YS_{0.2}$ and UTS were also reduced by 14.5% and 20.7%, respectively. New Hall-Petch constants are generated in Section 4.3.2.2 from the tensile results to account for the gamma double-prime (γ'') hardening in IN718. The creep-rupture results indicate that columnar nature of the grains provides a stronger effect than the average grain size. The loss of the columnar structure due to the MHT results in a reduction in the rupture life by 47.5% for vertically-oriented specimens. However, the rupture life did not decrease for the horizontal specimens, in spite of the equiaxed grain structure analyzed in Chapter 3. This difference between the two orientations yields a new hypothesis on the role of carbide (NbC) coarsening and the increase in rupture life.

4.1 Recap of Background

4.1.1 Hardness Recap.

As discussed in Section 2.3.5.3 (p. 51), the hardness of a metal is proportional to the tensile strength [96]. The hardness and tensile strength of IN718, whether wrought or additive manufacturing (AM), are primarily affected by the development of the strengthening γ'' phase. Solution-treated wrought IN718 typically has a Rockwell hardness C (*HRc*) of 20 or less. Hardness increases significantly after aging to 40–45 *HRc* [118]. As-built LPBF IN718 is typically harder than solution-treated wrought material but softer than solution-treatment and aged (STA) wrought IN718 [3]. Solution treatments decrease the hardness of LPBF IN718 as the age-hardening secondary phases are dissolved. Aging increases the hardness and strength of LPBF IN718 to the range of STA wrought IN718.

Strößner et al. [130] used a macro *HRc* measurement and reported no measurable anisotropy in LPBF IN718 with an STA hardness of 45 *HRc* for two different solution treatments (980 °C/1h and 1065 °C/1h) with the conventional aging treatment. This result indicates that macro-hardness techniques may not reveal the anisotropy caused by texture and grain shape and size that are possible with micro-hardness tests. Jiang et al. [54] reported an anisotropy of 9.6% from Vickers hardness (H_V) micro-hardness and nano-identation tests on as-built LPBF IN718. Using a modified solution treatment of 1120 °C, Jiang et al. [54] investigated the reduction in anisotropy with increasing durations culminating in a strain-free microstructure and isotropic hardness properties after 16 hours.

4.1.2 Tension Recap.

As covered in Section 2.3.5.4 (p. 55), previous researchers looked into the tensile properties of powder-bed fusion (PBF) metals and the resulting anisotropy. The tensile strength is greater in the horizontal/transverse direction due to a weakening of the vertical strength by delta (δ) formation at the build-layer boundaries [67, 130]. LPBF and electron-beam melting (EBM) IN718 meet aerospace materials specifications (AMS) standards for

UTS and $YS_{0.2}$ [114], but struggle to meet the elongation at failure (ε_f) requirements even after post-process heat treatment [60, 116]. Strößner et al. [130] showed tensile properties of LPBF IN718 comparable to wrought material in other literature. Tensile testing by Strößner et al showed anisotropic behavior up to 10% in the as-built and various heat-treated condition [130]. Cloots et al. [26] performed tensile testing on LPBF Alloy 738, low carbon (IN738LC) and found similar results, with anisotropy up to 20% [26].The anisotropy was reduced with a higher temperature solution anneal (1065 °C/1h). Muñoz-Moreno et al. [83] concludes that achieving recrystallization is necessary to reduce the anisotropy caused by the texture.

4.1.3 Creep Recap.

Creep performance is one of the properties of IN718 that make it highly desirable in aerospace applications. However, limited results have been published on creep behavior of LPBF IN718 for a variety of reasons as laid out in Section 2.3.5.5 (p. 56). Fortunately, there is a wealth of testing on wrought IN718 that can provide a basis for conducting and analyzing LPBF creep properties. Kuo et al. [66, 67] showed that horizontally-fabricated LPBF IN718 specimens performed much worse than vertical specimens. An important conclusion by Kuo et al. [68] was "the originally recommended heat treatment process, STA-908 °C, for cast and wrought materials is not effective in selective laser melting (SLM)-processed specimens [68, p. 12]." Testing traditional wrought IN718, Liu et al. [70] showed that the grain size affects the crack growth behavior during creep, such that larger grain sizes result in an increase in rupture life. Additionally, Liu et al. [70] concluded that the carbides influence the creep crack growth behavior. The Laves phase is detrimental to the rupture life [105], so a solution treatment is needed that can remove this detrimental phase. Additionally, the columnar grains formed via electron beam welding were beneficial to the creep resistance [105]. In the context of LPBF, the columnar grains would increase

the rupture life of vertical specimens when compared to horizontal specimens, which was clearly demonstrated by Kuo et al. [66].

4.2 Methodology, Mechanical Testing

The mechanical testing carried out as part of this dissertation covers three testing methods: 1) hardness testing, 2) tension testing, and 3) creep-rupture testing. The methods used for each testing area differs in the test execution, but there are many similarities regarding the specimen fabrication and post-process heat treatments which will be covered as a group in this section. The specific test methods will be covered in their own sections in this chapter. See Section 4.2.3 for hardness testing, Section 4.2.4 for tension testing, and Section 4.2.5 for creep testing.

4.2.1 Specimen Fabrication.

Several different specimen form factors were used for investigating the multiple research areas. Microstructural characterization was accomplished using the puck as described in Section 3.2. Hardness tests were performed on the microstructure pucks. Tensile and creep specimens were fabricated as dog-bones of various cross-section shapes and sizes.

In general, specimens were removed from their build plates by wire electrical discharge machining (EDM) by the AFIT Model Shop. Stress relief, if performed, was conducted by the Model Shop prior to removal from the plate. Post-process heat treatments (to be discussed in Section 4.2.2) were applied after build-plate removal by Winston Heat Treating (Dayton, OH, USA). Unless stated otherwise, the specimens were tested were the as-fabricated surface finish.

4.2.1.1 Hardness Specimen Fabrication.

As described in Section 3.2, the metallography pucks were designed to allow for microstructural examination of the X–Y and X–Z planes. This design turned out to be convenient to perform hardness testing on those same planes since the flat surface used for

the scanning electron microscopy (SEM) examination provided ample space to perform multiple hardness tests. Hardness tests are conducted perpendicular to the surface, so the build-direction mechanical properties were taken from hardness tests on the X–Y surfaces. Similarly, transverse properties were taken from the X–Z surfaces. Representative specimens are shown mounted in the specimen tray for the iMicro in Figure 4.1. After the pucks were mounted and polished, the test surface had a mirror-like finish in contrast with the as-built surface finish shown here with the unpolished pucks.

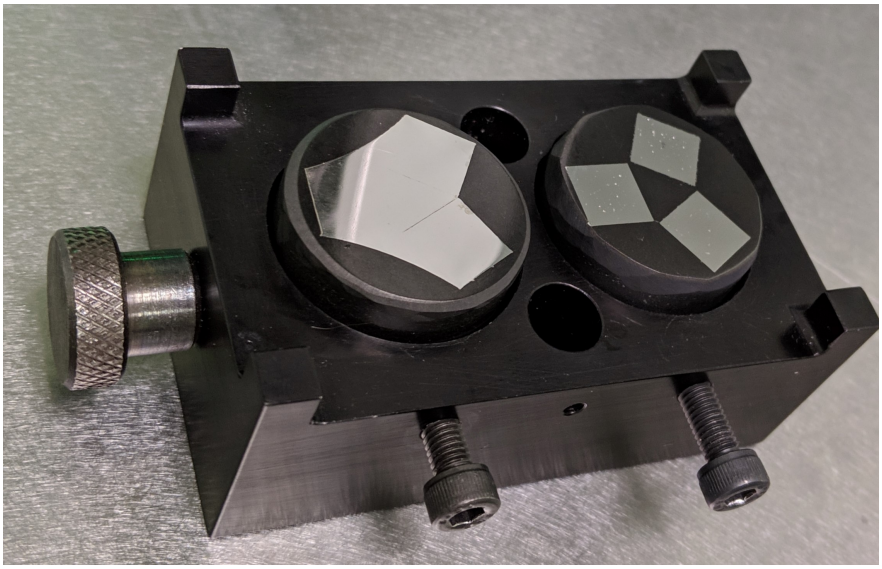

Figure 4.1: Mounted pucks are loaded in the specimen tray of the iMicro nanoindentor for hardness tests. The X–Z (L) and X–Y (R) pucks are mounted in conductive resin for SEM examination, then polished to a mirror finish. The polished surfaces also served as excellent test sites for nano-indentation testing. The build-direction properties were measured from the X–Y surfaces. Transverse properties were measured using the X–Z surfaces. The pucks were shown prior to mounting and polishing in Figure 3.5 (p. 93)

4.2.1.2 Tension Specimen Fabrication.

Dog-bones specimens with cylindrical and rectangular cross-sections were used in this research. Both specimen form factors were designed in accordance with ASTM E8/E8M [7, Sec. 6]. Section 3.2.5 described the cylindrical dog-bones used for tension testing to demonstrate the anisotropy of the LPBF process.

The cylindrical dog-bones had a cross-sectional gauge diameter of 10 mm. After heat treatments, a 1% taper was added to the gauge section by machining resulting in a minimum cross-sectional diameter of 9.9 mm and an area of 77.0 mm^2. The cylindrical dog-bones were fabricated in vertical (90°) and diagonal (45°) orientations. The specimen dimensions and build orientation were shown previously in Figure 3.6 (p. 97). As a result of machining the taper, the specimens were tested with a polished finish.

Multiple builds were attempted to fabricate cylindrical dog-bones in a horizontal orientation. However, many of the specimens exhibited cracking near their midpoints before the prints had finished. In investigating this phenomena, it was discovered that rectangular dog-bones did not present this issue when printed vertically. One theory as to this difference is based on how the cross-sections appear after slicing. As illustrated with Figure 4.2, when the cylindrical cross-section is sliced horizontally (represented by the red lines), each layer is a different width than the previous layer. By contrast, the slices of the rectangular cross-section are the same width throughout the specimen. The end result is that the amount of energy absorbed with each layer in the cylindrical specimen is not constant, leading to a build-up of thermal stresses within the part. Stress-relief heat treatments are designed to mitigate some imbalance of stresses, but from these results it was obvious that the stress-relief treatments could not solve the problem if the magnitude of the stresses causes the parts to fail during the build process.

The rectangular dog-bones were fabricated per ASTM E8 in horizontal and vertical orientations to supplement the vertical and diagonal cylindrical dog-bone specimens [7].

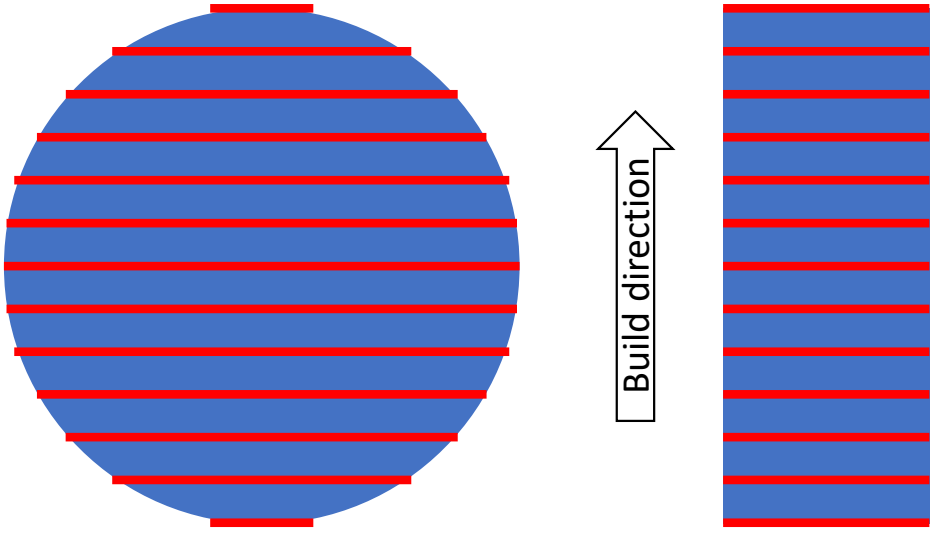

(a) Cylindrical cross-section with slices (b) Rectangular cross-section with slices

Figure 4.2: The transverse cross-sections of the cylindrical and rectangular dog-bones are shown with notional slices shown as red stripes. The slices of the cylindrical dog-bone change width with each layer, but the slices of the rectangular dog-bone are constant throughout. This is only a representative image; the geometries and slices are not shown to scale.

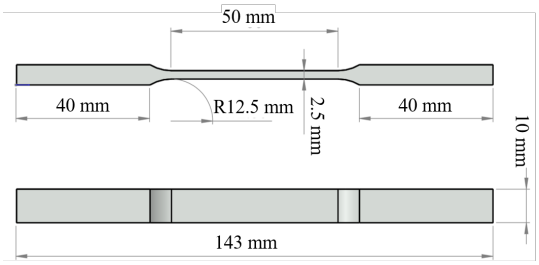

(a) Rectangular tensile specimen

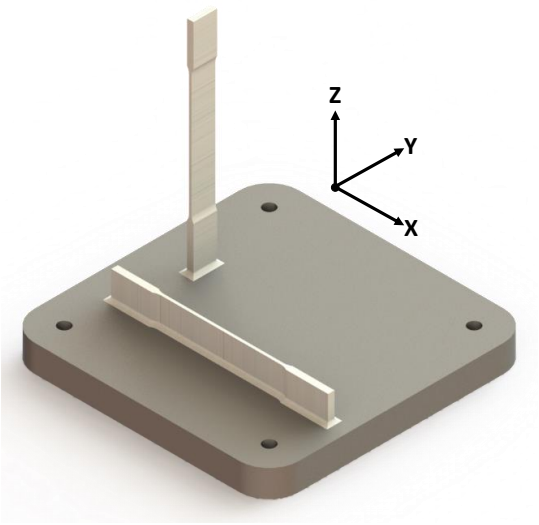

(b) Build orientations

Figure 4.3: Rectangular dog-bone specimens were built with a 10 mm × 2.5 mm cross-section and a 40 mm gauge length in the 50 mm reduced section. Specimens were built in the vertical (90°) and horizontal (0°) orientations.

The gauge cross-section had dimensions of 10 mm × 2.5 mm, and an area of 25.0 mm^2. The gauge section was printed using only the skin scan strategy as described previously in Section 3.2 (p. 92) and Table 3.1 (p. 92). Each specimen was individually measured before testing to provide an accurate cross-sectional area measurement. It was found that there was noticeable variability as a result of the build process. The finished specimens measured between 9.79–10.28 mm × 2.47–2.78 mm in the center of the gauge section. Due to the smaller cross-section of the rectangular specimens, the core/skin scan strategy was discarded in favor of fabricating each layer using only the skin strategy. The Concept Laser settings used for the rectangular dog-bones are the same as the skin strategy of the cylindrical dog-bones as shown in Table 3.1.

The final quantities of specimens fabricated and tested are shown in Table 4.1. Between the fabrication and testing steps, 4× cylindrical specimens were eliminated during machining due to a lack of material in portions of the gauge section. Additionally, 2× cylindrical specimens and 1× rectangular specimen were discarded from the testing averages due to premature failures during testing.

Table 4.1: Summmary of fabricated tension test specimens

Cross-section	Orientation	# Fabricated	# Tested	# Tests Discarded
Cylindrical	90°	30	29	0
	45°	30	27	2
Rectangular	90°	12	12	0
	0°	12	12	1

4.2.1.3 Creep Specimen Fabrication.

Creep specimens were designed with a rectangular cross-section in accordance with ASTM E8/E8M [7, Sec. 6] as shown in Figure 4.4. The gauge length of the creep specimens is increased over the tension specimens as recommended to accommodate the MTS furnace [8, Sec. 6.3]. The gauge cross-section measures 21 mm × 2.5 mm. Similar to the tension specimens, the orientation of the AM specimens with respect to the build plate and build direction is relevant to the mechanical properties and is reported with each specimen or batch of specimens.

The parts were fabricated in the same fashion as the tension specimens (Section 4.2.4 (p. 135)). Multiple builds of creep specimens were printed on AFIT's Concept Laser M2 LPBF printer equipped with a 400 W continuous-wave Ytterbium fiber laser using a skin-only processing strategy with parameters as shown in Table 3.1. The IN718 powder was acquired from Powder Alloy Corporation (Loveland, Ohio, USA) with an elemental

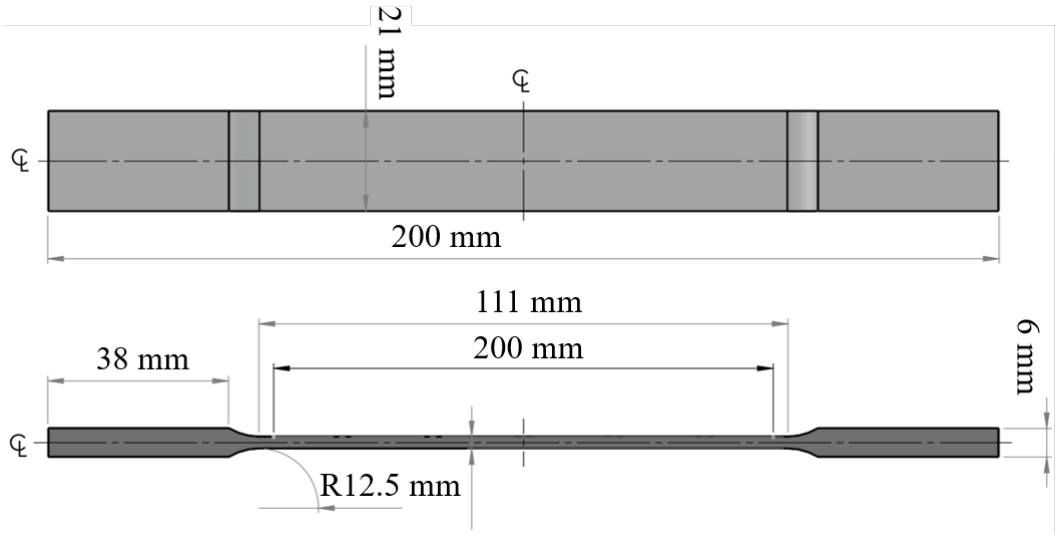

Figure 4.4: The creep specimen was designed per ASTM E8/E8M [7]. Specimens were printed with their longitudinal axis in the vertical and horizontal orientation.

composition shown in Table 3.2. The alloy was powderized via gas atomization resulting in spherical particles with a particle diameter distribution of 25–40 μm. 30 creep specimens were printed in two orientations: 15× vertical and 15× horizontal.

4.2.2 Post-process Heat Treatments.

The crux of this research is the solution treatment of the LPBF IN718. As discussed extensively in Section 2.3.3, the conventional heat treatment (CHT) for IN718 was designed to dissolve the secondary phases while also limiting grain growth. The CHT has been the best starting point for heat treatments as applied to LPBF IN718 and is used as a control for this experimental work. In order to transform columnar LPBF grains into an equaixed microstructure and achieve isotropy, it is necessary to recrystallize the existing grains. Jiang et al. [54] demonstrated the reduction in anistropy of hardness with a proposed modified solution treatment of 1120 °C for up to 4 hours. In the present research, an increased solution temperature of 1160 °C is applied to LPBF IN718 to increase the recrystallization and grain growth. This modified solution treatment has been shown to produce isotropic microstructures as covered previously in Chapter 3 and its associated paper [86]. Both solution treatments, CHT and MHT, provide a suitable dissolution of secondary precipitates [3, 130]. This allows for a full hardening response of $\gamma''$and γ'using the conventional aging treatment. Further research should be directed at fine tuning the solution treatment, aging treatment, and even the elemental composition of the alloy to optimize the material and aging response for the LPBF process. The heat treatments used in this research are presented again in Table 4.2.

4.2.2.1 Hardness Specimen Heat Treatments.

As described in detail in Section 3.2.3, the pucks were treated at 1160 °C for 1 to 8 hours at AFRL/RX. This allowed for the examination of the microstructural evolution in 1-hour increments from the as-built material (i.e., 0-hour solution-treated) to the 8-hour

Table 4.2: Heat treatment parameters used for the LPBF tension specimens

Heat treatment	Cycle parameters - temperature, time, and cooling
Stress-relief, ASTM F3055 [9]	1065 °C/1.5 h, air cool
Conventional solution anneal, AMS 5662 [115]	1010 °C/1 h, nitrogen cool
Modified solution anneal	1160 °C/4 h, nitrogen cool
Aging, AMS 5663 [113]	718 °C/8 h, furnace cool to 621 °C/8 h, nitrogen cool

solution-treated specimen. The hardness measurements were taken from the 0–4 and 8 hour-solution-treated specimens.

4.2.2.2 Tension Specimen Heat Treatments.

The specimens were mechanically removed from the build plate via wire EDM. The removed parts were sent to Winston Heat Treating (Dayton, OH, USA) and subjected to one of two solution anneal treatments, followed by aging. Half of the specimens in each orientation were subjected to the conventional solution anneal (CSA) prescribed by AMS 5662 [115]. The remaining specimens were subjected to a modified solution anneal (MSA). Both solution anneal treatments are shown in Table 4.2. All specimens underwent the conventional two-step aging treatment for IN718 as prescribed by AMS 5663 and also shown in Table 4.2.

Large specimens, specifically the horizontal tensile and creep bars, required the use of a stress relief step as introduced in Section 2.3.3 (p. 41) and discussed in Section 4.2.1.2 (p. 126). The horizontal dog-bones exhibited warping, and in extreme cases cracking, as they were removed from the build plate by wire EDM. It is hypothesized that the warping was caused by an uneven distribution of thermal stresses due to cross-sectional changes in the part that accumulated during the fabrication process. The stress relief serves to increase the movement of dislocations within the crystal lattice (same as via annealing), thereby

reducing the stored energy that causes the warping. It is hypothesized that vertical dog-bones and smaller specimens (e.g., metallographic pucks) did not require a stress relief due to a continuous cross-section (as illustrated in Figure 4.2 (p. 127)), or a small enough cross-section that cooling occured evenly across the build layer.

4.2.2.3 Creep Specimen Heat Treatments.

The build plate with horizontal creep specimens was stress-relieved in a Cress (Carson City, NV, USA) bench-top heat treating furnace operated by the AFIT Model Shop. The furnace has a maximum operating temperature of 1230 °C, which would allow for the application of any of the heat treatments listed in Table 4.2. However, due to operational concerns over the duration of the various processes, only the stress-relief step was performed at AFIT. The build plate with vertical specimens was not stress-relieved as previous research had not revealed any issues with residual stress, similar to the tension specimens in Section 4.2.1.2 and illustrated in Figure 4.2.

The creep specimens were mechanically removed from the build plate via wire EDM in the same manner as the tensile dog-bones. The removed parts were sent to Winston Heat Treating (Dayton, OH, USA) where they were solution-treated and aged. The specimens received one of two solution treatments: the conventional solution anneal (CSA) as prescribed by AMS 5662 [115], or the modified solution anneal (MSA) as developed in this research. Solution-treatment and aging were performed in a vacuum furnace with nitrogen-gas cooling. The nitrogen-gas cooling serves two purposes - it provides an inert atmosphere during the treatment and cooling to prevent oxidation, and it rapidly cools the specimens to lock the microstructure. All specimens were aged using the conventional double-aging treatment per AMS 5663 [113] for IN718 employment in high-temperature applications. The parameters for the solution and aging treatments are shown in Table 4.2. As there were an odd number of specimens in each orientation, the MHT was applied to 8× specimens and the CHT was applied to the remaining 7× specimens.

4.2.3 Methodology, Hardness Testing.

Hardness of the solution-treated LPBF IN718 specimens was measured using nanoindentation testing as described in Section 2.3.5.3 (p. 51). For the basic hardness measurements, a 3 × 3 grid with 40 μm spacing was placed near the center of each 10 mm × 10 mm surface. If an obvious pore or carbide would interfere with the grid collection, the test points were moved as necessary to avoid the obstruction as shown with the test grid and indentations in Figure 4.5. Figure 4.5b shows the after-effect of the hardness test, with the pyramidal indentations left by the Berkovich tip. The small red circles are the approximate locations of each indentation test. A large red plus indicates the start of the grid arrangement, accompanied by the specimen identity ('F07 topleft' for this image).

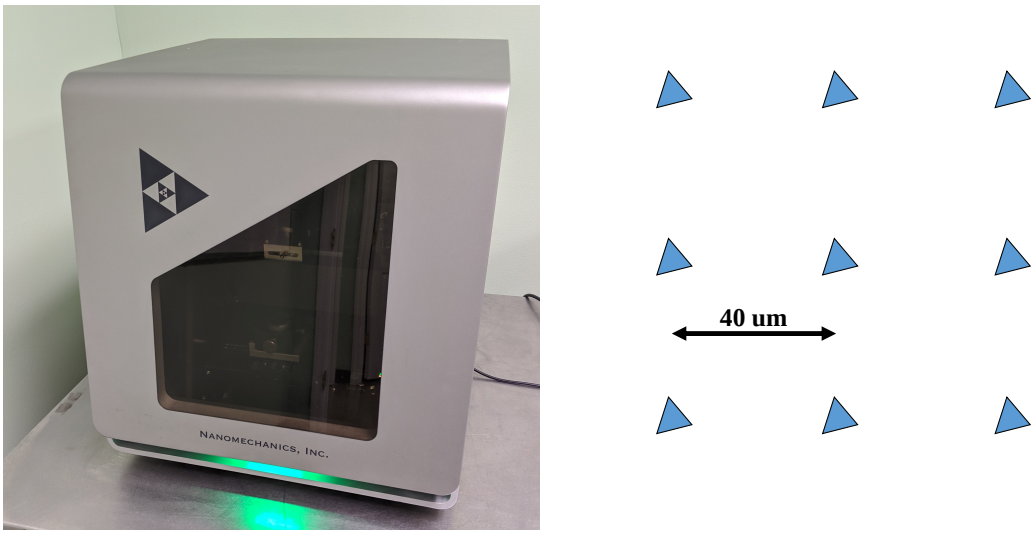

(a) iMicro nanoindentor

(b) 3 × 3 indentation grid

Figure 4.5: The iMicro nanoindentor was used to conduct hardness tests on the solution-treated LPBF IN718 specimens. Each test consisted of 9 indentations arranged in a 3 × 3 grid with 40 μm spacing.

4.2.4 Methodology, Tension Testing.

Tension testing was performed in accordance with ASTM E8 [7]. Tests were performed on an MTS 810 servo hydraulic machine using constant strain-rate of 0.04 mm/s (0.001 strain/s) until specimen failure. A clip-gauge extensometer with a 10-mm gauge length was used to measure the strain for the duration of the tests. Output from the strain gauge was displayed as a stress-strain curve from which Young's modulus (E), UTS, $YS_{0.2}$, and ε_f were derived per ASTM E8 [7].

4.2.5 Methodology, Creep Testing.

Tensile creep-rupture testing was performed on all specimens in accordance with ASTM E139 [8]. The standard specification for wrought IN718, ASTM B637 [10], was used to select the test parameters in order to compare the LPBF IN718's creep performance to the wrought standard. Per the stress-rupture requirements provided in [10, Table 4], the test temperature was set at 650°C and the stress was set at 690 MPa. The standard to meet for wrought specimens is a minimum rupture time of 23 hours. These standards were described in more detail in Section 2.3.5 and Table 2.7.

Each specimen was loaded in an MTS 810 servo hydraulic machine equipped with a two-zone clam-shell MTS 653 furnace as shown in Figure 4.6. Two K-type thermocouples were spot-welded to the reduced gauge section of each specimen and used as feedback controls for the heaters. The cross-sectional area of the reduced gauge section was re-measured for each specimen to account for slight variations in the final parts. The tension force was calculated to provide the desired 690 MPa based on the area. An Epsilon (Jackson, WY, USA) axial furnace extensometer with a 10 mm gauge length was used to measure the strain for the duration of the tests. The extensometer was place at the midpoint of the gauge section. The system controller recorded time, temperature, creep, strain, and elongation for each test. The test procedure gradually increased the temperature to the set-point, then held for one hour before applying the test load in accordance with ASTM E139

[8]. Specimens were tested in a randomized order, with CHT and MHT intermingled on two test stations.

Figure 4.6: A creep-rupture experiment is underway on the MTS 810 servo hydraulic machine. Also shown are the MTS 653 heater and Epsilon extensometer. A protective enclosure is in place to minimize airflow during the test, as well as to prevent accidental interference with the experiment.

4.3 Results and Discussion, Mechanical Testing

4.3.1 Results, Tensile Testing.

This section provides a summary of the tensile test data acquired from the testing of 60 cylindrical tensile dog-bones at MVMTC and 24 rectangular tensile dog-bones at AFIT. The full tabulated data is provided in Appendix A. The mechanical properties of the cylindrical and rectangular dog-bone specimens are evaluated and compared, as well as the differences between the build orientation and post-process heat treatments. All of the tensile specimens presented in this section were fully aged following the conventional or modified solution treatments. The specific heat treatments are defined in Table 4.2 (p. 132): stress-relief, CSA, MSA, and aging. After a specimen has been subjected to either of the solution treatments and aged, it is described as in the conventional heat treatment (CHT) or modified heat treatment (MHT) condition.

The tension test data was collected as engineering stress and engineering strain. Figure 4.7 displays a representative pair of stress-strain curves from the two rectangular specimens. The only difference between the specimens shown is the heat treated condition. The graph on the left is specimen P09, a 90° rectangular dog-bone in the CHT condition. The graph on the right is specimen P24, a 90° rectangular dog-bone in the MHT condition. A custom MATLAB script was written to process the raw test data from each test. E was calculated as the slope of the elastic region of the blue stress-strain curve. The orange line parallel to that slope was drawn from the X-axis starting at 0.2% (0.002 mm/mm) until it intersected the stress-strain curve. This intersection point dened the value for $YS_{0.2}$ (yellow line). UTS was taken as the maximum stress of the stress-strain (purple line), and ε_f was the final strain measurement before the sudden decrease in applied force (green line) (per ASTM E8 [7]).

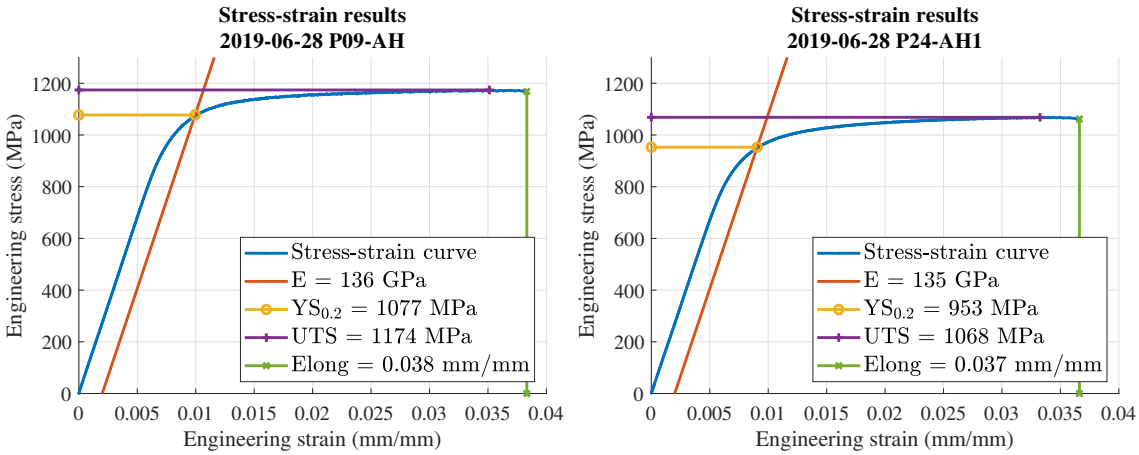

(a) Stress-strain curve for specimen P09, CHT (b) Stress-strain curve for specimen P24, MHT

Figure 4.7: Two comparable, representative stress-strain curves from tension testing are shown for specimens P09 and P24. Both specimens are 90° rectangular dog-bones. P09 is in the CHT condition, and P24 is in the MHT condition. The graphs show the various mechanical properties that were derived from the test data. A custom MATLAB script was written to process the raw test data for each specimen.

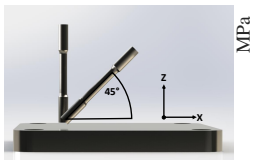

Cylindrical

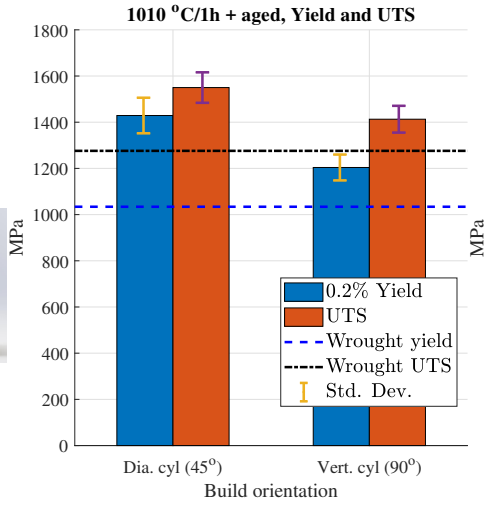

(a) CHT, cylindrical dog-bones

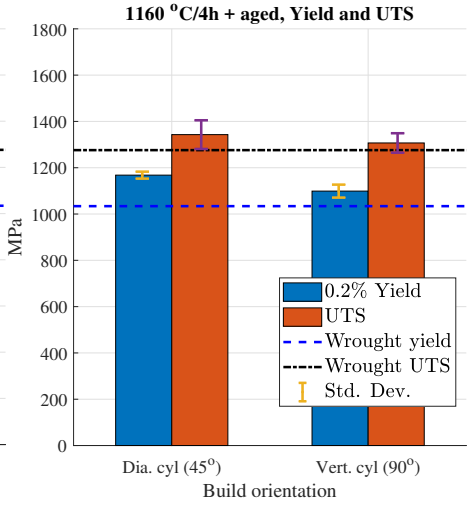

(b) MHT, cylindrical dog-bones

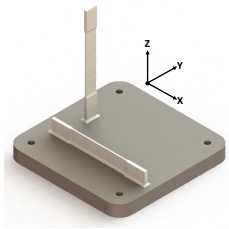

Rectangular

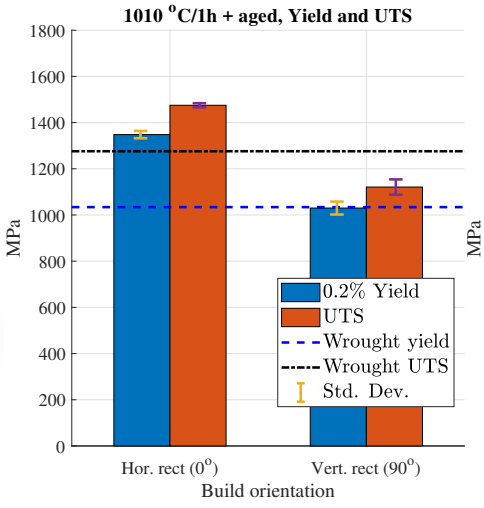

(c) CHT, rectangular dog-bones

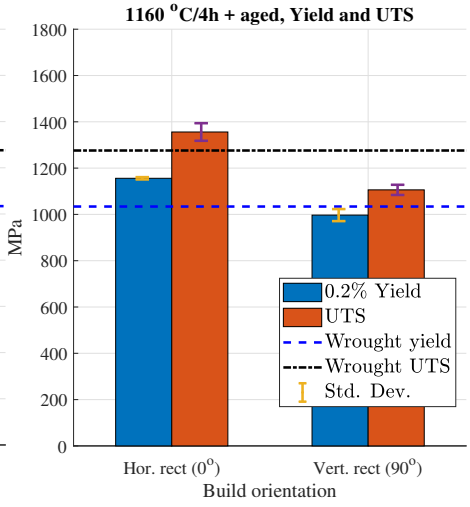

(d) MHT, rectangular dog-bones

Figure 4.8: $YS_{0.2}$ and UTS results for (a) CHT cylindrical dog-bones, (b) MHT cylindrical dog-bones, (c) CHT rectangular dog-bones, and (d) MHT dog-bones. The modified treatment decreased the overall strength of each orientation and dog-bone shape. The build orientations and form factors are represented in the graphic on the left.

The average $YS_{0.2}$ and UTS of the LPBF IN718 specimens are shown in Figure 4.8. Figures 4.8a and 4.8b display the tensile strength of the diagonal (45°) and vertical (90°) cylindrical dog-bone specimens in the CHT and MHT conditions, respectively. Figures 4.8c and 4.8d present the tensile strength of the horizontal (0°) and vertical (90°) rectangular specimens. The $YS_{0.2}$ and UTS standard specifications for wrought IN718, ASTM B637 [10], are indicated as horizontal dashed and dotted lines, respectively, for comparison with the AM specimens. The dog-bone shape and build orientations are displayed to the left of the charts. The tabulated average results of $YS_{0.2}$, UTS, E, and ε_f of the cylindrical dog-bones are presented in Tables 4.3 and 4.4. The results of the rectangular dog-bones are presented in Tables 4.5 and 4.6.

In Figure 4.8a, the tensile strength for the vertical CHT cylindrical specimens is 225 MPa (15.7%) lower than the diagonal specimens. Both LPBF orientations meet and exceed the strength requirement for wrought IN718. Figure 4.8b presents the same specimens in the MHT condition. The tensile strength of both orientations is decreased due to the heat treatment while the difference between the two orientations (i.e., anisotropy) has been reduced from 69 MPa (5.9%) to 36 MPa (2.7%). This reduction in anisotropy will be discussed further with Tables 4.3 and 4.4 and Figure 4.9a. The diagonal MHT cylinders still met the $YS_{0.2}$ and UTS wrought requirements. The vertical MHT cylinders met the $YS_{0.2}$ wrought requirement, but several specimens failed to meet the standard for UTS. The reduction in strength is predicted by the Hall-Petch relationship and correlates directly with the increased average grain size of the MHT microstructure (as presented in Section 3.3.1 (p. 98)). This is discussed further in Section 4.3.2 (p. 143).

Table 4.3: Summary of $YS_{0.2}$ and UTS with anisotropy for cylindrical dog-bones

Anneal temp. (°C)	Orient.	$YS_{0.2}$ (MPa)	$YS_{0.2}$ aniso.	UTS (MPa)	UTS aniso.
CHT, 1010 °C/1 h	45°	1429 ± 77	**15.7%**	1550 ± 66	**8.8%**
	90°	1204 ± 56		1413 ± 58	
MHT, 1160 °C/4 h	45°	1168 ± 15	**5.9%**	1343 ± 62	**2.7%**
	90°	1099 ± 28		1307 ± 42	
Reduction in anisotropy			9.8%	–	6.2%
Reduction as a % of CHT anisotropy			62.5%	–	69.7%

Table 4.4: Summary of E and ε_f with anisotropy for cylindrical dog-bones

Anneal temp. (°C)	Orient.	E (MPa)	E aniso.	ε_f (%)	ε_f aniso.
CHT, 1010 °C/1 h	45°	213377 ± 2149	**2.9%**	6.3 ± 3.3	**-11.1%**
	90°	207214 ± 6897		7.0 ± 3.8	
MHT, 1160 °C/4 h	45°	210601 ± 7040	**0.4%**	9.6 ± 6.4	**-14.6%**
	90°	209832 ± 3431		11.0 ± 5.6	
Reduction in anisotropy			2.5%	–	3.5%
Reduction as a % of CHT anisotropy			87.4%	–	-31.3%

Tables 4.3 and 4.4 present the tabulated average values from the tension tests with cylindrical specimens. In general, the MHT improved the isotropic behavior over the CHT for all of the tensile properties except ε_f. The reductions in anisotropy of E, $YS_{0.2}$, and UTS were 62%, 69% and 86%, respectively. The anisotropy metrics are also presented graphically in Figure 4.9a.

Table 4.5: Summary of $YS_{0.2}$ and UTS with anisotropy for rectangular dog-bones

Anneal temp. (°C)	Orient.	$YS_{0.2}$ (MPa)	$YS_{0.2}$ aniso.	UTS (MPa)	UTS aniso.
CHT, 1010 °C/1 h	0°	1347 ± 13	**23.6%**	1478 ± 08	**24.0%**
	90°	1030 ± 28		1121 ± 33	
MHT, 1160 °C/4 h	0°	1151 ± 32	**13.9%**	1358 ± 39	**19.5%**
	90°	997 ± 26		1106 ± 22	
Reduction in anisotropy			10.2%	–	5.6%
Reduction as a % of CHT anisotropy			43.1%	–	23.2%

Table 4.6: Summary of E and ε_f with anisotropy for rectangular dog-bones

Anneal temp. (°C)	Orient.	E (MPa)	E aniso.	ε_f (%)	ε_f aniso.
CHT, 1010 °C/1 h	0°	177833 ± 4087	**27.8%**	15.7 ± 2.3	**80.1%**
	90°	128231 ± 4757		3.1 ± 0.9	
MHT, 1160 °C/4 h	0°	176800 ± 7047	**19.4%**	18.5 ± 0.9	**79.4%**
	90°	140780 ± 4083		3.5 ± 1.2	
Reduction in anisotropy			7.5%	–	-0.8%
Reduction as a % of CHT anisotropy			27.0%	–	-1.0%

Tables 4.5 and 4.6 present the tabulated average values from the tension tests with rectangular specimens. In the same general trend as the cylindrical specimens, the MHT improved the isotropic behavior over the CHT for all of the tensile properties except for ε_f. The CHT anisotropy in the rectangular specimens was greater than the CHT cylindrical specimens by 8% for $YS_{0.2}$ and UTS, and a large amount of anisotropy remained after the MHT. It is hypothesized that the cross-sectional area or geometry of the tensile specimen has an influence on the effect of the post-process heat treatments. There were still

reductions of 10.2%, 5.6%, and 7.5% in the anisotropy of E, $YS_{0.2}$, and UTS, respectively. The anisotropy metrics are also presented graphically in Figure 4.9b.

4.3.2 Discussion, Tension Testing.

This section discusses the results as presented in Section 4.3.1 and provides an analysis of the tensile properties in conjunction with the microstructures presented in Section 3.3.1. Tension testing was used to characterize the mechanical behavior of LPBF IN718 specimens and measure the influence of grain size, build orientation, solution treatment, and the aging process. The results presented in the previous section showed several general trends to be expanded upon in this section:

1. The MHT reduced the anisotropic behavior of CHT in E, $YS_{0.2}$, and UTS.
2. The CHT produced $YS_{0.2}$ and UTS 8% higher than MHT.
3. The Young's moduli of the cylindrical and rectangular specimans differed by up to 38% between geometries, but did not vary based on build orientation or heat treatment.
4. ε_f was improved with the MHT, while anisotropy of ε_f was not affected.
5. The rectangular specimens had a significantly large 80% anisotropy in ε_f.
6. The cylindrical specimens had an 11.6%–11.7% lower anisotropy than the rectangular specimens with either heat treatment (CHT or MHT).

4.3.2.1 Anisotropy of Tensile Properties.

One of the primary purposes of this research was to improve the anisotropy of LPBF IN718 using post-process heat treatments. Figure 4.9 presents the anisotropy metric of percent difference previously given in Table 4.3 through Table 4.6. The horizontal axis displays each of the four mechanical properties, and the vertical axis displays the amount of anisotropy present as a percent (see Equation (3.1), 91). Figure 4.9a presents the cylindrical dog-bones and Figure 4.9b presents the rectangular dog-bones with the same vertical axis scale. The CHT properties are represented by blue symbols, and the red symbols represent

the MHT properties. The measure for isotropy and anisotropy are complementary. That is, a lower value of anisotropy represents a better isotropic performance.

Figure 4.9 illustrates the cylindrical specimens have a lower anisotropic behavior than the rectangular specimens under both heat-treated conditions. The improvement (i.e., decrease) in anisotropy is illustrated by a decrease in the percent difference of the response. In both figures, three of the four properties show a decrease in anisotropy after the MHT. Improvements in isotropy were found in E, $YS_{0.2}$, and UTS. Notably, neither the cylindrical nor rectangular set of specimens improved in ε_f with the MHT. The difference in anisotropy between CHT and MHT is further evidence of improvement made to the isotropy of the cylindrical specimen properties by the MHT. The anisotropy of $YS_{0.2}$

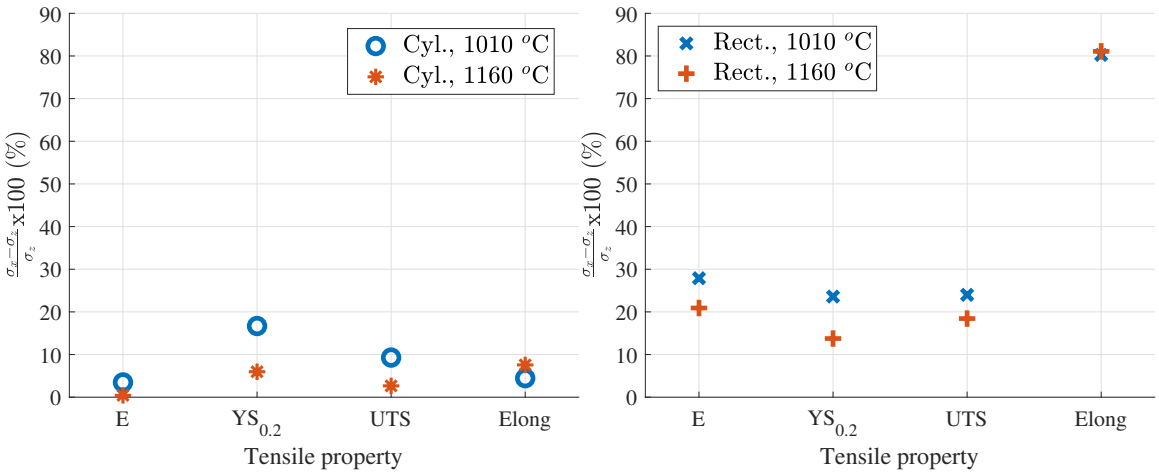

(a) Anisotropy in cylindrical dog-bones

(b) Anisotropy in rectangular dog-bones

Figure 4.9: Anisotropy of the tension tests showing the differences between the conventional and modified heat treatments. The MHT improves the isotropic behavior of the E, $YS_{0.2}$, and UTS properties by up to a 10% reduction. However, the smaller rectangular specimens still show a considerable amount of anisotropy, with 13.4%–20.4% compared to 0.4%–5.9% for the cylindrical specimens.

and UTS are greatly reduced, and E anisotropy is reduced to the point that is notionally isotropic in the MHT condition. The E anisotropy decreased to 0.4%, compared to the standard deviations of 3.3% and 1.6% for the 45° and 90° specimens, respectively.

The anisotropic behavior is driven by the microstructure presented in Section 3.3.1. The CHT microstructures are dominated by vertical, columnar grains while the MHT microstructures have equiaxed grains. The columnar grains of the CHT specimens result in a greater difference in strength when tested in the different orientations. And conversely, the MHT specimens have a reduced difference in the various orientations. While full isotropic behavior was not achieved with the modified solution anneal (MSA), the reduced anisotropy demonstrates that a recrystallizing solution treatment will be necessary to achieve fully isotropic mechanical properties.

4.3.2.2 Yield and UTS.

There are two significant factors driving the tensile strength of LPBF IN718: grain properties and γ'' formation. As shown in Chapter 3, the grain shape, size, and orientation of the as-built LPBF IN718 microstructure is relatively unchanged between the as-built and CHT conditions. However, the electron backscatter diffraction (EBSD) examination did not investigate the formation of the strengthening γ'' precipitates at the 10–100 nm scale. The formation of γ'' occurs during the two-step aging process described in Section 2.3.3 and increases the tensile strength of the CHT and MHT specimens compared to the as-built condition. Figure 4.10 shows the tensile strengths obtained experimentally of as-built, CHT, and MHT specimens to illustrate how much strength is added by the heat treatment processes. The aged specimens, CHT and MHT, have a much higher strength and corresponding loss of ductility due to the presence of the γ'' phase.

The CHT tensile strength is greater in the diagonal orientation than the vertical orientation. This result is in agreement with previous research that showed the vertical orientation presents the weakest tensile strength for LPBF IN718 specimens. Sun et al.

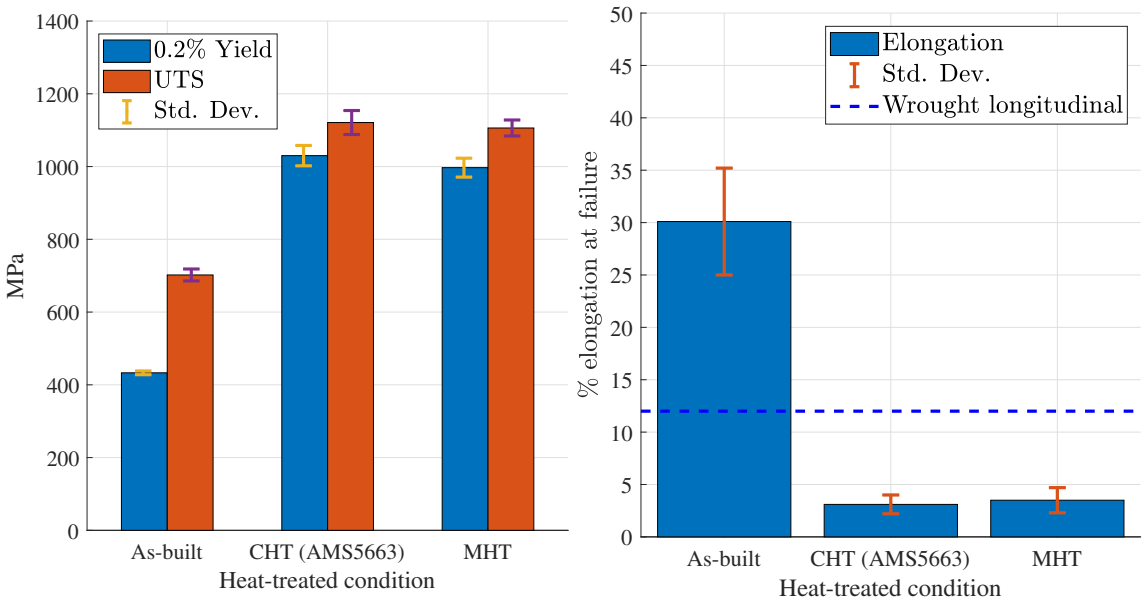

(a) $YS_{0.2}$ and UTS for as-built and CHT

(b) Elongation for as-built and CHT

Figure 4.10: Comparison of as-built, CHT, and MHT tension test results. Figure 4.10a shows the tensile strength of the as-built specimens with the CHT and MHT specimens. The CHT and MHT specimens have a higher tensile strength due to the formation of aging γ'' phases. Figure 4.10b shows the high elongation values of the as-built material compared to the hardened CHT and MHT material. The addition of the γ'' phase results in a loss in ductility corresponding to the increased tensile strength in the CHT and MHT specimens.

[131] tested the tensile strength of CHT EBM IN718 in a greater range of build orientations and found that a ⟨111⟩ (55°) orientation resulted in the highest tensile strength due to its alignment with the slip planes. However, due to limitations with the specimens in the current research, a conclusion can not be drawn on whether the 45° orientation is stronger than the horizontal (0°) orientation. This research could be extended by conducting tension tests on horizontal cylindrical tension specimens. Additionally, this research makes the assumption that the aging process generates an appropriate volume fraction of γ'' in both the CHT and MHT conditions. Further research could be focused on evaluating the microstructures at the 1 nm scale to verify the characterize the formation of γ'' in the CHT and MHT specimens.

Figure 4.8 reveals that the CHT specimens exhibit higher $YS_{0.2}$ and UTS than the MHT specimens, regardless of the orientation or shape of the tensile dog-bones. With the assumption of similar γ'' formation, the grain properties are now the leading factor behind the difference. This difference was previously discussed in Section 3.3.1 (p. 98) and directly tied to the grain size dependence of the Hall-Petch relationship as given in Equation (2.3) [45]. The figure shows that CHT material exceeds the wrought specification (AMS 5662, [115]) for both 0.2% yield and UTS. However, the ε_f values shown in Figure 4.10b reveal a short-coming of the material's ductility. These results are consistent with the tensile properties of LPBF and EBM IN718 reported in Section 2.3.5. The horizontal and diagonal MHT specimens performed above the wrought standard. However, the vertical MHT specimens had 2 out of the 11 specimens fail to meet the minimum UTS value of 1276 MPa.

$$\sigma_y = \sigma_0 + \frac{k_y}{\sqrt{d}} \tag{4.1}$$

The Hall-Petch relationship in Equation (4.1) was previously introduced in Problem Statement 3, described in Section 2.3.5.4, and discussed in the context of the microstruc-

tural analysis in Section 3.3.4. However, the published values in [126] used the σ_0 and k_y values for a gamma prime (γ')-strengthened alloy instead of a γ''-strengthening as found in IN718. Table 4.8 shows a comparison of the Hall-Petch relationship with the values of σ_k and k_y from [126] with newly derived values from this research. As can be seen in the first Hall-Petch column, the estimated yield strength of the hardened IN718 is grossly underestimated. The as-built (0-hour) X–Z test data was used to solve the Hall-Petch equation for σ_0, which provided a value of approximately 800 MPa. The new k_y was found to be approximately 1.5 when fitted to the remaining data. The second Hall-Petch column of Table 4.8 uses these new values for the estimate.

Table 4.7: Hall-Petch constants

Hardening phase	σ_0	k_y
	MPa	MPa·m$^{1/2}$
γ', Ni_3Al [126]	300	1.70
γ'', Ni_3Nb	800	1.50

4.3.2.3 Elongation at Fracture.

The presence of carbides and δ have been combined and attributed to the decrease in elongation by various other researchers [80, 100]. However, the results of Table 3.7 (p. 117) show that the overall elongation (but not the anisotropy) was moderately improved in the MHT versus the CHT conditions, in spite of the presence of coarsened carbides. Therefore, it is assessed that the carbides play less of a role in influencing the tensile properties of LPBF IN718. The carbides are also theorized to play a role in the creep properties and are investigated further in Section 4.5.

Table 4.8: Hall-Petch comparisons

Anneal time	Orient.	Avg. grain dia.	Hall-Petch [1]	Hall-Petch [2]	$YS_{0.2}$
		μm	MPa	MPa	MPa
0-hr	X–Y	9.50	552	487[3]	N/A
0-hr	X–Z	12.11	489	431[3]	433
1-hr, 1010 °C	X–Y	9.89	841	1277	1337
1-hr, 1010 °C	X–Z	13.81	757	1204	1204
4-hr, 1160 °C	X–Y	17.25	709	1161	1145
4-hr, 1160 °C	X–Z	18.30	697	1151	1099

[1] using the γ', Ni_3Al values from Table 4.7

[2] using the γ'', Ni_3Nb values from Table 4.7

[3] σ_0 was set to zero in the Hall-Petch equation due to a lack of hardening phases in the as-built condition

4.4 Results, Creep-rupture Testing

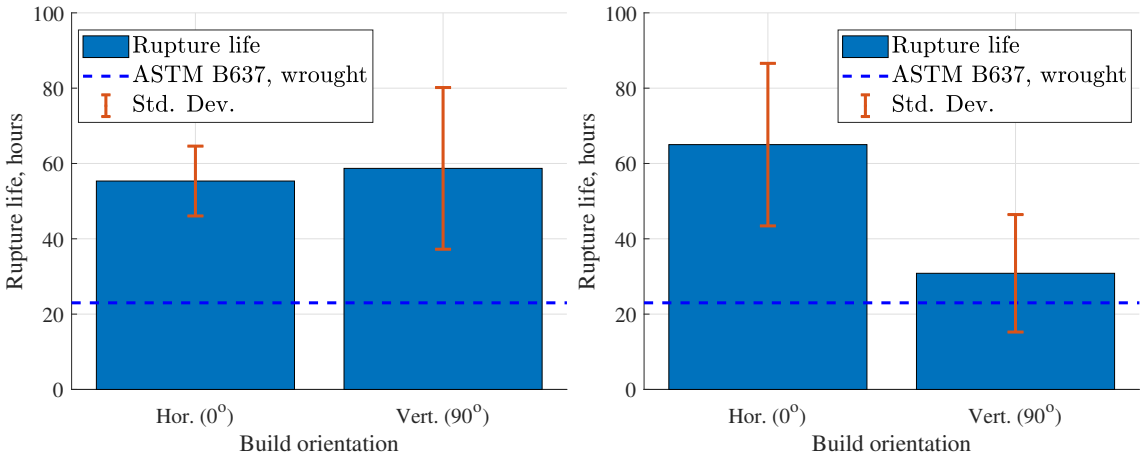

(a) Creep-rupture results, CHT

(b) Creep-rupture results, MHT

Figure 4.11: The creep-rupture life is presented for CHT and MHT specimens in the horizontal and vertical build orientations. MHT generated a very small increase in creep-rupture life for the horizontal specimens, but the vertical creep-rupture life was greatly reduced.

Table 4.9: Creep-rupture results

Test temp.	Stress	Heat treat.	Orient.	Creep-rupture life (hrs)	Std. dev. (hrs)
650 °C	690 MPa	CHT	0°	55.3	± 9.3
			90°	58.7	±21.5
		MHT	0°	65.0	±21.6
			90°	30.8	±15.6
		Wrought standard [10]		23.0	N/A

The purpose of a creep-rupture test is to simulate the long-term behavior of a structural component at high operating temperatures. The creep-rupture tests were carried out at 650 °C with an engineering stress of 690 MPa. The results from the creep-rupture testing of LPBF IN718 dog-bones are shown in Figure 4.11 and Table 4.9. The CHT results in Figure 4.11a reveal excellent creep performance with an average life of 57 h, easily surpassing the wrought standard for creep-rupture life. The vertical specimens were expected to show a higher creep life as a result of the columnar grain structure. While the average creep-rupture life of the vertical CHT specimens is higher than the horizontal specimens, the difference is not significant as seen in the error bars for each set of tests. The vertical and horizontal CHT specimens revealed an almost equivalent creep-rupture life expectancy. By contrast, the MHT specimens in Figure 4.11b exhibited a large difference in creep-rupture life of 24 h between the two build orientations. The horizontal MHT specimens showed a small improvement in creep-rupture life from 55.3 h to 65.0 h from the CHT specimens, which was expected by transforming the columnar microstructure into an equiaxed one. Unexpectedly, the vertical MHT specimens showed a precipitous loss of creep-rupture life as compared to the CHT specimens, 58.7 h vs 30.8 h for a loss of 47.5%. The hypothesis presented in Problem Statement 3 was that the equiaxed microstructure would result in an improved creep-rupture life and a reduction in the anisotropy. This increase in anisotropy and loss of performance of the vertical MHT specimens is explored further in Section 4.5.

4.5 Discussion, Creep Testing

The CHT specimens exhibited excellent creep-rupture properties, easily surpassing the rupture life as specified in ASTM B637 [10]. The horizontal and vertical CHT specimens exhibited similar performance, in spite of the directional-dependence of the microstructure as shown in Chapter 3. The vertical specimens displayed a marginally longer rupture life, but the difference was not statistically significant. The performance of the two build

orientations contrasts with the results presented in [66, 67], where the vertical specimens outperformed the horizontal specimens by a factor greater than 5×.

The MHT specimens displayed anisotropic behavior not seen in the CHT specimens. Relative to the CHT performance, the MHT horizontal specimen improved its creep-rupture life which was to be expected based on the change in microstructure. However, the vertical specimens saw a massive decrease in creep-rupture life. A decrease in creep-rupture life was expected in the vertical specimens due to the removal of the columnar grains, but the massive decrease shown in Figure 4.11 was more significant than expected. This loss of performance in creep properties has been encountered in other recent research [68]. Kuo et al. [68] showed that a modified STA (1180 °C/4h) LPBF IN718 exhibited poor creep properties, but the author only tested vertically oriented specimens and did not test the anisotropy of the creep response. These results are reinforced by the findings of this research.

Combining the creep-rupture performance with the analysis from Chapter 3, it should be concluded that creating an isotropic microstructure does not necessarily improve the isotropy of the creep performance. Additionally, the change of grain size doesn't lead to longer rupture lives, as also found in [34]. This requires other routes of investigation for the difference. In the MHT specimens, there is an obvious directional-dependence of the heat treatment that cannot be ascribed to the grain structure. The following section investigates the fracture surface of the creep specimens to identify another potential factor contributing to the directional dependence of the creep-rupture life.

4.5.1 Microstructural Differences of the Creep Specimens.

The grain structures of the MHT specimens are equiaxed (uniform in each direction), therefore this cannot be a cause of the anisotropic creep-rupture behavior. Additional SEM investigation of the annealed microstructure was carried out to identify other differences resulting from the difference in solution treatment. As previously shown in Chapter 3,

the as-built and CHT specimens exhibited almost identical microstructure. The as-built and 1160 °C/8 h specimens were re-examined to compare and contrast the microstructure as shown in Figure 4.12. Specimens were prepared with an etchant consisting of 18 mL H_2O, 60 mL HCl, and 2g Cu_2Cl_2 with an exposure of 5 seconds, followed by a water rinse. Figure 4.12a reveals the dendritic structures in the as-built specimen formed during the solidification of the gamma (γ) matrix. No carbides or other secondary phases are visible. The white arrows in Figure 4.12a indicate several visible crescent-shaped melt-pool contours. The dendritic formations are removed by the annealing process as early as one hour with the 1160 °C solution treatment. Figure 4.12b shows multiple strings of carbides in the 1160 °C/8 h specimen (Arrow 1). These carbides primarily form during solidification along existing grain boundaries, so the arrangement of these NbC "necklaces" indicate the original grain boundaries from the as-built material. As the carbides coarsen over the course of the solution treatment, they grow in their original positions to the sizes seen in Figure 4.12b. Carbide formations were not found in any of the as-built or CHT specimens. The current grain boundaries in Figure 4.12b are identified by the contrast between the bulk areas (Arrow 2), and several black circles represent pores (Arrow 3). These carbides were only visible after the etching process removed the softer γ matrix. Several non-etched specimens with similar annealing treatments were explored, but carbides were not easily identified in these specimens.

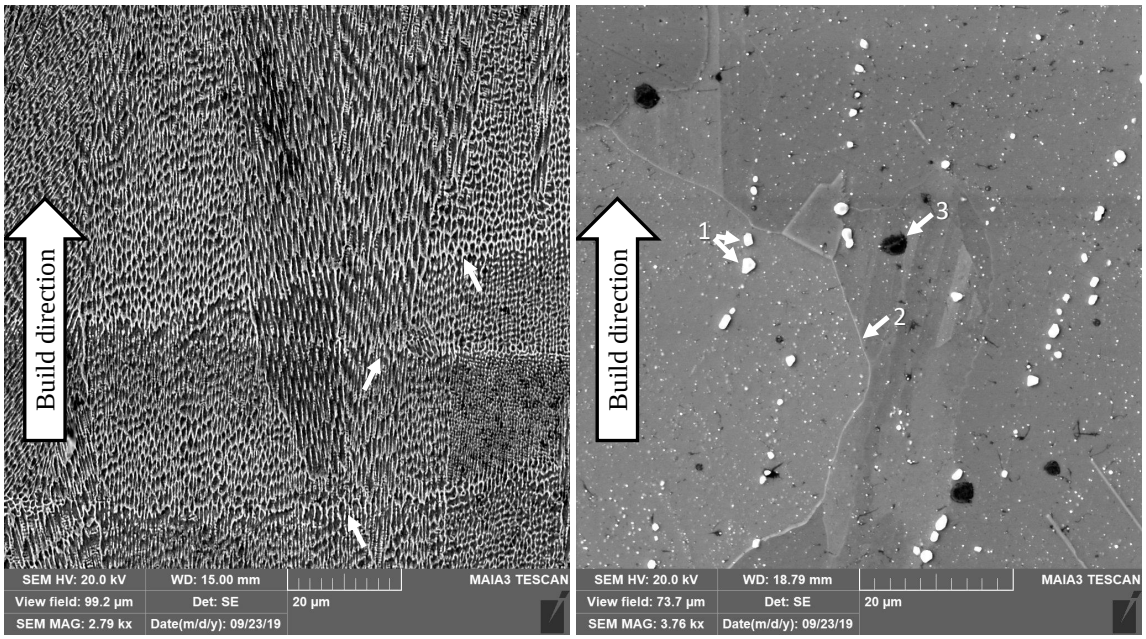

(a) As-built X–Z specimen D18 (b) 1160 °C/8 h annealed X–Z specimen D12

Figure 4.12: The etched microstructure is shown in the as-built (a) and 8-hr annealed (b) conditions via SEM. Figure 4.12a displays the dendrites formed during the solidification of the gamma matrix, but no carbides are readily visible. The white arrows indicate several visible crescent-shaped melt-pool contours. Figure 4.12b shows multiple strings of carbides as bright-white spheroids (arrow 1), arranged along what where the as-built grain boundaries. Annealed grain boundaries (arrow 2) and pores (arrow 3) are also visible.

The fracture surface of a representative CHT specimen is shown in Figure 4.14. The initiation of the creep-rupture failure is evident on the fracture surface by the increased oxidation at the initiation site as shown in Figure 4.13. While IN718 is typically resistant to oxidation, some oxidation occurs due to the extended test duration, the presence of the lab air, and the 650 °C furnace. This leaves a blueish zone where the specimen first cracked in contrast to the typical silver of the IN718. Examining the initiation area revealed a large quantity of "cup and cone" surfaces as seen in Figure 4.14a. The "cup and cone" geometry is indicative of intergranular failure as described in [112, 121]. Moving away from the crack initiation, the outer regions of the fracture surface show signs of transgranular fracture in the form of faceted surfaces (Figure 4.14b), which is indicative of sheer fracture.

The only discernible microstructural difference between the CHT and MHT specimens is the presence of linear carbide clusters in the MHT specimen as shown in Figure 4.12b. Individual carbides have been identified as crack-initiation sites, resulting in a decrease in mechanical properties [91, 100, 135]. However, in the creep-rupture results from Figure 4.11, the carbides appear to have a directional effect on the creep-rupture life -

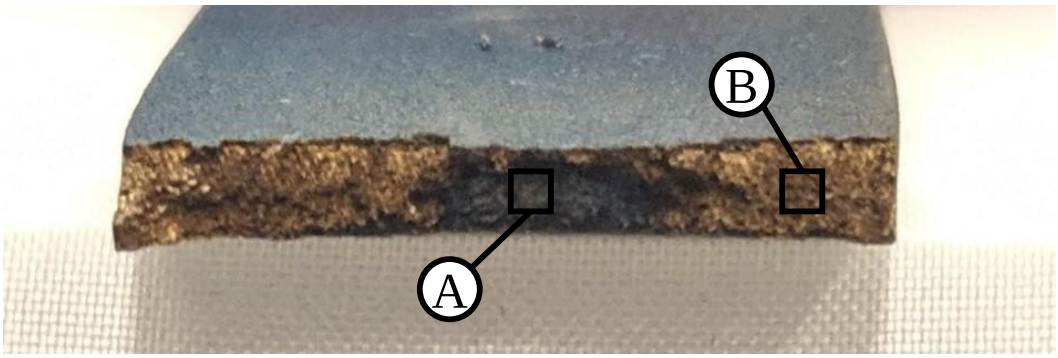

Figure 4.13: Optical image of the fracture surface of a vertical CHT specimen. The creep fracture initiated in the oxidized section indicated by (A) and is shown in Figure 4.14a. The failure transitioned to rapid shear on both sides of the initiation region. The fracture surface of (B) is shown in Figure 4.14b.

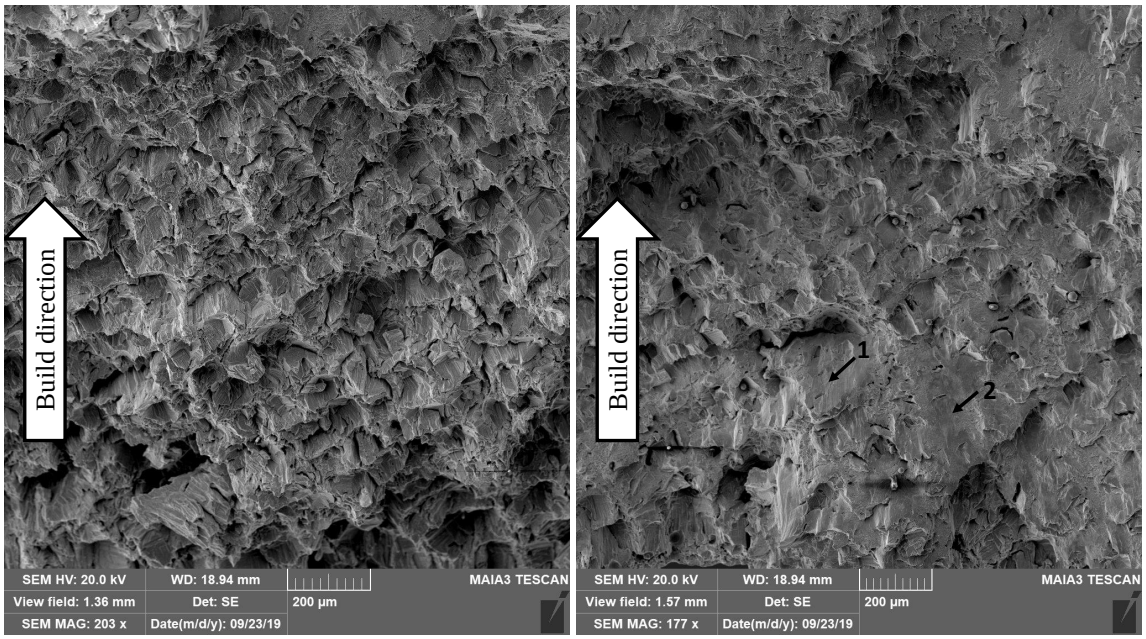

(a) Intergranular "cup and cone" fracture (b) Mixed fracture with transgranular "facets"

Figure 4.14: SEM microscopy was used to investigate the fracture surfaces of a vertical CHT creep specimen. The rupture initiated in the area shown in Figure 4.14a and reveals a predominantly intergranular "cup and cone" surface. The rupture accelerated into a tensile failure in the area shown in Figure 4.14b, resulting in the visible shear surfaces or "facets" interspersed with intergranular fractures.

increasing the horizontal MHT life while greatly decreasing the vertical life. A theory is proposed whereby the carbide formations prevent vertical crack formation during transverse loading, thus increasing the horizontal life during creep. The prevention of the vertical cracking accelerates cracking in the horizontal direction during loading aligned with the material's build direction, resulting in the reduction of rupture life.

MC carbides form exclusively on grain boundaries during the solidification and heat treatment processes [132, 135]. The microstructure examined in Figure 4.12b has gone through extensive recrystallization and grain growth. As a result, carbides that formed along the boundaries of the columnar as-built microstructure are now visible within the interior of the recrystallized grains. The carbides are arranged in "necklaces" along what would have been the vertical boundaries of the columnar as-built microstructure. As these carbides grow, they create local compressive stresses in the γ matrix [132]. The compressive stresses are enhanced by the close proximity of multiple carbides.

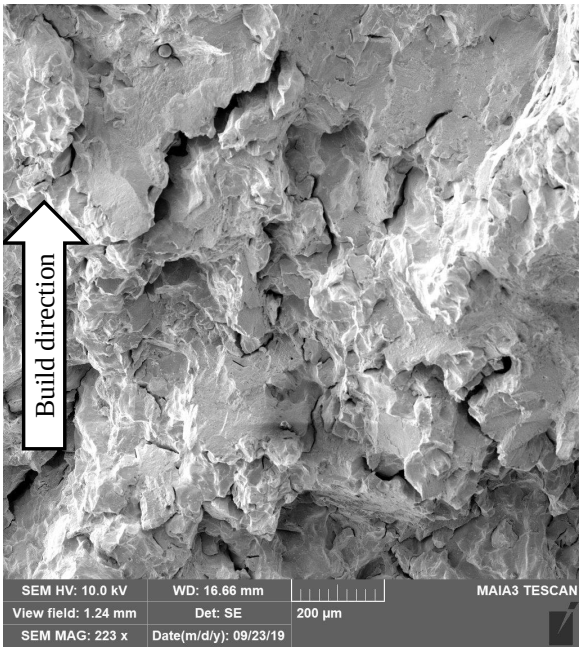

Figure 4.15: Mixed-mode fracture of a vertical MHT creep-rupture specimen

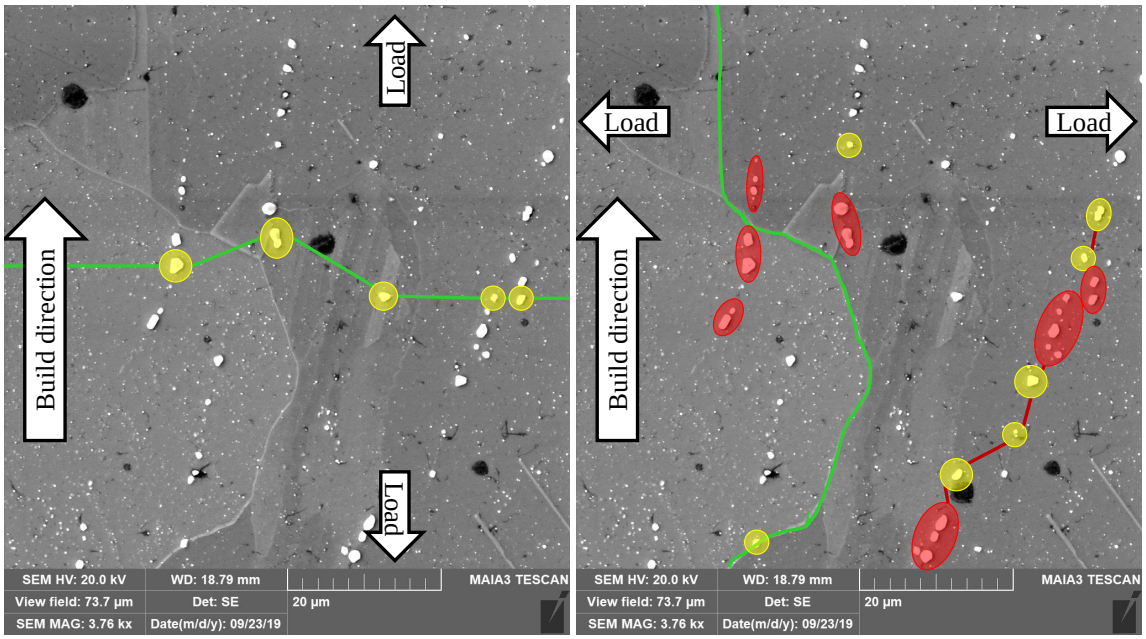

(a) Vertical transgranular fracture path (b) Horizontal intergranular fracture

Figure 4.16: Notional fracture paths in MHT creep-rupture specimens are shown by the green lines. In a vertically-oriented creep-rupture specimen (Figure 4.16a), the crack progresses transverse to the build direction, encountering several isolated carbides with their respective stress fields. Under horizontal loading (Figure 4.16b), the vertically-aligned carbide clusters present overlapping stress fields which increase the amount of energy needed to propagate the crack. The crack instead travels along the intergranular boundaries

The tensile creep-rupture tests generate cracks perpendicular to the loading direction. Transgranular fracture is promoted by the presence of the carbides within the interior of the grains [135]. Figure 4.16 illustrates the transgranular and intergranular fracture paths and the interaction between the crack and carbides. In a vertical specimen, the crack travels horizontally as illustrated in Figure 4.16a. When the crack encounters a carbide, it must overcome the residual compressive stresses before it moves through. The yellow circles in Figure 4.16a represent a low residual stress intensity around the carbides. The spacing between the carbides encountered by the crack are at least on the order of the grain size of the as-built material, so each carbide is relatively isolated from the next in the path. As the crack continues growing from carbide to carbide, it eventually splits the grain resulting in a transgranular fracture. This transgranular fracture requires less energy and is weaker than the intergranular fracture shown by the CHT specimen in Figure 4.14. During a horizontal test, the crack travels vertically through the grains and inline with the carbide "necklaces". Typically, the path from carbide to carbide would be the path of least resistance. However, the compressive stresses from the closely precipitated carbides creates additional resistance for crack growth. As in the previous figure, the yellow circles indicate regions of low residual stress. The red circles indicate a theoretical compounding of the residual stresses due to the proximity of neighboring carbides. The crack requires more energy to grow through the areas of higher compressive stress and ends up propagating along the weaker intergranular boundaries. The interior carbides have effectively increased the creep resistance of the horizontally fabricated creep-rupture specimens, which is an unheralded conclusion from this testing. Previous research into the creep behavior of AM IN718 missed this property as the research either didn't include higher-temperature solution treatments as in [66, 149] or the tests with higher-temperature solution treatments were only tested in the vertical orientation [68].

4.6 Mechanical Summary

This chapter addressed the research objective described by Problem Statement 3. Changes in the grain size resulted in a change in mechanical properties as demonstrated through hardness, tensile, and creep-rupture testing. The hypothesis posed with Problem Statement 3 was found to hold true regarding grain size and tensile strength, but was not found to be true regarding creep performance. The hardness and tensile testing revealed the MHT reduced the anisotropy of the $YS_{0.2}$ by 10% and UTS by 4–6%. However, the overall $YS_{0.2}$ and UTS were also reduced by 14.5% and 20.7%, respectively. New Hall-Petch constants were generated from the tensile results to account for the γ'' hardening in IN718. The creep-rupture results indicate the columnar nature of the grains provided a stronger effect than the average grain size. The loss of the columnar structure due to the MHT results in a reduction in the rupture life by 47.5% for vertically-oriented specimens. However, the rupture life did not decrease for the horizontal specimens, in spite of the equiaxed grain structure analyzed in Chapter 3. This difference between the two orientations yields a new hypothesis on the role of carbide (NbC) coarsening and the increase in rupture life.

V. Microstructure Modeling

This chapter addresses the research objective described by Problem Statement 4: previous mesoscale simulations of laser powder-bed fusion (LPBF) Inconel 718 (IN718) do not account for residual stresses in the as-built material. Stochastic Parallel PARticle Kinetic Simulator (SPPARKS) is a powerful open-source modeling tool capable of approximating the recrystallization behavior in metals via Kinetic Monte Carlo (KMC) simulations. A new module for SPPARKS was developed in collaboration with this research to allow SPPARKS to consider the stored energy from residual stresses in conjunction with boundary energy in the recrystallization simulations. Using the experimental electron backscatter diffraction (EBSD) data collected in Chapter 3, this new SPPARKS capability was calibrated to demonstrate its feasibility and functionality. As part of the calibration, a parameter screening was conducted to match the simulation outputs with the target parameters from the experimental data: average grain area (A_g), recrystallized fraction (X_V), and the Avrami constants from the Johnson-Mehl-Avrami-Kolmogorov (JMAK) equation (n and $\ln K$). The screening test was successfully completed, and has shown that it is possible to incorporate stored-energy-driven recrystallization within SPPARKS. This implementation of SPPARKS is the first demonstrated application of the stored-energy-driven recrystallization in conjunction with the previous curvature-driven model and pinning particles. The resulting model provided insight into microstructural features seen in the experimental data.

5.1 Background on Modeling Recrystallization Dynamics

Although materials interact with their environment at the atomic scale (micro), their response is observed at the continuum scale (macro) [43]. The KMC model is a powerful computational tool for spanning these length and time scales and is capable of recreating the

evolution of dynamic systems [43, 142]. The realm between the micro and macro scales is referred to as the mesoscale. Mesoscale models provide a bridge between the atomistic properties of the micro scale and the bulk properties of the macro scale. Mesoscale models also allow for a cost-effective simulation across the time domain. KMC has been extensively used in the modeling of solidification and recrystallization behavior of non-additive materials [103, 111, 143], and more recently in additive-specific applications [1, 43, 78, 106, 110, 144]. These efforts are limited to curvature-driven recrystallization using the Monte Carlo Potts model [103]. This research extends the previous efforts to incorporate a novel stored-energy-driven recrystallization based on the residual strains in the LPBF microstructure.

Simulating recrystallization accurately requires two parts - a model of the dynamics, and a basis by which to judge the accuracy of the model. In this research, the KMC model within SPPARKS was used to approximate the recrystallization dynamics. The EBSD data collected and analyzed in Chapter 3 was the basis against which the simulation was compared for accuracy.

5.1.1 Rejection Kinetic Monte Carlo (rKMC) Model and Parallel Processing.

In Section 2.5 (p. 70), a 'flip' was defined as the result of KMC event where a pixel moves from its parent grain to a neighboring grain. Additionally, Section 2.5 introduced the KMC model and its implementation in SPPARKS along with the Potts model [37], Equation (5.1), and the KMC flipping rate [43], Equation (5.2). The KMC flipping rate approximates the probability of a specific KMC event occurring, and the Potts model is used to select an event when multiple events could simultaneously occur, e.g., when a pixel is able to flip to multiple neighboring pixels (even when those neighboring pixels belong to one grain).

$$P_j = \frac{r_j}{\sum_{i=1}^{N} r_i} \tag{5.1}$$

where P_j is the probability of event j occurring, N is the total number of possible states, $i, j \in [1, N]$, and r_i and r_j are the rates of specific events in the system as determined by the KMC model, Equation (5.2):

$$r_j = \begin{cases} 1, & \text{if } \Delta E \leq 0 \\ \exp\left(-\frac{Q+\Delta E}{kT_B}\right), & \text{if } \Delta E > 0 \end{cases} \tag{5.2}$$

where Q is the activation energy for diffusion, k is the Boltzmann's constant, T_B is the Boltzmann (or simulation) temperature, and ΔE is the energy change associated with the reorientation as given by Equation (5.3) [43, 111]:

$$\Delta E = E_{final} - E_{initial} \tag{5.3}$$

Implementing a "true KMC" model is computationally intensive since every probability in the system is based on the overall state of the system, ΔE_{final} and $\Delta E_{initial}$, in Equation (5.2). Whenever an event is accepted (i.e., a grain boundary moves), the total energy of the state is changed, and the probability for every point in the lattice must be recalculated. In order to get around this constraint and enable parallel calculations, SPPARKS implements a KMC variant referred to as rejection Kinetic Monte Carlo (rKMC). When calculating the multiple permutations a lattice site can assume, rKMC introduces a 'null' event whereby no change occurs. The probability assigned to this null event is calculated such that the sum of all probabilities for each site is equal. This simplification greatly increases the processing speed of the simulation, providing rKMC an advantage in processing speed as compared to KMC. The disadvantage is the cumulative probability of the null events can end up being large when compared to the probability of a state flip, which causes an inefficiency in the model as it performs a large quantity of null events. Both models, true KMC and rKMC, perform the dynamic evolution of the system in a time-accurate manner. [43, Sect. 3.1]

The rKMC algorithm used by SPPARKS allows for events to be performed simultaneously by multiple processors. Some approximations were made in this approach,

specifically it has been assumed that the probability of an event at one location has a minimal dependence on the events occurring at a point at some large distance away. In this sense, the events are spatially decoupled and independent. SPPARKS adopts this approximation in two steps as illustrated by Figure 5.1a. In the first step, SPPARKS partitions the spatial domain and assigns these partitions to different processors. In the second step, the sequence of calculations for each processor partition is further divided, typically as 4 quadrants in 2D or 8 octants in 3D. Each processor performs calculation in the first quadrant, which avoids interacting with any calculations in neighboring partitions. The processors then move to the second quadrant, and repeat this process until the entire domain has been covered. This partitioning and subdivision is illustrated by Figure 5.1a where the processor partitions are indicated by the solid black lines, the 2D quadrants are indicated by the dotted line, and the active quadrant is highlighted green. In between the quadrant calculations, the processors share updates for changes that were made to the boundary sites surrounding the next quadrant. This surrounding domain is represented by the dashed box in Figure 5.1b. This allows the events calculated by one processor to be carried over into the next processor. [43]

5.1.2 Curvature-driven Growth as Currently Implemented in SPPARKS.

The existing SPPARKS implementation of the rKMC model considers only the boundary energy, i.e., curvature-driven growth (as described in Section 2.1.3.2 (p. 28)), in calculating the recrystallization behavior. The recrystallization is approximated through the process of flipping lattice points from their current grain to a neighboring grain. In this manner, the grain boundaries seek to minimize the combined energy of the system. In the strictest sense, curvature is defined as:

$$\kappa = \left| \frac{d\vec{T}}{ds} \right| \tag{5.4}$$

where $\vec{T}$ is the unit tangent to the curve (2D) or surface (3D), s is the arc length, and $|\vec{x}|$ is the magnitude of vector x. The rKMC algorithm does not directly calculate the curvature

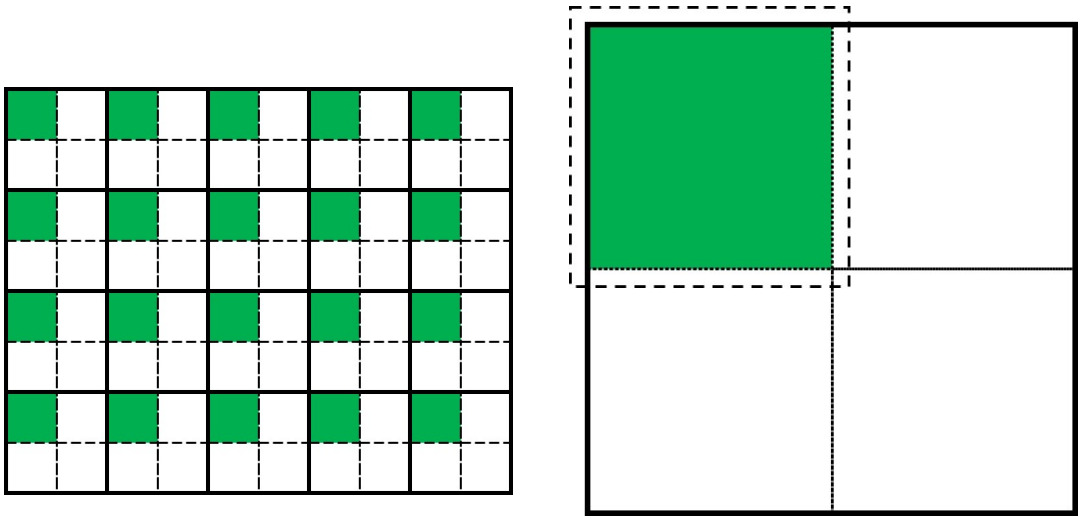

(a) SPPARKS domain subdivided for 20 processors. Figure adapted from [43, Fig. 12]

(b) Single processor domain, with the surrounding boundary region of a quadrant. Figure adapted from [43, Fig. 13]

Figure 5.1: SPPARKS performs parallel processing by subdividing the domain across multiple processors. In Figure 5.1a, a 2D domain has been partitioned for 20 processors in a 5×4 array. Each sub-domain is further divided into 4 quadrants. Each processor independently performs operations in the green quadrant to avoid conflicts with the other processors. The processors share information in the surrounding region in between rKMC steps. Figure 5.1b represents this surrounding region with the dashed box around the green quadrant. Both figures adapted from [43].

or boundary energy of the grain surface. Instead, it approximates boundary energy by counting the number of neighboring lattice points that belong to a different grain than the pixel of interest. In the 2D cases used in this research, this sets a boundary energy range of [0,8]. The pseudo-code for counting the energy as a function is as follows:

1. Load the grain identities (aka 'spins') for all pixels from the EBSD input file
2. For every pixel i, initialize the energy, $energy_i = 0$
3. Loop for the number of neighbors, j (Note: $j = 8$ in the 2D case)

   If i and j are in different grains, add 1 to the energy: $energy_i = energy_i + 1$
4. End

Figure 5.2 shows four examples of the boundary energy as calculated within SPPARKS. In each of the subfigures, the energy is given for the central pixel in a 3×3 grid. Figure 5.2a and Figure 5.2b represent the special cases of a single-pixel grain and an interior pixel, respectively. Figure 5.2c and Figure 5.2d illustrate two boundary pixels with the same $energy_i = 5$, but with one or two neighboring grains, respectively.

The Potts model is used to select a neighboring pixel from pixel i, with the probability given in Equations (5.2) and (5.3) using the $energy_i$ to determine ΔE. If pixel i's movement to join the grain of pixel j results in it having more neighbors in that grain, then the boundary energy, ΔE, is negative and the probability of that event, r_j is added to the Potts model with a value of $r_j = 1$. If the flipping of pixel i results in more dissimilar neighbors, then $\Delta E > 0$, and a relatively small probability is added to the Potts model for that event r_j. In this manner, the rKMC is minimizing the local energy of the system. As this process is repeated across the domain, the result is a global decrease in the boundary energy of the system.

5.1.3 Simulating Pinning Particles.

SPPARKS is able to represent pinning particles in the recrystallization calculations. As discussed in Section 2.3.2 (p. 37), the MC carbides act as pinning particles. The carbides

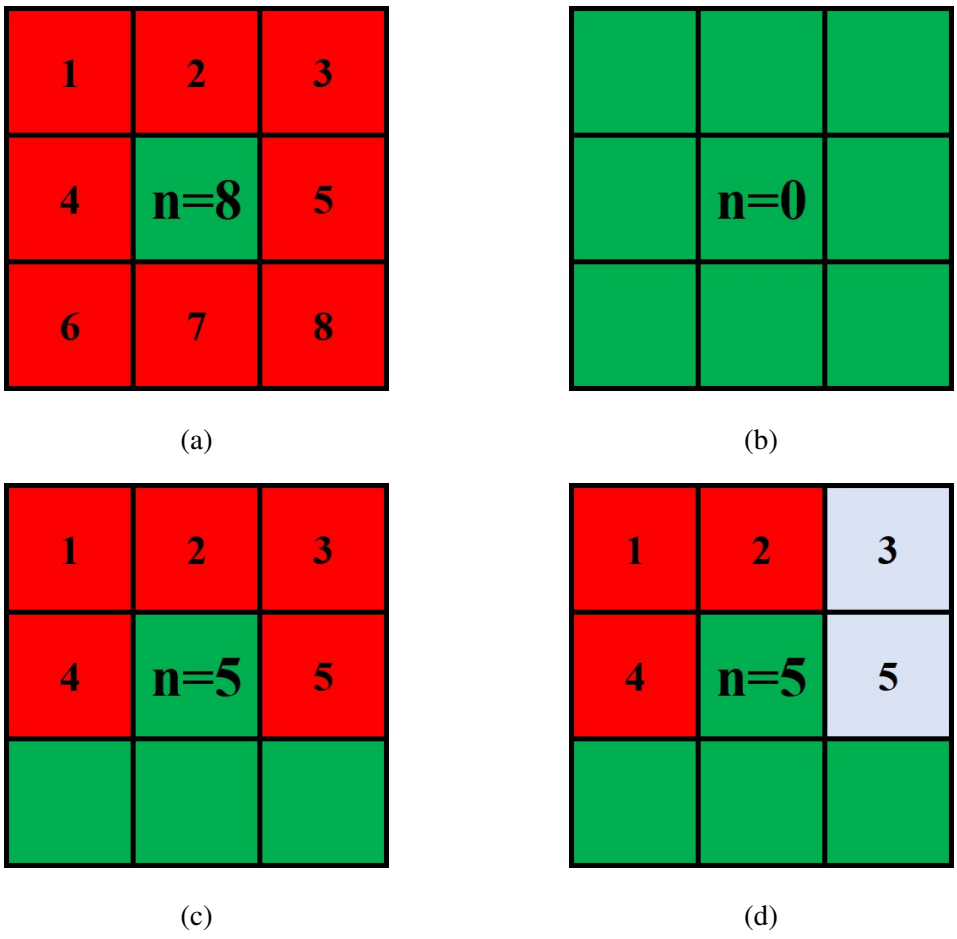

Figure 5.2: Curvature is calculated by the total number of neighboring pixels in a different grain. Grains are presented by the different colored pixels. This counting method approximates the boundary energy of a grain whereby a decrease in its radius of curvature increases its energy. Figure 5.2a and Figure 5.2b represent the special cases of a single-pixel grain and an interior pixel, respectively. Figure 5.2c and Figure 5.2d illustrate two boundary pixels with the same $energy_i = 5$, but with one or two neighboring grains, respectively.

play a key role in controlling the movement of grain boundaries by increasing the amount of energy needed to move a grain boundary past a pinning particle. SPPARKS simulates pinning particles by taking a given fraction of pixels (typically defined as a fraction of the total number of pixels) and removing them from the grain calculations by assigning a grain value of Q+1, where Q is the number of grains in the system. The boundary energy equation still counts pinned pixels as belonging to a different grain, but there is a zero probability that the grain will join the pinned pixel's grain. As determined by Doherty et al. [33], the pinning particles best approximate the effect of Zener pinning (Equation (5.5), [50]) by using a 3×3 array of pinned pixels to represent a single pinning particle.

$$P_{SZ} = \frac{3 f_V \gamma}{r} \tag{5.5}$$

where P_{SZ} is the pinning pressure, f_V is the volume fraction of spherical pinning particles of radius r (or area fraction for 2D), and γ is the boundary energy derived from the curvature.

5.1.4 Defining SPPARKS Parameters and Executing via Scripts.

SPPARKS simulations are executed through the use of scripts. The scripts are input files containing the model parameters, a data file containing the details of the sites, and commands to perform the rKMC steps. The scripts also define how the simulation is saved in output files. Options for outputs include image files (typically jpeg) and text files. These scripts allow the user to customize the parameters for the rKMC model and SPPARKS simulation. The data file contains the information on each pixel in the model - its location, grain identification, location, and energy level. The script determines the application of several functions to the inputted data file. Pinning particles, rKMC commands (described later in this section), and stored-energy manipulation (to be described in Section 5.2.3) are all controlled by the script. The script functionality is taken advantage of by writing a simple Python script that outputs script files using a range of parameter values. In this fashion, scripts covering the entire design of experiments range (to be described in Section 5.2) can be automatically generated. Table 5.1 lists the existing SPPARKS

parameters that are considered in this research. These parameters are defined and described further in this section.

Table 5.1: List of existing SPPARKS functions and parameters

Description	SPPARKS function/parameter
1) Boltzmann factor, kT_B	temperature M
2) Pinning fraction and location	pin N F_1 F_2
3) Number of runs of rKMC steps	run R

5.1.4.1 Existing SPPARKS Parameters.

T_B is the Boltzmann temperature in the kinetic Monte Carlo equation Equation 5.2 (p. 163) and influences the probability of a flip occurring during each rKMC step [43]. The parameter is combined with the Boltzmann constant, k, and implemented as a Boltzmann factor by 'temperature M', where M is a floating point number $\in [0, \infty]$. The Boltzmann factor remains a constant throughout the script and resulting simulation. The range of kT_B has units of energy, J, with a range of [0,∞]. However, values above 0.5 start causing excessive flips in the rKMC steps that raise, instead of lower, the energy of the system ($\Delta E > 0$) with results that do not bear any resemblance to experimental data. As discussed in Section 2.5, the simulation temperature is not a real temperature - it is a fictional constant used to control the rate of flipping in Equation (5.2). No correlations have been made between the Boltzmann and annealing 'temperatures.' The values of the Boltzmann factor used in the modeling of LPBF IN718 are given in Table 5.4.

The SPPARKS model in use for this research is the rKMC with the Potts model and pinning particles. The behavior of pinning particles is defined using the existing 'pin N F_1 F_2' command within SPPARKS. This command has 3 inputs: N ($N \in [0, 1]$) is the

area fraction of pins, F_1 is a size flag, and F_2 is a location flag. The values of F_1 an F_2 are flags with integer values that indicate to SPPARKS the desired location and size of the pinning particles. Before the first rKMC step is executed, a fraction of the pixels in the system (N=0.004 or 0.4% using the example script in Figure 5.3) are removed from their parent grains. The rKMC model then treats them as fixed, and will not attempt to change their orientation nor flip any neighboring pixels to the pin's orientation. The value of N can be anywhere in the range of [0,1]. However, the area fraction of pinning particles is constrained by the chemical composition of the material. For the LPBF IN718 in this research, the experimental area fraction of NbC carbides has been under 1% of the total area. The second pin command input, F_1, can toggle between a pin size of 1×1 or 3×3 pixels. As previously mentioned in this section, Doherty et al. [33] establishes a case for using the 3×3 particle to better approximate Zener pinning. The final pin input, F_2, sets a flag which controls where the pins can be placed. A value of $F_2 = 2$, used for IN718, only allows pinning particles to be placed on grain boundaries. This is justified as the pinning particles in this simulation represent the NbC carbides in LPBF IN718 as discussed in Section 2.3.2 (p. 37). The NbC carbides only form on grain boundaries during the solidification process, and no further nucleation has been seen in this research during the annealing process. [99]

The last of the existing SPPARKS parameters of interest to this research is the basic 'run R' command, where R is a non-negative integer ($R \in \mathbb{Z}^{\geq}$). This command executes R rKMC steps and generates any outputs commanded by the script. A 'run 0' command is found at the start of the executable portion of the script for the purpose of initializing the computational domain. As will be discussed in Section 5.2.3, the run command is used to balance the amount of energy dissipated via annealing with the energy dissipated through the recrystallization. Additionally, the run command is used to correlate the rKMC steps with the time domain of the experimental data.

5.1.4.2 Layout of a SPPARKS Script.

The SPPARKS script is set up in four main sections. A sample script is shown in Figure 5.3. Section 1 defines the solver to be used, rKMC with Potts model and pins in this case, along with the dimensionality of the problem. This is also where the input file is read by SPPARKS to generate the lattice sites. No parameters are defined in this section.

Section 2 defines how SPPARKS saves the output files with 'dump' commands. Dump commands define the format of text and image outputs. The frequency of the data files was user-selected to output at every rKMC step for most files. However, care must be taken when using the dump command, as it can generate a massive amount of data; the first iteration created 15+ TB of data files. The image files were spliced together to create animations of the microstructural evolution. The text files were used for post-processing in MATLAB and Python. Parameter values were only used in this section in setting the file names of the various dump files to ease post-processing the massive amounts of data generated. Section 3 is used to define several constants used in the model. T_B is defined here, as well as two new constants implemented for this research by AFRL/RXCM, 'dispersion_rate' and 'propagated_E.' These commands are introduced later in Section 5.2.3. Section 4 is final section of the script and sets up the annealing process with new functions written by AFRL/RX researchers to specifically address annealing behavior. In Section 4, the order of commands becomes non-trivial as they are executed in the order listed.

5.1.5 Limitations of SPPARKS.

SPPARKS is a powerful tool, but it does have a few limitations that come into play during the simulations in this research. The software is built to perform 3D simulations, but the data used in this research was only collected as 2D images. There exists a process by which a researcher would collect a similar array of EBSD data in three dimensions, and it involves using a focused ion beam to image and then etch the metallographic surface

Section 1

```
#============================================
#SIMULATION SETUP
#============================================
seed 8978971
app_style potts/pin/REX 4428
dimension 2
lattice sq/8n 1.0
region box block 0 919 0 723 0 0
create_box box
create_sites box
read_sites   ../Initial_KAM.init
sweep random
sector yes
diag_style   energy
stats        1
```

Section 2

```
#============================================
# OUTPUT
#============================================
diag_style   energy
stats        1

dumpKAM_MAP image 2 KAM_MAP.2.*.jpg d1 d1 crange 1 1000 drange 1 1 view 0 0
boundary i1 1.2 shape cube box no 1 zoom 2.55 size 919 723 sdiam 1.05
dump_modify  KAM_MAP cwrap yes boundcolor black backcolor black pad 4 thresh i1
<= 4428
dump_modify  KAM_MAP smap 0 10 ca 0.04 5 min blue 1.25 lime 2.5 yellow 3.75
orange max red

dump        TUNING     text 200 text_tune.*.txt i1 d1 x y
```

Sect. 3

```
#============================================
# CONSTANT MODEL PARAMETERS
#============================================
temperature 0.2
dispersion_rate 0.5
propagated_E 0.4
```

Section 4

```
#============================================
# RUN MODEL
#============================================
run 0                       # Initializes Model
pin 0.004 1 2               # Insert Carbide particles
recovery 1                  # Scale values in initial KAM map
add_dislocations 0          # evenly add energy to all points in initial KAM Map
run 200                     # run for MC equivilant of 30 minutes of real time

recovery 0.95               # CYCLE 1, simulate 30 minutes of annealing
run 200                     # run for MC equivilant of 30 minutes of real time

recovery 0.95               # CYCLE 2, simulate 30 minutes of annealing
run 200                     # run for MC equivilant of 30 minutes of real time

recovery 0.95               # CYCLE 3, simulate 30 minutes of annealing
run 200                     # run for MC equivilant of 30 minutes of real time

...                         # Repeat for a total of 16 cycles (8 hours)
```

Figure 5.3: A sample SPPARKS input file is shown with the four sections demarcated by the three sets of #====. Note that # is the command to comment out the following text. Several lines of the script are commented out in the output section to reduce the amount of data generated with each simulation.

to reveal the next layer. However, there are practical considerations in dealing with 3D datasets. The EBSD maps in this research were roughly 1000×1000 pixels and resulted in simulation outputs on the order of 1 GB. If the EBSD data was collected in cubes of 1000 pixels, the resulting simulations would each be 1 TB and quickly overwhelm the storage of the super-computing cluster. To adjust for dealing with the 2D data, SPPARKS treats the 2D dataset as if it were a 3D image of a repeated stack of the same image. The process described in this chapter could be extended to 3D, if a 3D dataset and sufficient storage space were provided.

The implementation of the rKMC model in this research only considers grain boundary pixels, so recrystallization can only occur on the grain boundaries. In theory, it is possible that a carbide or other secondary particle on the interior of a grain could generate enough residual stress within the grain to generate a particle-stimulated nucleation [62]. This grain boundary-only simplification reduces the number of calculations needed at each rKMC step to just the boundary pixels, greatly improving processing speed. It is justified for this research owing to IN718's behavior as a low stacking-fault energy alloy [49, 128]. Under dynamic recrystallization conditions associated with high annealing temperatures, recrystallization nuclei of low stacking fault energy systems will be concentrated on the grain boundaries [98, 128], and the researchers believe this approach to be valid.

5.2 Implementing Stored Energy to Drive Recrystallization

In conjunction with this research, AFRL/RXCM supplemented the existing SPPARKS code to account for stored energy in the recrystallization model. This was done by adding code to the existing module that controlled the pinning particles. Doing so allowed for seamless integration of the new code implementations associated with this research. The new module imports stored energy from an experimental EBSD data file, then calculates a new total energy by combining the stored energy with the boundary energy. Several new functions were included to allow for manipulation of the stored energy to 1) adjust its effect

with relation to the existing boundary energy, and 2) simulate the reduction in energy during the annealing process. A design of experiments was set up for the existing SPPARKS parameters as outlined in Section 5.1.4 (p. 168) as well as several new parameters which are introduced in Section 5.2.3. The set of simulations for the design of experiments were analyzed and compared to the experimental data by through the use of several quality metrics which are introduced in Section 5.2.5. These quality metrics also served as the objective functions in an optimization problem to select the 'best' SPPARKS parameters to match the simulated and experimental data.

5.2.1 Introducing Experimental Data into SPPARKS.

One limitation in previous KMC (true KMC or rKMC) simulations has been a lack of experimental data to validate and calibrate the model. Experimental data is needed to establish the relationship between a KMC step and a unit of time, e.g., one step $\approx$ 5 minutes. The EBSD data collected in Chapter 3 provides a unique contribution to this research to establish the linkage between the KMC step and the time domain. The sequential EBSD data for 0–8 hours also provided the recrystallization dynamics for the JMAK equations, which are used to establish a goal for the SPPARKS simulations.

Section 2.5.1 introduced two ways to characterize the stored energy using EBSD measurements: grain orientation spread (GOS) and kernel average misorientation (KAM) [148]. GOS provides a singular value for each grain that approximately represents the amount of lattice distortion present in a crystal. While this metric was useful for determining the recrystallized nature of each grain as used in Section 3.3.1, it does not provide a geometrically detailed account of the localized energy gradients. KAM provides a qualitative comparison of the localized residual stress distribution and is used as a direct stand-in for the stored energy to simulate the stored-energy-driven recrystallization behavior that will be presented throughout this chapter. Obtaining the quantitative residual energy is possible, but it requires higher resolution techniques such as neutron diffraction.

Neutron diffraction can also provide additional details on the stored energy in the system by mapping the defect density (plastic deformations) in addition to the crystal lattice deformation (elastic deformations) captured by EBSD. This combination of plastic and elastic stored energy could possibly be used in further research to refine process and results of this research.

The SPPARKS simulations are fed EBSD data from the microstructural analysis carried out in Chapter 3. Specifically, the KAM measurement from the as-built X–Z specimen was loaded by each script as the input. The EBSD data was collected on an EDAX Pegasus EBSD system installed on a Quanta 450 scanning electron microscopy (SEM) as described in Chapter 3. The EBSD maps were collected at a resolution of 1 pixel = 1 μm. The KAM was calculated using a square grid, 3rd-nearest neighbor kernel as shown in Figure 2.18 (p. 76), and only the points on the perimeter of the kernel were used in the calculation to reduce computational time. Figure 5.4 shows the inverse pole figure (IPF) and KAM maps for the specimen. The unique grain map is also provided in Figure 5.5.

The EBSD data needed to be pre-processed in order for it to serve as an input file for SPPARKS. This conversion was done through a sequence of steps to unpack the proprietary file type, convert it from a hexagonal to a square grid, insert the KAM data, and repackage the boundary and KAM data into a single file for SPPARKS. The process is illustrated in Figure 5.6. The first step, converting the proprietary OIMA scan data (*.osc) to an open-source EBSD file (*.ang), was done within the OIMA software used in Chapter 3. The *.ang file was then fed into Dream3D where the hexagonal grid was converted to a square grid by means of linear interpolation. Dream3D filters were used to pull the grain data (aka feature IDs) and KAM measurements associated with each pixel into separate files. Finally, a MATLAB script was used to splice the grain data and KAM files into a single *.init file used to initialize the SPPARKS model. Throughout the SPPARKS work in this research,

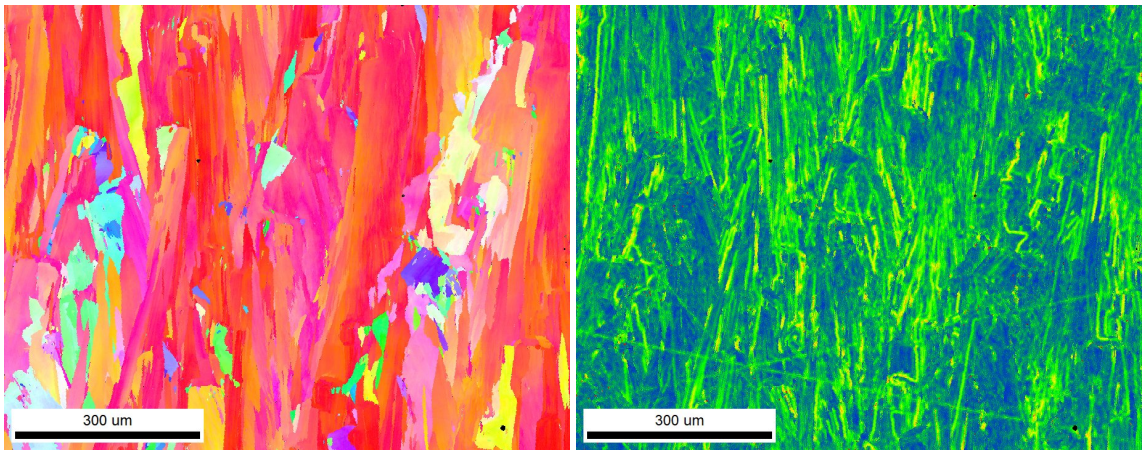

(a) IPF map, as-built LPBF IN718 (b) KAM map, as-built LPBF IN718

Figure 5.4: The EBSD data for the as-built X–Z specimen, D18, was used as the input for the SPPARKS simulations. Figure 5.4a is the IPF map showing the grain misorientations in the microstructure. Figure 5.4b reveals the local misorientations as measured by the 3rd-nearest neighbor KAM. The KAM values are used as the energy metric for the stored-energy-driven recrystallization in SPPARKS.

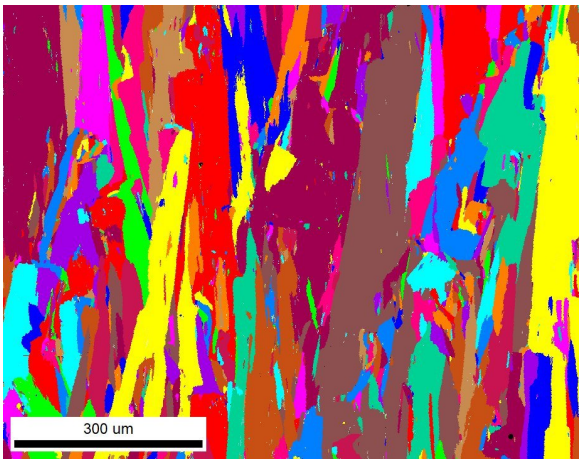

Figure 5.5: The unique grain map of the as-built specimen used as the SPPARKS input provides a little more detail into the grains. This information is not easily discernible in the KAM map from Figure 5.4b

the same source file was used as the seed data for the rKMC model. Using this conversion process, it would be a simple swap of the KAM data for another stored-energy metric to seed the rKMC model. Section 2.5.1 (p. 74) described several similar EBSD measurements that could be suitable in this regard.

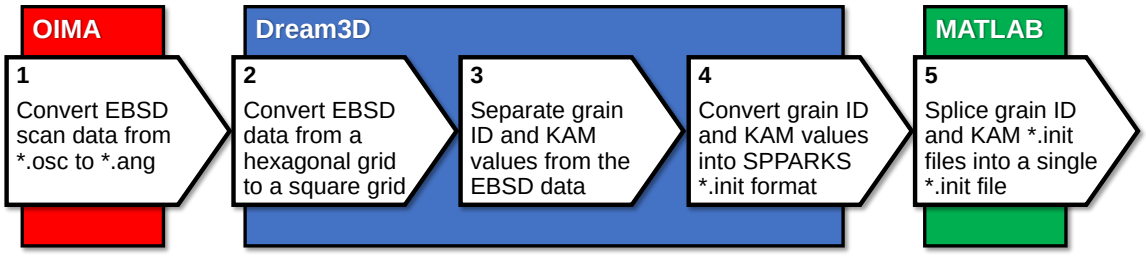

Figure 5.6: Flow chart for pre-processing EBSD data to create a SPPARKS input.

5.2.2 Combining Stored Energy with Boundary Energy.

The KAM inputs fed into SPPARKS have values based on the local misorientation. By the definition of a grain (set by the user in the EBSD software), the KAM values range from [0,5] with units of degrees. Conveniently, the magnitude of the KAM values is similar to magnitude of the boundary energy range of [0,8] described in Section 5.1.2. This makes combining the stored energy with the boundary energy relatively straightforward at first glance. A new module written by AFRL/RXCM takes the array of values for the KAM at each pixel and adds it to the boundary energy calculated. Thus, the pseudo-code presented previously has become (new lines in **bold**):

1. Load the grain identities (aka 'spins') for all pixels from the EBSD input file
2. **Load the KAM values for all pixels from the EBSD input file**
3. For every pixel i, initialize the energy, $energy_i = 0$
4. Loop for the number of neighbors, j (Note: $j = 8$ in the 2D case)

   If i and j are in different grains, add 1 to the energy: $energy_i = energy_i + 1$

5. **Add the KAM value to** $energy_i$**,** $energy_{total} = energy_i + KAM_i$
6. End

The results of combining the energy in this manner allows the rKMC model to evaluate flips based on the total energy of the system. Additional functions were written into the module by AFRL/RXCM to allow for the magnitude of the stored energy to be scaled up or down via multiplication, as well as shifting the range via addition. These functions permit the SPPARKS user to adjust the magnitude of stored energy with respect to the boundary energy.

5.2.3 Manipulating Stored Energy within SPPARKS.

With the introduction of stored energy into SPPARKS, AFRL/RXCM also developed several new functions and associated parameters to manipulate the stored energy before it is added to the boundary energy at each rKMC step. Table 5.2 lists these new functions and parameters.

Table 5.2: List of stored-energy parameters for SPPARKS. The parameters (N and M) for each function are a floating point number. $N \in [0, 1]$, $M \in [0, \infty]$.

Description	SPPARKS function/parameter
1) Energy transferred with each flip	dispersion_rate N
2) Energy propagated with each flip	propagated_E N
3) Add (or subtract) stored energy	add_dislocations M
4) Multiply (or reduce) energy	recovery M

The sample SPPARKS script, Figure 5.3 (p. 172), contains the functions from Table 5.2 as implemented in this research. 'dispersion_rate' and 'propagated_E' represent

rates of energy transfer associated with each rKMC flip. Both are defined as constants in Section 2, along with the Boltzmann temperature, T_B. The new boundary energy of a flipped pixel is simply approximated by counting the neighboring pixels in different grains as previously described. The dispersion and propagation functions were created to allow SPPARKS to approximate a new stored energy value. These functions approximate the stored energy of the flipped pixel, i, based on the stored energy of the neighbor pixel, j, selected by the Potts model. The stored energy of i is reset to zero after the flip, then energy is added based on the dispersion and propagated parameters. The 'dispersion_rate N' ($N \in [0, 1]$) defines the fraction of energy transferred to i from j. This fraction of energy is removed from j and given to i. Similarly, 'propagated_E N' defines the portion of the stored energy in j to be copied by SPPARKS and given to i. Values of N in the higher end of the range ($N > 0.5$) for the propagation function should mostly be avoided as the function could result in violations of the laws of thermodynamics by adding energy to the system and should not be considered.

The 'add_dislocations' and 'recovery' functions were written to permit the user to modify the stored energy values loaded by the *.init file, or at any point in between rKMC steps. These functions only appear in Section 4 of the SPPARKS scripts and control the behavior of the stored-energy-driven recrystallization with respect to the curvature-driven recrystallization. 'add_dislocations M' allows the user to displace all KAM values in the model by a positive floating point number M. Similarly, 'recovery M' multiplies all KAM values by a floating point number M. When $M \geq 1.0$, the recovery command is also referred to in the scripts and this paper as 'multiplied_energy.' Recall that the KAM values could range from [0,5] as defined by the EBSD software, and the boundary energy could take values in the range [0,8]. With these two commands, the user can effectively vary the range of KAM values using the addition function or stretch the range using the multiplication function. These commands are used in the initialization of the rKMC model

in conjunction with the 'run 0' and 'pin X M N' command. This allows the model to displace or stretch the seeded KAM values before the first rKMC step. The parameters for each function can range from [0,∞). However, large values ($N > 5$) were found to lead to unstable microstructures which deviated greatly from any physically realizable recrystallization behavior.

The 'recovery' function also serves a second purpose to approximate the annealing response of the stored energy. When used with a parameter value $M < 1.0$, the recovery function reduces the model's KAM values uniformly across the domain. This is used to approximate the effect of annealing and the overall relaxation of stored energy within the physical system. The 'recovery' command is combined with a 'run' command and looped for 16 cycles. The parameter combination of the recovery and run determines the rate at which grain boundaries move in the model. Recovery values close to $M = 1.0$ maintain higher energy levels, resulting in more accepted flips and therefore more boundary movement. Similarly, a higher number of rKMC steps within each loop allow for more flips to occur. Eventually, the cumulative effect of numerous recovery commands, as well as energy lost via the dispersion and propagation functions, lowers the energy of the each pixel to the point where flips are less likely to occur, thereby slowing boundary movement. In the sense of the physical model, the residual stresses that were driving recrystallization have been successfully annealed out.

5.2.4 Selecting Suitable Parameter Ranges.

The implementation of each of these parameters in SPPARKS was done by assigning a range of values to each parameter, then generating a multitude of scripts with each possible combination of parameters. A full-factorial design of experiments was laid out using the eight parameters identified in Table 5.3. Table 5.3 combines the original SPPARKS parameters presented previously in Table 5.1 (p. 169) with the new functions and parameters presented in Table 5.2 (p. 178). These scripts were batch-processed on a super-

computing cluster, enable in part by the massively-parallel capabilities of the SPPARKS code. Suitable ranges for each parameter were determined through a screening test and correlation to analysis of the experimental microstructure. This section discusses the identification of the suitable ranges for each of the eight parameters identified in Table 5.3.

Table 5.3: List of SPPARKS functions and parameters

Description	SPPARKS function/parameter	Units
1) Boltzmann factor, kT_B	temperature M	Energy (J)
2) Energy transferred with each flip	dispersion_rate N	Percentage
3) Energy propagated with each flip	propagated_E N	Percentage
4) Multiply (or reduce) energy	multiplied_energy M	Unitless
5) Add (or subtract) stored energy	add_dislocations M	Energy (J)
6) Pinning fraction	pin N	Percentage
7) rKMC steps per recovery loop	run R	Runs
8) Fraction of energy retained in loop	recovery M	Percentage

The Boltzmann temperature was experimented with in the range from [0,1], but valid solutions were only found when $T_B \leq 0.5$. Higher values resulted in rapid and excessive recrystallization and grain growth that was inconsistent with the experimental data. The range for simulation temperature inputs was eventually constrained to the set of set as [0.2, 0.3, 0.4, 0.5]. These parameters are presented in Table 5.4.

The 'dispersion_rate' and 'propagated_E' functions were written specifically for this research. As a result, no prior knowledge existed of what would be acceptable ranges for their associated parameters. For the screening test, both parameters were given values of

[0.3, 0.4, 0.5]. Similarly, the 'multiplied_energy' and 'add_dislocations' functions did not have previous research to rely upon. Their starting ranges were set to [1, 2, 4] and [0, 1, 2, 3], respectively, to develop an idea of what an appropriate energy increase to allow the energy-driven recrystallization to compete with the curvature-driven model. These parameters are presented in Table 5.4.

The area fraction of pinning particles was evaluated based off the presence of carbides in the microstructural analysis. The area fraction of carbides found by energy dispersive X-ray spectroscopy (EDS) in the 8-hour EBSD IN718 specimens ranged from 0.0% to 0.9%, depending on the annealed condition. Based on this analysis, the range for the carbide fraction in the screening test were set to [1%, 2%, 4%]. These parameters are presented in Table 5.4.

The number of rKMC steps per recovery loop controls the pace at which the rKMC model runs in conjunction with the annealing or recovery process. Balancing the number of steps per loops is critical to controlling the ratio of boundary-energy-driven to stored-energy-driven recrystallization. Too many steps, and the stored energy drives the recrystallization; too few, and the system's energy is decreased by the 'recovery' command to the point that the recrystallization is only driven by geometry. The runs per loop were set at [200, 400, 600, 800] for the screening test. The parameter associated with the 'recovery' command represents the fraction of energy retained by the simulation with each rKMC step: a value of 1 imparts no change, and a value of zero would completely remove all energy from the system. Again, this was a first-time implementation of stored-energy-driven recrystallization for the SPPARKS model and no prior data was available. Initial testing revealed that values below 95% (0.95) resulted in the stored energy diminishing too quickly, so the initial range of values was set to [95, 98]. These parameter ranges are presented en masse in Table 5.4.

Table 5.4: SPPARKS parameter ranges for initial screening test. Linear ranges are presented in MATLAB vector format as (start value):(step size):(end value) [77]. The total permutations value represents the number of simulations to be created to cover the full-factorial design space.

Parameter	**Initial Screening (Mk10)**	**Qty of Levels**
kT_B **(J)**	0.2, 0.3, 0.4, 0.5	4
dispersion_rate (%)	30, 40, 50	3
propagated_E (%)	30, 40, 50	3
multiplied_E	1, 2, 4	3
add_dislocations (J)	0, 1, 2, 3	4
pin fraction (%)	1, 2, 4	3
runs per loop	200, 400, 600, 800	4
recovery_loop (%)	95, 98	2
Total permutations		10,368

5.2.5 Optimization Problem and Quality Metrics.

The accuracy of SPPARKS is evaluated for accuracy against the experimental data by comparing the microstructure properties and recrystallization dynamics. The microstructure properties are captured in the metrics of average grain area (A_g) and recrystallized fraction (X_V), as characterized from the EBSD data in Chapter 3. The recrystallization dynamics are captured by the Avrami exponent (n), and Avrami intercept ($\ln K$), from the JMAK equation (Equation (5.6)) previously introduced in Section 2.5.2 (p. 79). The values of these four metrics were taken directly from the experimental data to establish a target for the simulations. A_g and X_V were measured directly from EBSD the specimen solution treated at 1160 °C/8 h. The Avrami values were taken by performing a linear regression of the recrystallized fractions of each of the 9 solution-treated specimens (0–8 h) from Chapter 3. The values obtained from the measurements and linear regression are given in Table 5.5.

$$\ln\left[\ln\left\{1/(1-X_V)\right\}\right] = \ln K + n \ln t \tag{5.6}$$

Table 5.5: Experimental values used as targets for the SPPARKS simulations

μS_Q and $JMAK_Q$ targets	A_{gt}, μm^2	X_{Vt}	$\ln K_t$	n_t
1160 °C/8 h	15790 μm^2	0.922	-0.138	4.089

Each SPPARKS simulation generates a unique microstructure at the end of the sequence of rKMC steps. The output files were post-processed to characterize these four metrics: A_g, X_V, n, and $\ln K$. A_g and X_V capture the end state of the simulation, and were measured directly from the final output files. n and $\ln K$ characterize the recrystallization rate of the system. Their values were calculated by fitting the recrystallized fractions at multiple rKMC steps to the Avrami equation (Equation (5.6)). A linear regression was

performed on the simulation data using Python. The recrystallized fraction was taken from the SPPARKS output file from the end of each of the 16 recovery loops.

These four metrics for each of the simulations are combined to generate two quality metrics: microstructure quality and JMAK quality. The microstructure quality, μS_Q is calculated using Equation (5.7) and is the normalized Euclidean distance of average grain area, A_g, and recrystallized fraction, X_V, from the simulation end state and the experimental target. The JMAK quality is similarly calculated using Equation (5.8) as the normalized distance of the Avrami intercept, $\ln K$ and the Avrami exponent, n. The JMAK equation was previously discussed in Section 2.5.2. The values of the experimental results, i.e., the targets are annotated with a subscript t in the equations below. The normalizing values (50000, 1, 50, and 50) were chosen to be greater than the maximum values for each metric based initial simulations. These values effect the weighting of the individual metrics to the quality value and can be adjusted to emphasize one metric over the other; the current selection values recrystallization over average grain area by a factor of about 3:1.

$$\text{Microstructure Quality}\,(\mu S_Q) = 100 * \left(1 - \sqrt{\left(\frac{A_g - A_{gt}}{50000}\right)^2 + \left(\frac{X_V - X_{Vt}}{1}\right)^2}\right) \tag{5.7}$$

$$\text{JMAK Quality}\,(JMAK_Q) = 100 * \left(1 - \sqrt{\left(\frac{\ln K - \ln K_t}{50}\right)^2 + \left(\frac{n - n_t}{50}\right)^2}\right) \tag{5.8}$$

A non-linear, constrained optimization problem was set up using the two quality metrics and the parameter screening test laid out in Table 5.4. The optimization problem is presented in Equation (5.9). The design variables of the problem, $\bar{x}$, are the eight SPPARKS parameters discussed extensively so far in this chapter. The goal of the optimization problem is to maximize the fit between the simulation outputs with the experimental data. The problem is non-linear as there is no direct correlation between the choice of any specific parameter and the output metrics. SPPARKS is required to convert the constraints into the quality metrics.

Table 5.6: Equation (5.9) presents the non-linear, constrained optimization problem:

$$
\begin{aligned}
\underset{\bar{x}}{\text{maximize}} \quad & f(\mu S_Q, JMAK_Q) \\
\text{subject to} \quad & g_1(x) = T_B \in [0.2, 0.5], \\
& g_2(x) = dispersion_rate \in [0.3, 0.5], \\
& g_3(x) = propagated_E \in [0.3, 0.5], \\
& g_4(x) = multiplied_energy \in [1.0, 4.0], \\
& g_5(x) = add_dislocations \in [0.0, 3.0], \\
& g_6(x) = pin\ fraction \in [0.001, 0.004], \\
& g_7(x) = runs\ per\ loop \in [200, 800], \\
& g_8(x) = recovery \in [0.95, 0.98]
\end{aligned}
\tag{5.9}
$$

where $\bar{x} = [T_B, dispersion_rate, propagated_E, multiplied_E, add_dislocations, ...$
$pin\ fraction, runs\ per\ loop, recovery]$

5.3 SPPARKS Model Results

An initial screening test was conducted using the optimization problem described by Equation (5.9). The full-factorial design space, based on the parameters in Table 5.4, was implemented through the creation of 10,368 SPPARKS scripts using a custom-built Python script. Of these 10k+ scripts, a random sampling of 416 were batch processed with massive parallelization on a super-computing cluster. The results of the simulations were characterized using the Quality Metrics described by Equation 5.7 (p. 185) and Equation 5.8 (p. 185). For this initial screening, the optimization function was defined by a simple, linear combination of the two Quality Metrics, i.e.,

$$f(\mu S_Q, JMAK_Q) = \mu S_Q + JMAK_Q \tag{5.10}$$

Using this optimization function, Equation (5.10), the maximum value was found with a 93.7% match of the JMAK metric and a 55.8% of the microstructure metric. The parameters for this maximum value are provided in Table 5.7, along with the measurements and Quality Metrics in Table 5.8. The screening results from the 416 simulations are shown in Figure 5.7 and Figure 5.8. Each sub-figure contains the same Quality Metrics data points, but each data point has been color-coded using the given scale to represent one specific parameter. The x and y axes represent the Quality Metrics. A value of 100% on either axis represents a perfect match between the experimental and simulated microstructure. In addition to the optimized simulation, Table 5.7 also provides the parameters of the run with the highest recrystallized fraction, X_V, and the run that produced the largest average grain area, A_g. These runs of interest are indicated by arrows in Figure 5.7a.

Table 5.7: SPPARKS parameters from selected screening tests. The characterization of these runs is presented in Table 5.8.

Parameter	**Run 19**	**Run 301**	**Run 357**
1) kT_B **(J)**	0.5	0.4	0.5
2) dispersion_rate (%)	40	30	50
3) propagated_E (%)	50	40	40
4) multiplied_E	2	1	1
5) add_dislocations (J)	3	0	0
6) pin fraction (%)	1	1	1
7) runs per loop	200	800	800
8) recovery_loop (%)	95	95	98

Table 5.8: SPPARKS parameters from selected screening tests. Run 19 had the highest recrystallized fraction, X_V, of the screening test. Similarly, Run 301 maximized the optimization function, Equation (5.10), and Run 357 had the highest average grain area, A_g.

Parameter	**Run 19**	**Run 301**	**Run 357**
A_g, μm^2	2940	6970	**8030**
X_V, %	**99.0**	90.0	73.3
μS_Q, %	35.4	55.8	56.8
$\ln K$	-7.82	-1.48	0.64
n	6.40	6.92	10.3
$JMAK_Q$, %	84.0	93.7	87.5
$f(\mu S_Q, JMAK_Q)$	119.4	**149.5**	144.3

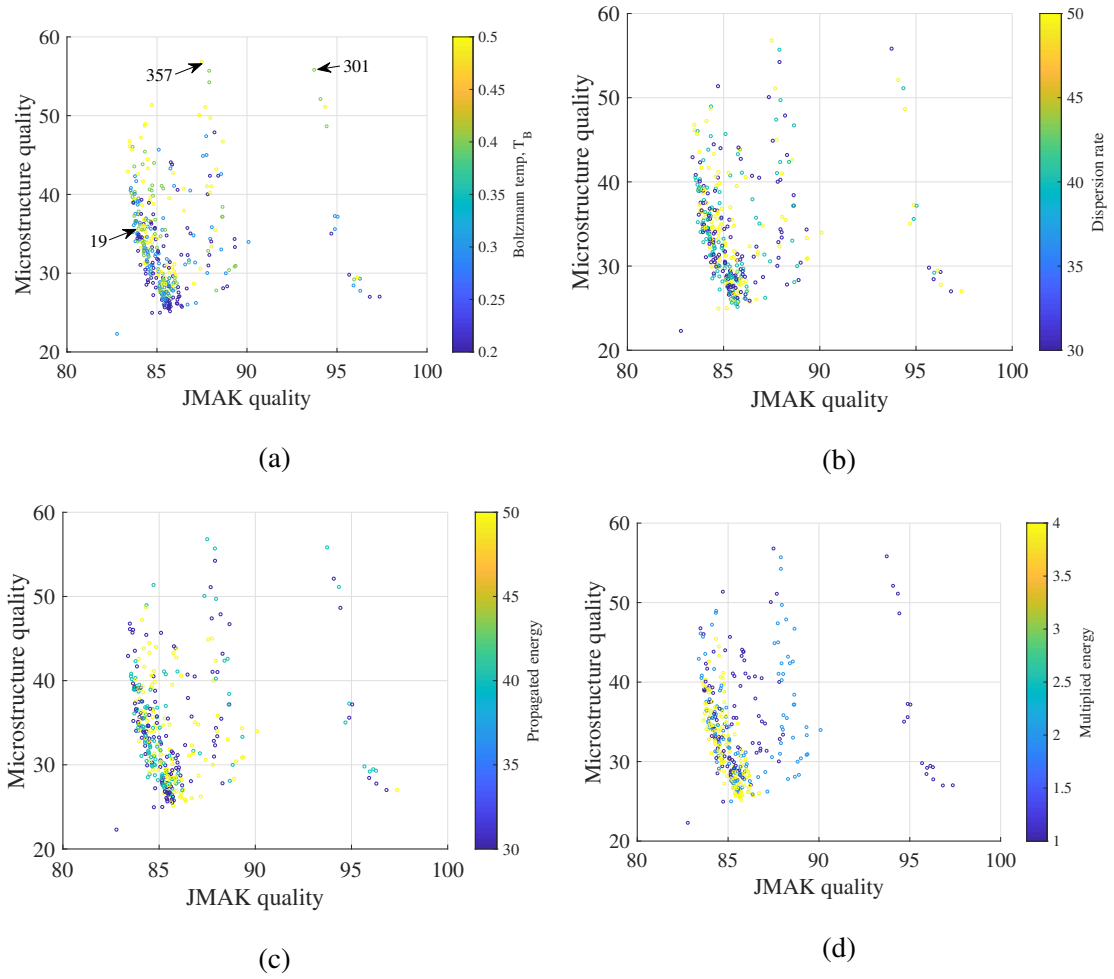

Figure 5.7: SPPARKS quality metrics (1 of 2) as a function of T_B, dispersion rate, propagated energy, and mulitplied energy. Each figure is color coded to represent the values of the parameters that produced each quality metric data point. The x- and y-axis represent the quality metrics. A value of 100 on either axis represents a perfect match between the experimental and simulated recrystallized microstructures. Figure 5.7a is marked with the locations of the three selected runs (19, 301, and 357) presented in Table 5.7 and Table 5.8.

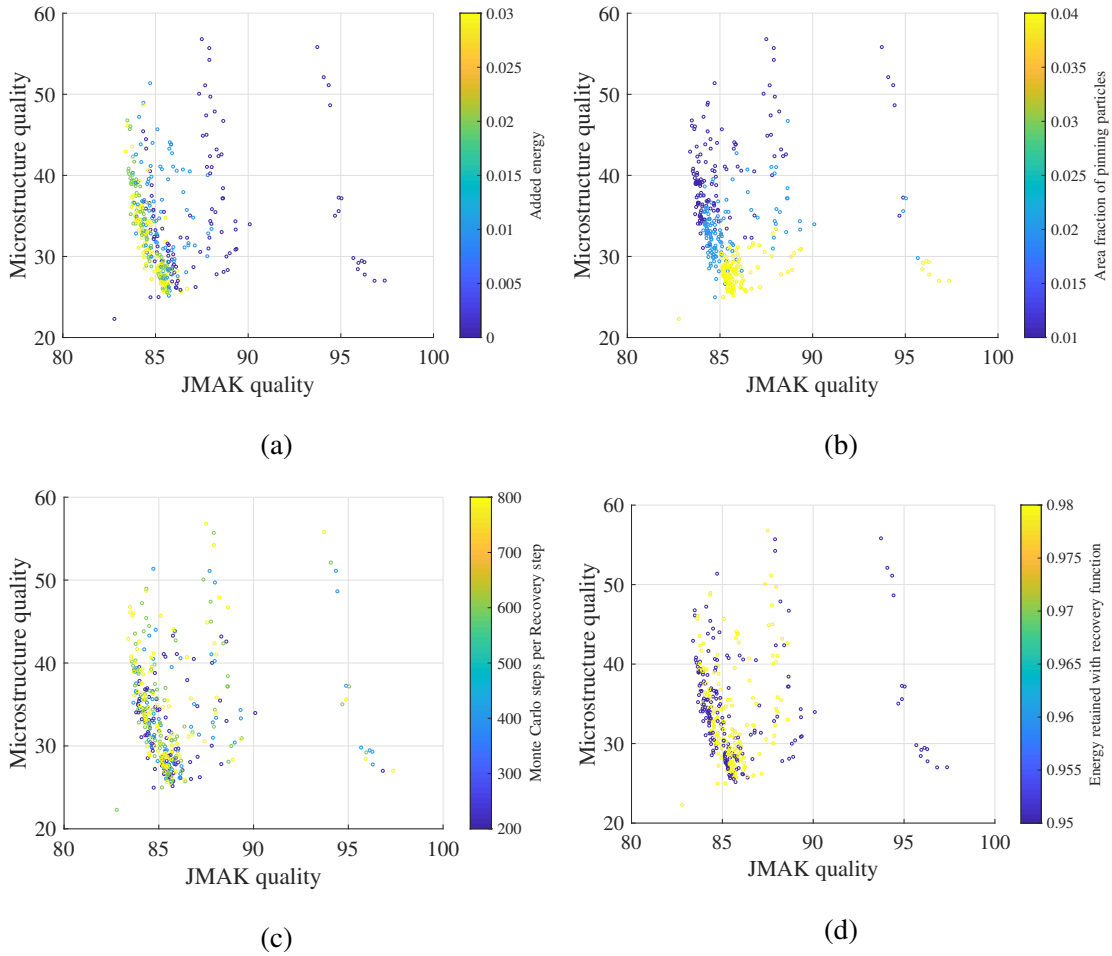

Figure 5.8: SPPARKS quality metrics (2 of 2) as a function of added energy, pin fraction, runs per recovery loop, and recovery fraction per loop. Each figure is color coded to represent the values of the parameters that produced each quality metric data point. The x- and y-axis represent the quality metrics. A value of 100 on either axis represents a perfect match between the experimental and simulated recrystallized microstructures.

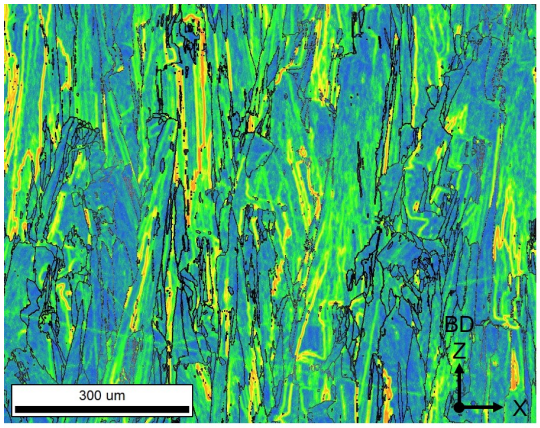

(a) Initial KAM map

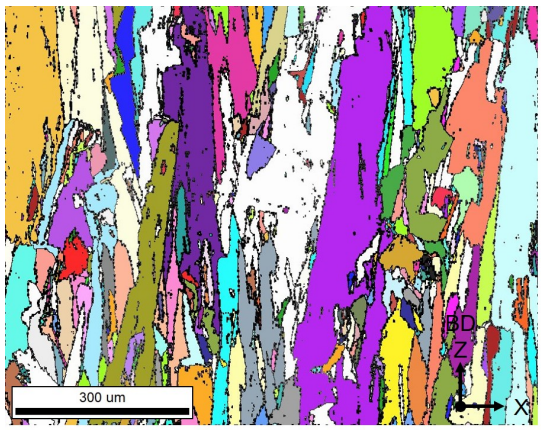

(b) Initial grain map with pinning particles added

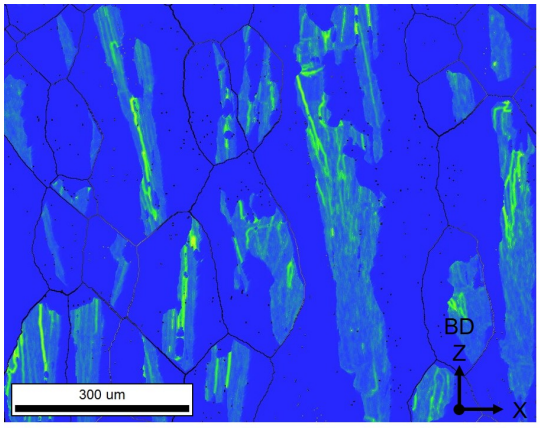

(c) Final KAM distribution, $X_V = 90.0\%$

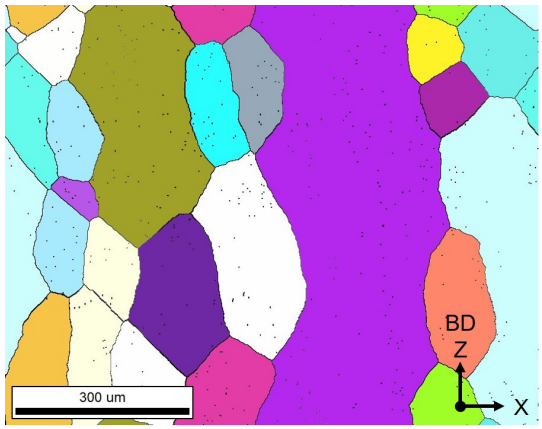

(d) Final grain structure, $A_g = 6970\ \mu m^2$

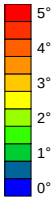

(e) Color scale for KAM maps

Figure 5.9: SPPARKS KAM and grain maps of the simulation input and output for the optimized parameter set. The simulation outputs, Figures 5.9c and 5.9d, are taken from Run 301, the parameter set that maximized the optimization problem described by Equation (5.9). The legend for the KAM maps is given in Figure 5.9e. The grain maps are colored to indicate unique grains. Grain boundaries and pins are shown in black.

5.4 SPPARKS Model Discussion

The results of the previous section indicate that SPPARKS is capable of handling the stored energy with boundary energy in calculating the recrystallization dynamics. In this research, the KAM metric was used as a qualitative representation of residual stresses in the LPBF IN718. The process of combining the boundary and stored energies is made easier owing to the relatively simple method by which the rKMC calculated the "energy" based on neighboring pixels. The functions added to SPPARKS were capable of modifying and manipulating the stored energy. This functionality should enable further research into the recrystallization behavior of LPBF IN718. It has been demonstrated that the stored energy is at a sufficient level to drive dynamic recrystallization in the LPBF IN718.

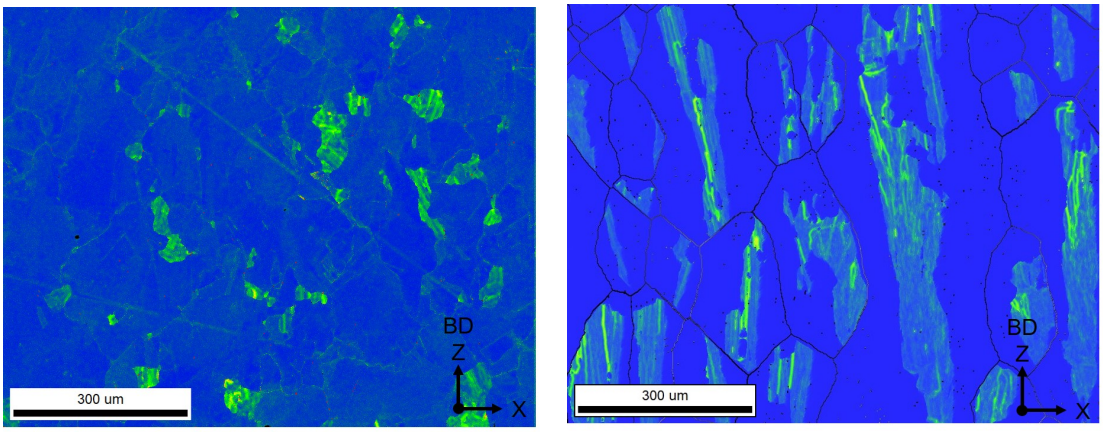

(a) 1160 °C/8 h anneal, X_V = 92.2%

(b) SPPARKS simulation, Run 301, X_V = 90.0%

Figure 5.10: Side-by-side comparison of an 1160 °C/8 h annealed specimen (Figure 5.10a) with the simulated SPPARKS KAM map from Run 301 (Figure 5.10b). Both figures feature large recrystallized areas with pockets of residual strains as indicated by the green and yellow areas. The EBSD map (a) displays several larger pockets whereas the SPPARKS output (b) shows a distribution of smaller pockets of stored energy. Figure 5.9e provides the KAM legend for these images.

Figure 5.10 compares the KAM data from a specimen annealed at 1160 °C/8 h (Figure 5.10a) with the optimized simulated results from the screening test (Figure 5.10b). From Chapter 3, recrystallized areas were defined as those with a KAM value below 1.2°. Therefore, it can be assumed that areas below this threshold in an annealed specimen have undergone recrystallization. Both KAM maps show large areas with a low KAM (< 1.2°) and pockets of areas with higher KAM values. Additionally, the unrecrystallized areas in the experimental specimen show localized concentrations of high KAM values. These same features are evident in the simulated data. Prior to the simulation results of this research, it had been hypothesized that residual strains may dissipate on their own when exposed to high annealing temperatures. This evidence shows that the residual strains do not dissipate on their own and require recrystallization to be fully removed.

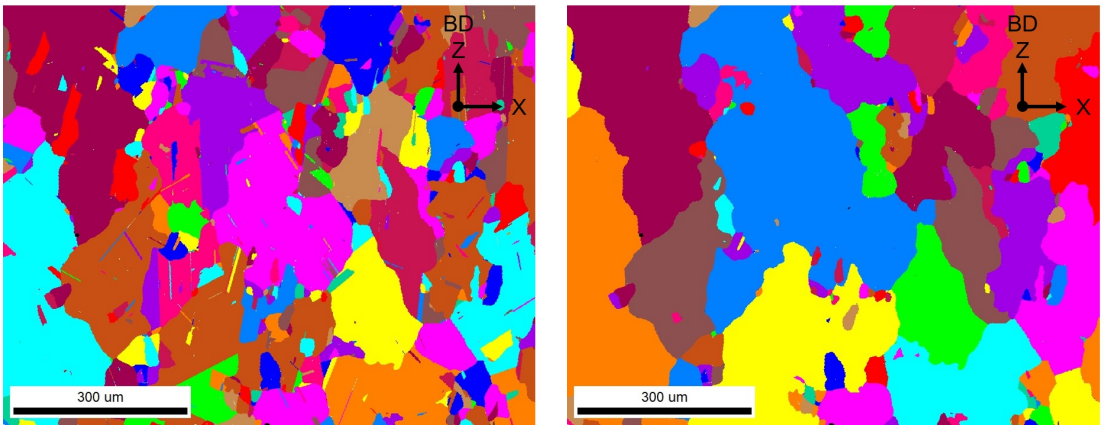

(a) Showing annealing twins (b) Annealing twins combined with parents

Figure 5.11: Appearance of annealing twins in annealed IN718 microstructure. Figure 5.11a shows the 1160 °C/8 h annealed microstructure with twins as separate grains. Combining the twins with their parents produces Figure 5.11b, greatly affecting the microstructural analysis (e.g., average grain size).

Figure 5.11 illustrates one challenge in modeling the annealed microstructure. In order to model twins, SPPARKS would require the specific misorientations between grains in the model. Figure 5.11a shows the unique grains in the 1160 °C/8 h annealed microstructure. If twins are combined with their parent grain, the result is Figure 5.11b. Note that due to the coloring scheme, similar grains in both images are not likely to remain the same color. For the purposes of the microstructural analysis in Chapter 3, twins were considered as individual grains. However, since SPPARKS cannot distinguish twins from parents with the data provided, the SPPARKS models will more closely resemble Figure 5.11b.

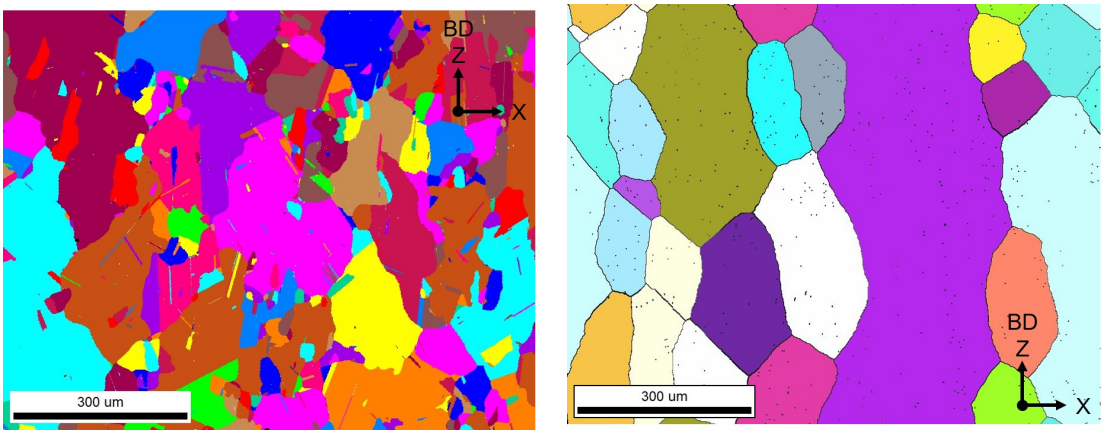

(a) 1160 °C/8 h anneal, $A_g = 15,790$ μm^2 (b) SPPARKS Run 301, $A_g = 6,970$ μm^2

Figure 5.12: Comparison of an 1160 °C/8 h annealed specimen and the SPPARKS unique grain maps. The average grain sizes are calculated while excluding edge grains. However, as the grains increase in size, a larger fraction of the grain map is excluded from this calculation. This also ends up excluding the largest grains, which are more likely to intersect a map boundary.

Figure 5.12 compares the grain structure between the experimental and simulated annealed specimens. When these grain maps are compared to Figure 5.9b (p. 191), it can be distinguished that most of the columnar grains have been removed. However, Figure 5.12b

still contains one dominant columnar grain and several more vertically elongated grains. The large purple grain present in the grain map has two specific issues worth discussing. The first is that it is excluded from the average grain values since it intercepts at least one edge of the grain map. Therefore the average grain area reported for this map is lower than it would initially appear. Second, SPPARKS was implemented with periodic boundary conditions. This allowed the progenitor grain in Figure 5.9b to effectively lock itself into place as its upper and lower ends effectively wrapped around the boundary of the map. Removing the periodic conditions would solve some of the issue of the grain locking, but it does not solve the issue of it being excluded from the analysis. While the resulting map shows that the columnar grains have been reduced, it may be possible to more finely control the optimization problem. One additional metric for consideration is the elongation of the grains. The columnar nature of the grains can be measured by the applying an ellipse to each grain and measuring the angle of its major axis. This angle, or rather its offset from vertical (90°), could be used as a metric in the fashion that average grain area and recrystallized area were used in this screening test. This would provide more precise monitoring of the transition from columnar to equaixed grains as demonstrated in the screening tests.

The average grain area found in best result from the screening test is only 44.1% of the experimental target (6970 μm^2 vs. 15790 μm^2). The largest grain area of the screening test was only found to be 50.8% of the experimental target (8030 μm^2 vs. 15790 μm^2). The main parameters limiting grain growth was the fraction of pinning particles. The pinning particles were removed entirely ($N = 0.000$), and the simulation produced idealized grain growth that did not resemble any of the experimentally annealed microstructures. The lowest pinning fraction in the screening test was 1%. For optimizing the parameters, it is recommended to use lower pinning fractions in the range of [0.1%,1.0%] to evaluate if larger grains can be achieved while still maintaining the presence of pinning particles.

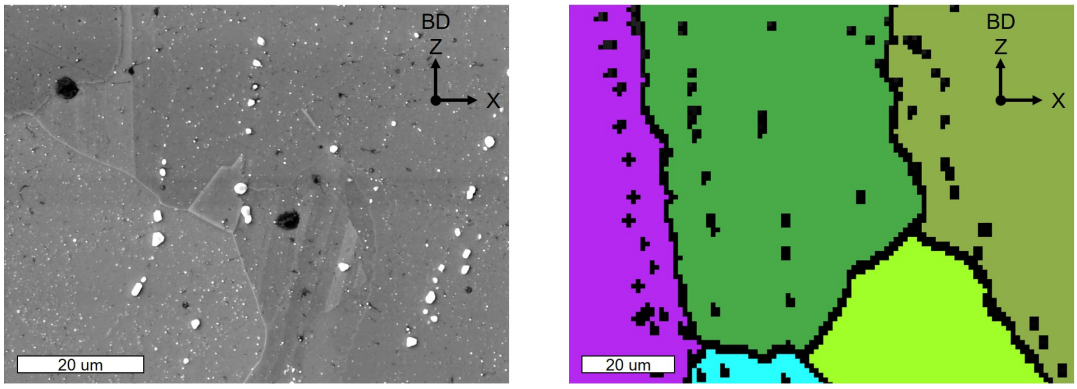

(a) Carbides in an annealed specimen

(b) Simulated carbides

Figure 5.13: Comparison of carbides in the annealed and simulated microstructures. Figure 5.13a presents the etched surface of a specimen annealed at 1160 °C/8 h. The carbides are visible as bright white spheroids and are arranged in necklaces tracing the original grain boundaries. Figure 5.13b was generated by a SPPARKS simulation. The carbides in SPPARKS are shown as black clusters. The same necklace formations from the annealed specimen are visible in the SPPARKS output.

Section 4.5 (p. 151) presented a hypothesis on the role of carbides in the creep behavior. Carbide "necklaces", identified by EDS analysis, were found in the 8-hr annealed specimens as seen in Figure 4.12b (p. 154) and Figure 5.13a. The results of the SPPARKS models recreated the formation of these carbide necklaces as illustrated in Figure 5.13b. The vertical alignment of the necklaces is clearly tied by the model to the grain structures of the as-built LPBF IN718 as the carbides are only initiated on grain boundaries. This is another example of physical phenomena successfully recreated by the SPPARKS model.

The quality metrics and optimization function in this section were presented as a simple implementation of the proposed optimization problem. A generalized expression of $f(\mu S_Q, JMAK_Q)$ could be defined using the measured quantities $A_g, X_V, \ln K, n$ instead of using the quality metrics defined in Equation (5.7) and Equation (5.8), and represented as $f(A_g, X_V, \ln K, n)$. The normalizing factors in the quality metric equations (50000, 1, 50, and 50) were originally chosen to be much larger than the values of their related metrics to avoid processing errors. However, based on the screening test it should be feasible to update these factors based on the target metrics for the optimization function. A proposed update to the quality metrics is given by Equation (5.11) and Equation (5.12). These new metrics would turn the optimization problem from a maximization problem into a minimization problem.

$$\text{Microstructure Quality}\,(\mu S_Q) = 100 * \sqrt{\left(\frac{A_g - A_{gt}}{A_{gt}}\right)^2 + \left(\frac{X_V - X_{Vt}}{X_{Vt}}\right)^2} \tag{5.11}$$

$$\text{JMAK Quality}\,(JMAK_Q) = 100 * \sqrt{\left(\frac{\ln K - \ln K_t}{\ln K_t}\right)^2 + \left(\frac{n - n_t}{n_t}\right)^2} \tag{5.12}$$

Additionally, the choice of metrics extends far beyond the four values chosen in this screening test, and could be tailored to specific properties of interest by future researchers. Further work to refine the choice of quality metrics and the optimization function would be a valuable topic of future research. The screening test presented here is also only a fraction of the optimization problem. The optimization could be carried out by running

and analyzing a larger fraction of the 10,000+ scripts generated in the full-factorial design space. Additionally, the results of the screening test and subsequent optimization steps can be used to refine the range and discretization of parameters.

Lastly, the process that has been presented sets the path for follow-on research into the optimization of the combined stored & boundary energy SPPARKS model. The tools provided by AFRL/RXCM as part of this research will give additional insights into the recrystallization of LPBF IN718. At the same time, the experimental data collected as part of Chapter 3 drove the development of the stored-energy SPPARKS model. The experimental data helped to validate or rule out various assumptions made as part of converting a non-linear thermodynamic problem into a stochastic model.

5.5 Conclusion

This research demonstrated that stored energy could be implemented in SPPARKS in conjunction with boundary energy to drive recrystallization. The SPPARKS model made it possible to connect the various parameters to the experimental annealing microstructures. The functionality provided by the new SPPARKS implementation should enable further research into the recrystallization behavior of LPBF IN718. One major take-away from these results is that it appears that the stored energy is at a sufficient level to drive dynamic recrystallization in the LPBF IN718. The model was also able to validate several physical phenomena discussed in the previous chapters, such as the transition from columnar to equiaxed grains and the presence of NbC carbide "necklaces."

This chapter addressed the research objective described by Problem Statement 4: previous mesoscale simulations of LPBF IN718 did not account for residual stresses in the as-built material. The results of the modeling analysis indicate that SPPARKS is capable of coupling stored energy with boundary energy to calculate the recrystallization dynamics in LPBF IN718. The experimental EBSD data collected in Chapter 3 was used to calibrate a novel implementation of annealing within SPPARKS. A parameter screening

was conducted, resulting in the SPPARKS simulation matching the target parameters of recrystallized fraction X_V and the JMAK constants, n and $\ln K$ to within 90% or better. As an initial investigation, this has proven that it is possible to incorporate energy-driven recrystallization within SPPARKS. A_g was not successfully matched, with the best models achieving only 50% of the target. This implementation of SPPARKS is the first demonstrated application of the energy-driven recrystallization and grain growth in conjunction with the curvature-driven.

This page intentionally left blank.

VI. Conclusions and Recommendations

The major objectives of this research into laser powder-bed fusion (LPBF) Inconel 718 (IN718) were to: identify a solution treatment that would drive recrystallization, examine the microstructural changes, compare the microstructure to conventional heat treatments, test the mechanical properties, and develop a model to simulate the microstructural evolution. These objectives were successfully reached through the microstructural analysis, mechanical testing, and Kinetic Monte Carlo (KMC) simulations covered in this dissertation. The following sections address each stage of research with relationship to the corresponding Problem Statements and Hypothesis proposed in Section 1.3 and identify which hypotheses were verified through the research and analysis performed in this dissertation. This chapter concludes with a recommendation for the use of the modified solution treatment proposed in this dissertation.

6.1 Microstructural Summary and Contributions

The microstructural analysis in Chapter 3 addressed the research objectives described by **Problem Statements 1, 2, & 3**. **Problem Statement 1** identified the need to achieve recrystallization and grain growth in order to mitigate the columnar grains, strong (001) texture, and resulting anisotropy found in LPBF IN718. Two hypotheses were proposed under **Problem Statement 1**. **Hypothesis 1.A** proposed that an annealing temperature that could dissolve delta (δ) and Laves phase would allow the grains to recrystallize and remove the LPBF process-induced columnar grains. **Hypothesis 1.B** proposed the recrystallization and grain growth that removed the columnar grains would reduce the anisotropy in the LPBF IN718 specimens. The objectives of **Problem Statement 1** were achieved by applying the modified solution temperature of 1160 °C to specimens for durations ranging from 1–8 h. The resulting microstructures were characterized using

electron backscatter diffraction (EBSD) and compared to the microstructure of specimens in the as-built and conventional heat treatment (CHT) (1010 °C/1 h) conditions. The modified heat treatment (MHT) was successful in eliminating the columnar microstructure by increasing recrystallization, resulting in an isotropic microstructure with equiaxed grains at 1160 °C/4 h and verifying **Hypothesis 1.A**. By comparison, the CHT specimens retained the columnar grains from the as-built structure. Additionally, the recrystallized fraction was calculated using the grain orientation spread (GOS) metric to evaluate the annealing kinetics. The recrystallization behavior was an important input to the rejection Kinetic Monte Carlo (rKMC) effort in Chapter 5. Hardness and tension testing confirmed the equiaxed microstructure reduced the anisotropy of material properties, verifying **Hypothesis 1.B**.

Problem Statement 2 highlighted that different manufacturers use various scan strategies to fabricate LPBF parts which create small variations in the microstructure of the as-built parts. **Hypothesis 2** proposed that the scan strategy differences could be eliminated if the modified solution treatment caused sufficient recrystallization and grain growth. Specimens were fabricated using three different scan strategies then annealed using the modified solution treatment for 1–8 h to accomplish the objective for **Problem Statement 2**. The microstructural differences in grain size and texture intensity between the scan strategies were found to be negligible as the result of the MHT, verifying **Hypothesis 2**.

Problem Statement 3 recognized the relationship between grain size and mechanical properties. **Hypothesis 3** proposed that shorter annealing times would produce smaller grains and a corresponding increase in tensile strength. This objective was assessed through hardness and tension tests of specimens fabricated in multiple orientations and annealed for various durations. The results revealed a decrease in tensile strength correlated with an increase in average grain size, thereby verifying this portion of **Hypothesis 3**. **Problem Statement 3** was addressed further in Chapter 4.

1. Identified 1160 °C as a suitable non-hot isostatic pressing (HIP) solution treatment to achieve recrystallization of LPBF IN718.
2. Published the first characterization and analysis of the LPBF IN718 microstructure resulting from the MHT solution treatment (1160 °C) for annealing times ranging from 1–8 hours [86].
3. First equiaxed grains obtained in LPBF IN718 through a solution treatment [86].
4. Documented the reduction in texture caused by the recrystallization of the MHT [86].
5. Identified differences in the microstructure created by suitable scan strategies can be mitigated through the application of the modified solution treatment [86].
6. First characterization of the recrystallization behavior of the supersolvus annealing process for LPBF IN718 [86].
7. Compared hardness and tensile properties between MHT and CHT revealing an increased isotropy and reduced strength as a result of the MHT [86].

6.2 Mechanical Summary and Contributions

The mechanical testing in Chapter 4 addressed the research objective described by **Problem Statement 3**. **Problem Statement 3** recognized the relationship between grain size and mechanical properties and changing the grain properties via solution treatments would change the mechanical performance. Tension testing was performed in Chapter 3 and confirmed the relationship between grain size and tensile performance proposed by **Hypothesis 3**. Chapter 4 conducted additional tension and creep-rupture testing. The changes in the grain size caused by modifying the solution treatment resulted in a change in mechanical properties as demonstrated through hardness, tension, and creep-rupture testing. **Hypothesis 3** was verified regarding grain size and tensile strength, but was not found to be true regarding creep performance. MHT reduced the tensile anisotropy, but lowered the ultimate tensile strength (UTS) and 0.2% yield strength ($YS_{0.2}$) strengths. The hardness and tensile testing revealed the MHT reduced the anisotropy of the $YS_{0.2}$ by 10%

and UTS by 4–6%. However, the overall $YS_{0.2}$ and UTS were also reduced by 14.5% and 20.7%, respectively. New Hall-Petch constants were generated from the tensile results to account for the gamma double-prime (γ'') hardening in IN718. The creep-rupture results indicated the columnar nature of the grains provided a stronger effect than the average grain size. The loss of the columnar structure due to the MHT results in a reduction in the rupture life by 47.5% for vertically-oriented specimens. However, the rupture life did not decrease for the horizontal specimens, in spite of the equiaxed grain structure analyzed in Chapter 3. This difference between the two orientations yields a new hypothesis on the role of carbide (NbC) coarsening leading to an increase in the rupture life of horizontally printed specimens.

1. Conducted tensile testing and compared specimens fabricated in horizontal, diagonal, and vertical orientations and treated with CHT and MHT. Results showed the horizontal and diagonal specimens were stronger than the vertical.
2. Measured 10–15% anisotropy for CHT between the orientations. MHT reduced the anisotropy to 3–5%, but also reduced the overall tensile strength 10%.
3. Proposed new Hall-Petch constants for γ'' hardening in place of existing gamma prime (γ') values:

   σ_0 = 800 MPa

   k_y = 1.5 MPa·$m^{1/2}$
4. Performed creep-rupture testing which revealed that the isotropic MHT microstructure did not improve the creep resistance. By contrast, the large reduction in creep life of the vertical MHT specimens indicates how vertical, columnar grains contribute to the creep resistance.
5. Performed the first creep tests on MHT horizontal specimens and revealed a new role of carbide coarsening in increasing creep resistance.

6.3 Modeling Summary and Contributions

The rKMC modeling efforts in Chapter 5 addressed the research objective described by **Problem Statement 4**. **Problem Statement 4** noted that prior mesoscale simulations of LPBF IN718 did not account for the residual stresses within the as-built material. **Hypothesis 4** proposed an implementation of rKMC models within Stochastic Parallel PARticle Kinetic Simulator (SPPARKS) incorporating residual stresses from EBSD data and calibrated using the experimental data gathered in Chapter 3. A parameter screening and optimization were conducted, resulting in the SPPARKS simulation matching the target parameters of recrystallized fraction X_V, and the Johnson-Mehl-Avrami-Kolmogorov (JMAK) constants n and $\ln K$, to within 90% and verifying **Hypothesis 4**. The model was not as successful in matching the average grain size, but still managed a 55% match. This implementation of SPPARKS was the first demonstrated application of the energy-driven recrystallization and grain growth in conjunction with the curvature-driven model. The addition of pinning particles was also modelled and compared to the NbC "necklaces" seen in Figure 4.12b (p. 154) that resulted from the higher solution temperature of 1160 °C/8 h.

1. First use of energy-driven recrystallization in a KMC annealing simulation.
2. Used the experimental EBSD data gathered in this research to calibrate the novel SPPARKS implementation of energy-driven recrystallization.
3. Combined the energy-driven and curvature-driven recrystallization with carbide pinning in an end-to-end simulation of the recrystallization and grain growth of LPBF IN718.
4. Successfully simulated the transition from the as-built LPBF columnar grains to the equiaxed recrystallized structure.
5. Successfully simulated the NbC "necklaces" as they appeared in the annealed microstructure.

6.4 Recommendations

The modified solution treatment of 1160 °C/4 h is suitable to achieve an isotropic grain structure. It should be used in conjunction with the aging treatment per AMS 5663 for tensile applications where isotropy is a primary concern [113]. If overall strength is the main engineering requirement, and the build orientation can be controlled, it is recommended to use the CHT of 1010 °C/1 h. The choice of scan strategy is not significant to the overall mechanical properties and can generally be chosen from the manufacturer's recommended settings. The use of the MHT is not recommended for vertically-oriented specimens. The creep behavior of MHT horizontal specimens warrants additional research to evaluate the effect of the carbide formations on creep resistance.

Bibliography

[1] Akram, J., Chalavadi, P., Pal, D., and Stucker, B. (2018). Understanding grain evolution in additive manufacturing through modeling. *Additive Manufacturing*, 21:255–268.

[2] Alcisto, J., Enriquez, A., Garcia, H., Hinkson, S., Steelman, T., Silverman, E., Valdovino, P., Gigerenzer, H., Foyos, J., Ogren, J., Dorey, J., Karg, K., McDonald, T., and Es-Said, O. S. (2011). Tensile Properties and Microstructures of Laser-Formed Ti-6Al-4V. *Journal of Materials Engineering and Performance*, 20(2):203–212.

[3] Amato, K., Gaytan, S., Murr, L., Martinez, E., Shindo, P., Hernandez, J., Collins, S., and Medina, F. (2012). Microstructures and mechanical behavior of Inconel 718 fabricated by selective laser melting. *Acta Materialia*, 60(5):2229–2239.

[4] Arcam AB (2009). Arcam A1: The future in implant manufacturing.

[5] Arcam AB (2011). EBM hardware.

[6] Arcam AB (2018). History - Arcam AB.

[7] ASTM International (2009). ASTM E8/E8M-16: Standard Test Methods for Tension Testing of Metallic Materials. In *Annual Book of ASTM Standards*, volume 03.01, pages 1–27. ASTM International.

[8] ASTM International (2011). ASTM E139-11 Standard Test Methods for Elevated Temperature Tension Tests of Metallic Materials. *Annual Book of ASTM Standards*, i:1–14.

[9] ASTM International (2014). ASTM F3055-14a: Standard Specification for Additive Manufacturing Nickel Alloy (UNS N07718) with Powder Bed Fusion. *Annual Book of ASTM Standards*, pages 1–8.

[10] ASTM International (2016). ASTM B637-16: Standard Specification for Precipitation-Hardening and Cold Worked Nickel Alloy Bars, Forgings, and Forging Stock for Moderate or High Temperature Service. *Annual Book of ASTM Standards*, pages 1–7.

[11] ASTM International (2018). ASTM F3301-18: Standard for Additive Manufacturing Post Processing Methods Standard Specification for Thermal Post-Processing Metal Parts Made Via Powder Bed Fusion.

[12] Avrami, M. (1939). Kinetics of Phase Change. I General Theory. *The Journal of Chemical Physics*, 7(12):1103–1112.

[13] Aydinöz, M., Brenne, F., Schaper, M., Schaak, C., Tillmann, W., Nellesen, J., and Niendorf, T. (2016). On the microstructural and mechanical properties of post-treated additively manufactured Inconel 718 superalloy under quasi-static and cyclic loading. *Materials Science and Engineering: A*, 669:246–258.

[14] Barker, J. (1989). The Initial Years of Alloy 718: A GE Perspective. In *Superalloys 718 Metallurgy and Applications (1989)*, pages 269–277. TMS.

[15] Boesch, W. J. and Canada, H. B. (1969). Precipitation Reactions and Stability of Ni_3Nb in Inconel Alloy 718. *J. Metals*, J. Metals.

[16] Brooks, J. and Bridges, P. (1988). Metallurgical Stability of Inconel Alloy 718. In *Superalloys 1988 (Sixth International Symposium)*, pages 33–42. TMS.

[17] Cao, W., Kennedy, R., and Willis, M. (1991). Differential Thermal Analysis (DTA) Study of the Homogenization Process in Alloy 718. In *Superalloys 718, 625 and Various Derivatives (1991)*, pages 147–160. TMS.

[18] Cao, Y., Di, H., Zhang, J., Zhang, J., Ma, T., and Misra, R. (2013). An electron backscattered diffraction study on the dynamic recrystallization behavior of a nickelchromium alloy (800H) during hot deformation. *Materials Science and Engineering: A*, 585:71–85.

[19] Carlson, R. and Radavich, J. (1989). Microstructural Characterization of Cast 718. In *Superalloys 718 Metallurgy and Applications (1989)*, pages 79–95. TMS.

[20] Carter, L. N., Attallah, M. M., and Reed, R. C. (2012). Laser Powder Bed Fabrication of Nickel-Base Superalloys: Influence of Parameters; Characterisation, Quantification and Mitigation of Cracking. *Superalloys 2012*.

[21] Carter, L. N., Martin, C., Withers, P. J., and Attallah, M. M. (2014). The influence of the laser scan strategy on grain structure and cracking behaviour in SLM powder-bed fabricated nickel superalloy. *Journal of Alloys and Compounds*, 615:338–347.

[22] Chaturvedi, M. C. and Han, Y. (1987). Effect of particle size on the creep rate of superalloy Inconel 718. *Materials Science and Engineering*, 89(C):L7–L10.

[23] Chlebus, E., Gruber, K., Kuźnicka, B., Kurzac, J., and Kurzynowski, T. (2015). Effect of heat treatment on the microstructure and mechanical properties of Inconel 718 processed by selective laser melting. *Materials Science and Engineering A*, 639:647–655.

[24] Chung, K. H., Rodriguez, R., Lavernia, E. J., and Lee, J. (2002). Grain growth behavior of cryomilled INCONEL 625 powder during isothermal heat treatment. *Metallurgical and Materials Transactions A*, 33(1):125–134.

[25] Clarivate Analytics (2018). Journal Citation Reports. Technical report, Clarivate Analytics.

[26] Cloots, M., Kunze, K., Uggowitzer, P. J., and Wegener, K. (2016). Microstructural characteristics of the nickel-based alloy IN738LC and the cobalt-based alloy Mar-M509 produced by selective laser melting. *Materials Science and Engineering A*, 658:68–76.

[27] ConceptLaser (2016). M2 cusing: Metal laser melting system.

[28] CustomPartNet (2008). DMLS - Direct Metal Laser Sintering.

[29] Daines, G. (2015). NASA Media Usage Guidelines.

[30] Deckard, C. R. (1986). *Part generation by layer-wise selective laser sintering*. PhD thesis, University of Texas at Austin.

[31] Dehoff, R. R., Kirka, M. M., Sames, W. J., Bilheux, H., Tremsin, A. S., Lowe, L. E., and Babu, S. S. (2015). Site specific control of crystallographic grain orientation through electron beam additive manufacturing. *Materials Science and Technology*, 31(8):931–938.

[32] Deng, D., Moverare, J., Peng, R. L., and Söderberg, H. (2017). Microstructure and anisotropic mechanical properties of EBM manufactured Inconel 718 and effects of post heat treatments. *Materials Science and Engineering: A*, 693:151–163.

[33] Doherty, R. D., Srolovitz, D. J., Rollett, A. D., and Anderson, M. P. (1987). On the volume fraction dependence of particle limited grain growth. *Scripta Metallurgica*, 21(5):675–679.

[34] Donachie, M. J. and Donachie, S. J. (2002). *Superalloys : A Technical Guide*. ASM International.

[35] Eiselstein, H. L. (1965). Metallurgy of a Columbium-Hardened Nickel-Chromium-Iron Alloy. In *Advances in the Technology of Stainless Steels and Related Alloys*, volume 369, pages 62–62. ASTM International, 100 Barr Harbor Drive, PO Box C700, West Conshohocken, PA 19428-2959.

[36] Eiselstein, H. L. and Tillack, D. J. (1991). The Invention and Definition of Alloy 625. In *Superalloys 718, 625 and Various Derivatives (1991)*, pages 1–14. TMS.

[37] Ellis-Monaghan, J. (2006). A gentle introduction to the Potts Model.

[38] Elsevier (2019). Materials Science and Engineering: A.

[39] Everton, S. K., Hirsch, M., Stravroulakis, P., Leach, R. K., and Clare, A. T. (2016). Review of in-situ process monitoring and in-situ metrology for metal additive manufacturing. *Materials and Design*, 95:431–445.

[40] FAA (1975). Accident Overview of National Airlines Flight 27.

[41] Farber, B., Small, K. A., Allen, C., Causton, R. J., Nichols, A., Simbolick, J., and Taheri, M. L. (2018). Correlation of mechanical properties to microstructure in Metal Laser Sintering Inconel 718. *Materials Science and Engineering A*, 712:539–547.

[42] Field, D., Bradford, L., Nowell, M., and Lillo, T. (2007). The role of annealing twins during recrystallization of Cu. *Acta Materialia*, 55(12):4233–4241.

[43] Garcia Cardona, C., Webb, Edmund Blackburn, I., Wagner, G. J., Tikare, V., Holm, E. A., Plimpton, S. J., Thompson, A. P., Slepoy, A., Zhou, X. W., Battaile, C. C., and Chandross, M. E. (2009). Crossing the mesoscale no-mans land via parallel kinetic Monte Carlo. Technical report, Sandia National Laboratories (SNL), Albuquerque, NM, and Livermore, CA (United States).

[44] Gong, H., Christiansen, D., Beuth, J., and Lewandowski, J. J. (2014). Melt Pool Characterization for Selective Laser Melting of Ti-6Al-4V Pre-alloyed Powder. *Solid Freeform Fabrication Symposium*, pages 256–267.

[45] Hall, E. O. (1951). The Deformation and Ageing of Mild Steel: III Discussion of Results. *Proceedings of the Physical Society. Section B*, 64(9):747–753.

[46] Hansen, N. (2004). Hall-Petch relation and boundary strengthening. *Scripta Materialia*, 51(8):801–806.

[47] Herring, C. (1950). Diffusional Viscosity of a Polycrystalline Solid. *Journal of Applied Physics*, 21(5):437–445.

[48] Hillert, M. (1965). On the theory of normal and abnormal grain growth. *Acta Metallurgica*, 13(3):227–238.

[49] Howe, J. M. (1997). *Interfaces in materials : atomic structure, thermodynamics and kinetics of solid-vapor, solid-liquid and solid-solid interfaces*. Wiley.

[50] Humphreys, J., Rohrer, G. S., and Rollett, A. D. (2017). *Recrystallization and Related Annealing Phenomena*. Elsevier, 3rd edition.

[51] ISO (2015). ISO 14577 - Metallic materials – Instrumented indentation test for hardness and materials parameters. Technical report, ISO.

[52] ISO and ASTM International (2015). ISO/ASTM 52900-15(E): Standard Terminology for Additive manufacturing General principles Terminology. *Annual Book of ASTM Standards*, pages 1–26.

[53] Jacobs, P. and Reid, D. (1992). Rapid prototyping, and manufacturing: fundamentals of stereolithography. *Society of Manufacturing Engineers*.

[54] Jiang, R., Mostafaei, A., Pauza, J., Kantzos, C., and Rollett, A. D. (2019). Varied heat treatments and properties of laser powder bed printed Inconel 718. *Materials Science and Engineering: A*.

[55] Johnson, W. and Mehl, K. (1939). Reaction Kinetics in Processes of Nucleation and Growth. *Transactions of the American Institute of Mining, Metallurgical and Petroleum Engineers*, 135:416–458.

[56] Kassner, M. E. (2015). Creep Fracture. In Kassner, M. E., editor, *Fundamentals of Creep in Metals and Alloys: Third Edition*, pages 233–260. Elsevier Ltd, third edit edition.

[57] Kassner, M. E. and Kassner, M. E. (2015). Fundamentals of Creep in Materials. In Kassner, M. E., editor, *Fundamentals of Creep in Metals and Alloys: Third Edition*, volume 1, pages 1–6. Elsevier.

[58] Kirka, M. M., Greeley, D., Hawkins, C., and Dehoff, R. (2017a). Effect of anisotropy and texture on the low cycle fatigue behavior of Inconel 718 processed via electron beam melting. *International Journal of Fatigue*, 105:235–243.

[59] Kirka, M. M., Medina, F., Dehoff, R., and Okello, A. (2017b). Mechanical behavior of post-processed Inconel 718 manufactured through the electron beam melting process. *Materials Science and Engineering: A*, 680:338–346.

[60] Kirka, M. M., Plotkowski, A., Nandwana, P., Chaudhary, A., Babu, S. S., and Dehoff, R. R. (2018). Progress in the Processing and Understanding of Alloy 718 Fabricated Through Powder Bed Additive Manufacturing Processes. In Ott, E., editor, *Proceedings of the 9th International Symposium on Superalloy 718 & Derivatives: Energy, Aerospace, and Industrial Applications*, pages 69–88. Springer, Cham.

[61] Knorovsky, G. A., Cieslak, M. J., Headley, T. J., Romig, A. D., and Hammetter, W. F. (1989). INCONEL 718: A solidification diagram. *Metallurgical Transactions A*, 20(10):2149–2158.

[62] Ko, L. C. L. (2014). *Particle Stimulated Nucleation: Deformation around Particles*. PhD thesis, University of Manchester.

[63] Kolmogorov, A. N. (1937). On the Statistical Theory of the Crystallization of Metals. *Bulletin of the Academy of Sciences of the USSR, Mathematics Series*, 1:355–359.

[64] Körner, C., Attar, E., and Heinl, P. (2011). Mesoscopic simulation of selective beam melting processes. *Journal of Materials Processing Technology*, 211(6):978–987.

[65] Kunze, K., Etter, T., Grässlin, J., and Shklover, V. (2014). Texture, anisotropy in microstructure and mechanical properties of IN738LC alloy processed by selective laser melting (SLM). *Materials Science and Engineering A*, 620:213–222.

[66] Kuo, Y.-L., Horikawa, S., and Kakehi, K. (2017a). Effects of build direction and heat treatment on creep properties of Ni-base superalloy built up by additive manufacturing. *Scripta Materialia*, 129:74–78.

[67] Kuo, Y.-L., Horikawa, S., and Kakehi, K. (2017b). The effect of interdendritic δ phase on the mechanical properties of Alloy 718 built up by additive manufacturing. *Materials and Design*, 116:411–418.

[68] Kuo, Y.-L., Nagahari, T., Kakehi, K., Kuo, Y.-L., Nagahari, T., and Kakehi, K. (2018). The Effect of Post-Processes on the Microstructure and Creep Properties of Alloy718 Built Up by Selective Laser Melting. *Materials*, 11(6):996.

[69] Lingenfelter, A. (1989). Welding of Inconel Alloy 718: A Historical Overview. *Superalloys 718 Metallurgy and Applications (1989)*, pages 673–683.

[70] Liu, C., Han, Y., Yan, M., and Chaturvedi, M. (1991). Creep Crack Growth Behaviour of Alloy 718. In *Superalloys 718, 625 and Various Derivatives (1991)*, pages 537–548. TMS.

[71] Liu, F., Lin, X., Huang, C., Song, M., Yang, G., Chen, J., and Huang, W. (2011). The effect of laser scanning path on microstructures and mechanical properties of laser solid formed nickel-base superalloy Inconel 718. *Journal of Alloys and Compounds*, 509(13):4505–4509.

[72] Liu, M., Zheng, W.-j., Xiang, J.-z., Song, Z.-g., Pu, E.-x., and Feng, H. (2016). Grain Growth Behavior of Inconel 625 Superalloy. *Journal of Iron and Steel Research International*, 23(10):1111–1118.

[73] Liu, W., Xiao, F., Yao, M., Chen, Z., Jiang, Z., and Wang, S. (1997). Relationship between the lattice constant of phase and the content of δ phase, γ and γ phases in inconel 718. *Scripta Materialia*, 37(1):59–64.

[74] Liu, Z. and Qi, H. (2015). Effects of processing parameters on crystal growth and microstructure formation in laser powder deposition of single-crystal superalloy. *Journal of Materials Processing Technology*, 216:19–27.

[75] Lou, A. and Grosvenor, C. (2012). Selective Laser Sintering , Birth of an Industry. *the University of Texas at Austin, Department of Mechanical Engineering 100 Years*, pages 1–19.

[76] Lu, Y., Wu, S., Gan, Y., Huang, T., Yang, C., Junjie, L., and Lin, J. (2015). Study on the microstructure, mechanical property and residual stress of SLM Inconel-718 alloy manufactured by differing island scanning strategy. *Optics & Laser Technology*, 75(December):197–206.

[77] MATLAB (2006). Vector creation, array subscripting, and for-loop iteration - MATLAB colon :.

[78] Meier, C., Penny, R. W., Zou, Y., Gibbs, J. S., and Hart, A. J. (2018). Thermophysical Phenomena in Metal Additive Manufacturing by Selective Laser Melting: Fundamentals, Modeling, Simulation and Experimentation. *Annual Review of Heat Transfer*, pages 241–316.

[79] Metropolis, N. and Ulam, S. (1949). The Monte Carlo Method. *Journal of the American Statistical Association*, 44(247):335–341.

[80] Michel, D. J. and Smith, H. H. (1989). Mechanical Properties and Microstructure of Fine Grain, Centrifugally Cast Alloy 718. In *Superalloys 718 Metallurgy and Applications (1989)*, volume 16, pages 533–544. TMS.

[81] Mindt, H.-W., Megahed, M., Shula, B., Peralta, A. D., Neumann, J., and Introduction, I. (2016). Powder Bed Models Numercial Assessment of As-Built Quality. In *57th AIAA/ASCE/AHS/ASC Structures, Structural Dynamics, and Materials Conference*, San Diego. AIAA.

[82] Mostafa, A., Picazo Rubio, I., Brailovski, V., Jahazi, M., and Medraj, M. (2017). Structure, Texture and Phases in 3D Printed IN718 Alloy Subjected to Homogenization and HIP Treatments. *Metals*, 7(6):196.

[83] Muñoz-Moreno, R., Divya, V. D., Driver, S. L., Messé, O., Illston, T., Baker, S., Carpenter, M. A., and Stone, H. J. (2016). Effect of heat treatment on the microstructure, texture and elastic anisotropy of the nickel-based superalloy CM247LC processed by selective laser melting. *Materials Science and Engineering: A*, 674:529–539.

[84] NASA (1972). Inconel Alloy 718. In Muraca, R. F. and Whittick, J. S., editors, *Materials Data Handbook*. NASA, San Carlos, California, 2nd editio edition.

[85] NASA (2016). NASA Experimental Aircraft: North American Aviation XB-70 Valkyrie.

[86] Newell, D. J., O'Hara, R. P., Cobb, G. R., Palazotto, A. N., Kirka, M. M., Burggraf, L. W., and Hess, J. A. (2019). Mitigation of Scan Strategy Effects and Material Anisotropy Through Supersolvus Annealing in LPBF IN718. *Materials Science and Engineering A*, 764:138230.

[87] Ning, Y. (2005). Process Parameter Optimization for Direct Metal Laser Sintering (DMLS). *PHD Thesis*, page 167.

[88] Oblak, J. M., Paulonis, D. F., and Duvall, D. S. (1974). Coherency strengthening in Ni base alloys hardened by DO22 gamma double-prime precipitates. *Metallurgical Transactions*, 5(1):143–153.

[89] Oliver, W. and Pharr, G. (1992). An improved technique for determining hardness and elastic modulus using load and displacement sensing indentation experiments. *Journal of Materials Research*, 7(6):1564–1583.

[90] Oliver, W. and Pharr, G. (2004). Measurement of hardness and elastic modulus by instrumented indentation: Advances in understanding and refinements to methodology. *Journal of Materials Research*, 19(01):3–20.

[91] Ono, Y., Yuri, T., Sumiyoshi, H., Takeuchi, E., Matsuoka, S., and Ogata, T. (2004). High-Cycle Fatigue Properties at Cryogenic Temperatures in Inconel 718 Nickel-based Superalloy. *Materials Transactions*, 45(2):342–345.

[92] O'Regan, P., Prickett, P., Setchi, R., Hankins, G., Jones, N., ORegan, P., Prickett, P., Setchi, R., Hankins, G., Jones, N., Regan, P. O., Prickett, P., Setchi, R., Hankins, G., and Jones, N. (2016). Metal Based Additive Layer Manufacturing: Variations, Correlations and Process Control. *Procedia Computer Science*, 96:216–224.

[93] Oyen, M. L. (2010). *Handbook of Nanoindentation: With Biological Applications*. Pan Stanford, Singapore.

[94] Paulonis, D. F., Oblak, J. M., and Duvall, D. S. (1969). Precipitation in Nickel-base Alloy 718. Technical report, Pratt and Whitney Aircraft.

[95] Paulonis, D. F. and Schirra, J. J. (2001). Alloy 718 at Pratt & Whitney: Historical Perspective and Future Challenges. *Superalloys*, 718(625,706):13–23.

[96] Pavlina, E. and Van Tyne, C. (2008). Correlation of Yield Strength and Tensile Strength with Hardness for Steels. *Journal of Materials Engineering and Performance*, 17(6):888–893.

[97] Perez-Prado, M.-T. and Kassner, M. (2015). Diffusional Creep. In Kassner, M. E., editor, *Fundamentals of Creep in Metals and Alloys*, pages 103–108. Elsevier, third edit edition.

[98] Peyton, E. (2019). Conversation with Eric Peyton, 25 Nov 2019.

[99] Plimpton, S., Thompson, A., and Slepoy, A. (2017). SPPARKS pin command.

[100] Popovich, V. A., Borisov, E. V., Popovich, A. A., Sufiiarov, V. S., Masaylo, D. V., and Alzina, L. (2017). Impact of heat treatment on mechanical behaviour of Inconel 718 processed with tailored microstructure by selective laser melting. *Materials & Design*, 131:12–22.

[101] Pröbstle, M., Neumeier, S., Hopfenmüller, J., Freund, L., Niendorf, T., Schwarze, D., and Göken, M. (2016). Superior creep strength of a nickel-based superalloy produced by selective laser melting. *Materials Science and Engineering: A*, 674:299–307.

[102] Qi, H., Azer, M., and Ritter, A. (2009). Studies of Standard Heat Treatment Effects on Microstructure and Mechanical Properties of Laser Net Shape Manufactured INCONEL 718. *Metallurgical and Materials Transactions A*, 40(10):2410–2422.

[103] Raabe, D. (2002). Cellular Automata in Materials Science with Particular Reference to Recrystallization Simulation. *Annual Review of Materials Research*, 32(1):53–76.

[104] Radavich, J. (1989). The Physical Metallurgy of Cast and Wrought Alloy 718. In *Superalloys 718 Metallurgy and Applications (1989)*, pages 229–240. TMS.

[105] Radhakrishnan, B. and Thompson, R. G. (1989). Solidification of the nickel-base superalloy 718: A phase diagram approach. *Metallurgical Transactions A*, 20(12):2866–2868.

[106] Raghavan, A., Wei, H. L., Palmer, T. A., and DebRoy, T. (2013). Heat transfer and fluid flow in additive manufacturing. *Journal of Laser Applications*, 25(5):52006.

[107] Raghavan, N., Dehoff, R. R., Pannala, S., Simunovic, S., Kirka, M. M., Turner, J., Carlson, N., and Babu, S. S. (2016). Numerical modeling of heat-transfer and the influence of process parameters on tailoring the grain morphology of IN718 in electron beam additive manufacturing. *Acta Materialia*, 112:303–314.

[108] Raghavan, S., Zhang, B., Wang, P., Sun, C.-N., Nai, M. L. S., Li, T., and Wei, J. (2017). Effect of different heat treatments on the microstructure and mechanical properties in selective laser melted INCONEL 718 alloy. *Materials and Manufacturing Processes*, 32(14):1588–1595.

[109] Reed, R. C. (2006). *The Superalloys*. Cambridge University Press, Cambridge.

[110] Rodgers, T. M., Madison, J. D., and Tikare, V. (2017). Simulation of metal additive manufacturing microstructures using kinetic Monte Carlo. *Computational Materials Science*, 135:78–89.

[111] Rollett, A. D., Srolovitz, D. J., and Anderson, M. P. (1989). Simulation and theory of abnormal grain growth-anisotropic grain boundary energies and mobilities. *Acta Metallurgica*, 37(4):1227–1240.

[112] Roylance, D. (2001). Stress-Strain Curves. Technical report, MIT.

[113] SAE International (2009). AMS5663: UNS N07718, 1775 °F (968 °C) Solution Heat Treated, Precipitation Hardenable.

[114] SAE International (2011). AMS2774: Heat Treatment Wrought Nickel Alloy and Cobalt Alloy Parts.

[115] SAE International (2016). AMS5662: UNS N07718 1775 °F (968 °C) Solution Heat Treated, Precipitation Hardenable.

[116] Sames, W. J. (2015). *Additive manufacturing of inconel 718 using electron beam melting: processing, post-processing, & mechanical properties*. PhD thesis, Texas A&M University.

[117] Sames, W. J., List, F. A., Pannala, S., Dehoff, R. R., and Babu, S. S. (2016). The metallurgy and processing science of metal additive manufacturing. *International Materials Reviews*, 6608(March):1–46.

[118] Schafrik, R., Ward, D., and Groh, J. (2001). Application of Alloy 718 in GE Aircraft Engines: Past, Present and Next Five Years. *Superalloys 718, 625, 706 and Various Derivatives (2001)*, pages 1–11.

[119] Schirra, J., Caless, R., and Hatala, R. (1991). The Effect of Laves Phase on the Mechanical Properties of Wrought and Cast + HIP Inconel 718. In *Superalloys 718, 625 and Various Derivatives (1991)*, pages 375–388. TMS.

[120] Schneider, J., Lund, B., and Fullen, M. (2018). Effect of heat treatment variations on the mechanical properties of Inconel 718 selective laser melted specimens. *Additive Manufacturing*, 21:248–254.

[121] Shassere, B., Greeley, D., Okello, A., Kirka, M. M., Nandwana, P., and Dehoff, R. (2018). Correlation of Microstructure to Creep Response of Hot Isostatically Pressed and Aged Electron Beam Melted Inconel 718. *Metallurgical and Materials Transactions A*, pages 1–11.

[122] Shellabear, M. and Nyrhilä, O. (2004). DMLS Development History and State of the Art. *Lane 2004*, pages 1–12.

[123] Siemens (2017). Siemens achieves breakthrough with 3D printed gas turbine blades. Technical report, Siemens.

[124] Simonelli, M., Tse, Y. Y., and Tuck, C. (2012). Microstructure of Ti-6Al-4V produced by selective laser melting. *Journal of Physics: Conference Series*, 371:12084.

[125] Slama, C. and Abdellaoui, M. (2000). Structural characterization of the aged Inconel 718. *Journal of Alloys and Compounds*, 306(1-2):277–284.

[126] Smith, W. F. and Hashemi, J. (2005). *Foundations of Materials Science and Engineering*. McGraw-Hill Science/Engineering/Math, 4th editio edition.

[127] Sochalski-Kolbus, L. M., Payzant, E. A., Cornwell, P. A., Watkins, T. R., Babu, S. S., Dehoff, R. R., Lorenz, M., Ovchinnikova, O., and Duty, C. (2015). Comparison of Residual Stresses in Inconel 718 Simple Parts Made by Electron Beam Melting and Direct Laser Metal Sintering. *Metallurgical and Materials Transactions A: Physical Metallurgy and Materials Science*, 46(3):1419–1432.

[128] Song, K. H. and Nakata, K. (2010). Microstructural and mechanical properties of friction-stir-welded and post-heat-treated Inconel 718 alloy. *Journal of Alloys and Compounds*, 505(1):144–150.

[129] Special Metals (2007). INCONEL alloy 718. Technical report, Special Metals.

[130] Strößner, J., Terock, M., and Glatzel, U. (2015). Mechanical and Microstructural Investigation of Nickel-Based Superalloy IN718 Manufactured by Selective Laser Melting (SLM). *Advanced Engineering Materials*, 17(8):1099–1105.

[131] Sun, S. H., Koizumi, Y., Saito, T., Yamanaka, K., Li, Y. P., Cui, Y., and Chiba, A. (2018). Electron beam additive manufacturing of Inconel 718 alloy rods: Impact of build direction on microstructure and high-temperature tensile properties. *Additive Manufacturing*, 23:457–470.

[132] Sundararaman, M. and Mukhopadhyay, P. (1993). Carbide Precipitation in Inconel 718. *High Temperature Materials and Processes*, 11(1-4):351–368.

[133] Sundararaman, M., Mukhopadhyay, P., and Banerjee, S. (1988a). Deformation behaviour of γ" strengthened inconel 718. *Acta Metallurgica*, 36(4):847–864.

[134] Sundararaman, M., Mukhopadhyay, P., and Banerjee, S. (1988b). Precipitation of the δ-Ni3Nb phase in two nickel base superalloys. *Metallurgical Transactions A*, 19(3):453–465.

[135] Sundararaman, M., Mukhopadhyay, P., and Banerjee, S. (1997). Carbide precipitation in nickel base superalloys 718 and 625 and their effect on mechanical properties. *TMS: Superalloys 718*, pages 625–706.

[136] Thomas, L. (2019). How Fast Do You Have to Quench? Hardenability of Steel.

[137] Thompson, R. G., Dobbs, J. R., and Mayo, D. E. (1986). The Effect of Heat Treatment on Microfissuring in Alloy 718. *Welding Journal*, pages 299–304.

[138] Tillmann, W., Schaak, C., Nellesen, J., Schaper, M., Aydinöz, M., and Hoyer, K.-P. (2017). Hot isostatic pressing of IN718 components manufactured by selective laser melting. *Additive Manufacturing*, 13:93–102.

[139] Tucho, W. M., Cuvillier, P., Sjolyst-Kverneland, A., and Hansen, V. (2017). Microstructure and hardness studies of Inconel 718 manufactured by selective laser melting before and after solution heat treatment. *Materials Science and Engineering: A*, 689:220–232.

[140] US Air Force (2006). C-5M Super Galaxy.

[141] Vastola, G., Zhang, G., Pei, Q. X., and Zhang, Y. W. (2016). Controlling of residual stress in additive manufacturing of Ti6Al4V by finite element modeling. *Additive Manufacturing*, 12:231–239.

[142] Voter, A. F. (2007). Introduction to the Kinetic Monte Carlo Method. In *Radiation Effects in Solids*, pages 1–23. Springer Netherlands.

[143] Wang, L., Fang, G., and Qian, L. (2018). Modeling of dynamic recrystallization of magnesium alloy using cellular automata considering initial topology of grains. *Materials Science and Engineering A*, 711:268–283.

[144] Wang, Y., Shi, J., and Liu, Y. (2019). Competitive grain growth and dendrite morphology evolution in selective laser melting of Inconel 718 superalloy. *Journal of Crystal Growth*, 521:15–29.

[145] Wang, Z., Guan, K., Gao, M., Li, X., Chen, X., and Zeng, X. (2012). The microstructure and mechanical properties of deposited-IN718 by selective laser melting. *Journal of Alloys and Compounds*, 513:518–523.

[146] Weisstein, E. W. (2019). Matrix Trace. *MathWorld - A Wolfram Web Resource*.

[147] Wright, J. (1933). INCONEL Trademark.

[148] Wright, S. I., Nowell, M. M., and Field, D. P. (2011). A Review of Strain Analysis Using Electron Backscatter Diffraction. *Microscopy and Microanalysis*, 17(03):316–329.

[149] Xu, Z., Murray, J., Hyde, C., and Clare, A. (2018). Effect of post processing on the creep performance of laser powder bed fused Inconel 718. *Additive Manufacturing*, 24:486–497.

[150] Zhao, X., Chen, J., Lin, X., and Huang, W. (2008). Study on microstructure and mechanical properties of laser rapid forming Inconel 718. *Materials Science and Engineering: A*, 478(1-2):119–124.

Appendix: Tabulated Tensile Data

The data in this section is presented in summary in Section 4.3.1 (p. 137) and discussed in Section 4.3.2 (p. 143).

Table A.1: Tensile test results for the vertical (90°) rectangular dog-bones

Spec. ID	Scan	Anneal Temp (°C)	E (MPa)	$YS_{0.2}$ (MPa)	UTS (MPa)	Elong. (%)
P09	skin	1010 °C/1h	135590	1069	1174	3.8
P12			126320	1042	1139	4.3
P16			127630	1027	1109	2.2
P17			130210	1025	1108	2.0
P18			121090	984	1076	2.9
P21			128550	1030	1121	3.6
Average	90°, skin	1010 °C/1h	128231	1030	1121	3.1
Std. Dev			4757	28	33	0.9
P07	skin	1160 °C/4h	140020	998	1112	3.5
P08			145430	1015	1129	4.2
P10			144710	1025	1091	1.4
P11			142050	1007	1121	3.3
P15			137490	984	1112	5.0
P24			135010	953	1068	3.7
Average	90°, skin	1160 °C/4h	140780	997	1106	3.5
Std. Dev			4083	26	22	1.2

Table A.2: Tensile test results for the horizontal (0°) rectangular dog-bones

Spec. ID	Scan	Anneal Temp (°C)	E (MPa)	$YS_{0.2}$ (MPa)	UTS (MPa)	Elong. (%)
O1	skin	1010 °C/1h	177500	1348	1481	16.6
O3			182440	1360	1464	11.9
O5			180860	1352	1477	15.1
O7			171870	1337	1478	18.9
O9			180150	1362	1477	15.9
O11			174350	1354	1490	15.9
Average	0°, skin	1010 °C/1h	177833	1347	1478	15.7
Std. Dev			4087	13.3	8.4	2.3
O2	skin	1160 °C/4h	179970	1167	1373	17.6
O4			179830	1172	1382	18.9
O6			180280	1159	1372	17.5
O8			179710	1162	1373	19.1
O10			164200	1095	1288	19.6
O12*			160630	1063	1226	9.7
Average	0°, skin	1160 °C/4h	176800	1151	1358	18.5
Std. Dev			7047	32	39	0.9

* premature failure during testing; all values are omitted from group averages.

Table A.3: Tensile test results for the vertical (90°) cylindrical specimens

Spec.	Scan	Anneal Temp (°C)	Young's Mod (MPa)	Yield (MPa)	UTS (MPa)	Elongation (%)
F13	cont	1010 °C/1h	192470	1260	1410	3.6
F21			204510	1260	1460	9.6
F35			211440	1180	1370	3.6
F36			218690	1100	1300	3.9
F41			210990	1170	1400	3.8
F14	island	1010 °C/1h	200430	1260	1450	8.0
F19			202010	1270	1460	10.0
F31			213420	1230	1470	9.9
F33			211890	1230	1450	12.5
F37			211570	1190	1470	10.6
F20	strip	1010 °C/1h	199850	1250	1460	12.4
F22			204490	1200	1420	5.4
F24			specimen not tested	–	–	–
F29			208160	1140	1330	2.1
F42			211080	1120	1330	2.6
Average	all, 90°	1010 °C/1h	207214	1204	1413	7.0
Std. Dev			6897	56	58	3.8
F16	cont	1160 °C/4h	212480	1110	1260	4.9
F17			213633	1099	1240	4.4
F23			209920	1100	1290	6.9
F32			212120	1050	1330	17.6
F34			211340	1100	1320	7.6
F25	island	1160 °C/4h	207160	1120	1340	15.4
F26			207070	1090	1340	16.9
F28			202850	1120	1270	5.4
F30			208410	1020	1240	5.1
F38			211290	1110	1340	15.6
F15	strip	1160 °C/4h	213133	1120	1332	9.9
F18			203030	1100	1260	5.1
F27			212390	1120	1340	14.5
F39			211460	1110	1350	19.1
F40			211190	1120	1350	17.1
Average	all, 90°	1160 °C/4h	209832	1099	1307	11.0
Std. Dev			3431	28	42	5.6

Table A.4: Tensile test results for the diagonal (45°) cylindrical specimens

Spec.	Scan	Anneal Temp (°C)	Young's Mod (MPa)	Yield (MPa)	UTS (MPa)	Elongation (%)
G23	cont	1010 °C/1h	211300	1450	1610	12.5
G24			219020	1510	1610	4.2
H06			specimen not tested	–	–	–
H07			212600	1470	1620	7.9
H10			213680	1510	1590	3.4
G16	island	1010 °C/1h	215840	1420	1570	9.1
G18			214500	1400	1470	2.7
G22			214870	1420	1510	3.8
H05			211870	1400	1490	3.6
H11			212680	1430	1590	8.5
G25	strip	1010 °C/1h	212850	1190	1390	8.6
G27			211230	1460	1570	5.1
H03			213490	1450	1600	11.1
H08			211990	1440	1540	3.6
H13			211360	1460	1540	3.6
Average	all, 45°	1010 °C/1h	213377	1429	1550	6.3
Std. Dev			2149	77	66	3.3
G15	cont	1160 °C/4h	212110	1160	1390	16.2
G17			213310	1150	1270	3.0
G19			212180	1190	1380	8.2
H01			210630	1170	1410	17.4
H15			211900	1170	1290	4.9
G14	island	1160 °C/4h	213560	1150	1230	2.3
G20			213460	1180	1400	16.8
H02			212880	1180	1360	7.6
H04			211990	1170	1330	5.8
H14			211050	1150	1300	4.9
G13	strip	1160 °C/4h	211910	1150	1410	18.9
G21			specimen not tested	–	–	–
G26			specimen not tested	–	–	–
H09*			215310	1170	1210	3.1
H12*			187520	1190	1240	4.5
Average	all, 45°	1160 °C/4h	210601	1168	1343	9.6
Std. Dev			7040	15	62	6.4

* premature failure during testing; UTS and elongation are omitted from group averages.

REPORT DOCUMENTATION PAGE

Form Approved
OMB No. 0704–0188

The public reporting burden for this collection of information is estimated to average 1 hour per response, including the time for reviewing instructions, searching existing data sources, gathering and maintaining the data needed, and completing and reviewing the collection of information. Send comments regarding this burden estimate or any other aspect of this collection of information, including suggestions for reducing this burden to Department of Defense, Washington Headquarters Services, Directorate for Information Operations and Reports (0704–0188), 1215 Jefferson Davis Highway, Suite 1204, Arlington, VA 22202–4302. Respondents should be aware that notwithstanding any other provision of law, no person shall be subject to any penalty for failing to comply with a collection of information if it does not display a currently valid OMB control number. **PLEASE DO NOT RETURN YOUR FORM TO THE ABOVE ADDRESS.**

1. REPORT DATE *(DD–MM–YYYY)*	2. REPORT TYPE	3. DATES COVERED *(From — To)*
26–03–2020	Doctoral Dissertation	Sep 2016–Mar 2020

4. TITLE AND SUBTITLE

Solution Anneal Heat Treatment to Enhance Mechanical Performance of Additively Manufactured IN718

5a. CONTRACT NUMBER

5b. GRANT NUMBER

5c. PROGRAM ELEMENT NUMBER

6. AUTHOR(S)

Newell, David J., Major, USAF

5d. PROJECT NUMBER

5e. TASK NUMBER

5f. WORK UNIT NUMBER

7. PERFORMING ORGANIZATION NAME(S) AND ADDRESS(ES)

Air Force Institute of Technology
Graduate School of Engineering and Management (AFIT/EN)
2950 Hobson Way
WPAFB, OH 45433-7765

8. PERFORMING ORGANIZATION REPORT NUMBER

AFIT-ENY-DS-20-M-274

9. SPONSORING / MONITORING AGENCY NAME(S) AND ADDRESS(ES)

Air Force Research Laboratory
Aerospace Systems Directorate
2130 Eighth Street
WPAFB, OH 45433-7542

10. SPONSOR/MONITOR'S ACRONYM(S)

AFRL/RQ

11. SPONSOR/MONITOR'S REPORT NUMBER(S)

12. DISTRIBUTION / AVAILABILITY STATEMENT

DISTRIBUTION STATEMENT A. APPROVED FOR PUBLIC RELEASE; DISTRIBUTION UNLIMITED

13. SUPPLEMENTARY NOTES

This work is declared a work of the U.S. Government and is not subject to copyright protection in the United States.

14. ABSTRACT

Nickel-based superalloy IN718 is an excellent alloy for AM via LPBF. As-built LPBF IN718 has a vertically aligned, columnar microstructure which translates into orthotropic mechanical behavior. Post-process heat treatments for IN718 were developed 60 years ago for wrought processes and do not mitigate the microstructure of AM processes. Recrystallization is required to remove the columnar microstructure. This research investigated the evolution of LPBF IN718 microstructure under a recrystallizing solution treatment of 1160 °C. It was shown that this higher temperature mitigated the anisotropy resulting from the fabrication process. Grain size and recrystallization were evaluated throughout the evolution. The X–Y and X–Z planes were compared to find the point in time at which the annealing process produced equiaxed, isotropic grains. An equiaxed microstructure was successfully achieved through recrystallization and grain growth. Isotropic tensile properties were achieved with a recrystallization treatment of 1160 °C for 4 hours and validated via tensile testing. Microstructural evolution was simulated in a kinetic Monte Carlo model using a novel approach of combining stored and boundary energies of the as-built LPBF IN718 with pinning particles. The models accurately approximated the experimental results of recrystallization and JMAK model constants.

15. SUBJECT TERMS

IN718, additive manufacturing, solution treatment, recrystallization, anisotropy

16. SECURITY CLASSIFICATION OF:			17. LIMITATION OF ABSTRACT	18. NUMBER OF PAGES	19a. NAME OF RESPONSIBLE PERSON
a. REPORT	b. ABSTRACT	c. THIS PAGE			Dr Anthony Palazotto, AFIT/ENY
U	U	U	U	244	19b. TELEPHONE NUMBER *(include area code)* (937) 255-3636 x4599 anthony.palazotto@afit.edu